Fabrication of hierarchical hybrid nanostructured electrodes based on nanoparticles decorated carbon nanotubes for Li-Ion batteries

Mariam Ezzedine

NNT : 2017SACLX105

Thèse de doctorat de l'Université Paris-Saclay préparée Ecole Polytechnique

Ecole doctorale n°573
INTERFACES : Approches Interdisciplinaires / Fondements, Applications Et Innovations

par

Mme. Mariam Ezzedine

Fabrication d'électrodes nanostructurées hybrides hiérarchisées à base de nanotubes de carbone décorés par des nanoparticules pour les batteries Li-Ion

Thèse présentée et soutenue à l'Ecole Polytechnique, le 20.12.17.

Composition du Jury :

M.	Sylvain FRANGER Professeur, Université Paris-Sud (ICMMO)	(Président)
M.	Lorenzo STIEVANO Professeur, Université de Montpellier (ICGM)	(Rapporteur)
Mme.	Katia GUERIN-ARAUJO DA SILVA Maitre de Conférences, Université Clermont Auvergne (ICCF)	(Rapportrice)
M.	Jean-Pierre PEREIRA-RAMOS Directeur de Recherche CNRS, Université Paris-Est (ICMPE)	(Examinateur)
M.	Costel-Sorin Cojocaru Directeur de Recherche CNRS, Ecole Polytechnique (LPICM)	(Directeur de thèse)
Mme.	Ileana FLOREA Ingénieur de Recherche, Ecole Polytechnique (LPICM)	(Co-encadrante)

Acknowledgements

Trois ans déjà, me voilà finalement arrivée au bout de mon aventure. Ce travail de thèse à la fois stimulant et pesant est accompli. Trois années formidables qui sont passées à la vitesse de la lumière au sein de LPICM.

Au premier chef, je remercie la "Chaire et Energie" qui a financé ma thèse. Je remercie également les membres de mon jury: Lorenzo Stievano, Katia Guerin-Araujo Da Silva, Jean-Pierre Pereira-Ramos et Sylvain Franger pour avoir accepté de juger ce travail.

Je voudrais exprimer ma plus profonde gratitude, ma gratitude incommensurable à mon directeur de thèse Costel-Sorin Cojocaru. Merci d'abord d'avoir cru en moi, de m'avoir soutenue dans les moments les plus difficiles. Ces moments de doute où tout espoir à mes yeux était vain. Merci d'avoir répété sans cesse ces mots magiques: "mais non il ne faut pas perdre espoir tu vas y arriver". Merci pour ta disponibilité, pour m'avoir permis lors des moments difficiles de te poser maintes questions. Merci d'avoir pris le temps de discuter avec moi. Merci pour les réparations et les bricoles qui m'ont permis d'avancer dans la décoration de mes beaux nanotubes de carbone. Merci aussi pour ces discussions passées dans la salle Fenix. Enfin, mille merci pour tes conseils et surtout pour ta grande patience. Les mots me manquent pour t'exprimer toute la gratitude que je ressens. Merci !

Ileana Florea ma super encadrante, sache aussi qu'un simple merci n'est point suffisant pour te remercier de ta présence et de ton aide qui sont très précieux à mes yeux. Toutefois, merci pour tous les beaux clichés de microscopie et les heures que tu as passées à Nanomax pour moi. Je te suis éternellement reconnaissante pour avoir été à mes côtés, pour m'avoir épaulée, conseillée, soutenue et pour m'avoir surtout remonté le moral. Chacun de ces moments passés dans ton bureau et à Nanomax sont inoubliables. Je pense à nos discussions de tout et rien, à mes larmes versées et à tes mots doux qui me réconcilie avec mon travail. Ma thèse n'aurait jamais été pareil sans TOI !!

Je tiens à remercier également mon équipe NanoMade : Léo, Garry, Didier, Marc, Fatima, Salomé, Leandro et Mihai. Salomé, merci d'avoir été présente quand j'avais besoin de toi et surtout pendant les derniers jours de rédaction sur Latex (beaucoup de panique). Leandro merci de m'avoir avisé à l'électrodéposition. Mihai, "mon collègue de batterie", merci pour toutes nos discussions et surtout merci pour ta patience, et pour m'avoir éclairé avec tes réponses à mes questions avant ma soutenance.

Fatima Jardali "babe" ma très chère amie et ma très chère collègue de bureau. Merci pour ta compagnie pendant ces trois ans. Trois ans de joie, de rires, de larmes et surtout de stress. Je suis reconnaissante de t'avoir croisé et surtout d'avoir partagé un temps et un espace avec toi. Je suis reconnaissante à cette amitié qui est née entre nous.

Je tiens à remercier Sandrine Tusseau-Nenez pour m'avoir formé sur la DRX et pour les heures que tu as passées en ma compagnie devant la machine afin de comprendre son

obstination à ne pas démarrer.
Je remercie toute l'équipe administrative, ainsi que l'équipe de support du LPICM.
Je finis ces remerciements en pensant à ma famille: mon père, ma mère et mon frère. Merci de m'avoir soutenue pendant 8 ans d'études, et merci de m'avoir encouragée à viser haut.
Je suis émue et triste à l'idée de quitter ce labo un jour. Merci pour m'avoir accordé encore un an pour travailler parmi vous. Désormais adviendra le jour où je dois me séparer de vous, ce jour fatidique qui m'obligera à quitter le nid m'attriste déjà.

Contents

List of Figures

List of Tables

General Introduction

Most of the energy used on earth is originated from the sun. Primary energy sources take many forms, including nuclear energy and fossil energy such as coal, oil and natural gas. Other than these, energy resources also include renewable sources e.g., wind, solar, geothermal and hydropower. These sources are then converted to electricity to serve the humans. The constantly improving standards of living of the world's population heavily rely on energy consumption, which is increasing rapidly in proportion to the growth in the economy as well as in the global population. When considering the increasing population of our world, we could imagine extraordinary large energy consumption in the near future. According to recent studies, the annual worldwide energy consumption is currently estimated to be 13 trillion watts.[1] The world energy consumption will grow by 48% between 2012 and 2040. Most of this growth will come from emerging countries, such as China and India. Out of all energy resources, fossil fuels (oil, coal, and natural gas) will still account for more than three-quarters of the world energy consumption through 2040 (see figure 1). [2] However, most of the non-renewable fossil fuel energy will be exhausted within the next 200 years.[3] Additionally, greenhouse gas emission is rapidly becoming a serious problem of environmental pollution. The conservation of natural resources and reduction of greenhouse gases are considered as major challenges of the global economies and governments.[4] As the world population keeps rising and our lifestyle demands more resources, humankind is forced to move towards sustainable and renewable resources. In the recent years, various clean energies have been explored as energy alternatives, such as solar and wind power.[5] These clean renewable energy resources are highly time or region-dependent. It is essential, therefore, to develop effective energy storage media in order to use such intermittent energy sources in an efficient way.[6] Great efforts have been made in searching for viable solutions, including Electrical Energy Storage (EES), load shifting through demand management, interconnection with external grids, etc. Amongst all the possible solutions, EES has been recognized as one of the most promising approaches. EES technology refers to the process of converting energy from one form (mainly electrical energy) to a storable form and reserving it in various mediums. Thereafter, the stored energy can be converted

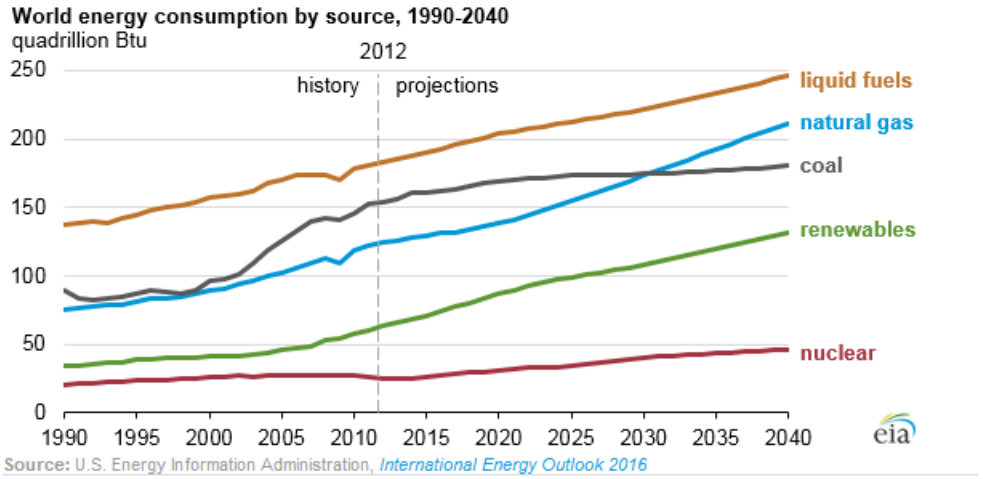

FIGURE 1: **World energy consumption of the year 1990-2040.** [2]

back into electrical energy when needed.[7]

Among the different EES technologies, lithium-ion batteries (LIBs) is one of the most promising candidates for energy storage due to their high operating voltage, high energy and high power density.[8] Current Li-ion batteries do not yet meet the expectation of tomorrow′s energy storage system. New batteries with significantly higher energy density and long cycle life would have significant benefits. The enhancement of energy density of LIBs can be achieved by developing either high capacity cathode and anode materials, or high voltage cathode materials. The development of new electrode materials with improved electrochemical performance is highly required. In the early 20th century, the discovery of the allotropes of carbon (fullerene C_{60} and carbon nanotubes) gave a stimulus to the development of nanomaterials and made researchers ready to explore more avidly the potential use of these materials, including Li-ion battery applications.[9] From this perspective, the choice of electrode materials will play an important role in the next-generation battery design. Electric vehicles manufacturers and renewable energy storage facilities require an increase in both energy and power density of current batteries technology. This is where nanomaterials are expected to provide a sizeable increment in performance owing to their unique properties. In fact, nanomaterials are potentially able to store more charge than conventional micron-sized materials because they offer additional lithium storage sites. Also, nanosized materials can accommodate with lithium ions in much shorter time than bulk structures, making quick charge and discharge possible, thus providing the tremendous power density necessary to accelerate a car and to store energy under peak conditions of wind and solar energy generation.[10]

Outline of the thesis

Sulfur and silicon are both attractive electrode materials for next generation rechargeable lithium ions batteries because of their abundance, high theoretical capacity, and low cost. This thesis is mainly focused on the fabrication of nanostructured sulfur cathode and nanostructured silicon anode, and then the assembly of the full cell based on nanostructured electrodes for LIBs with improved energy and power densities, and cycle life.

The manuscript begins with a general introduction, which gives an overview on the importance of the electrical energy storage in the context of the world energy demands, and is composed of five Chapters.

In the first Chapter, an introduction to generalities a LIB system and a brief history of the LIB development are given. The operating principles of LIBs are also explained. Summaries on the cathode and anode materials used in LIBs system are presented. Finally, the challenges that are existing nowadays in LIBs and the solutions that are offered by different nanomaterials are reviewed. The second Chapter offers an overview on carbon nanotubes and their fabrication methods and presents the synthesis method of vertically aligned carbon nanotubes on two different commercial substrates, allowing for the design of the nanostructured current collector. The third Chapter is devoted to the sulfur cathode electrode. It begins by a general background on Li/S batteries. Then, it describes the experimental work for the nanofabrication of the sulfur electrode based on carbon nanotube carpets and proposes further improvements of the sulfur electrode by coating it with two different materials. The corresponding results obtained for the electrochemical testing are reviewed. The fourth Chapter is focused on the silicon anode electrode. It covers the literature background of silicon as anode material for LIBs. To tackle the problems of silicon anode, such as poor cyclability and early capacity fading due to significant volume variation during lithiation/ delithiation processes, nanostructuration of the silicon anode based on silicon nanoparticles-decorated-carbon-nanotubes was fabricated by two different techniques. The detailed experimental procedures and the electrochemical performances are also presented. The fifth Chapter is devoted to a metallic-lithium-free battery. The two electrodes based on hybrid nanostructured cathode (S@VACNTs) and anode (Si@VACNTs) electrodes were assembled in order to obtain the full cell. A first trial and a proof of our concept was demonstrated.
Finally, a general conclusion summarizes the overall work and provides some perspectives for further research work related to such nanostructured electrodes.

Chapter 1

Introduction

1.1 A brief history

A battery is a system that converts chemical energy into electrical energy. The first battery was created in 1800 by Alessandro Volta. It consisted of a column made with superimposed discs of three different substances: two metals, such as Zn and Cu, and pieces of wet cardboard soaked in salt water, placed in the same order. When connecting the two metal discs at the extremities of the column, the apparatus produced a steady electric current.[11] Batteries can be broadly divided into two categories; primary (or disposable) batteries and secondary (or rechargeable) batteries, depending on whether or not they can be charged. The primary batteries are not rechargeable and their electrochemical reaction is irreversible, while the secondary batteries are built to be charged and discharged for multiple cycles, i.e the electrochemical reaction is reversible. In primary batteries category, one can find the "Daniel cell" battery developed in 1820 followed by "Leclanché" battery (Zn/MnO_2) in 1866. In 1859, Gaston Planté invented the lead-acid battery: the first rechargeable battery. These batteries are still widely available today, equipping almost all of our thermal vehicles. Their main advantage is their low cost, but they posses low specific energy and power density. To increase the energy density, new types of secondary batteries have started to appear gradually during the 20th century. Nickel-cadmium (Ni-Cd) technology was proposed in 1900 by Waldmar Jungner. However, the hazardous nature of cadmium has raised major environmental problems leading to the development, starting in 1975, of nickel-metal hydrides (Ni-MH) systems which are less toxic and have a higher energy density.

The discovery of reversible lithium intercalation in titanium disulfide (TiS_2) [12, 13] and molybdenum disulphide (MoS_2) [14] led to the development of rechargeable lithium batteries in the 1970s. However, various safety problems have been encountered on

TABLE 1.1: Characteristics and performance of commonly used rechargeable batteries.

Battery type	**Lead-Acid**	**Ni-Cd**	**Ni-MH**	**Li-ion**
Voltage (V)	2.0	1.2	1.2	4.1
Specific energy (Wh/kg)	35	35	75	150
Energy density (Wh/L)	70	100	240	400
Cycle life	200-250	400-500	400-500	>1000

the first batteries which used a lithium metal electrode and a liquid electrolyte. Upon continuous reversible charge and discharge cycles, dendritic Li forms on lithium surfaces due to uneven Li plating and hence causing short circuits and battery failure; hence, metallic lithium is not widely used as anode material in rechargeable batteries. Two solutions have been proposed to overcome these problems. The first one was proposed by Armand et al [15] and consists in replacing the liquid electrolyte with a solid electrolyte made of polymers, which is then referred to as a Li-polymer battery. The second was proposed in 1980 by D.W. Murphy [16] and B. Scrosati [17] and consists in replacing the metallic lithium electrode with a host material which receives lithium reversibly. Later in 1991, LIBs were commercialized and emerged for the first time by Sony Corporation. Since then, LIBs have gained a huge interest and a rapid development and advancement both in academic research and in business market.

1.2 Lithium-ion battery

Among a wide range of energy storage technologies, lithium-ion batteries, commonly abbreviated as LIBs or Li-ion batteries, have gained considerable interest because of their high specific energy, good cycle life, good power performance and lighter weight [18] compared to other battery systems (see figure 1.1 and Table 1.1).[19] Owing to their great characteristics, LIBs have been first widely applied in portable electronic devices. According to the recent market investigations, the share of worldwide sales for Ni-Cd and Ni-MH batteries are 23 and 14%, respectively. However, Li-ion portable batteries take up to 63% of the battery market.[20] Recently, Li-ion batteries are being intensively pursued in large-scale transportation applications especially in hybrid electric vehicles (HEV), plug in hybrid electric vehicles (PHEV) and electric vehicles (EV). LIBs are starting to be seriously considered as a solution to the intermittency problem in renewable energies, e.g. solar and wind.[21] The energy and power density of LIBs are generally higher than those of other rechargeable batteries such as lead acid, Ni-Cd or Ni-MH batteries (see Table 1.1).

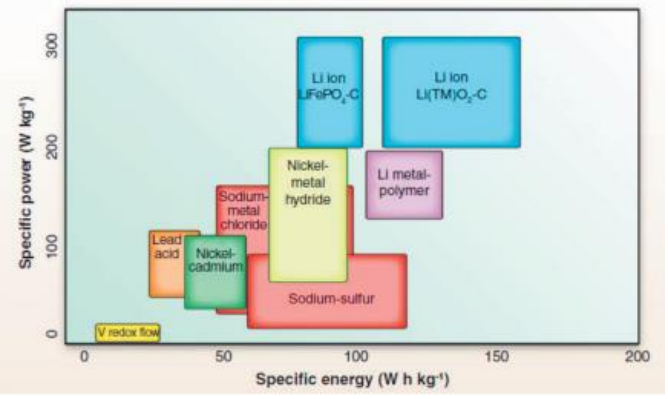

FIGURE 1.1: **Specific energy vs. specific power for different types of rechargeable batteries.**[22]

1.2.1 Why a Lithium-ion battery?

Lithium-ion systems are appealing for their use in batteries because of the lithium particularities. Lithium, the third element in the periodic table, is the most electropositive element (-3.04V at 25°C vs standard hydrogen electrode (SHE)), generating a large potential difference when paired with a positive electrode material (see Table 1.1) In addition, due to its small radius, 78 ppm, Li^+ ion is the lightest amongst all metallic ions. This characteristic gives it a great mobility during the intercalation/ deintercalation processes in a material and during the migration inside the electrolyte. Additionally, Li^+ ion can easily penetrate within the vacant sites of many crystalline meshes to form a wide variety of compounds. Finally, and thanks to its low density (0.53 g cm^{-3}), LIBs present higher gravimetric and volumetric energy densities than other battery systems (see figure 1.1).[19]

1.2.2 Mechanisms of charging and discharging

A Li-ion system is composed of an electrochemical cell including a positive electrode, commonly named cathode and a negative electrode called anode separated by an electrolyte which allows a good ion transfer and a poor electron conductivity. The cathode materials are intercalation compounds of Li^+ ion often made from a lithium metal oxide whilst the anode materials, most of the time, consist of graphitic carbon. The electrolyte is an organic solvent composed of a lithium salt, usually $LiPF_6$, dissolved in a mixture of ethylene carbonate (EC) and dimethyl carbonate (DMC). A separator which

is a porous polymer is placed between the positive and the negative electrodes to prevent their contact, but still allowing the transport of Li^+ ions. Throughout the working process of the battery, redox reactions take place inside the cell. During the discharging process, the Li^+ ions flow spontaneously from the anode, through the electrolyte, and embeds into the cathode. This generates an electron flow from the negative to the positive electrode through the external circuit. During the charging process, the ionic and electronic processes are reversed, i.e., the ions migrate from the positive to the negative electrode. These two processes are referred as deintercalation and intercalation mechanisms of lithium. The lithium-ion battery is also known as a "rocking-chair battery", since Li^+ ions migrate back and forth between the two electrodes during cycling without being reduced to a metallic form (see figure 1.2).

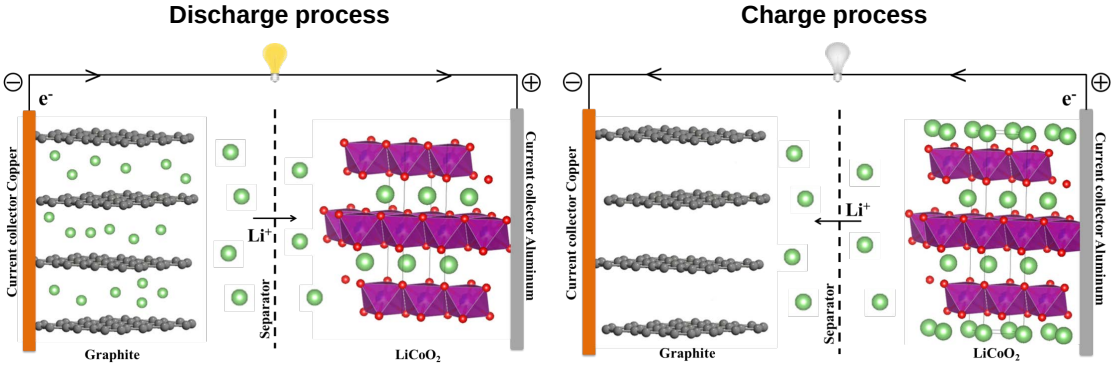

FIGURE 1.2: **Schematic of a Li-ion battery operating during discharge and charge processes**. Left: discharging process; Right: charging process.

For example, in a commercial Li-ion battery composed of graphite (anode) and $LiCoO_2$ (cathode), the reactions that take place during the discharging and charging processes on the anode and cathode are the following:

At the anode: $Li_xC_6 \overset{discharge}{\underset{charge}{\rightleftharpoons}} C_6 + x\mathbf{e}^- + xLi^+$

At the cathode: $Li_{1-x}CoO_2 + x\mathbf{e}^- + xLi^+ \overset{discharge}{\underset{charge}{\rightleftharpoons}} LiCoO_2$

Overall reaction: $Li_{1-x}CoO_2 + Li_xC_6 \overset{discharge}{\underset{charge}{\rightleftharpoons}} LiCoO_2 + C_6$

The performance of LIBs crucially depends on the nature and the characteristics (morphology, structure and composition) of the electrode material considered for both electrodes. The main parameters generally used to evaluate the quality of the electrode material are the following:

- Cell potential (V): is the potential difference between the positive and the negative electrode which, in turn, depends on the composition of the electrodes. A larger difference of the standard potential between cathode and anode is desired for a full cell, since the output energy is the product of voltage and capacity. However, this potential difference has to be within the potential window of the electrolyte that is in use, in order to prevent electrolyte decomposition.

- Cell capacity: is the quantity of charge that a battery can deliver to a given current. It is expressed in Ampere-hour (Ah). The performance of each electrode can be estimated by its specific capacity, expressed in Ah kg^{-1}, which corresponds to the ratio of the capacity to the mass of the active material. The theoretical specific capacity of an electrode depends on the number of electrons that can be exchanged during the same charge or discharge process per mole of active material. It can be calculated using the following equation:

$$capacity_{theo} = \frac{F \times ne^{-}}{3600 \times M} \tag{1.1}$$

  Where ne^{-} is the number of electrons transferred during the electrochemical reactions, F is the Faraday constant (96,485.33 C mol^{-1}) and M is the molecular weight of the active material (g mol^{-1}).

- Coulombic efficiency: is the ratio of number of charges that enter the battery during charging (charge capacity) to the number of charges that can be extracted during discharging (discharge capacity).

- Gravimetric and volumetric energy density: are the energy per unit weight (gravimetric Wh Kg^{-1}) or unit volume (volumetric Wh L^{-1}).
  Gravimetric energy density= (Specific capacity/ Kg) × Cell voltage
  Volumetric energy density= (Specific capacity/ L) × Cell voltage

- Power density: is the battery power that represents the speed at which the energy can be delivered to the load and it is expressed in (W/Kg or W/L) .
  Power density= Energy density/ Time.

- Rate capability or (C-rate): is used to evaluate how fast Li^{+} ions can be transferred. For example, C/2 means a current allowing a full charge or discharge in 2 hours.

1.2.3 Electrode materials

As mentioned previously, the electrochemical performance of the LIBs is largely dictated by the choice of the electrode materials. In general, the electrode materials are a mixture of an active material, a conductive material and a binder cohered to the current collector (typically copper foil for anode and respectively aluminium foil for cathode). The different electrode materials are classified according to their specific capacities and their electrochemical potentials. The materials with a potential higher than 2V are defined as a cathode material and those with a potential lower than 2V is defined as an anode material. In order to obtain a battery with a high energy density, the two electrode materials must have a high specific capacity and a large potential difference between them. For a high specific capacity, the quantity of Li^+ ions inserted and extracted from the electrode materials must be large during the charge and the discharge processes. For obtaining a large potential difference, the negative electrodes must have a low reduction/ oxidation potential, typically as close as possible to that of the lithium, whereas the positive electrodes must work at a high potential. The potentials and specific capacities of various electrode materials are summarized in figure 1.3.[20]

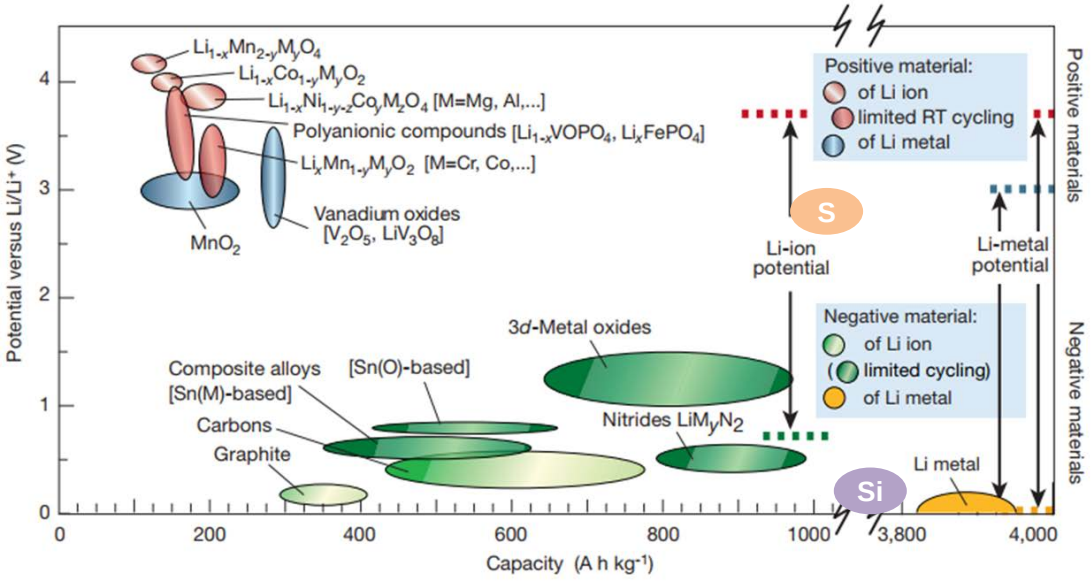

FIGURE 1.3: **Schematic illustration of electrode materials and their electrochemical performances in the current and the future Li-ion technologies.**[20]

1.2.3.1 Cathode materials

There are several possible types or families of materials that can potentially be considered for the positive electrode of a Li-ion battery. The cathode materials can be divided into three major categories:

1. Layered transition metal materials ($LiMO_2$)
2. Spinel materials (LiM_2O_4)
3. Olivine structured oxide materials ($LiMPO_4$)

The schematic representation of their crystal structure is illustrated in figure 1.4.[23]

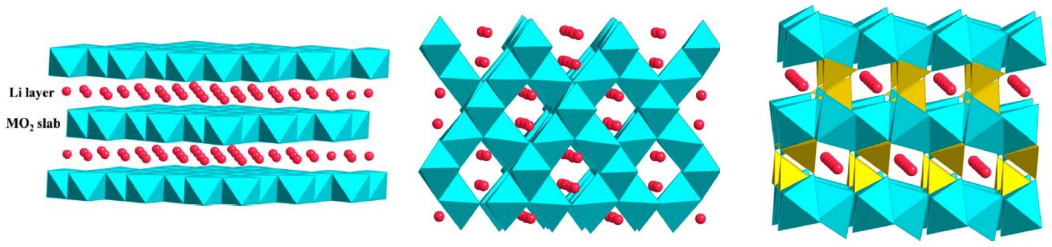

FIGURE 1.4: **Crystal structure of layered $LiMO_2$ (left), Spinel LiM_2O_4 (middle) and Olivine $LiMPO_4$ (right)**[23]

.

- **Layered transition metal materials ($LiMO_2$)**

  The discovery of lithium cobalt oxide $LiCoO_2$ (LCO) was attributed to Goodenough's team in 1980.[24] It was the first cathode material to be commercialized by Sony Corporation in 1991 and is still used in many commercial LIBs.[25] The structure of LCO consists of alternating cobalt dioxide CoO_2 and Li layers where Li and Co are octahedrally coordinated. In such a layered structure, Li^+ ions can be easily extracted and inserted in the two dimensional path. The intercalation/ deintercalation of lithium ions occurs between 3.5 - 4.2V vs Li/Li^+.[26] The theoretical capacity of LCO is 273 mAh g^{-1} , however it can only deliver a practical capacity of about 140 mAh g^{-1} due to instability of the structure when more than half of the Li^+ ions are extracted. In addition, LCO based Li-ion batteries are rather expensive due to the high price and low abundancy of Co in comparison to others environmental friendly transition metal ions, such as nickel [25] and iron [27].

Among the transition metal oxides, $LiNiO_2$ has drawn a great interest as an alternative cathode for rechargeable LIBs. This is mostly because of its high theoretical specific capacity of 275 mAh g^{-1}[25], the relative low toxicity and the low production cost as compared to other layered oxides. However, stoichiometric $LiNiO_2$ is very difficult to be synthesized compared to LCO. $LiNiO_2$ requires an utmost care in the synthesis process, else the resulting $LiNiO_2$ sample would suffer from twin intricacies: off-stoichiometry and cation mixing.[28] In the former case, $Li_{1-x}Ni_{1+x}O_2$ would form rather than a stoichiometric $LiNiO_2$ during preparation. In the latter case, Ni^{2+} tends to occupy the Li sites, which would cause a cation mixing in $LiNiO_2$. This ruins the ideally layered structure and disturbs the Li^+ ions from undergoing the easy movement for intercalation and deintercalation during cycling, thus resulting in a declined electrochemical performance.

- **Spinel materials (LiM_2O_4)**

  The first successful effort on reversible Li-ion intercalation on a spinel material, lithium-manganese oxide $LiMn_2O_4$ (LMO), was proposed in the early 1980s by Thackeray et al [29], as an alternative positive electrode material. Despite that the manganese is considered as a cheap, abundant and environmentally friendly element, the practical capacity of the LMO cathode is below 120 mAh g^{-1}. Additionally, LMO based cells have a low cycle life due to the dissolution of Mn^{2+} in the electrolyte during cycling.[30] Several approaches have been proposed to stabilize LMO electrodes, as for instance substitution of Mn with other cations such as magnesium (Mg), chromium (Cr), iron (Fe) and copper (Cu) [31] and coating of LMO with zinc oxide (ZnO).[32] However, more work is still needed in order to commercialize this electrode material.

- **Olivine structured oxide materials ($LiMPO_4$)**

  From the olivine class of cathode materials for LIBs, lithium iron phosphate $LiFePO_4$ (LFP), was introduced in 1997.[27] LPF has gathered huge attention and has also been already commercialized. It has been widely studied as a cathode material due to several advantages: lower cost, availability, environmental benignity and thermal stability compared to LCO. The material has a relatively lower voltage of 3.4V vs Li/Li^+ but the voltage of LFP is well inside the electrolyte stability window. The practical capacity obtained with LFP is close to the theoretical capacity which is 170 mAh g^{-1}. The main drawback of the LFP material comes from its poor ionic and electronic conductivity. Several technologies have been explored to overcome this problem, including minimizing the particle size up to the nanoscale range and coating the LFP particles with a thin carbon layer.

When these two methods are combined, the practical capacity of LFP approaches its theoretical capacity at high rates.[33]

It is well known that the cathode materials are lacking in capacity, compared to anode materials, and are hindering the performance of LIBs. Recently, it has been shown that one of the most promising materials for the cathode electrode is the sulfur (S) element due to its high specific capacity and energy density.[34] The electrochemical properties of this element as cathode in Li-ion batteries are reviewed in Chapter 3.

1.2.3.2 Anode materials

Ideally, lithium metal should be an appropriate anode material for LIBs, mostly because of its very high specific capacity (3862 mAh g^{-1}), low molecular weight and being the lowest negative electrochemical potential of all elements (-3.04V vs SHE).[35] The drawback of using metallic lithium as a negative electrode relates to the safety of use and reversibility issues. During the charging process, the morphology of the deposited lithium layer is not flat and homogeneous on the anode, but instead it forms needle-like structures called "dendrites".[36] These dendrites can pierce the separator and cause short-circuiting, start a thermal runway reaction on the cathode and ensue explosions.

The anode materials can be divided into three main groups:

1. Intercalation/ de-intercalation materials. Amongst these materials, the most used are the carbon based materials know as carbonaceous and the lithium titanate materials ($Li_4Ti_5O_{12}$).
2. Alloy/ de-alloy materials, such as Si, Ge, Sn, Al.
3. Conversion materials like transition metal oxides: nickel oxide (NiO), iron oxides (Fe_xO_y), molybdenum oxides (MoO_x) and cobalt oxide (Co_3O_4).

1. Intercalation/ de-intercalation materials:

   - **Carbonaceous Materials**

     Carbonaceous structures are the most commonly used negative electrode materials in LIBs. Up to now, different types of carbon materials have been tested and commercialized.[37] For instance, graphite which is the most common material used as anode, has the advantage of being a low cost and a highly abundant material, has a high electrical conductivity and a relatively high energy density because of its low intercalation potential between 0.2 and

0.05V vs Li/Li^+. During the battery operation, Li^+ ions are inserted into the graphitic layers [38], forming the LiC_6, which corresponds to a theoretical capacity of 372 mAh g^{-1}.[37] In the half-cell reaction coupled with lithium, the discharge process involves Li^+ ion intercalation into carbon, while in reverse, the Li^+ ion de-intercalation process corresponds to the charge step:

$6\ C + Li^+ + e^- \rightleftharpoons LiC_6$

Since the lithium intercalation within graphite occurs at a very low potential, the electrolyte solvent does not remain stable at this potential leading, thus, to a reduction/decomposition of the electrolyte components. Consequently, a Solid-Electrolyte Interphase (SEI) forms on the electrode surface.[39, 40] This, in turn, causes an irreversible capacity that occurs during the first charge step for all types of carbonaceous materials. The SEI layer grows mainly during the first cycle, and is essential for the good operation of the graphite electrodes as it prevents further electrolyte decomposition in subsequent cycles. However, the graphite anodes have a low specific capacity preventing their use in large-scale batteries.

- **Titanium based anodes**

  Lithium titanate $Li_4Ti_5O_{12}$ (LTO) is an alternative negative electrode material to carbonaceous electrodes. The electrode reaction is presented below:

  $Li_4Ti_5O_{12} + 3\ Li^+ + e^- \rightleftharpoons Li_7Ti_5O_{12}$

  It has a lower theoretical capacity than graphite (175 mAh g^{-1} and a lithium intercalation potential of about 1.55V vs Li/Li^+).[41] Thus, the relatively low capacity and high lithium insertion potential lead to a low cell voltage, and thus to a low energy density of the cell. But, there are several benefits of using LTO as an active material for the anode. One advantage comes from the high insertion potential which is well above the electrochemical stability potential window of the electrolyte and, hence, no SEI is expected to form to the same extent as with graphite. Another advantage is that lithium plating does not occur even at high currents or low temperatures which greatly improves the cycle lifetime. Lastly, LTO represents a zero strain material that allows intercalation and deintercalation of Li^+ ions without any volume change.[42] However, its electronic conductivity is low, thereby carbon coating [43] and other doping methods [44] have been used in order to increase the conductivity. This makes LTO a great candidate material for high power applications.[45]

2. Alloy/de-alloy materials:

   - **Lithium-metal alloy materials**

Lithium can be electrochemically alloyed with metallic and semi-metallic elements to form lithium-metal alloys. The reaction is usually described by the following reversible process:

$Li_xM \rightleftharpoons M + xLi^+ + e^-$

where, M represents the elements reacting with lithium, e.g., Si, Sn, Sb, Al, Mg, Bi, In, Zn, Pb, Ag, Pt, Au, Cd, As, Ga and Ge. Only the first five elements have been widely studied due to their low cost and their abundance.[46] Lithium metal alloys present a great interest due to their ability to store large amounts of lithium, allowing them to have a theroretical capacity 2-10 times greater than that of conventional graphite anodes.[47] (see Table 1.2)

TABLE 1.2: Comparison of the theoretical specific capacity, charge density, volume change and onset potential of various anode materials.

Materials	Li	C	$Li_4Ti_5O_{12}$	Si	Sn	Al	Bi
Lithiated phase	Li	LiC_6	$Li_7Ti_5O_{12}$	$Li_{4.4}Si$	$Li_{4.4}Sn$	LiAl	Li_3Bi
Theoretical specific capacity ($mAhg^{-1}$)	3862	372	175	4200	994	993	385
Theoretical charge density ($mAhcm^{-3}$)	2047	837	613	9786	7246	2681	3765
Volume change (%)	100	12	1	320	260	96	215
Potential vs. Li (V)	0	0.05	1.6	0.4	0.6	0.3	0.8

The main problem with these alloying materials, is the important volume change during the lithiation/ delithiation processes. The significant volume changes lead to severe cracking and pulverization of the electrode and subsequent loss of electrical contact between the individual particles, which in turn results in a severe capacity fading. In order to overcome those problems, considerable research efforts have been devoted to preserve their structural integrity. One of the earliest approaches involves replacing the bulk material with nanostructured alloys. The unique nanostructure can alleviate the generated mechanical strain due to the volume change as the Li^+ ion intercalated to and de-intercalated from the host electrode materials. Moreover, it reduces the electronic and ionic transport pathways and provides additional lithium storage sites.[48] The second approach is to form nanocomposites; for example, metal nanoparticles coated with carbon or dispersed in a carbon matrix. Carbonaceous materials have the benefits to accommodate the stress associated with the volume expansion, and have good ionic conductivity.[49] Owing to its highest capacity, silicon has been the main focus in Li-alloying metals. The electrochemical properties of this element as anode in Li-ion batteries are reviewed in Chapter 4.

3. **Conversion Materials**

   Another extensively investigated category of anode materials for LIBs are transition metal oxides (M_xO_y, where M= can be: Fe, Co, Ni, Cu, Mn, Mo, Ru, etc.). These metal oxides do not possess vacant sites to accommodate lithium, excluding the possibility of an intercalation mechanism. The actual mechanism involves the formation and decomposition of Li_2O, along with the reduction and oxidation of metal nanoparticles. The conversion reaction can be represented as the following:

   $MO + 2\ Li^+ + 2\ e^- \rightleftharpoons Li_2O + M$

   In 2000, Poizot et al. reported for the first time that lithium can be stored reversibly in transition metal oxides through a conversion reaction.[50] These metal oxides can deliver a stable gravimetric capacity three times higher than that of carbon, and show a high energy density because the oxidation state is completely used and more than one electron is involved in the conversion reaction. However, transition metal oxide anodes still face several issues that keep those materials far from commercial application. The disadvantages include low Coulombic efficiency at the first cycle, large voltage hysteresis between the discharge and charge process, unstable formation of the SEI layer and poor cycling stability.[51] These limitations of transition metal oxides could be possibly overcome by preparing nanostructured transition metal oxides and transition metal oxide nanocomposites to improve the electrochemical performance of transition metal oxide anodes.[52]

1.2.3.3 Electrolyte

Usually in a commercial Li-ion cell, the electrolyte consists of a lithium salt dissolved in a solvent mixture that also contains small amounts of additives. The role of an electrolyte is to transport Li^+ ion between the anode and the cathode and to block the transport of electrons. It is at the electrode/ electrolyte interfaces that the redox reactions governing the proper operation of the battery take place. The electrolyte must satisfy the following requirements [53]:

1. High ionic conductivity $\sigma_{Li} > 10^{-4}$ S cm^{-1} and low electronic conductivity $\sigma_e < 10^{-10}$ S cm^{-1},
2. Transference number $\sigma_{Li^+}/\ \sigma_{total} \approx 1$, where σ_{total} is the sum of the conductivities of all the other ions in the electrolyte ($\sigma_{Li^+} + \sigma_{total}$),
3. Chemical stability over ambient temperature,
4. A wide electrochemical window, that is stable in large range of potential (0∼5V),

5. Chemical stability with respect to the electrodes, including the ability to form a passivating SEI layer rapidly, where the kinetic stability is required because the electrode potential lies outside the electrolyte window,

6. High safety, low toxicity and low cost.

Nevertheless, obtaining all these requirements has been a challenging task up to date. Carbonates are the most popular solvents used for commercial LIBs. They have an oxidation potential, the "highest occupied molecular orbital (HOMO)" at 4.7V vs. Li/Li^+ and a reduction potential, the "lowest unoccupied molecular orbital (LUMO)" near 1.0 V vs. Li/Li^+.[53] The most commonly used electrolyte solvents are alkyl carbonates or alkyl carbonate mixtures such as: ethylene carbonate (EC), dimethyl carbonate (DMC), propylene carbonate (PC), diethyl carbonate (DEC) and ethyl methyl carbonate (EMC). The structural formulae of alkyl carbonates are shown in figure 1.5.[54]

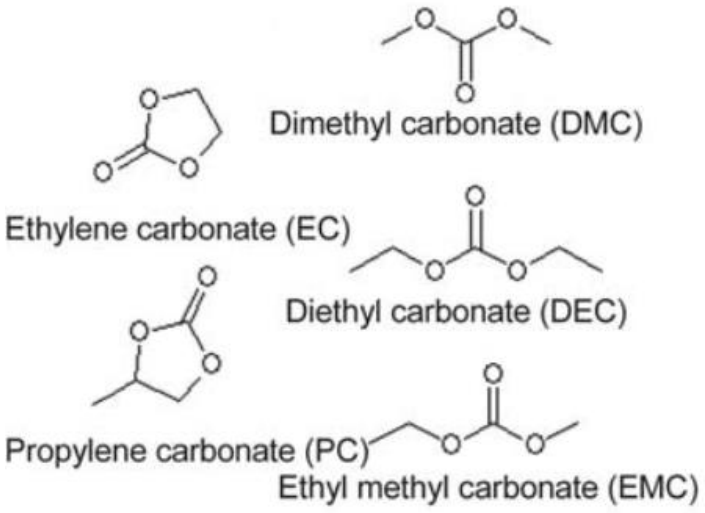

FIGURE 1.5: **Chemical formulae of the main carbonate solvents used in the electrolyte in Li-ion batteries.**

These alkyl carbonates, mixed with lithium salt hexafluorophosphate ($LiPF_6$), are regarded as the basic standard electrolyte solutions for LIBs.

Recently, room-temperature ionic liquids (ILs) have been proposed as promising alternative solvents in electrolytes for the next generation of Li-ion batteries, mainly because of their high oxidation potential ($\sim$ 5.3V vs Li/Li^+), their low vapor pressure i.e non

volatile, non-flammable nature, and good chemical electrochemical stability.[55] However, the main drawback in ILs is their high viscosity, which engender reduced conductivities and they are expensive.

Regarding the lithium salt, it provides the lithium source in the electrolyte for the insertion/ extraction between the electrodes, while the solvents provide a medium for Li^+ ion diffusion. Several lithium salts have been studied, such as lithium perchlorate ($LiClO_4$), lithium tetrafluoroborate ($LiBF_4$), lithium hexafluoroarsenate(V) ($LiAsF_6$), lithium bis-trifluoromethanesulfonimide (LiTFSI) and lithium bis(oxalato) borate (LiBOB). $LiPF_6$ still remains dominant as it best combines necessary properties/ characteristics: ionic conductivity, dissociation constant, ionic mobility and anodic stability. Nevertheless, it is expensive and forms hydrofluoric acid (HF) in contact with water. The electrolytes must therefore be prepared from perfectly anhydrous solvents and under controlled atmosphere.

Additionally to lithium salt and solvents, the liquid electrolyte also contains additives that are used for instance to improve formation of the SEI, stabilize $LiPF_6$ and protect from overcharging. The most commonly used electrolyte additives appear to be vinylene carbonate (VC) and fluoroethylene carbonate (FEC). VC is an electrolyte additive, which is commercialized for LIBs in order to increase the Coulombic efficiency and thermal stability of graphite.[56] Its influence on the silicon electrodes have also proved to be very encouraging, on thin films of amorphous silicon[57] and on nanostructured silicon/ carbon (Si@C).[58] Jaumann et al [58] reported that VC-additive increases the Coulombic efficiency to reach 99% after the 20th cycle and also improved the lifetime of nano-silicon anodes. The use of the FEC additive has been reported in several studies of silicon electrodes for example, on thin films [59] and on silicon nanoparticles.[60] Choi et al [59] were the first to use FEC-added electrolytes with silicon thin film electrodes. They observed that the presence of FEC in the electrolyte resulted in a smoother SEI layer on the silicon film. Lin and coworkers [60] investigated the presence of FEC-based electrolytes for silicon nanoparticle anodes made by a conventional slurry. They reported an outperformance of the electrode in the FEC-based electrolyte in terms of capacity retention and Coulombic efficiency. The enhancement of the performance is due to the better properties of the FEC-derived SEI formed on the surface of the silicon.
In the present work, different electrolytes have been used because for the positive electrode (sulfur), it is well know that the carbonate-based solvents such as ethylene carbonate and diethyl carbonate react with polysulfides irreversibly.[61] An electrolyte solution containing 1 M LiTFSI in a 1:1 (volume ratio) 1,3-dioxolane: 1,2-dimethoxyethane (DOL:DME) with the addition of $LiNO_3$ was used in the electrochemical testing of the sulfur electrode. Whereas, another electrolyte solution containing 1 M $LiPF_6$ in a 1:1 (volume ratio) ethylene carbonate: dimethyl carbonate (EC:DMC) and for certain

experiments with the addition of FEC was used in the electrochemical testing of the silicon material. In the full cell, the 1 M LiTFSI in a 1:1 (volume ratio) 1,3-dioxolane: 1,2-dimethoxyethane (DOL:DME) with $LiNO_3$ was used.

Solid Electrolyte Interphase

The electrode/ electrolyte interphase is one of the most crucial parameters affecting the LIBs electrochemical performance (i.e. cycling performance, rate capability, safety).[62] In the early 1970s, Peled firstly suggested that the layer formed instantly by the contact of the metal with the solution, acts as an interphase between the metal and the solution and named it the SEI.[63] Negative electrodes such as graphite or silicon operate at potential between 0-1V vs Li/Li^+, whereas positive electrodes (e.g. $LiCoO_2$, $LiMn_2O_4$) have an operating potential higher than 3V vs Li/Li^+. No electrolyte components can remain thermodynamically stable against reduction potential at negative electrodes and against oxidation potential at the positive electrodes.[64] In the case of carbonaceous electrodes, the formation of the SEI layer proceeds from the deposition of organic and inorganic compounds during the first charge/ discharge cycle on the surface of the graphite electrode. The formed SEI prevents further reduction and co-intercalation of the electrolyte and allows only Li^+ ion diffusion. Therefore, SEI acts as a protective surface film making the carbon electrode stable even at potentials lower than 1V.

The existence of the SEI on the cathode is still highly debated. In the case of LFP or transition metal oxides, they store Li^+ ion between 3.5-4.2V, which is still on the border of oxidation stability limits for most electrolyte components. But, when the cathode potential is above 4.2V (e.g., $LiNi_{0,5}Mn_{1,5}O_4$, $LiCoPO_4$,...), the existence of a surface film on the cathode will become certain.[64, 65]

1.2.3.4 Current collectors

Aluminium (Al) and copper (Cu) are usually used as the current collectors at the cathode and the anode, respectively. The collector materials require good electrical conductivity and inertness to any electrochemical lithium reaction at the respective electrodes. Aluminium is extensively used as a current collector with lithiated transition metal oxides for the positive electrode in commercial LIBs, as it is stable up to 4.3 V vs. Li/Li^+ in most organic electrolytes.[66] Its low price and good electric conductivity due to the high purity of Al metal expand the application potential for LIBs.[67] Aluminium was shown in 1971 to alloy with lithium at low potentials vs. Li/Li^+.[68] As a result, the use of Al as negative electrode in Li-ion batteries has been hindered because the formation of alloys always results in volume expansion.[67] Copper is used as a current collector for the negative electrodes in almost all commercial LIBs. It has a high conductivity

and is readily available in many forms. At high potential (1.5V to 3.0V vs. Li/Li^+), a large cathodic peak was observed in the cyclic voltammogram curve, which corresponds to the corrosion of Cu.[67] At low potential between 0V to 1.0V, there is no peak corresponding to the Li-Cu alloy in this system since no apparent redox peaks appeared near 0V vs. Li/Li^+. This makes Cu a good choice to be used as the negative electrode current collector in LIBs.[67]
Nevertheless, break up of the metallic foil and detachment of the active materials from the current collectors can be problematic for the future generations of LIBs. A current collector should therefore be lightweight, thin, mechanically stable, durable under deformation stress and chemically stable.[69] Carbon nanotubes are potential candidates as current collectors owing to their properties [70–73] which will be detailed in Chapter 2.

1.3 Advantages of nanomaterials structure

Micro-sized electrode materials are commonly used in commercial Li-ion batteries. The electrode materials ought to have some specifications, such as high reversible capacity, fast Li^+ ion diffusion, ecological, long cycle life, low cost and improved safety hazards. In solid-state, the diffusion coefficient of Li^+ ions in most electrode materials is very low (10^{-7} - 10^{-11} cm^2/s) [74] and, thus, the diffusion path length becomes important and can easily become a limiting factor of the insertion/ extraction rate, and hence of the charge-discharge rate performance. In order, to meet the future demands of EVs and HEVs, the development of new strategies is required for LIBs. One of these strategies is the miniaturization of the electrode materials. The use of nanostructured materials instead of existing micro-sized materials are considered to be the most encouraging strategy to overcome present limitations. Nanostructures can provide reduced distance for Li^+ ion diffusion path length and can improve the intercalation/ deintercalation rate of LIBs.[75]

The benefits as well as drawbacks of nanostructured electrode materials are summarized as follows:

Benefits [76]

- Increase charge/ discharge rates due to short distance for Li^+ ion diffusion within the particles,[75]
- Enhanced electron transport and thus alleviate the limitation of electronic conductivity,[77]

- Nanostructured materials with high specific surface area permit a high contact area between electrode and electrolyte, enabling high lithium exchange flux,[78]
- The nanometer-sized electrode materials can accommodate large volume expansion/ contraction during cycling, preserving the integrity of the electrode and leading to stable cycling performance,[79]
- Enable reactions that cannot occur in micron-sized particles,[77, 80]
- Chemical potential for lithium ions may be modified leading to potential shifts.[75, 81]

Drawbacks [78]

- Difficult to synthesize and control the size or shape of the desired nanometer-sized electrode materials,
- High surface area and high surface energy of nanomaterials also increase undesirable side reactions between electrode and electrolyte, which may result in a high irreversibility and reduced cycle life,
- The packing density of nanomaterial-based electrodes is lower than that of micromaterial-based electrodes thus reducing the volumetric energy density,
- Electron and Li^+ ion transportation through the nanoparticulate layers can be restricted due to random walk limiting the battery performance and reducing the electrical conductivity. Nanomaterials tend to form agglomerates during the electrode fabrication process, making it difficult to uniformly disperse them in the electrodes, and their nanoscale dimensions are rather difficult to control.

1.4 Ideal material

A wide variety of nanostructured materials with miscellaneous geometric shapes and morphologies have been extensively explored, such as nanoparticles (0-D), nanowires (NW), nanorods (NR) and nanotubes (NT) (1-D) and nano films (2-D). Despite the benefits of nanostructured materials, particularly in case of 0-D nanoparticles, their performance is still limited by many factors. Over several cycles, the intercalation/ deintercalation of Li^+ ions induce a volume expansion and craking of the nanoparticles, leading to a reduction in the cyclability and the battery life.[82] In addition, nanoparticles tend to form agglomerates during the electrode fabrication process resulting in a random paths of electrons and Li^+ ions through the nanoparticles. Moreover, the grain

boundaries and voids in between the nanoparticles restrict the battery performance and reduce the overall electrical conductivity.[75, 82]

1-D nanostructures are particularly attractive and are considered to be superior to nanoparticles. The small diameter of 1-D nanostructure allows for better accommodation of the large volume changes without initiation of mechanical degradation, such as pulverization and fracturing that can occur in bulk or micron-sized materials.[83]

To get more advantages from 1-D nanostructures and to avoid poor electronic/ ionic transportation by random paths, each 1-D nanostructure should be directly electrically connected and thus preferably vertically aligned to the metallic macroscopic current collector. Thus, a direct 1-D electronic pathway can be achieved which drastically improves the charge transport during the charge and the discharge processes and prevents the requirement of conductive additives or binders which add extra weight to the battery.[84]

However, the choice of the nanomaterial properties is crucial to avoid any resistance, which may cause the failing of performance (e.g., capacity fading) of the LIBs.

What would then be the ideal 1-D nanostructured material that should be used?

The optimal 1-D nanostructured material should be very thin and light-weighted, should ensure optimal Li^+ ions conductivity/ electrons transportation, preferably be vertically-aligned and should have a direct electrical contact of each nano-object with the current collector.

One of the best choices appears to be the carbon nanotubes (CNTs) which will be reviewed in detail in the next Chapter. Vertically aligned CNTs forest directly grown on an appropriate current collector can provide a quasi-ideal highly conductive physical framework for subsequent formation of 1-D hierarchical nanostructures of various natures, and enable, for example, the use of nanostructured high-capacity electrode materials as Sulfur and/ or Silicon.

Chapter 2

Carbon nanotubes acting as nanostructured current collectors

The present chapter is divided into two main parts: the first part gives a short and general overview of the main characteristics and properties of the carbon nanotubes. The second part describes the experimental approach used to obtain vertically aligned carbon nanotube (VACNT) carpets on two different conductive substrates: aluminum and copper. In particular, we present the main steps that were developed and optimized for growing reproducible and controlled properties of VACNT carpets using a modified Chemical Vapor Deposition (CVD) process. The benefit of growing VACNTs directly on a conductive substrate, such as copper and/or aluminum is to obtain a direct electrical contact of each of the nanotubes with the substrate which makes them very good candidates as current collectors in LIBs. This approach avoids the use of binders or additives, optimizes the active material/ current collector interface and simplifies the fabrication of the battery device.

2.1 Carbon allotropes

In its organic form, carbon has an extremely rich and varied chemistry, whilst in its inorganic form it has various allotropes, including graphite, diamond, fullerene (e.g., buckyball C_{60}), amorphous carbon (a-C), carbon nanotube (CNT) and so on.[85] The structure of the different carbon allotropes is shown in figure 2.1.

Diamond and graphite are pure forms of carbon, but their physical properties are widely different. Diamond is transparent and the hardest carbon structure.[86] It has a tetrahedral structure, i.e, each carbon atom is surrounded by four other carbon atoms with

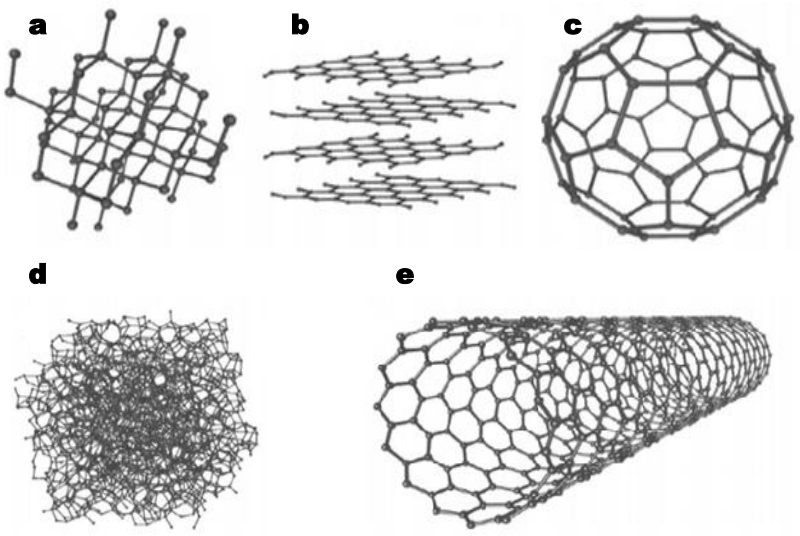

FIGURE 2.1: **Structure of different allotropes of carbon: (a) Diamond, (b) Graphite, (c) C_{60} (Buckminsterfullerene or buckyball), (d) Amorphous carbon, (e) Single-wall carbon nanotube or buckytube.**

tetrahedral connections. The conductivity of diamond is extremely low due to the lack of free electrons, since all the valence electrons are used to form the sp^3 bonds.[87] In contrast, graphite is black, very soft and slippery. Its structure consists of Van der Waals stacked graphene layers (a single, tightly packed layer of carbon atoms bonded together in a hexagonal honeycomb lattice). It has high thermal and electrical conductivity. The properties of graphite from its crystalline structure, for example its high electrical conductivity is related to the π bonding between the carbon atoms in the graphene layers. The softness and lubricating nature of graphite arises from the weak Van der Waals forces binding the carbon sheets. The amorphous carbon (disordered carbon) having no crystalline structure, results in a totally random distribution of sp^2 and sp^3 hybridized carbon atoms.

A new era in carbon materials began in the middle of the 1980s when the discovery of carbon nanostrutures triggered an ever-growing research interest. These carbon nanostructures include: fullerenes - the most common one is the buckyball-like molecules (i.e. fullerene C_{60}) and the CNTs. Fullerenes were discovered in 1985 by Kroto et al during the vaporization of graphite by laser irradiation, producing a remarkably stable cluster consisting of 60 carbon atoms arranged in hexagons and pentagons.[88] Carbon nanotubes were theoretically imagined and described as "rolled up" sheets of graphene. The first observation of the tubular structure of some nano-sized carbon filament was in 1952 by Radushkevich and Lukyanovich.[89] Experimental evidence of the existence of

CNT dates back to 1991 when Iijima observed multiwalled carbon nanotubes (MWCNTs) using a transmission electron microscopy.[90] In 1993, Iijima et al [91] and Bethune et al [92] simultaneously and independently reported the existence of CNT consisting of a cylindrical graphene sheet called single walled carbon nanotubes (SWCNTs). Carbon nanotubes stimulated an ever increasing interest from the whole scientific community; physicists, chemists, and materials scientists due to their varied and astonishing properties (electronic, physical, mechanical) that can find potential use in wide range of applications.

2.2 Carbon nanotubes

Carbon nanotubes have a cylindrical structure where each C shares a sp^2 covalent bond with its three nearest-neighboring atoms. CNTs can be viewed as a graphene sheet rolled up into a nanotube. CNTs have a typical diameter of 1-5 nm, about 100,000 times thinner than an average human hair, and they can be several hundred microns long. CNTs may be broadly classified into SWCNTs and MWCNTs based on their structure as shown in figure 2.2. A MWCNT constitutes of several cylindrical sheets, generally between 2 and 50, each corresponding to a graphitic plane. Different possible structures of MWCNTs are described in literature. A CNT containing another tube inside it is referred to the Russian Doll model, while a single graphene sheet wrapped around itself manifold times is called the Parchment model.[93] The internal diameter of the tube ranges between 1 and 40 nm and its external diameter ranges between 2 to 100 nm. Its length is of the order of microns, but can reach few centimeters. The distance between the successive walls, determined for the first time by Iijima, is 0.34 nm, slightly greater with respect to the graphite interplane distance (0.33 nm). This difference is not only due to the constraints caused by the tube curvature, but also to the strengths of Van der Waals forces between the sheets comprising the nanotube. A SWCNT consists of a single graphene sheet rolled up and closed on itself. The way this sheet is rolled determines the tubes helicity. Regarding its size characteristics, a SWCNT presents a perfectly rectilinear tubular structure of nanometer diameter, between 1 and 50 nm, and of micrometric length. Its exceptional physicochemical properties result from its structural characteristics (cylindrical shape, helicity, nanometric size and aspect ratio or length to diameter).

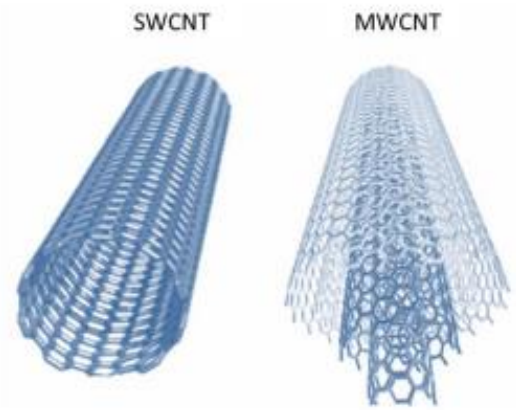

FIGURE 2.2: **Schematic representation of a SWCNT and a MWCNT.**

2.3 Physical properties

Carbon nanotubes have been widely studied and were found to possess several outstanding properties, including high mechanical properties, excellent electrical conductivity, and high thermal stability. Here we review the electronic, mechanical, thermal and electrochemical properties of CNTs from the point of view of their possible use as a current collector in LIBs.

2.3.1 Electronic properties

The electronic properties of the CNTs are related to their geometric structure. CNTs can either be metals or semiconductors with different energy gaps, depending on the diameter and the helicity (also called chirality) of the tubes.[94] In general, 1/3 of SWCNTs behave as metals and 2/3 have a semiconductor behavior. Since MWCNTs contain multiple layers with different chiralities, the electronic properties are more complex. However, the majority of MWCNTs present a metallic behavior. Because of their 1-D structure, electronic transport occurs ballistically over long distances in a CNT [95, 96], indicative of their high electrical conductivities. According to these reports, the electron crosses the CNT (along the axis) without collisions and without dissipating energy. Experimental results confirmed a low resistivity along the axis of the CNT of 2.6×10^{-7} Ω.m at 300 K for SWCNTs and 9.5×10^{-5} to 5.3×10^{-8} Ω.m for MWCNTs. The CNT can carry large current density up to 10^{10}A/cm^2, whereas the maximum current densities for normal metals are $\sim 10^5$ A/cm^2.[97, 98] Therefore, the CNTs have an electrical resistivity close

to that of copper (1.7×10^{-8} Ω.m), for a much lower density that can vary around 2.0 g cm^{-3} as a function of the diameter and the number of walls. [99] CNTs are thus excellent candidates for applications requiring lightweight combined with a good electrical conductivity.

2.3.2 Mechanical properties

The structural properties of CNTs with strong σ bonds between the neighboring carbon atoms give the nanotubes an extremely high Young's modulus and tensile strength. Experimental and theoretical investigations show remarkable mechanical properties of individual MWCNTs with Youngs modulus being over 1 TPa and a tensile strength of 10 - 200 GPa [100, 101], which is several hundred times more than that of steel, while they are only one-sixth as heavy. The elastic response of a nanotube to deformation is also exceptional: CNTs can sustain up to 15% tensile strain before fracture. Nanotubes are shown to be very flexible, with the reversible bending up to angles of 110° for both SWCNT and MWCNT.[102] Due to the extremely high strength of CNTs, they can bend without cracking.

2.3.3 Thermal properties

Furthermore, CNTs have exceptional thermal conductivity and thermal stability.[103, 104] Berber et al [103] found the thermal conductivity of SWNT at room temperature to be about 6600 W/m K, which is almost double of the thermal conductivity of diamond (3320 W/m K). CNTs are also thermally stable up to 2800°C in vacuum and could endure up to 750°C in air.[104]

2.3.4 Electrochemical properties

As it is well known, carbon nanotubes can be obtained by rolling up a defined projected area within the hexagonal lattice of a graphene sheet in a seamless fashion, such that all carbon-carbon (C-C) valences are satisfied and the direction in which the roll up is performed transforms into the circumference of the tube. Due to the nature of π-orbital overlap in metallic CNT chiralities, the electron conduction can occur via ballistic transport (i.e. electrons can transfer with mean free paths on the order of microns along the length of the nanotube unless scattered by a defect).[105] CNTs have a quasi-perfect crystalline structure, offer enhanced electron transport and provide continuous paths for Li^+ ions for the LIBs. In the case of decorated CNTs with metal nanoparticles, the CNTs are able to transport the electrons to and from the metal nanoparticles when they are

alloying and dealloying with lithium. It was demonstrated that decorated CNTs directly grown on a current collector lead to a residual capacity which never exceeds a few μAh after a few cycles, that is to say, CNTs are electrochemical stable and inactive.[72]

2.4 Carbon nanotubes based devices

As mentioned previously, CNTs exhibit unique and extraordinary characteristics in terms of their electronic properties determined by their chirality and are envisioned to a wide variety of applications in nanoscale electronics. Figure 2.3 summarizes the implementation of CNTs by different industry sectors.

- Field emitters: CNTs have been shown to have good field (cold) emission characteristics: emission has been observed at fields lower than 1 V/μm, and high current density of over 1 A/cm^2 have been obtained.[106]
- Sensors: Strong dependence of the properties of CNTs on surface modification, mechanical deformation, doping, coating, etc. make them a very attractive material for chemical, biological, and physical sensors. Small changes in the environment of the CNT can cause drastic changes into its electrical properties.[107–109]
- Transistors: CNT-based working transistor outperformed larger transistors made with silicon.[110]
- Energy conversion and storage devices: CNTs are being used in electrochemical energy conversion, such as LIBs [111, 112], supercapacitors [113], hydrogen storage.[114] The electrochemical properties of CNTs are dominated by their mesoporous character. CNTs have a high rate of electron transfer and allow an easy access of the ions to the electrode/ electrolyte interface.

CNTs have many others applications, such as in the aerospace industry[115], the sporting goods (e.g., fabrication of baseball bats and skis), and the electronics related field such as use for scanning probe microscopy tips or conductive inks as shown in figure 2.3.[116] Due to their excellent characteristics, such as high surface to volume ratio, outstanding mechanical and electronic properties and self-aligned structure (for CNT forest), CNTs are probably the most studied nanomaterial so far, and have broad practical and fundamental applications

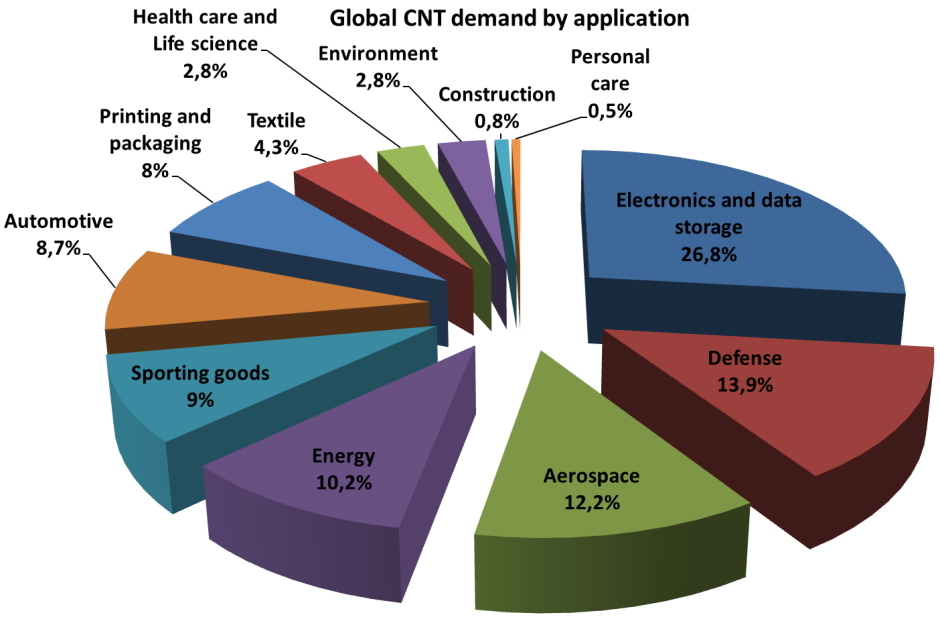

FIGURE 2.3: **Global CNT request by different fields of application.** [116]

2.4.1 CNT-based LIBs

A short overview and evaluation of the potential use of CNTs in LIBs are given in the following paragraphs. Shortly, because of their high surface area, chemical and mechanical robustness and their high electron conductivity, CNTs match ideally with the specifications needed in the fields of LIBs. CNTs are regarded as a potential material candidate for use in both cathode and anode fabrication. For example, for the positive electrode, CNTs can be used to enhance the conductivity and improve the mechanical stability.[117] As for the negative electrode, CNTs could potentially be used as a replacement for graphite.[118] Furthermore, CNTs are being investigated as a reinforcement structure for the unstable silicon-anodes that could be used in the next generation of batteries.[119] Their use as an additive for either the anode or cathode has several advantages compared to other forms of carbon additives like carbon black or acetylene black. For example, for the cathode formulation, MWCNTs have been employed as an additive with LCO [120] and LFP [121, 122] exhibiting $\sim$ 10% improvement in the reversible capacity of the as-fabricated electrodes as compared to ones incorporating carbon black counterparts. Another example highlighting the outstanding properties of CNTs, LMO-MWCNTs composite material has been produced by Liu et al [123] using a sol-gel method. Such nanocomposites showed high cycle stability with a remarkable

capacity retention of 99% after 20 cycles while capacity retention of pure LMO nanoparticles is only 9%. The 1-D structure of CNTs cannot only improve the electrical conductivity, but also improve the Li^+ diffusion coefficient and the overall electrochemical performance.

The specific capacities of CNTs were usually reported to exceed the capacity of graphite. For instance, the reversible capacity of SWCNTs synthesized by laser ablation is 600 mAh g^{-1} and the specific capacity of SWCNTs could be increased from 600 to 1000 mAh g^{-1} by ball-milling, which is significantly higher than the ideal value of graphite (372 mAh g^{-1}).[124] The reasons are attributed to 1) Li^+ can not only be stored into stable sites located in graphitic layers, but also on the surface of nanotubes.[125] 2) the 1-D structure of CNTs can shorten the path lengths for Li^+ diffusion, meanwhile keeping excellent electron transport along the tubes. Both factors are beneficial for the improvement of LIB performance.

Additionally, CNTs not only have a higher capacity than graphite, but they can be used as a support matrix in the case of a lithium-metal alloy material. Metal nanoparticles such as Si [72] and Sn [126] can be deposited on the surfaces and onto the CNT sidewalls, and then are able to form an alloy with the lithium without impeding the insertion/ deinsertion of lithium into the CNTs themselves. This method has many advantages. First and foremost, this enables the anode electrode to take advantage of the high lithium capacity that metals have to offer without confronting the pulverization problem and breakdown of the electrode. This is because the highly conductive CNTs act as "glue" matrix for the metallic nanoparticles. When the nanoparticles start to form an alloy with lithium and undergo a large volume change, the anode is able to remain structurally intact because the highly conductive CNTs act as a flexible wire mesh, allowing the metal particles to remain attached to the anode's current collector. The CNTs are then able to transport the electrons to and from the metal nanoparticles when they are alloying and dealloying with lithium. Second, the CNTs are capable of storing any additional lithium which is not alloyed with the metallic nanoparticles.[127]

Recently, new studies demonstrated the feasibility of using CNTs as current collectors in LIBs. There are several advantages in using such an approach:

- CNTs are extremely lightweight, thin and with significantly lower densities than copper (0.3-1.0 g cm^{-3} vs 8.9 g cm^{-3}).[128]
- The porous structure of CNT enables easier slurry infiltration, larger contact area, better wetting, stronger adhesion, and lower contact resistance at the electrode/ CNT interface. CNT themselves are flexible and strong enough for insuring/ securing the structural integrity of the electrodes. Accordingly, any volumetric changes

of the electrodes during electrochemical reaction and repeated mechanical deformation in flexible LIBs can be better accommodated, leading to better cycling stability, rate capability, and mechanical durability.[129]

- CNTs are much more chemically stable than metal current collectors; therefore, long-term stability of LIBs with CNT current collectors is expected.[129]

Sooner or later, CNTs will play an important supporting role in high-performance LIBs, not only by being involved directly in the lithium storage, but also by providing a conductive network and a structural scaffold for traditional electrode materials.

2.5 Carbon nanotubes synthesis

At present, CNTs are manufactured by different methods in laboratories and industry. The production of CNTs with a high degree of purity, large amount, low costs, and reproducibility are still some of the biggest issues for the carbon nanotube community. Three major methods are used for CNT synthesis today, laser or arc discharge carbon vaporization, and chemical vapor deposition (CVD).

- Laser ablation: in this process, a target consisting of graphitic carbon doped with catalyst (i.e. Co, Ni,...) is vaporized using a laser pulse at high temperatures (1200°C) inside a tube furnace. The vapors are then flushed, using inert Ar, towards the end of the tube which houses a water-cooled copper collector tip where CNTs are formed and collected as the vapor condenses. Such a technique is mostly used for obtaining high purity SWCNTs, but their production yield is very low.[130, 131]

- Arc discharge method: this method is based on an electric arc discharge that is generated between two graphite electrodes in a chamber filled by an inert gas (Ar, He). The arc is generated by running a DC current and voltage bias between the electrodes that can reach very high temperature above 3000°C. The chamber is kept at subatmospheric pressure (500 Torr). The carbon vaporizes at the anode and deposits onto the cathode where CNTs form. If no transition metal catalyst is used, bundles of MWCNTs form in the inner region of the cathode. The CNTs are mixed with nanoparticles, amorphous carbon and fullerene and need to be purified for extraction. Catalysts such as Co, Ni, and Fe have been shown to produce SWCNTs. This method produces a mixture of different unwanted forms of carbon (including fullerenes, amorphous carbon, and some graphite sheets). The CNTs need to be separated from the soot and the catalytic metals present in the

crude product. CNTs produced using this method present a tangled morphology with poor control over the length and diameter. CNTs are short with diameters ranging from 1.2 - 1.4 nm (SWCNTs) and 1 - several nm (MWCNTs).[132, 133]
Unfortunately, despite that these two methods produce high quality nanotubes, they also suffer from many drawbacks which limit their use in large scale industrial processes, i.e. both methods are energy extensive methods where a large amount of energy is required to produce the arc or the laser used in the ablation processes. Such a huge amount of energy uneconomical for large scale production. Moreover, the nanotubes created by both processes are in highly tangled form and mixed with different allotropic components of carbon or catalysts. Therefore, CNTs formed need complex purification to get pure and assembled forms. The design of such refining processes is difficult and expensive. All these disadvantages restrict their wide application for producing CNTs at a large scale. For these reasons, the CVD technique has been widely implemented as a preferred method for large scale production.

- Chemical Vapor Deposition method: CVD technique is the most popular method for producing CNTs, due to its low-cost and scalability for mass production. CVD is a simple method to synthesize CNTs under relatively low temperature and pressure. This technique involves the decomposition of hydrocarbon gases in the presence of metal catalyst particles. During the CVD process, the hydrocarbon vapor flow through a tube furnace. The gas precursor decomposes into hydrocarbon molecules and then dissociates at the surface of catalyst to produce CNTs. The growth of CNTs is affected by several parameters, such as the type of the carbon precursor, the catalyst nature and size, the growth temperature and the growth time. Consequently, the structural properties and the density of CNTs can be adjusted to some extent by controlling such parameters. The CVD technique is suitable for a large-scale industrial production of nanotubes. Another great advantage of CVD technique is in its ability to synthesize aligned arrays of CNTs with controlled diameter and length.[130]
  Depending on the application targeted, any of these three methods may be used for CNTs synthesis. There are numerous variations for these techniques operating under different conditions, with different set-ups, and process parameters. Every technique has various benefits and drawbacks regarding the quality and the type of synthesized CNTs. An overview of these techniques is given in Table 2.1.

In the present study, we used CVD with hot-filament assistance in order to help decrease the process temperature, while the local temperature around the hot-filament is kept much higher, sufficient to break the gas precursor molecules and to prevent parasitic amorphous carbon deposition.

TABLE 2.1: An overview on the most common CNTs synthesis methods and their advantages and disadvantges.

Method	CVD	Arc discharge	Laser ablation
Basics	Decomposition of hydrocarbon gases in the presence of metal catalyst particle	Electric arc discharge generated between two graphite electrodes under an inert atmosphere	Graphite target is vaporized by laser irradiation under flowing inert atmosphere and high temperature
Yield	up to 100%	up to 90%	up to 65%
Advantages	high purity, large scale production, simple	easy to implement, defect-free nanotubes, no catalyst	high purity, defect free SWNTs
Disadvantages	limited control over the structures, defects incorporation	short, tangled nanotubes, random structures	expensive, low scale production

2.5.1 Chemical Vapor Deposition method

Since their discovery, the growth mechanism of CNTs has been highly debated. Several groups of experimentalists and theoreticians have proposed several growth mechanisms which are often contradicting. Therefore, no single CNT growth mechanism is well established till date. The widely-accepted general mechanism can be summarized as follows: mainly, a hydrocarbon vapor comes in contact with hot metal catalyst nanoparticles, and decomposes into carbon and hydrogen species; hydrogen return to the vapor phase while resulting carbon gets dissolved into the catalyst. When the catalyst is saturated with the carbon, the excess dissolved carbon precipitates out and crystallizes in the form of a cylindrical shape.[131] There are two different mechanisms assigned for the growth of CNTs:

- Vapor-Liquid-Solid mechanism (VLS): The catalyst particle form liquid alloy. The carbon feedstock is cracked or broken down on the surface of the metal particle. The metal nanoparticle dissolves the carbon until it reaches saturation, at which point a CNT extrudes.[134, 135]
- Vapor-Solid-Solid mechanism (VSS): The metal particle remains solid, the cracked carbon diffuses through the catalyst and/ or around the surface, and CNT nucleates on the side of the metal particle. Since carbon continually breaks down on the particle, the tube continues to grow.[136, 137]

At the substrate surface, once the nanotube begins to grow by either VLS or VSS, the CNT will undergo either tip growth or base growth mode (figure 2.4).[138] For the tip

growth mode, the catalyst-substrate interaction is weak and the metal nanoparticle has an acute contact angle with the substrate. The hydrocarbon can decompose on the top of the metal nanoparticle, then carbon diffuse down through the metal and CNTs grow out across the metal bottom, which pushes the metal particle to detach itself from the substrate. The CNTs grow longer and longer until the metal is fully covered by an excess of carbon. Concisely, the end of the nanotube remains attached to the surface and the catalyst particle remains attached at the opposite end of the extruding nanotube (figure 2.4-a). In the base growth mode, the catalyst-substrate interaction is strong and the metal nanoparticle has an obtuse contact angle with the substrate. In this case, the initial decomposition of the hydrocarbon and the diffusion of carbon occur similar to the previous mechanism, but the CNT precipitation fails to push the metal particle up. As a result, CNTs are compelled to grow out from the top of the metal. Carbon first crystallizes out to make a hemispherical dome which then grows up in the shape of a graphitic cylinder. Subsequent decomposition of hydrocarbon takes place on the lower peripheral surface of the metal particle, and the dissolved carbon diffuses upward to grow the graphitic cylinder. Briefly, the catalyst particle remains attached to the surface and the nanotube is extruded into the air or along the surface (figure 2.4-b). The catalyst particles will result in a tip or a base growth depending largely on the sticking of the nanoparticle to the substrate or the support material.

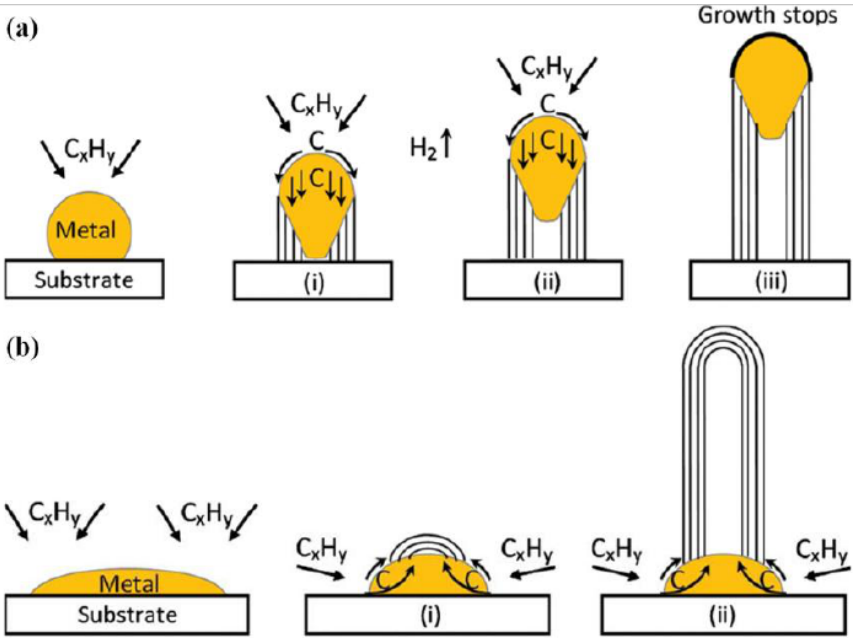

FIGURE 2.4: **Growth mechanisms for CNTs: (a) tip-growth mode, (b) base-growth mode.**

There are several parameters that impact over the CNT structures synthesized using the CVD approach [139]: the process temperature, the precursor gas, the vapor pressure and the catalyst nature. The temperature is a crucial parameter in the growth and remains very closely related to the other parameters governing the synthesis. It plays a major role on the structure of the nanotube. Generally, CNTs can be synthesized in a wide temperature range from 500 to 1100°C. The quality of graphitization of the as-synthesized CNTs is affected by the process temperature. Generally, to obtain a superior quality of graphitization of CNTs (i.e. less defects), the temperature of the synthesis has to be increased. Depending on the carbon precursors and catalysts, there is always a temperature range for successful CNT growth. In order to synthesize SWCNTs, high temperature above 700°C is required since at low temperature MWCNTs are dominant.[140] Together with the temperature, the catalyst nanoparticle diameter is another factor that impacts the CNTs diameter.[141, 142]

The gas precursor is another factor that has a great impact on the final carbon structure and can induce generation of by-products due to a carbon excess feedstock. Basically, the only condition that has to satisfy the feedstock gas is the presence of carbon in their molecular composition. Many precursor gases can be used for the synthesis of CNTs, such as methane (CH_4) [143, 144], acetylene (C_2H_2) [145], ethylene (C_2H_4) [146], xylene [147], eventually their mixture.[148] One of the obvious variations in the feedstock choice is the reactivity. For instance, methane is much less reactive than ethylene or acetylene. As a result, the decomposition of acetylene takes place at a relatively low temperature. However, the high carbon content can lead to the deposition of amorphous carbon on the sidewalls of the CNTs. Methane is one of the most simple carbon precursors. It is an alternative to acetylene that prevents a carbon over deposition, but a higher temperature is required during the synthesis of CNTs. The gas precursor is often injected in the presence of a dilution gas e.g. H_2, NH_3, Ar, N_2. The role of this additive is to avoid any excess of amorphous carbon undesirable and potentially harmful to the catalytic activity of the nanoparticles. Indeed, an accumulation of unstructured carbon in the vicinity of the catalyst can lead to its poisoning. Additionally, in order to control the growth of CNTs and the carbon supply, the vapor pressure is an important parameter.[149, 150] The total vapor pressure is given by the sum of the partial pressure of each injected gas, i.e. carbon feedstock precursor, reductive gas, and carrier gas. By changing the vapor pressure, a surplus or deficiency of carbon occurs due to either too high or too low vapor pressure, respectively. Therefore, a proper balance among each gas has to be achieved. In the case of a too low vapor pressure of the gas precursor, CNTs will not be formed. On the contrary, deposition of parasitic amorphous carbon and poisoning of the metal catalyst can take place easily. Finally, for synthesizing CNTs, nanometer-sized metal particles are required to promote the decomposition process of hydrocarbon

precursors at a lower temperature than the spontaneous decomposition temperature of the hydrocarbon. Generally, transition-metal nanoparticles are used as catalysts for the growth of CNTs. Among the transition metal nanoparticles, Fe, Ni and Co, are the most frequently used catalysts, due to the high solubility and high diffusion rate of carbon atoms at high temperature. The high melting point and low equilibrium vapor pressure of these metals also provide a widely suitable temperature range for a wide range of carbon precursors. Different metals have been tested and have been demonstrated to be adequate catalysts, e.g. Pd, Pt, Au, Al, Mg, etc.[138] Fe, Co and Ni are the most effective catalysts to grow CNTs, because they have a strong adhesion with the growing CNT and they allow to form CNTs with smaller diameters.[138]

2.6 Vertically Aligned Carbon Nanotubes

Typically, in case of using a high areal density of metal catalyst nanoparticles, every growing nanotube will be surrounded by adjacent nanotubes. A self- alignment of the growing CNTs can be achieved via a steric effect. During the growth process, the Van der Waals forces between neighboring CNTs will force all tubes to grow vertically-aligned and to form a forest structure.[151] Compared with non-aligned CNTs, when implemented in a LIB cell, the vertical alignment of CNTs in the direction of the ion diffusion can have positive effects for an increase in both the storage capacity and the rate capability. Vertically aligned CNTs (VACNTs) ensure better contact and adhesion with the substrate, resulting in an increase in the ion diffusivity as well as an improvement of the electron transport properties, which allow improvements in the rate capabilities.[152, 153] Furthermore, the intimate contact between each of the VACNTs and the substrate provides a low resistance pathway allowing for an effective connectivity throughout the electrode.[153] Finally, VACNTs exhibit a porous structure with a large surface area, which may greatly facilitate the chemical transport and the interfacial reaction.[154] These great properties (regular pore structure, high surface area and excellent conductivity) of VACNTs make them extremely attractive potential candidates to act as electrode materials or as current collectors that can enhance the performance of energy storage devices.

2.6.1 Synthesis of vertically aligned carbon nanotubes

2.6.2 Experimental setup

The VACNTs were synthesized using a double hot-filament chemical vapor deposition (dHF-CVD) technique. Thanks to this technique, it was possible to grow straight CNTs

over a large area with excellent uniformity in diameter, length and density and at relatively low growth temperatures. The dHF-CVD method efficiently allows a local thermal decomposition of the precursor molecules (H_2 and CH_4) around the hot-filaments before reaching the substrate withstanding the catalyst. Thanks to the hot filaments, the synthesis of the CNTs occurs at relatively lower temperature than the conventional thermal CVD process. Figure 2.5 shows the schematic of the dHF-CVD reactor that was used in this work. All VACNTs were synthesized using CH_4 as the carbon feedstock precursor. CH_4 was diluted in H_2 in order to etch parasitic amorphous carbon (a-C) during the growth process and H_2 has also been used to perform the catalyst pretreatment prior to the growth of the VACNTs. As shown in figure 2.5, the two gases were introduced through two different inlets. Tungsten filaments were placed at each gas inlet. The filaments were powered independently in order to increase the temperature locally and allow independent decomposition of the molecules. Consequently, the gas molecules were decomposed at the gases inlet creating hydrocarbon radicals, and respectively hydrogen radicals.[155]

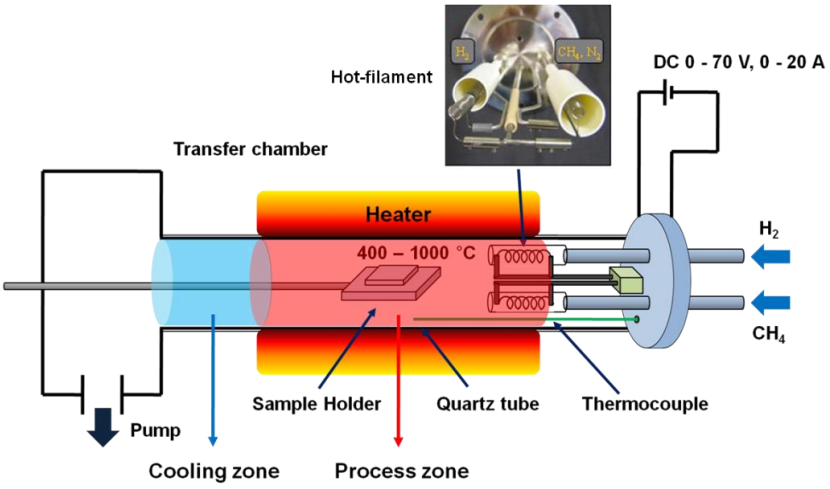

FIGURE 2.5: **Schematic design of the hot filament chemical vapor deposition system.**

The dHF-CVD reactor includes two different zones: a cold zone where the sample is introduced and removed and a hot process zone where the growth happens (figure 2.6). The schematics summarize the general steps of the growth of VACNTs in this work. In the first step, the sample was placed in the cold zone meanwhile the process zone was being heated at 600°C. When the temperature and pressure reached target values, the sample was translated into the hot process zone. Before growing the CNTs, a pretreatment of the sample under pure, activated hydrogen was performed. The highly

powered hot-filament at the H_2 inlet was used. After finishing the pretreatment process, without removal of the sample from the hot zone, the CNTs growth was performed by injecting the CH_4 carbon precursor. The ratio between CH_4 and H_2 were adjusted for the CNTs growth process. Finally, when the synthesis of VACNTs was finished, the sample was transferred again to the cold zone.

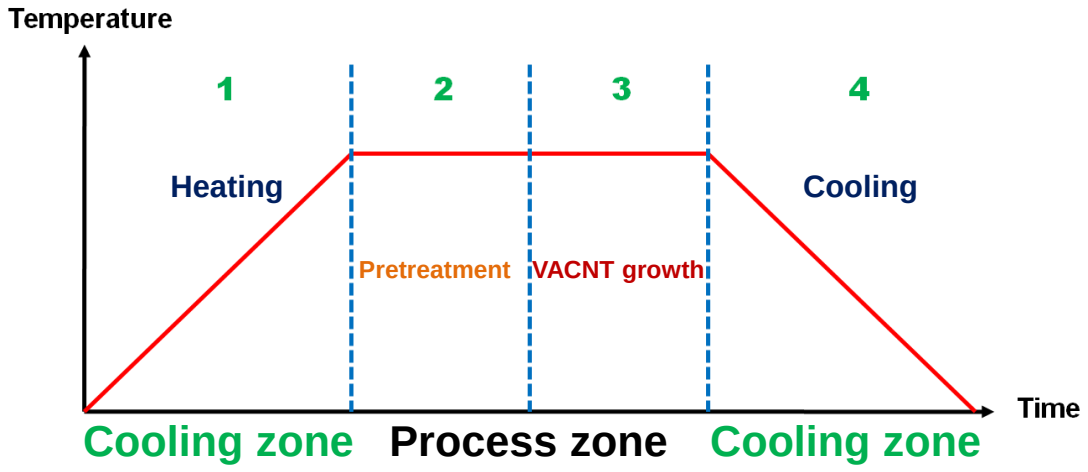

FIGURE 2.6: **General procedure of the synthesis of VACNTs by dHF-CVD approach.**

2.6.3 Synthesis of VACNTs-based nanostructured current collector

This part of the Chapter is focused on the description of the experimental approach that has been implemented for synthesizing VACNTs-based nanostructured current collectors. In particular, a detailed description of the main steps developed for obtaining a dense VACNTs carpet on both aluminium and copper substrates is given. Figure 2.7 illustrates the main experimental steps we have developed and improved in our work for the synthesis of dense carpets of VACNT on aluminum and copper substrates, which will make it possible to obtain a nanostructured current collector. Commercial, thin sheets of Cu and Al were used as substrates for the negative and the positive electrode, respectively. Both substrates were used without any specific pretreatment (e.g. electropolishing) keeping the initial roughness of the surfaces. It is worth mentioning that literature is very poor on the use of Cu and Al used as substrates for the synthesis of VACNTs. For both substrates, a 50 nm thick aluminum oxide (Al_2O_3) layer was evaporated under ultra high vaccum (10^{-9} mbar). The Al_2O_3 layer acts as a barrier layer between the catalyst Fe and the substrate, Cu (or Al), thus preventing the intermixing

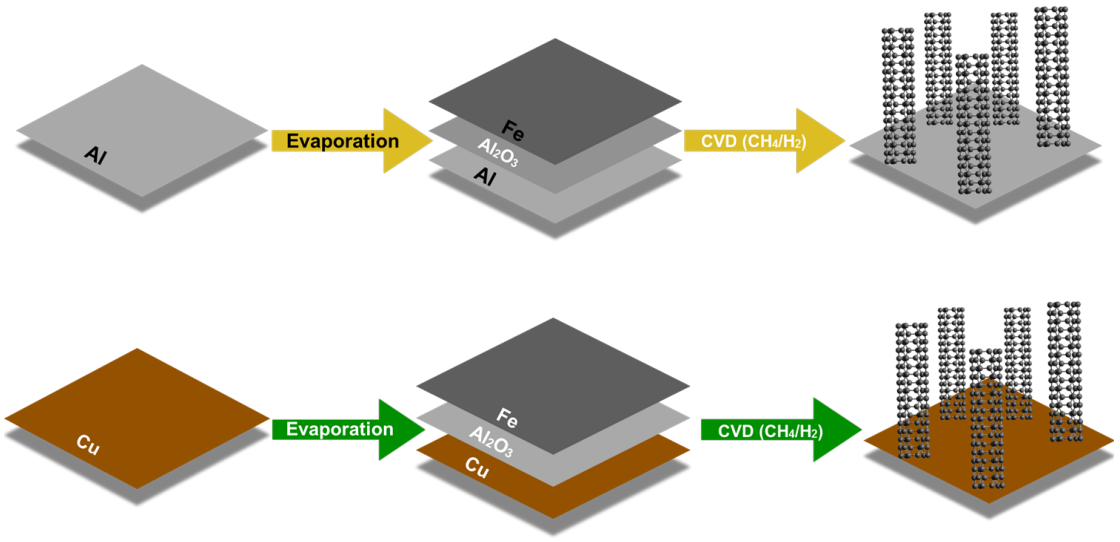

FIGURE 2.7: **Schematical representation of the main stages of the synthesis of VACNT on Al and Cu substrates.**

of the Fe catalyst with the substrate, at high temperatures. This step is followed by evaporation (in the same experimental set-up, without sample exposure to ambient air) of 10-20 nm thick Fe catalyst layer on top of the alumina coating, with the substrates heated at 300°C during the evaporation process. The heating process is essential for different reasons: 1) insures the outgasing of all impurities from the substrates, 2) enables the diffusion of the atoms on the surface of the predeposited alumina layer, and 3) favors the adhesion of the multilayer structure with the substrates and also improve the adhesion of the subsequent as-growth VACNTs. The growth of CNTs on both type of substrates is performed individually, but using similar dHF-CVD parameters. Initially, the Cu or the Al substrates were inserted into the cold zone. As mentioned above, the growth process included two steps:

1. Prior to the CNTs growth, the catalyst nanoparticle formation was achieved by a catalyst pretreatment process under atomic hydrogen atmosphere. The tungsten filament, located at the inlet of the gas source, was heated up to 2000°C by applying a power of 180W. H_2 gas (ϕ_{H_2}= 100 sccm) was forced during 5 minutes to flow through the heated filament, generating atomic hydrogen at a reactor pressure of 50 mbar. Reduction of oxidized metal nanoparticles and dewetting of the catalyst layer, i.e. a catalytic metal cluster formation, were attained.

2. Subsequently the VACNT growth was performed using CH_4/H_2 gas mixture: ϕ_{H_2}= 50 sccm, $P_{filament}$= 180 W and respectively ϕ_{CH_4}= 50 sccm, $P_{filament}$= 205 W, p= 50 mbar during a time varying from 5 min to 50 min.

The pretreatment step and the CNTs synthesis have been carried out at 600°C for the two type of substrates (i.e. below the melting point of Al at 660°C). During the pretreatment step, at the process temperature, the Fe surface diffusion is strongly activated while under the effect of the atomic hydrogen, creates trap sites on the Al_2O_3 layer that uniformly hold the Fe atoms on the surface, resulting in the formation of a dispersed catalytic NPs layer of very small diameters and very high density.[156, 157] Figure

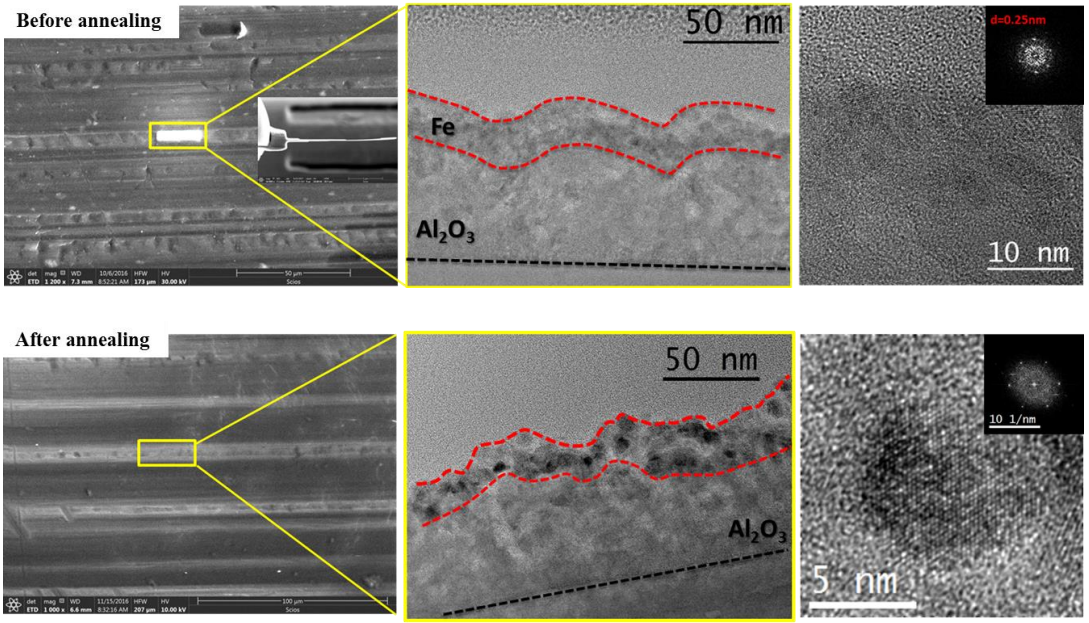

FIGURE 2.8: **SEM and TEM observations on FIB cross-section lamellas of Al_2O_3@Fe layers assembly deposited onto the Al substrate before (top) and after annealing (bottom) the sample.** Top: left SEM image showing the area where the FIB lamella was prepared with an inset of the obtained lamella; middle TEM image illustrating the Al_2O_3 and Fe layers on Al substrate; and right HRTEM image of the Fe catalyst layer with an inset of its FFT evidencing its crystalline structure. Bottom: left SEM image showing the area where the FIB lamella was prepared; middle TEM image illustrating the Fe NPs formation on the Al_2O_3 with sizes between 5-10 nm layer; and right HRTEM image of an Fe NP with an inset of its FFT evidencing its crystalline structure.

2.8 displays scanning electron microscope (SEM) and transmission electron microscope (TEM) images on FIB cross-section lamellas of Al_2O_3@Fe layers assembly deposited onto the Al substrate before and after annealing the sample with the Fe catalyst layer for 5 minutes under H_2 atmosphere. The left top and bottom panels show the SEM images on the areas where the FIB lamella were prepared before and after annealing, respectively.

The middle panels show the TEM images before (top) and after (bottom) annealing and illustrate the formation of Fe NPs with sizes between 5-10 nm on the Al_2O_3 layer. The right panels show high resolution TEM (HRTEM) images of the Fe catalyst layer before annealing (top panel) and an Fe catalyst NPs after annealing (bottom panel), with their FFT evidencing their crystalline structure. Subsequently, this layer of NPs was exposed to a CH_4/ H_2 gas mixture for the synthesis of the densely packed VACNT by steric effect. The use of the H_2 gas during the VACNT growth, is essential to prevent the deposition of amorphous carbon during the whole growth process.

The growth of VACNTs forests are influenced by several factors, such as temperature, carbon precursor, gas pressure, gas flow rates and catalyst size and nature. Amongst these parameters, the nature and size of the catalyst metal has been largely investigated by the CNT research community with the applications targeted to the field of electronics.[158] In the present study, we investigated the impact of the catalyst thickness on the growth of the tubes. Under the same synthesis conditions, VACNTs are shown to grow densely if Fe with 10 nm thickness is deposited. For Fe layer less than 10 nm thick, however, the dense carpet fails to form, resulting in some CNTs randomly spread on the surface of the substrate as shown in figure 2.9.

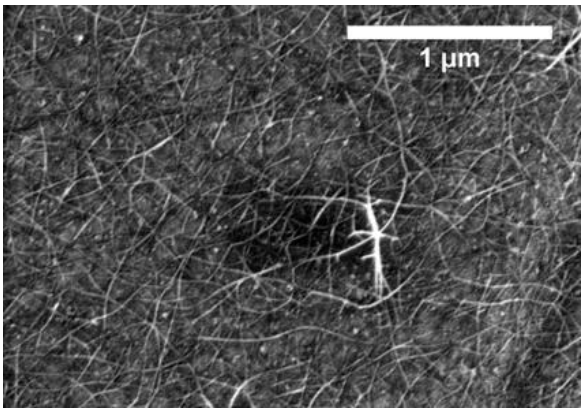

FIGURE 2.9: **SEM image of random CNTs synthesized on Al and Cu substrates during 30 minutes with starting Fe catalyst layer less of 10 nm thick.**

2.6.4 Electron microscopy: VACNTs morphological and structural characterization

Electron microscopy based techniques, such as scanning electron microscope (SEM) and transmission electron microscope (TEM) were used to access information on the structural and morphological characteristics of the as-synthesized VACNTs carpets. These techniques are commonly used in material science and by the nanotubes research community for obtaining structural and morphological properties at nanometer scale.[159, 160] The length of the VACNT carpets was deduced from several SEM analyses on the different samples synthesized under the various growth conditions. Concerning the characteristics of the tubes, HRTEM observations were mandatory for determining their crystalline structure, i.e. the numbers of graphitic planes and the defects density. HRTEM analyses were performed for VACNTs synthesized at the different growth conditions. As previously mentioned, dense VACNTs were obtained by hot filament assisted CVD at a relatively low temperature compared to other reported studies.[161, 162] Different temperatures and growth durations were studied and will be presented in following paragraphs. For the fabrication of the nanostructured collectors, we chose the CNT carpets obtained at 600°C for a growth duration of 30 minutes on both Al and Cu substrates. Figure 2.10 shows typical SEM images in which the cross-sectional morphologies of the as-grown tubes on the Al and Cu substrates is illustrated. A closer analysis of these two SEM images allowed us to study the nanotube carpet characteristics, i.e density, vertical alignment and length. As it can be perceived, under these growth parameters, we can synthesize well aligned and dense carpets of nanotubes with a CNT length (carpet thickness) up to 79 μm on Al substrate (see figure 2.10-a) and 51 μm on Cu substrate (see figure 2.10-b). Moreover, we can observe that the tubes are tightly connected to the Al and the Cu substrates underneath which is expected to be leading to a very good conductivity when used as nanostructured current collector.

TEM observations at different magnifications were performed to study the tube characteristics, i.e. crystalline structure, number of walls and defects density. Figure 2.11 illustrates the results of the TEM analyses performed on the VACNTs. The TEM observations were acquired by scratching the substrates containing the as-grown CNTs and dispersing a small amount of them in ethanol. After few minutes sonication, a drop of the solution was deposited onto a microscopy copper grid supported by a thin holey carbon film. The TEM observations on different agglomerates of the nanotubes reveal that the as-grown CNTs are very long with continuous graphitic planes (walls) presenting a tubular morphology with small amount of detectable defects. Concerning the number of the graphitic planes, a mixture of triple- and multi-wall CNTs, with an outer diameter approximately between 5-10 nm and an inner diameter of 3 nm were

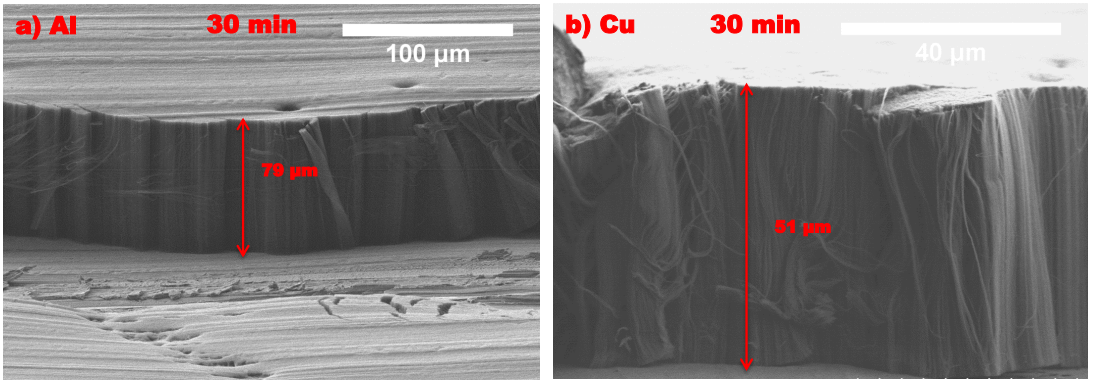

FIGURE 2.10: **Cross-sectional SEM images of VACNTs carpets grown on Al (left) and Cu (right) substrates during 30 minutes.**

obtained, which is attributed to the size of the catalyst nanoparticles formed during the pre-treatement step. The CNTs are homogenous on a centimeter scale surface on both type of substrates with same parameters of synthesis. The HRTEM images presented in figure 2.11 on different nanotubes synthesized under the same conditions illustrate the very good crystalline structure for the tubes. From these TEM analysis, we can note that, no, or very little amorphous carbon is present on the external walls of the tubes, confirming the high purity of the as-grown CNTs even at low temperature.

2.6.5 Effect of the growth time on the length of the VACNTs

The following section presents the results on the impact of the growth duration on the length of the VACNT carpets. Figure 2.12 shows the experimental results regarding the height of the CNT forest synthesized at different growth times. All growth conditions are the same except the growth time. A linear relationship is obtained within 50 minutes growth time range and the average growth rates are about 0.8μm min^{-1} and 0.6 μm min^{-1} for Al and Cu, respectively. The cross-sectional SEM images (figure 2.12) and TEM analyses (figure 2.11) show the very good alignment, high density and cleanliness of the CNTs obtained, i.e. absence of deposition of a-C or of an eventual high residual level of catalytic particles. Furthermore, an average inter-tube distance of 5 nm is estimated. With increased growth time, the VACNTs become longer. However, CNTs tend to stop their growth at prolonged growth durations, especially for the Cu substrate. To explain such growth stagnation, one popular hypothesis is the catalyst-poisoning. During the growth process, the catalyst nanoparticles are losing their catalytic activity which results

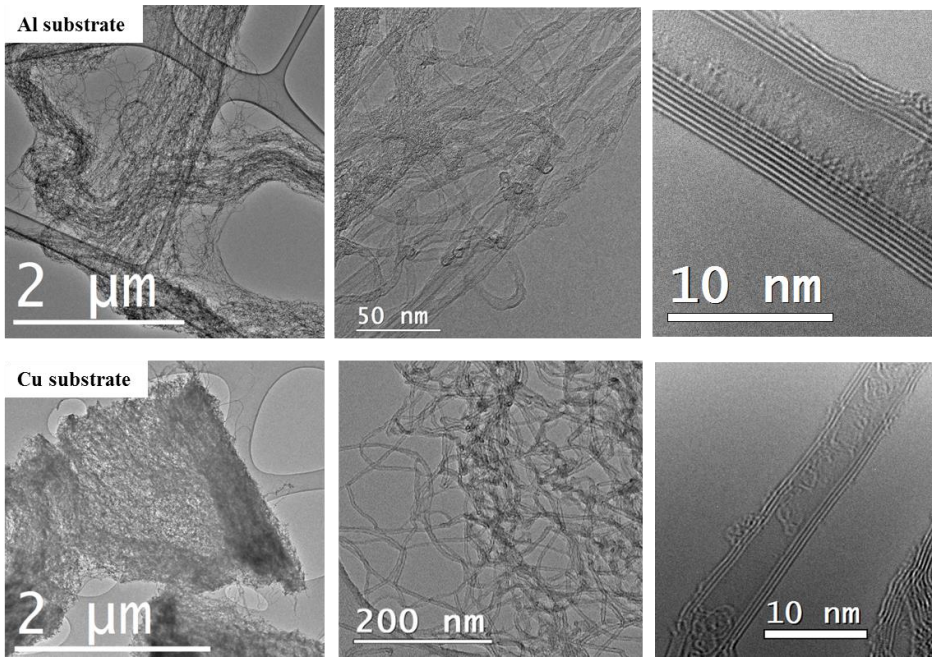

FIGURE 2.11: **TEM observations on the CNTs synthesized on Al (top) and Cu (bottom) substrates.**Top: (left) low magnification TEM image on a dense area of tubes on a holey carbon film; (middle) medium magnification TEM image illustrating the tubes diameter size; and (right) HRTEM image of a CNT with 7 walls. Bottom: (left) low magnification TEM image on a dense area of CNTs on a holey carbon; (middle) medium magnification TEM image illustrating the tubes diameter size; and (right) HRTEM image on a CNT with 3 walls.

in the CNTs growth stopping. One explanation can be related to amorphous carbon that is gradually accumulated and can cover the catalyst particle and thus blocks the access of additional carbon precursor gas to the catalyst particles.

In our case, it can be observed that we have a tip growth mode which is reasonable for high-density VACNTs since carbon species may be unable to penetrate to the forest bottom.[163]

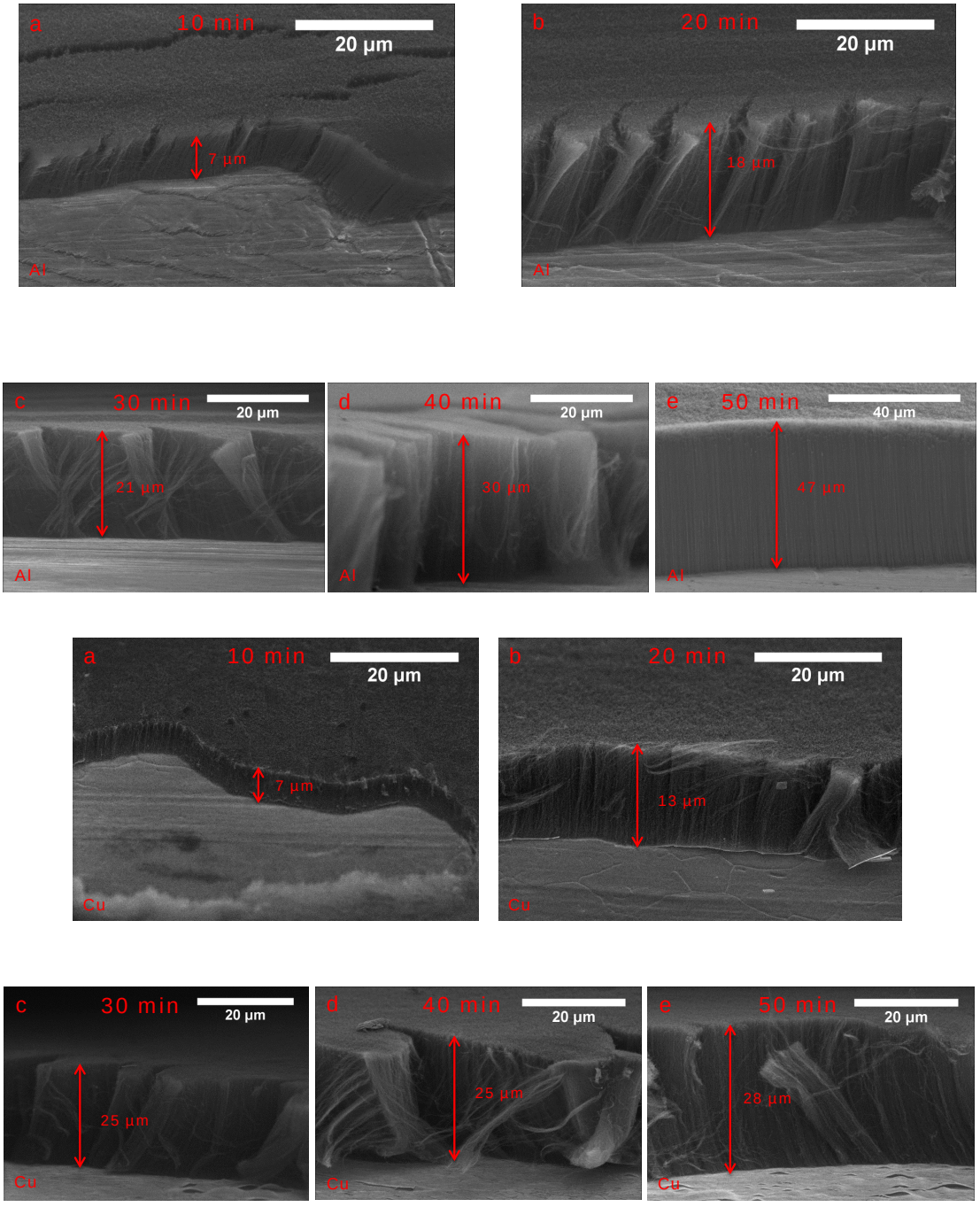

FIGURE 2.12: **Cross-sectional SEM images of VACNTs carpets grown on Al and Cu substrates at different growth times.**

2.7 Conclusion

In this Chapter, the growth of dense, VACNT carpets has been studied and optimized on two different substrates (thin commercial Cu and Al foils) by a hot filament assisted CVD process. This study was performed in order to be enable the use of VACNTs as a current collector for both cathode and anode electrodes in LIBs. The VACNTs have regular porous structures which facilitate the transport of the ions and the nanotubes composing such carpets are ensuring a conduction paths along the whole tube's length. Such CNTs in the form of aligned carpets have then well suited characteristics for use in electrochemical energy storage systems, in particular in terms of discharge/ charge rate and power.

Chapter 3

Cathode nano-fabrication

This Chapter is devoted to the nano-fabrication of the positive electrode of the LIB. The first part presents a general background on Li/S batteries, and an overview of the most relevant research realized in the last decade concerning the cathode of a Li/S battery. The second part is devoted to the experimental methods, including the main steps that have been developed for the fabrication of the nanostructured electrode. Several potential active materials have been considered and tested, such as sulfur, nickel and iron. This chapter mainly focuses on the results obtained on the S@VACNTs based nanostructured electrodes.

Sulfur cathodes offer a very high theoretical capacity compared to other cathode materials. However, the use of sulfur as active material for cathode electrode faces several challenges: development of methods allowing to achieve an increase in the active mass utilization, suppression of the capacity fading over long cycle life and constrains of the safety hazards related to the use of the lithium metal anode. The development of Li/S battery is inhibited by its severe capacity fading, which is mainly caused by the high solubility of polysulfides in organic electrolytes.

A new cell configuration for Li/S cells is proposed in figure 3.1. As it can be seen it is composed of VACNTs (synthesized on an Al substrate) and sulfur nanoparticles coated by a polymer and/ or metal oxide after their deposition on the VACNTs. Good specific capacities were obtained due to the highly conductive VACNTs nanostructured current collector. As mentioned in the previous Chapter, VACNTs offer abundant electron pathways and traps for the dissolved active material. In addition, such electrode is free of binders and carbon additives, which eliminates the use of traditional solvents necessary during the regular electrode fabrication in Li-ion battery industry and reduce the dead weight.

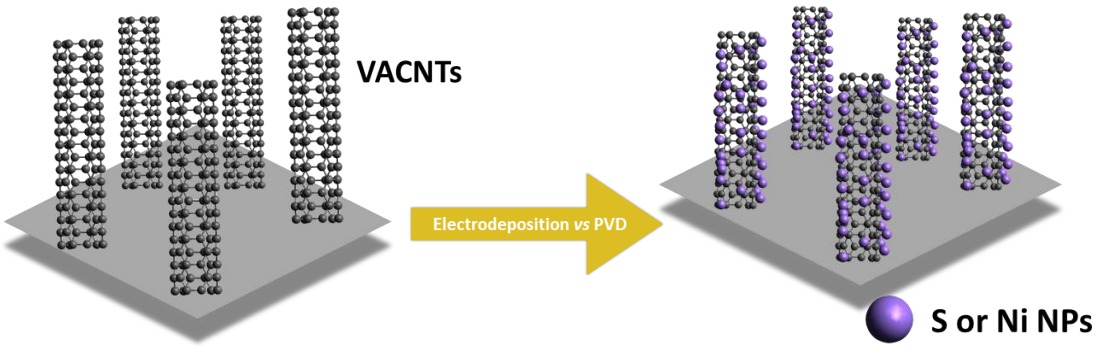

FIGURE 3.1: **Schematic illustration presenting the hybrid nanostructured cathode nano-fabrication concept.**

3.1 Concept of a lithium-sulfur battery

The concept of using elemental sulfur as a cathode electrode material was introduced for the first time in 1962 by Herbet and Ulam.[164] However, since the commercialization of LIBs in 1991, the research on Li/S battery has stagnated. After 2008, the rapid development of emerging renewable energy applications, e.g. electric vehicles, military power supplies and stationary storage systems, required a higher demand for high performing batteries.[22] Since 2009, Li/S batteries have received extensive attention as one of the most promising candidates for the next-generation energy storage applications after Nazar et al [34] reported a Li/S battery with a significantly improved cycling performance. Sulfur has one of the highest theoretical specific capacity of 1675 mAh g^{-1} among all existing positive electrode materials. The coupling of the high-capacity electrodes, lithium (3840 mAh g^{-1}) and sulfur (1675 mAh g^{-1}), affords an average cell voltage of 2.15V and a theoretical specific energy of 2570 W h kg^{-1} (based on the two electrodes), which is an order of magnitude higher than that of traditional LIBs. Furthermore, sulfur is an abundant element, possess low environmental concern and is extremely cheap, which may drastically decrease the final cost of the battery. Sulfur forms polyatomic molecules with different structures, and the orthorhombic alpha-sulfur (α-S_8) is the most stable allotrope at room temperature. In a Li/S system, the electrochemical reactions occuring involve lithium, lithium ions, sulfur and polysulfides ions. Compared to Li-ion battery, a typical Li/S battery is based on lithium metal anode and an elemental sulfur cathode both separated with a porous polymeric separator soaked with a dilute ether-based electrolyte. The cell operation starts from discharge because

sulfur is in the charged state (no Li^+). During the discharge process at the negative electrode, metallic lithium is oxidized, releasing lithium ions into the electrolyte to the positive electrode and electrons go through the outer circuit. The oxidation reaction taking place at the anode electrode is described as follows:

$$16Li^0 \rightarrow 16Li^+ + 16e^- \tag{3.1}$$

At the positive electrode, sulfur is reduced by accepting Li^+ ions and electrons as follows:

$$S_8 + 16e^- \rightarrow 8Li_2S \tag{3.2}$$

The overall reduction-oxidation reaction of Li/S system, at the voltage of 2.15V vs Li/Li^+ is mentioned below:

$$16Li + S_8 \leftrightarrow 8Li_2S \tag{3.3}$$

Although the above reaction appears simple, the actual reaction occurring at the cathode during discharge is far more complex than the intercalation reactions at transition metal oxide cathodes in LIBs. Sulfur undergoes a series of electrochemical reactions [165] as described below:

$$2Li^+ + S_8 + 2e^- \leftrightarrow 2Li_2S_8 \tag{3.4}$$

$$2Li^+ + Li_2S_8 + 2e^- \leftrightarrow 2Li_2S_6 \tag{3.5}$$

$$2Li^+ + Li_2S_6 + 2e^- \leftrightarrow 2Li_2S_4 \tag{3.6}$$

$$2Li^+ + Li_2S_4 + 2e^- \leftrightarrow 2Li_2S_2 \tag{3.7}$$

$$2Li^+ + Li_2S_2 + 2e^- \leftrightarrow 2Li_2S \tag{3.8}$$

It is worth mentioning that the operation of a Li/S cell depends on the successful evolution of each of these reactions and the physical properties of each of the species diverge greatly. For instance, while S_8 and Li_2S are solid and insoluble in common electrolytes, each of the intermediate polysulfide reduction species are soluble in organic solvents as well as ionic liquids and polymers. During cycling, the sulphides are sequentially produced and consumed as shown in figure 3.2.[61]

Each polysulfide specie formed can diffuse from the positive electrode to the electrolyte solution, reducing the overall quantity of the available active material resulting in a decrease in the capacity of the battery. Furthermore, the species can migrate through the electrolyte towards the metallic lithium anode; at that point the species can be further reduced to a shorter polysulfide chain resulting in polysulfide shuttle. This reaction can be represented as a parasitic reduction of useful energy as the species migrate and react

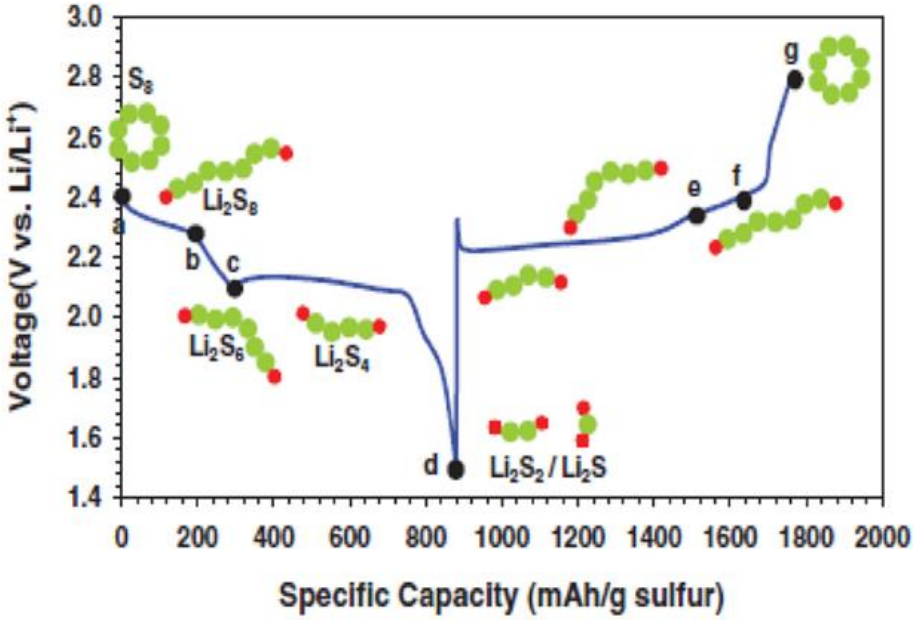

FIGURE 3.2: **Typical voltage vs. capacity plot for a Li/S cell explaining the evolution of the polysulphide species.**[61]

at each electrode, and is designated as one of the greatest challenges associated with Li/S batteries. When the series of sulfur reduction intermediates undergo migration, they will precipitate as solid Li_2S once fully reduced. This species is completely insoluble and is potentially impossible to regain use of those molecules.[61, 165]

The discharge and charge profiles are shown in figure 3.3. Based on the phase change of sulfur species, the discharge process can be divided into four regions [166]:

- Region 1: A solid-liquid two-phase reduction from elemental sulfur to long chain polysulphides (Li_2S_8), which corresponds to the first upper voltage plateau at 2.3V vs Li/Li^+ (see Eq 3.4). In this region, Li_2S_8 dissolves into liquid electrolyte to become a liquid cathode.
- Region 2: A liquid-liquid single-phase reduction from the dissolved Li_2S_8 to lower chain polysulphides, during which the cell's voltage declines (see Eqs 3.5 3.6).
- Region 3: A liquid-solid two-phase reduction from the dissolved low-order polysulphides to insoluble Li_2S_2 or Li_2S, during which Eqs 3.7 and 3.8 are competing with each other giving a plateau at 2.1V vs. Li/Li^+, which provides the major capacity of a Li/S battery.

- Region 4: A solid-solid reduction from insoluble Li_2S_2 to Li_2S. This process is kinetically slow and generally suffers from high polarization due to the non-conductive and insoluble natures of Li_2S_2 and Li_2S (see Eq 3.8).

In figure 3.3, the first arrow points to the viscosity of the electrolytic solution concentrated by polysulfides. The second arrow represents a reduced polarization as a result of the phase transition from the solid Li_2S_2 and Li_2S to the dissolved polysulfides. Upon charge process, the long plateau seen firstly corresponds to the oxidation of solid Li_2S to polysulfides and the final short plateau, which is rather hard to define, represents oxidation to S_8.[166] Nevertheless, there are still many discussions about the reactions steps occurring during cycling. Different hypothesis were presented in the last years which often includes several additional reactions and radical intermediates.

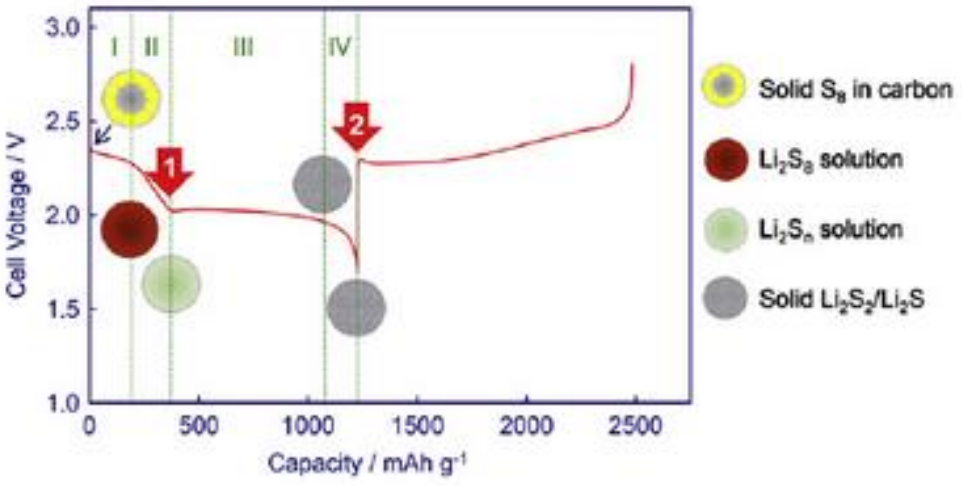

FIGURE 3.3: **Typical discharge and charge voltage profile at the first cycle of a Li/S cell.**[166]

3.1.1 Challenges in a Li/S battery

Despite the many advantages of Li/S batteries, there are several limitations that have hindered the practical application of this cell. These challenges are described in details as follows:

- Insulating active material: sulfur is an insulator due to its very low electrical conductivity of 5×10^{-30} S cm^{-1} at 25°C.[167] It requires an additional electronically conductive material, such as carbon. High carbon content increases the electrical

conductivity, but it also reduces the final volumetric and gravimetric energy densities due to the presence of inactive mass.

- Polysulfides dissolution - shuttle phenomenon: the intermediate products from the electrochemical reactions, (Li_2S_x with $2 \leq x \leq 8$), can easily dissolve in the liquid electrolyte leading to loss of the active material.[168, 169] Upon discharge and charge processes, the dissolved polysulfides species can freely migrate back and forth between the anode and the cathode. This migration is a parasitic reaction that gives rise to a characteristic mechanism of Li/S cell, so-called "shuttle phenomenon" described in the pioneer work of Mikhaylik et al.[170] At the positive electrode, high-order polysulfides are formed and then diffuse through the separator to the Li anode side to get reduced into low-order polysulfides. These low-order polysulfides can diffuse backward to the cathode side and be re-oxidized to high-order polysulfides. This parasitic process takes place continuously, even when the cell is reaching its theoretical capacity. This phenomenon leads to a self-discharge, low Coulombic efficiency, as well as active material loss and rapid capacity fading.[166, 170] Furthermore, the dissolution of lithium polysulfides causes an increase in the viscosity of the electrolyte, consequently decreasing the ion mobility between the electrodes.[171]

- Volume expansion - morphology change: the volume change of the positive electrode is also an important issue in the Li/S battery system. The difference in the densities between α-S_8 (2.07 g cm^{-3}) and Li_2S (1.66 g cm^{-3}) [166] leads to a large volumetric expansion ($\sim$ 80%) upon lithiation, which results in a rapid capacity decay and low Coulombic efficiency.[172] Furthermore, when the cell starts to run, the sulfur leaves the conductive network and dissolves into the electrolyte in the form of soluble polysulfides. This leads to a pulverization and a disconnection of the active material from the current collector, resulting in the loss of the active surface area. The volume expansion and the significant morphology change are strongly responsible for the failure of the battery.

- Li_2S and sulfur plating: the final solid Li_2S product formed at the end of the discharge is highly insulating. It can easily form thick and insulating layers covering the electrodes.[173] This plating behavior may lead to the formation of some inactive areas over the electrode and also this insulating layer may not be completely oxidized in the subsequent charge cycle, leading to inactive material losses because it will not participate in the further reactions. Consequently, a capacity fading of Li/S cell takes place.

- Lithium anode: Li metal is the standard negative electrode used in Li/S batteries. Dendrite deposition of Li metal can be formed during cycling, which may cause

short circuits in the battery resulting in cell death and safety issues. It is worth noting that the dendrite issue has several particularities in case of the Li/S battery system. The soluble polysulfides generated during cycles can react with Li, which could possibly suppress the growth of Li dendrite. Nevertheless, Li anodes cycled in electrolytes with low solubility for polysulfides may still involve dendrite generation. The other problem of the Li anode comes from the shuttle effect of polysulfides. Soluble polysulfides migrating through the separator can react with Li to form the insoluble sulfides (Li_2S_2, Li_2S). The gradual growth of insulating sulfides on the Li anode during cell operation may seriously retard the rapid access of Li, and result in poor rate capability.[174]

During the last decade, researchers have explored new strategies for the development of Li/S batteries in order to overcome the aforementioned limitations. The following section presents an overview of various approaches that have been employed for the fabrication of sulfur cathode focused to improve their performances. Some of the issues listed above are another major challenges and are beyond the scope of this thesis.

3.1.2 Cathodes for Li/S batteries

Most attempts to improve the electrochemical performance of Li/S batteries have been focused on the positive electrode. To address the sulfur cathode challenges, rational design of the electrode structure is necessary. Based on literature studies from the past several years, the sulfur electrode structure should have the following characteristics [165, 170, 175, 176]:

- Sufficient space to accommodate sulfur volumetric expansion;
- Small dimensions of the active material to avoid pulverization;
- Short transport pathways for both electrons and Li^+ ions to achieve high capacity and high power capability;
- A large conductive surface area for deposition of insulating Li_2S_2 and Li_2S in order to preserve the morphology of the electrode;
- Minimize lithium polysulfide dissolution and shuttling in the electrolyte.

The difficulties associated with fulfilling all these requirements with one electrode design explain why it is very challenging to realize sulfur electrodes with high specific capacity and long cycle life. Nanostructuring the sulfur cathode can be an effective strategy

to address the above-mentioned challenges. By making the sulfur electrode smaller, or by encapsulating sulfur in nanostructured carbon, sulfur pulverization can be decreased while polysulfide dissolution can be reduced. Nazar et al [34] firstly reported high specific capacity that can be realized by impregnating sulfur into a highly ordered mesoporous nano-sized carbon material in 2009.

3.1.2.1 Sulfur-carbon composites

Different approaches were developed associated to the selection of the conductive material and the method of incorporating sulfur in the composite. Carbon black [175, 177, 178], microporous carbon [179, 180], mesoporous carbon [181, 182], hierarchical porous carbon [34, 183], carbon nanotubes [176, 184–187], carbon nanofibers [188–190] and graphene [191–193] have been employed as host for accommodating active sulfur and as common conductive materials. Porous carbon substrates are considered as the suitable matrix for the composite because of their absorbability of soluble polysulfides. The sulfur composite can be prepared by mechanical mixing [194], ball-milling [184], melting route [34, 175], sulfur vaporization [195], etc. In their work, Schuster et al [183] have synthesized a carbon/ sulfur spherical electrode which showed a high reversible charge capacity up to 1200 mAh g^{-1} and good cycling stability. Furthermore, the performance of the cell can be improved by removing the external sulfur on the surface or by adding a thin coating of SiO_x. Fu et al [196] used dissolved polysulfides as an active material and a free-standing MWCNT paper as a host electrode. This system offers high reversible capacities because the dissolved polysulfide can easily be fully employed compared to the solid sulfur. The carbon properties reduce the charge transfer resistance of sulfur cathodes significantly, capture the migrating active material at the end of cycles and improve the cathode performance in the Li/S battery.[197, 198]

- **Graphene composites:**
  Graphene, with its excellent conductivity, high surface area and good mechanical property, has also been widely considered as additive for the cathode fabrication. In their study, Wang et al [199] reported graphene-sulfur composites that have been synthesized by heating a mixture of elemental sulfur and graphene nanosheets. Nevertheless, the results suggested that this approach is not very effective in trapping polysulfides, since the composite does not have a closed structure and polysulfides diffused out easily. Since then, successive optimization of the synthesis methods resulted in diverse configurations of the graphene-sulfur composites: graphene-wrapped sulfur particles [187, 200], sandwich type composites [201], and sulfur coated graphene sheets.[202, 203] The flexible characteristic

of graphene renders it suitable to be the sulfur host in the Li/S battery. The graphene in the composites coating or wrapping the sulfur can suppress the loss of active sulfur species due to the dissolution during cycling. The high electrical conductivity of graphene can improve the active material utilization as well.

- **CNTs/ sulfur cathode:**
  The MWCNTs are attractive candidates to be used as the electric conductor for sulfur cathode because they could provide more effective electronically conductive network than other conductive additives, such as carbon black, acetylene black and graphite.[176] Furthermore, MWCNTs offer large chemically active surface, have hierarchical porous structure, accommodate the volume change during lithiation/ delithiation processes and provide stable electrical and ionic transfer channels.[186] According to the work in ref. [204, 205], CNTs with sulfur reinforce the electrical conductivity of the cathode and effectively prevents the dissolution of lithium polysulfide into the electrolyte. This indicates that the usage of sulfur as a cathode material is improved during the lithiation/ delithiation processes. Another benefit when CNTs are used as current collectors is that the porous structure allows high loads of sulfur per cm^{-2} compared with classical Al based electrodes. Such collectors enhance the electronic conductivity of the cathode, by providing better connection of sulfur particles to the 3-D conductive network. As a result, the electrode resistance is reduced because of the facility of the electrons propagation along the 3-D continuous conductive network. Dorfler et al [206] reported an electrode based on binder free VACNT/ sulfur composite delivering discharge capacity higher than 800 mAh g^{-1} to respect of the composite electrode mass.

3.1.2.2 Sulfur-polymer composites

Besides carbon materials, conductive polymers have been employed for the modification of sulfur cathodes. The polymers used in Li/S system are divided into two types: conducting polymers and non-conducting polymers. Conducting polymers such as polypyrrole (PPy) [207–209], polyaniline (PANI) [210, 211], polythiophene (PT) [212, 213] and poly(3,4-ethylenedioxythiophene) (PEDOT) [214] have been used for sulfur coating, facilitating the electron transport and improving the active material utilization. Additionally, the polymer coating works as a barrier to retard the polysulfide dissolution in the electrolyte. Non-conducting polymers, such as polyacrylonitrile (PAN) [215, 216], polyvinylpyrrolidone (PVP) [214], polyethylene glycol (PEG) [217] and block copolymer [218] were employed to offer a chemical gradient to suppress the out-diffusion of active polysulfide anions. In general, polymers in Li/S batteries play a protective role to reduce the capacity fading by localizing the soluble polysulfides at the cathode region, but a

certain amount of carbon additives into the composition of the electrode is still needed to enhance the sulfur conductivity and cyclability.[214, 216, 218]

3.1.2.3 Alternative composites

Not only carbon materials and polymers, but also other materials could be applied for the sulfur composite synthesis. Various nano-sized metal oxides have been used as additives in sulfur composites, such as magnesium nickel oxide (MnNiO) [219, 220], alumina (Al_2O_3) [221], silica (SiO_2) [222] and titanium oxide (TiO_2).[223] These nano additives function as adsorbing agents to improve cycle stability and reduce polysulfide shuttle. In their work, Seh et al [172] designed a TiO_2-sulfur yolk-shell nanoarchitecture that exhibits prolonged cyclability over 1000 charge/ discharge cycles in Li/S batteries. The yolk-shell structure can accommodate the large volumetric expansion of sulfur cathode during lithiation and can minimize the dissolution of polysulfide. Despite that, the sulfur loading needs to be further increased for practical use.

3.1.3 Li_2S acting as the cathode material

Recently, lithium sulfide (Li_2S), the final product of sulfur lithiation, has received increasing attention as a promising candidate for Li/S batteries. Li_2S as the starting cathode material offers a high theoretical capacity of 1166 mAh g^{-1}. The use of Li_2S cathode obviates the need for metallic Li anodes. The cathode can thus be paired with various Li-free anode materials with large capacity and higher lithiation potential when assembling the battery (e.g. silicon and tin).[224–226] As a result, the common problem of Li anode, such as dendrite growth, might be eliminated. This approach also contribute to a much enhanced battery safety. Nevertheless, the implementation of Li_2S cathode is still impeded by several problems. Li_2S has hydroscopic property, which makes it highly unstable in air.[227] The preparation and the storage of Li_2S should be implemented with strict isolation from ambient environment. Li_2S has a high electronic resistivity and poor ionic conductivity (10^{-13} S cm^{-1}), which makes the cathode electrochemically inactive. Cui et al [228] have found that, for micrometer-sized Li_2S particles, a large potential barrier ($\sim$ 1 V) should be overcome at the beginning of charging process. To improve the Li storage kinetics, a combination of Li_2S with electronic conductors, such as carbon, is highly desired in preparing the cathode materials.[228] The last problem results from the electrochemistry of sulfur. Given that Li_2S shares the same but reverse electrochemical processes as sulfur, polysulfide dissolution and shuttle are also observed on the cathode.[174] To overcome the problem, Li_2S is often encapsulated into porous substrates to limit the active material loss during cycling.

Yang et al [224] made a full cell with Li-free Li_2S cathode and Si anode. The cathode comprised of a nanocomposite in which Li_2S fills the pores of CMK-3 mesoporous carbon particles. The cathode was then paired with Si nanowires anode to assemble the full cell. The nanostructured designs of both electrodes allowed overcoming the issues associated with active sulfur loss and drastic Si expansion, contributing to a high specific energy (630 Wh kg^{-1}, based on Li_2S mass only). However, if the masses of all electrode additives (CMK-3, PVDF, Super P conductive carbon) are considered, the initial specific energy was found to be 349 Wh kg^{-1}, which is similar to that of commercial Li-ion batteries (335 Wh kg^{-1}).[224]

3.2 Synthesis methods for the cathode materials

3.2.1 Electrodepositon process

In recent years, electrochemical deposition or electrodeposition has become an established technology for materials deposition for different applications and is considered to be a clean technique while it has maintained its cost advantage over more traditional methods such as sputtering or evaporation.[229] During this process, electrodeposits are formed by the action of an electric current passing through an electrochemical cell, a device that consists of two conductive electrodes immersed in an electrolyte; the working electrode (WE), consisting of the substrate where electrodeposition is planned, and the counter-electrode (CE), necessary to complete the electrical circuit. Electrolytes for electrodeposition are usually aqueous solutions containing positive and negative ions, prepared by dissolving metal salts. The electric current that flows between the two conductive electrodes in the presence of an external voltage is due to the motion of charged species, via migration and diffusion, towards the surfaces of the polarized electrodes. At the electrodes surface, the conduction mechanism must change from ionic to electronic, an interface process mediated by the occurrence of electrochemical reactions that promote the reduction or the oxidation (redox reactions) of the ionic species. An essential characteristic of electrochemical reactions is that the exchange of charges does not occur between chemical species, as it does in a typical chemical reaction, but between chemical species and the electrode. The electrochemical reaction that is most important for the electrodeposition process is the one that occurs at the working electrode [230]; i.e.

$M^{n+} + n\mathbf{e}^- \leftrightarrow M_{(s)}$

Where n is the number of the electrons involved in the reaction. When the reaction occurs in such a way that M^{n+} is reduced by receiving n electrons, its known as reduction (metal deposition). In the reverse case, the reaction is called oxidation.

Generally, there are two different ways to electrodeposit a metal onto an electrode: 1)

deposition under constant current, where a galvanostat method is used to automatically vary the potential within a certain range to provide a constant current flow, and 2) deposition under constant potential, so called potentiostat method, where a fixed potential is applied while the deposition current is measured. The pulse electrodeposition process (PED) brings a new approach in the electrodeposition of metals. Basically, it consists in applying a short pulse in order to reduce the metallic ions. The cycle is completed by a rest time (delay time) quite long to facilitate the recovery of the ionic concentration close to the electrolyte and the deposited material. The PED method allows more homogeneous and uniform deposition of the material on the substrate.[231, 232]
In the present work, we used a three electrode configuration, including the WE, the CE, and a reference electrode (RE) with a fixed and known potential that measures the WE potential. The PED process was used with the deposition voltage and pulse shape chosen depending on the desired metals to be deposited on the VACNTs. A simple pulse shape, i.e. pulse regime/ rest regime as shown in figure 3.4, was employed for avoiding a complicated electrodeposition behavior. In order to help refreshing the electrolyte solution more easily and to help migration of metal ions on the substrate, metal ions containing electrolyte was vigorously stirred.
Electrodeposition of various materials such as Ni, S and Si was carried out and the results will be further discussed.

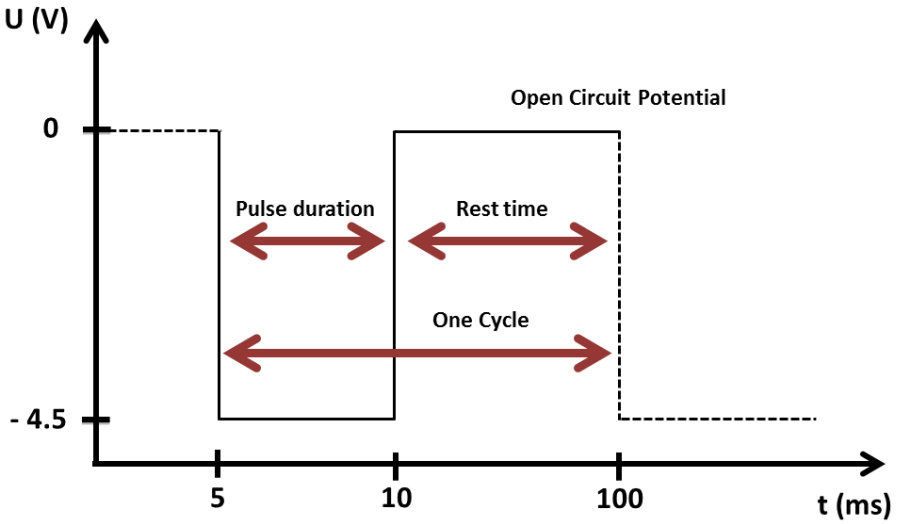

FIGURE 3.4: **Applied pulse for the electrodeposition process**

3.2.1.1 Experimental setup for the electrodeposition of sulfur

The schematic representation of the three-electrode cell for electrodeposition is shown in figure 3.5. The setup was supplied by a Bio-Logic potentiostat. In order to set the electrodeposition parameters (pulse duration, rest time, potential, sweeps) the EC-lab software was employed. Electrodeposition was carried out under potentiostatic mode.

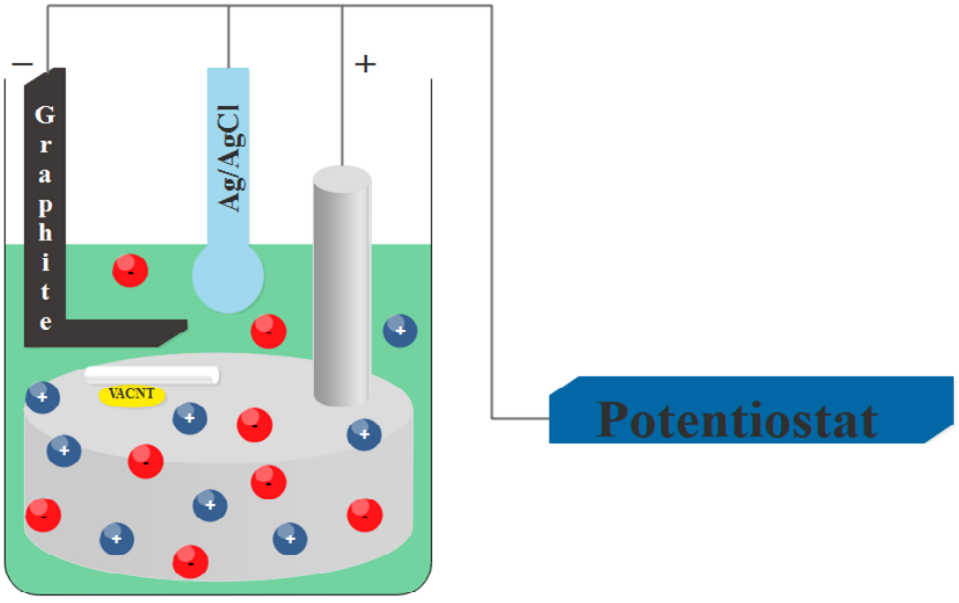

FIGURE 3.5: **Schematic representation of the experimental set-up used for the electrodeposition process.**

Sulfur NPs were deposited on the VACNTs as the active material for the positive electrode at room temperature. The working-solution constituted of 0.1 mol.L^{-1} of sodium sulfide (Na_2S) and 0.5 mol.L^{-1} of sulfuric acid (H_2SO_4) aqueous solution. H_2SO_4 was added to modify the pH of the solution to become acidic. This will prevent the Na_2S from attacking the Al substrate. The following reactions take place in the cell:

$Na_2S + H_2SO_4 \rightarrow Na_2SO_4 + H_2S$

S^{2-} - 2 e^- $\rightarrow$ S°

The WE constituted of VACNT carpets on Al. For the CE and the RE, graphite and Ag/AgCl were used, respectively. A short pulse of 2V was applied between the WE and the RE during 5 ms, followed by a longer rest time of 500 ms in the open circuit potential (OCP). This potential corresponds to the potential that exists between both electrodes immersed in the electrolyte. Therefore, the OCP establishes the zero potential with respect to the chemical cell. The number of sweeps was varied between 50-500 in order

to deposit and to adjust the size of the deposited NPs. The mass loading of S was found to be 0.20 mg cm^{-2}, a value far from the necessary loading for commercial batteries.

3.2.1.2 SEM and EDS characterizations of S NPs obtained by electrodeposition

In order to access morphological information of the S@VACNTs assembly, SEM analyses have been performed and are presented in figure 3.6. The SEM micrographs illustrated in figure 3.6-a reveal that the S NPs deposition is rather inhomogeneous with NPs deposited preferentially in the surface of the CNT carpet, and no deposition on the CNT sidewalls took place. Taking a closer look at the surface of the CNT carpet, we notice that there are only few areas where the S NPs form leaving several areas bare from NPs. From the SEM micrograph, the particle size was found to range between 20 to 50 nm. The S presence was evidenced by performing energy dispersive spectra (EDS) (refer to Appendix A-2) on the sample obtained from the SEM analysis in figure 3.6-b. The EDS spectrum is presented in figure 3.7. The EDS analysis reveals the presence of sulfur NPs in this area of the sample. The other peaks are attributed to the presence of C from the CNTs, Fe from the catalyst, Al from the substrate, and O. We tried to optimize the parameters of the electrodeposition, such as potential, number of sweeps and deposition time, in order to obtain a better deposition, i.e. a homogeneous deposition of S on the surface as well as on the sidewalls of the VACNT carpet.
Unfortunately, none of our trials have succeeded in obtaining a better deposition. One of the reasons could be attributed to the concentration of Na_2S with respect to that of H_2SO_4 in the total volume of the solution, i.e. the concentration of Na_2S must exceed the concentration of H_2SO_4 by more than two times in order to compensate for the quantity of S that escapes from the cell after being transformed to H_2S gas. It is also recommended to perform the electrodeposition process in a closed cell to minimize the loss of S as much as possible.

3.2.2 PVD technique

Since the amount of S deposited using the electrodeposition method described in the previous section is not homogeneous, we attempted to use a physical approach by using the physical vapor deposition (PVD) method. This is a deposition process in which atoms or molecules of a certain material are vaporized from a solid or liquid source, transported in the vapor form through a vacuum or low-pressure gaseous environment, and condensed on a substrate.[233] The PVD process can be used to deposit films of different elements, alloys, and compound materials as well as some polymeric materials.

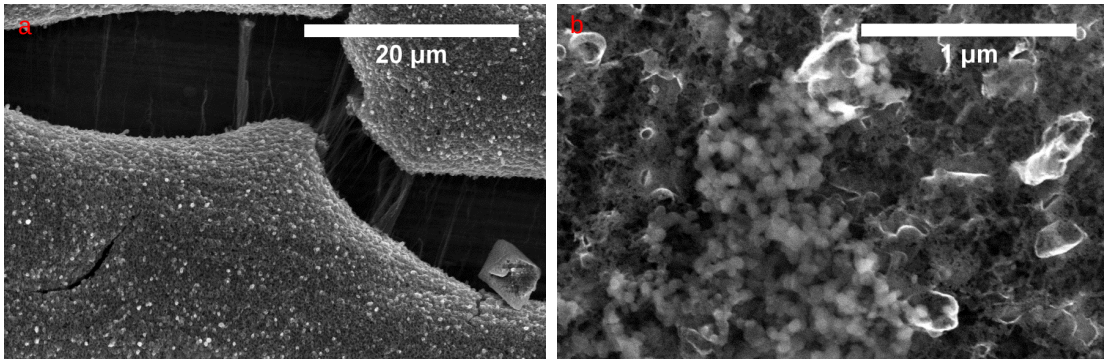

FIGURE 3.6: **SEM images of S NPs cathode on VACNT carpets.**

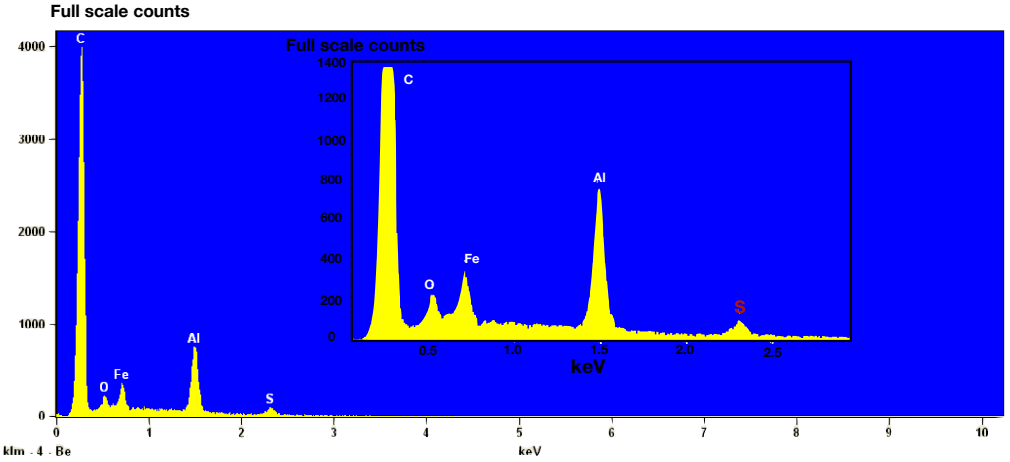

FIGURE 3.7: **EDS analysis of S NPs synthesized from an electrodeposition process.**

The typical film thickness that can be deposited using the PVD method ranges from a few angstroms to thousands of angstroms. The PVD method has the advantage that almost any inorganic material and many organic materials can be deposited using a pollution-free deposition process. The PVD processes can be categorized as follows:

- Vacuum evaporation: material from a thermal vaporization source reaches the substrate without collision with gas molecules in the space between the source and substrate.
- Sputter deposition: a source of vaporized material is a surface (target) being exposed to physical sputtering.

- Arc vapor deposition: uses a high current, low voltage electric arc in a low-pressure gas to erode the solid cathodic electrode by a moving arc or to melt and evaporate the anodic electrode.
- Ion plating: uses concurrent or periodic bombardment of the depositing film by atomic-sized energetic particles to modify and control the composition and properties of the depositing film.

3.2.2.1 Sulfur Evaporation

Alternatively, the decoration of the VACNT carpets with sulfur was performed using a new approach. It consists of a home-made evaporation system which was fabricated for the purposes presented in this work as shown in figure 3.8. The system consisted of a metallic ampoule with the CNTs substrate placed in the upper part of the ampoule and the elemental sulfur in the bottom part. The ampoule was pumped down $\sim 10^{-2}$ mbar vacuum for about 30 minutes to remove potential impurities. Then, the sealed ampoule was placed on a hot plate, so that its bottom part is exposed to direct heating. A thermocouple, to measure the temperature, was placed on the upper and lower walls of the ampoule. Sulfur was deposited directly onto the CNT carpets by thermal evaporation. In order to minimize the temperature gradient on the opposite sides of the ampoule, the temperature was raised up to 100°C from room temperature, and the heating system was then switched off for few minutes. Thereafter, the ampoule was heated up to 200°C and cooled back to room temperature. Knowing that the melting point of S is 115°C, sulfur thus is evaporated and deposited to form NPs onto the VACNT side walls.

3.2.2.2 SEM characterization of S@VACNT obtained by evaporation

The sulfur deposition results have been verified by means of SEM observations (figures 3.9), evidencing the morphology of the S@VACNT obtained after evaporation of elemental sulfur. From figure 3.9-a, we notice the formation of a thin sulfur film of 5μm on the surface of the CNT carpet. A zoom into a specific area, 3.9-b, clearly shows that the CNTs are loosing some of their vertical alignment, due to the sulfur layer that has been deposited on top of the tubes. Moreover, we notice that the evaporated sulfur encompass the whole nanotubes.

3.2.2.3 GIXRD characterization of S@VACNT obtained by evaporation

In our work, GIXRD characterizations were carried out using a D8 Discover Bruker diffractomer with Cu K_α radiation source and an applied voltage and current of 40 kV

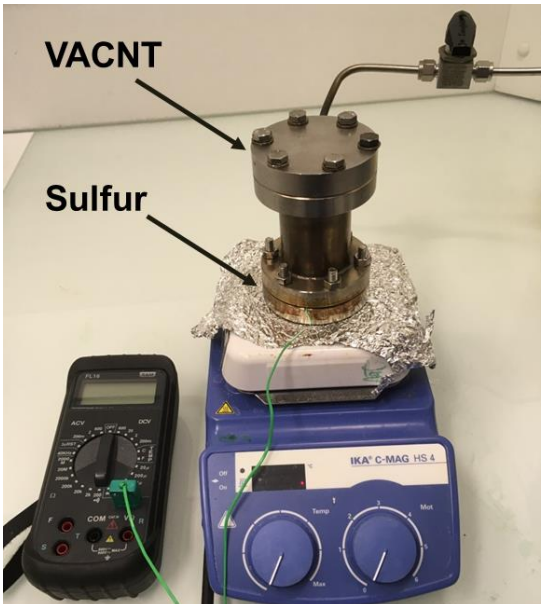

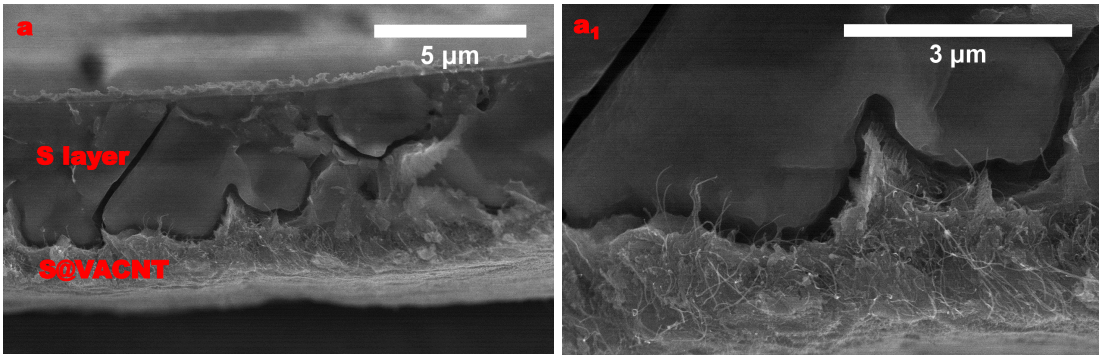

FIGURE 3.9: **Cross-sectional SEM images of S@VACNT obtained after evaporation of S.**

and 40 mA, respectively (refer to Appendix B). The 2θ scanned angle was chosen to be from 10 to 60° with a step size of 0.03° 2θ and a counting time per step of 20 seconds. Different angles of incidence were used in order to get depth sensitive information. Figure 3.10 shows the CNTs broad peak centered around 2θ=24°. Figure 3.11 presents the GIXRD patterns of S@VACNT recorded with 2° and 8° angles of incidence. The vertical red and blue lines in the graph correspond to elemental S (COD2310804) and Al (COD4313210), respectively. After sulfur deposition, VACNTs had no obvious peaks except for the appearance of a large broad peak centered at 2θ=24°. The XRD analysis of the evaporated sulfur exhibits a series of sharp and strong peaks with two prominent

peaks at 2θ=22.9° and 27.6°, indicating a well-defined orthorhombic crystalline structure with space group Fddd, which are in excellent agreement with results reported in literature.[210, 234, 235] Compared with the pattern of elemental sulfur (COD2310804-red peaks), our XRD spectrum indicates that no new peaks are obtained. Consequently, we can assume that no phase transformation of sulfur as well as no compounds formation occur during the preparation step. By changing the GIRXD angle of incidence to 2° (black line), we notice the absence of any peaks related to the crystalline Al_2O_3 at 35.15° and 57.49° or the Al substrate located at 38.47° and 44.74°. Changing the angle of incidence to 8° (orange line), i.e. at a higher depth of the material, we observe the appearance of the Al peak at 44.74°.

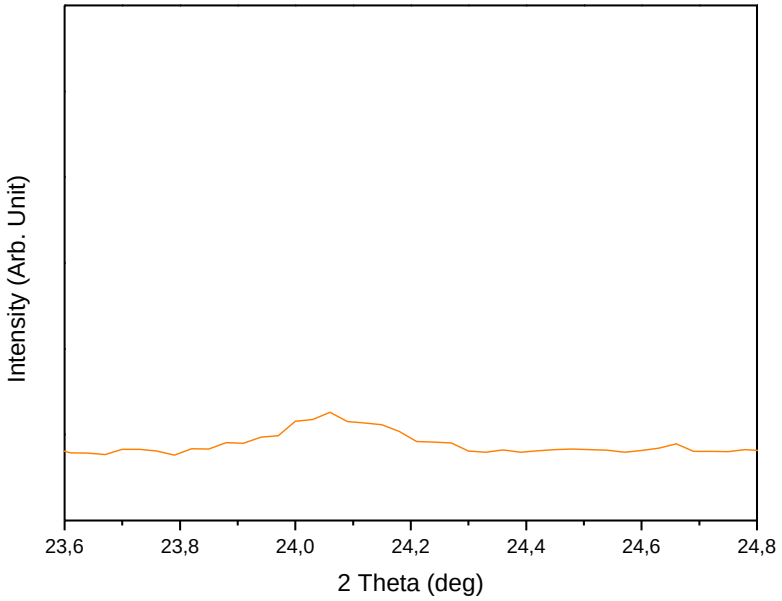

FIGURE 3.10: **A zoom of the GIXRD pattern of CNTs around 24°.**

3.2.2.4 Cell assembly

In this work, all the battery electrochemical tests were performed in a coin-cell configuration. The coin-cell is more adequate for laboratory uses since it is conceived to work for small quantities of electrode material during the testing. The electrochemical properties of the synthesized samples were evaluated with CR2032 format coin-cells. The coin-cells were fabricated in a glove box under argon atmosphere in order to avoid any reaction of the lithium metal and the electrolyte with air. Figure 3.12 shows a schematic representation of the coin-cell. The external stainless steel casings, served as both current collectors and a container of the battery, were separated by a plastic gasket to avoid any electronic contact between them and to provide a perfect sealing of the cell. Metallic

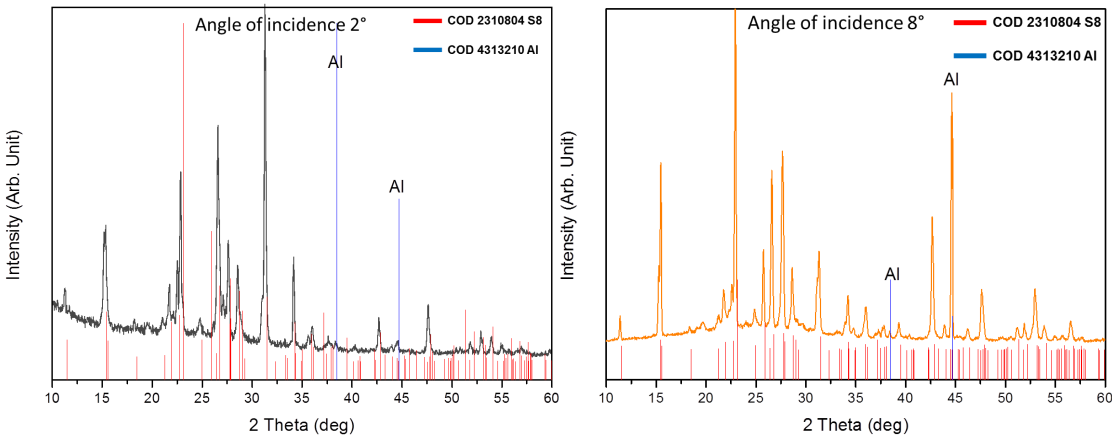

FIGURE 3.11: **GIXRD patterns of S@VACNT.**

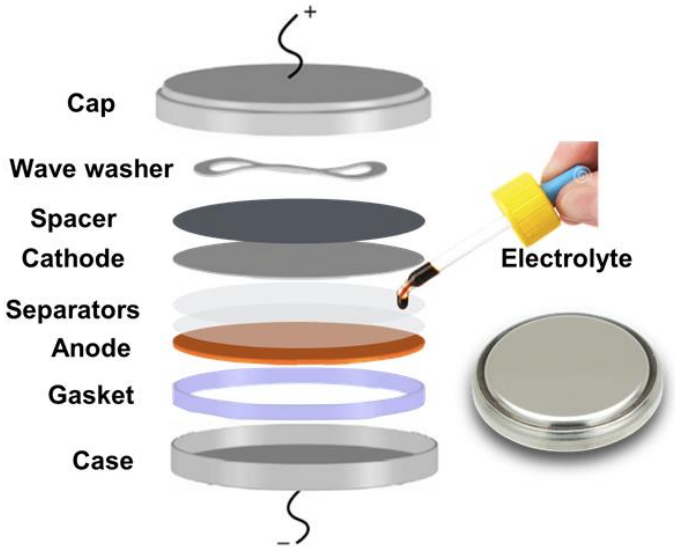

FIGURE 3.12: **A schematic representation of a coin-cell.**

lithium, used as a CE, was placed on the negative case and covered with two separator layers (16.5 mm in diameter): Whatman (fiber glass) 240 μm thick and Celgard 2400 25 μm thick polypropylene microporous layer. The Celgard separator was placed in contact with the WE because of its smooth surface that does not leave any fibers on the WE for any post-characterization of the electrode. The Whatman separator was placed in contact with the CE and it is able to impregnate a sufficient volume of electrolyte so that the amount of the electrolyte will not be a limiting point during long cycling times. The liquid electrolyte was then poured onto the separators. The positive electrode was placed on the Celgard separator and was covered with a stainless steel spacer. A stainless steel spring was placed on the spacer in order to provide sufficient pressure and contact between all the components. Finally, the cell was sealed by a crimper coin cell. The electrolyte was prepared in an argon-filled glove box by dissolving 1 M of lithium bis(trifluormethane sulfone) imide salt (LiTFSI, 99% of purity, Sigma Aldrich) in a mixture of solvents: 1,3-dioxolane (DOL, Sigma Aldrich) and 1,2-dimethoxyethane (DME, Sigma Aldrich) in 1:1 volume ratio. To further improve the battery performance, 0.25 M of lithium nitrate ($LiNO_3$, Sigma Aldrich) was added to the electrolyte as an additive. $LiNO_3$ has shown to passivate the surface of lithium anode and, thus, reduce the redox shuttle of the dissolved lithium polysulfides.[236, 237]

3.2.2.5 Electrochemical testing of S@VACNT nanostructured electrode

In order to test the stability of the electrochemical system, we performed successive lithiation/ delithiation cycles using the galvanostatic mode, i.e. at constant current, to follow the evolution of the potential and to determine the capacity stored and delivered by the battery as a function of the number of cycles. The cycling was carried out using a VMP3 Bio-logic potentiostat. In this part of the work, a half-cell configuration was tested. The tests presented here were performed against lithium metal CE which has a stable potential at 0 V and which makes it possible to have a quasi-infinite source of lithium to test the limits of our material. In this half-cell, S@VACNT was the positive electrode and the VACNTs on Al foil were used as nanostructured current collectors. The CNTs adhesion, substrate flexibility and mechanical stability were good enough to allow for easy manipulation of the VACNT electrode and for cells assembly, even when considering carpets of relatively long tubes. Since the terms of charge and discharge can be sometimes confusing, the terms of lithiation (insertion of lithium in sulfur or silicon) and delithiation (extraction of lithium) will be used throughout the thesis. The current values and the cell capacities were calculated based on the theoretical specific capacity of sulfur active material (1675 mAh g^{-1}) and the weighted amount of sulfur in each electrode.

The S@VACNT/ Li half-cells were cycled between 1.5-2.8 V vs Li/Li^+ at room temperature. Sulfur loading is definitely a key parameter for the Li/S batteries. To benefit from the high gravimetric energy density of sulfur, large sulfur loadings must be generally accomplished to compensate the mass of inactive battery materials. The loading mass of sulfur was about 0.95 mg cm^{-2}. Figure 3.13 shows the voltage-capacity curves of S@VACNT cathode in the first, second and third cycles at a C/20 rate. Since CNTs are electrochemically inert in the selected voltage range, the redox peaks can only be ascribed to the reactions between lithium ions and sulfur. Three lithiation plateaus of sulfur can be distinguished in the figure 3.13. The first cathodic plateau, located at 2.4 V, corresponds to the reduction of elemental sulfur to soluble polysulfides (Li_2S_x, $2<x<8$). The second cathodic plateau, around 2.1 V, can be assigned to further reduction of polysulfides to insoluble polysulfides (Li_2S or Li_2S_2). Moreover, a third cathodic plateau around 1.68 V is observed which corresponds to the lithiation of small sulfur molecules that can be trapped in the pores of the CNTs.[179, 180] The small sulfur molecules exist as short chain formation (S_4^{2-}, S_3^{2-}) when sulfur diffuses into the pores. Lithiated (small sulfur) reaction is considered to occur under solid phase leading to a lower cathodic plateau (1.68 V) compared with the solution phase reaction (2.1 V).[238] However, after the first cycle, the plateau-voltage shifts towards more positive direction (around 1.71 V). The low voltage in the first lithiation scan is attributed to a large strain/ stress due to large volume change requiring a large overpotential, while in the second lithiation, the strain/ stress was reduced due to the introduction of large defects in the electrode and pore size expansion of CNTs in the first lithiation, thus reducing the overpotential and shifting the voltage to a higher value in the second lithiation.[239] In addition, the small sulfur molecules electrochemical process is irreversible, i.e., the plateau at 1.68 V almost disappears in the second and third cycles. The anodic plateau around 2.4 V corresponds to the conversion of polysulfides to sulfur during the delithiation process. However, this plateau is not well defined and can be attributed to an incomplete conversion of the polysulfide chains to sulfur. This can be explained by the contribution of the thick layer of sulfur mainly in the lithiation process. In addition, the abrupt peaks at the beginning of the delithiation stage, as indicated by the green circles in figure 3.13, are assigned to the serious polarization of the electrode, which results from the low kinetics for the oxidation of Li_2S_2 and Li_2S to soluble long-chain polysulfides.[240] During lithiation, the thick layer of sulfur completely transforms to lithium polysulfides that dissolve into the electrolyte. Consequently, a large irreversible capacity in the delithiation process is obtained.

The lithiation/ delithiation processes of S@VACNT with Coulombic efficiency is presented in figure 3.14. The first lithiation presents an impressive capacity of 1600 mAh

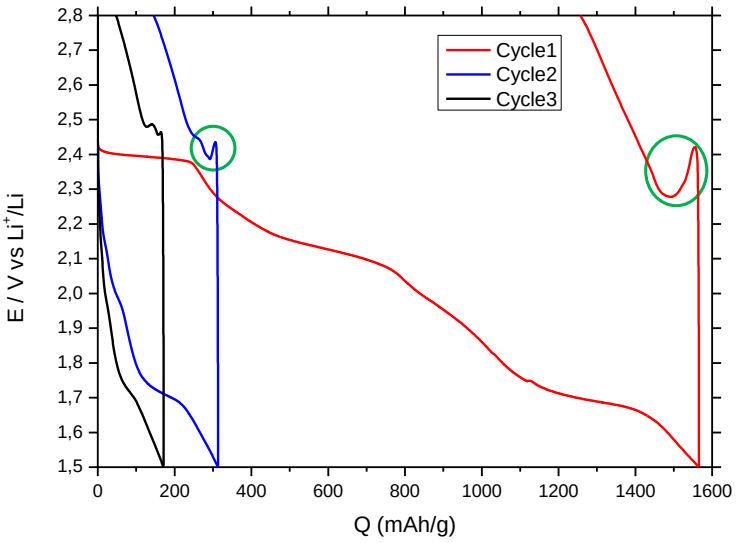

FIGURE 3.13: **Voltage capacity curves of S@VACNT at C/20 between 1.5-2.8 V vs Li/Li$^+$.**

g^{-1} very close to the theoretical capacity, but a large irreversible capacity in the delithiation process is observed (308 mAh g^{-1}). After the first cycle, the capacity of lithiation drops to 171 mAh g^{-1} in the third cycle. Thereafter, a fast declining capacity is obtained. At 100 cycles, the lithiation capacity reaches 11 mAh g^{-1}. The capacity decay in the first five cycles is probably due to the dissolution of lithium polysulfides (Li_2S_x, 4<x<8) in the electrolyte, leading to a self-discharge, low Coulombic efficiency, as well as active material loss and rapid capacity fading. The high lithiation at the first cycle may be attributed to CNTs reinforcing the electric conductivity of the sulfur. This can be an indication that the CNTs provided a direct 1-D electronic pathway improving the charge transport during the lithiation process.

3.2.3 Alumina coating of S@VACNT nanostructured cathode

Dissolution of polysulfides is one of the crucial challenges of sulfur cathodes. The dissolved polysulfides will trigger shuttle effect which results in serious loss of the sulfur active material and also corrosion of the lithium anode. Except of encapsulated sulfur in a carbon host, coating is another popular strategy employed for sulfur cathodes to prevent the dissolution of polysulfides. An ideal coating material should be uniform and integrate to protect the sulfur cathode, ultrathin to allow Li^+ ions penetration and should exhibit excellent mechanical properties to accommodate the volume expansion of the sulfur cathode with long cycle life.

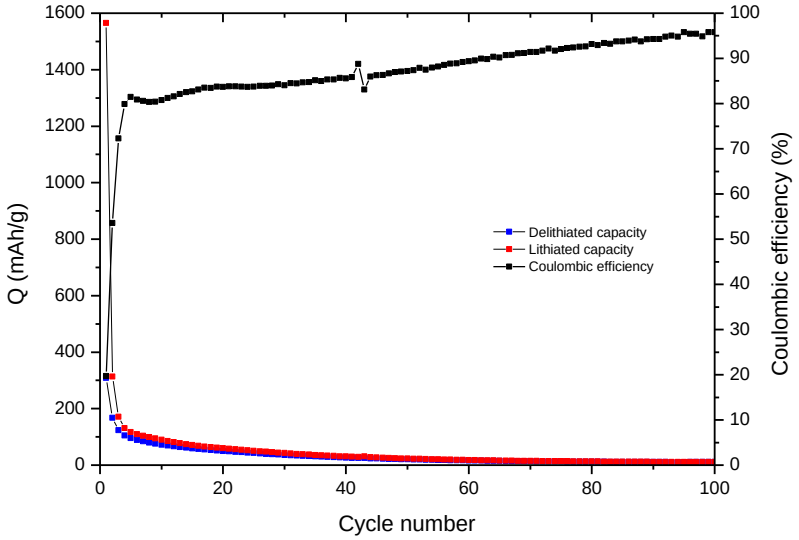

FIGURE 3.14: **Cyclic behavior of S@VACNT nanostructured electrode with Coulombic efficiency at C/20 rate between 1.5-2.8V vs Li/Li$^+$.**

The evaporation technique enables to grow a metal oxide thin film with precisely controlled thickness. The evaporation of the thin film enables to penetrate through the whole electrode and deposit very uniform layers on the substrate, which may give effective protection for the sulfur cathode. Further, the ultrathin film facilitates the Li^+ ions penetration, which maintains the conductivity of the electrode network. Al_2O_3 is employed as coating materials for sulfur based electrodes. It has been widely accepted that the shuttle effect could be alleviated by coating S-based composites with conductive polymers [208, 211, 213, 241, 242], graphene [191, 243] and metal oxides. [172, 244, 245] Different routes for metal oxide deposition have been recently proposed. Lee et al [244] soaked S-infiltrated functionalized porous C in the solution of metal alkoxide precursors, which initiated the formation of oxide coatings (either silicon oxide or vanadium oxide, depending on the precursor) on the particles outer surfaces. Seh et al [172] produced titanium oxide (TiO_x) coatings on the surface of S nanoparticles via hydrolysis of a solgel precursor. Yushin et al [245] reported that Al_2O_3 coating by plasma-enhanced ALD could improve the cycling performance of Li/ S batteries, owing to the suppressed deposition of Li_2S on electrodes by Al_2O_3 coating. Metallic oxides such as Al_2O_3 can offer stronger chemical reactions with polysulfides and can effectively minimize the shuttle effect.[246]

Herein, the influence of evaporated Al_2O_3 coatings the performance of sulfur-based electrodes is studied (denoted as Al_2O_3@S@VACNT).

3.2.3.1 Evaporation of alumina barrier on S@VACNT cathode

In general, there are three steps in any PVD process: creation of an evaporant from the source material, transport of the evaporant from the source to the substrate (item to be coated), and condensation of the evaporant onto the substrate to form the thin film deposit. There are two reasons why this process is best conducted under vacuum: first, the process of evaporation involves significant amounts of heat, if oxygen were present, any reactive metal would form oxides. Second, collisions with gas molecules during the transport of evaporant from source to substrate would reduce the net deposition rate significantly, and would also prevent growth of dense films.[247] The evaporation technique we used rely on electron bombardment for heating the crucible. A tungsten filament is heated by Joule effect and emits an electron flux. This flow is accelerated and directed towards the material to be evaporated by an electric field. When absorbed by the evaporant, the electrons will transform their kinetic energy into thermal energy leading to the local heating of the material and ultimately its evaporation. The experiments were performed in an ultra-high vacuum (UHV) chamber at a background pressure of 10^{-9} mbar. When performing the deposition of alumina by using this method on S@VACNTs, a very high electron flux was used in order to fasten the evaporation process of alumina (only 3 to 5 minutes), so that parasitic evaporation of sulfur due to thermal effects is avoided.

3.2.3.2 Electrochemical testing of Al_2O_3@S@VACNT nanostructured electrode

To evaluate the electrochemical performance of the Al_2O_3@S@VACNT electrode, the coin cell was assembled using lithium metal as the CE. The electrolyte was a freshly prepared solution of 1M LiTSFI salt dissolved in DOL:DME of 1:1 volume ratio containing 0.25 M $LiNO_3$. Lithiation and delithiation characteristics were galvanostatically tested in the range of 1.7-2.45 V vs Li/ Li^+ at room temperature. The capacity was calculated based on the mass of sulfur in the electrode, which was 1.45 mg cm^{-2}. Electrochemical performance of S@VACNT electrode with Al_2O_3 coating is illustrated in figure 3.15. Figure 3.15-a shows the galvanostatic lithiation and delithiation profiles of the Al_2O_3@S@VACNT electrode at a C/20 rate (1C= 1675 mA g^{-1}). The Al_2O_3@S@VACNT electrode shows two apparent lithiation plateaus and two delithiation plateaus in the first cycle, which agree well with the current peaks in the differential capacity plot (see figure 3.15-b). The first lithiation cyle capacity of Al_2O_3@S@VACNT was measured to be 1559 mAh g^{-1}. If the theoretical capacity of sulfur is assumed to be 1675 mAh g^{-1}, then the sulfur utilization of Al_2O_3@S@VACNT is 93%. Bearing in mind that the sulfur is uniformly coated on the VACNTs and the active material is

well dispersed over the entire electrode, it is reasonable to attribute the high degree of sulfur utilization, low polarization, and enhanced capacity retention of the S@VACNTs electrode to the facile kinetics of the charge-transfer reaction due to highly conductive electron paths, which originate from the VACNTs. The delithiation capacity of the Al_2O_3@S@VACNT in the first cycle was 1046 mAh g^{-1}. The irreversible capacity in the first lithiation/ delithiation cycle is likely due to the dissolution of high-order polysulfide intermediates and side reaction between dissolved polysulfide and carbonate solvent, which coincide with the reported result in the literature. [179] The lithiation and delithiation capacities of the Al_2O_3@S@VACNT electrode after the 40th cycle are 164 and 160 mAh g^{-1}, respectively. These capacity values largely exceed those of the S@VACNT cathode, indicating the superior cyclability of the Al_2O_3@S@VACNT cathode due to the coated Al_2O_3 layer which acts as electrolyte absorbent and limits the polysulfides shuttle effect.[248]

Figure 3.15-b shows the differential capacity curve plotted with the first, second, tenth, twentieth, thirtieth and fortieth cycles of the Al_2O_3@S@VACNT@Al_2O_3 electrode. During the lithiation process, two reduction peaks positioned around 2.4 and 2.1 V were observed, indicating a two-step reduction of elemental sulfur. The first reduction peak at ∼2.4 V corresponds to the transformation of cyclo-octasulfur (S_8) to long-chain soluble lithium polysulfides (Li_2S_x, 4<x<8). The second peak at ∼2.1 V is attributed to the decomposition of the polysulfides to form insoluble short-chain lithium sulfides (Li_2S_2 and/ or Li_2S). During the delithiation process, two broad peaks at around 2.20 and 2.35 V were also identified, and are correlated to the oxidation of lithium sulfide to lithium polysulfide and further oxidation to elemental sulfur, respectively.[176] In the second lithiation, the cathodic peak at ∼2.4 V vs Li/ Li^+ vanishes and only one peak at ∼2.1 V can be observed. The disappeared peak is probably to be attributed to the dissolution or the reaction of high-order polysulfides with the electrolyte.[239, 249]

3.2.4 Polyaniline coating of S@VACNT nanostructured cathode

Polymer materials have been widely used for drug delivery and are effective in encapsulating and controlling the release of desired chemicals in the internal pore space within the polymer matrix. Indeed, conductive polymers, such as polythiophene and polypyrrole containing different tailored porosities and have been explored as matrices to physically absorb and hold sulfur.[212, 213, 250] Wu et al [213] constructed a sulfur/ polythiophene composite with a core/ shell structure. The composite produced a high initial discharge capacity of 1119 mA g^{-1} and retained 69.5% of the capacity after 80 cycles. These results show that a simple physical confinement and absorption process is not sufficient in retarding polysulfide dissolution to provide an adequate cycle

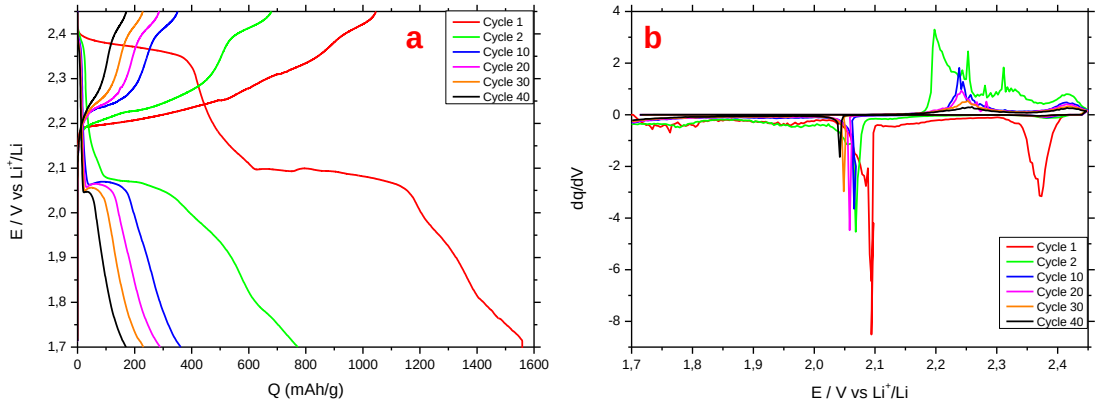

FIGURE 3.15: **a) Lithiation/ delithiation profiles and b) the differential capacity plot of the Al_2O_3@S@VACNT electrode obtained after one, two, ten, twenty, thirty, and forty cycles between 1.7-2.45 V vs Li/ Li^+ at a C/20 rate.**

life while still retaining high capacity. Several groups have explored polyacrylonitrile (PAN)/ S systems.[215, 241, 251] It was reported that PAN becomes dehydrogenated and cyclized at 450°C, and all sulfur reacts with PAN to form a heterocyclic polymer interconnected with disulfide bonds on the side chain. The chemically bonded sulfur showed good cycling retention of 90% up to 380 cycles, [251] but the capacity (470 mAh g^{-1}) and operating voltage (lower than 2.0 V) were relatively low. Regardless, these results show that organic disulfides bonded on the polymer chains have good electrochemical reversibility and the polymer backbone is stable during electrochemical cycling. In this work, by combining the advantages of VACNTs and polyaniline, we developed a novel electrode, sulfur supported by vertically-aligned carbon nanotubes and coated with polyaniline (denoted as PANI@S@VACNT), as cathode material for lithium-sulfur battery.

3.2.4.1 Electrodeposition of polyaniline barrier on S@VACNT cathode

After the sulfur evaporation on VACNT, PANI barrier was electrodeposited in an electrolytic bath, which contained aqueous solution of 0.2 mol L^{-1} aniline and 1.0 mol L^{-1} hydrochloric acid.[252] The cycling voltammetry technique was employed here again for electrodepositing the polyaniline layer on the surface of the S@VACNT electrode. The WE was S@VACNT on Al, the CE was graphite and the RE was Ag/AgCl. The cyclic

voltammogram was recorded at a scan rate of 50 mV s^{-1}, a potential sweep between 0 and 1V vs Ag/AgCl and a number of 15 cycles were performed (figure 3.16).

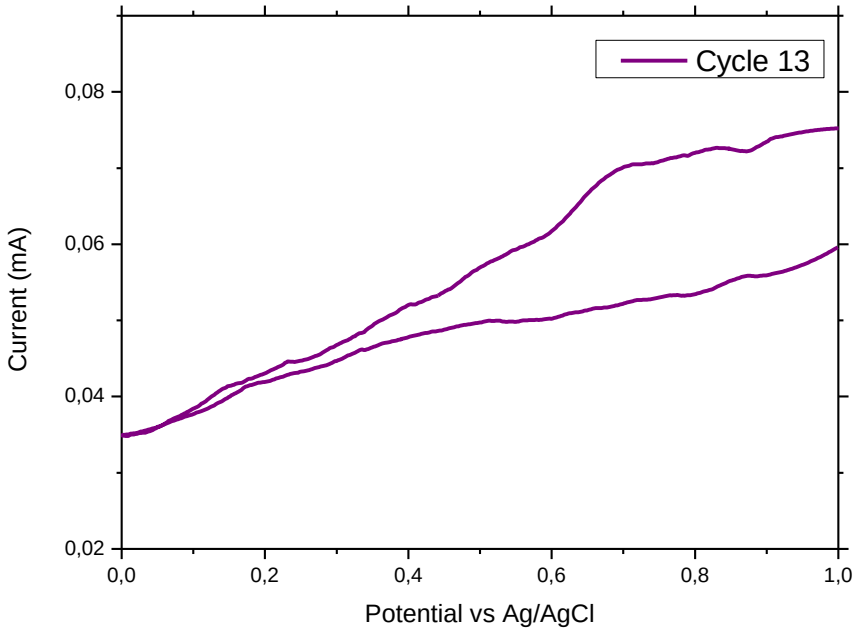

FIGURE 3.16: **PANI electrodeposition by CV technique on S@VACNT electrode**

3.2.4.2 SEM characterization of PANI@S@VACNT

The morphology of the PANI electroposited on S@VACNT electrode was observed by SEM, and is shown in figure 3.17. The sulfur covers the entire VACNT carpet framework and a layer of around 3 μm was deposited during the evaporation process. An inhomogeneous layer of PANI with a thickness of around 1μm was electrodeposited on top of the sulfur layer.

3.2.4.3 GIXRD characterization of PANI@S@VACNT

Figure 3.18 shows the GIXRD collected data. A similar configuration of S@VACNT was used in order to analyze the new as-fabricated electrode. The S@VACNT@PANI exhibits the same XRD patterns obtained previously, corresponding to the standard orthorhombic phase of sulfur (COD2310804). In literature, PANI has shown only a broad peak centered at $2\theta = 25°$, i.e., it has a typical amorphous structure.[210, 234, 235] It can be clearly seen that at an angle of incidence 2° (black line), i.e. grazing the surface of the sample, the electrodeposited PANI does not modify the crystalline structure of

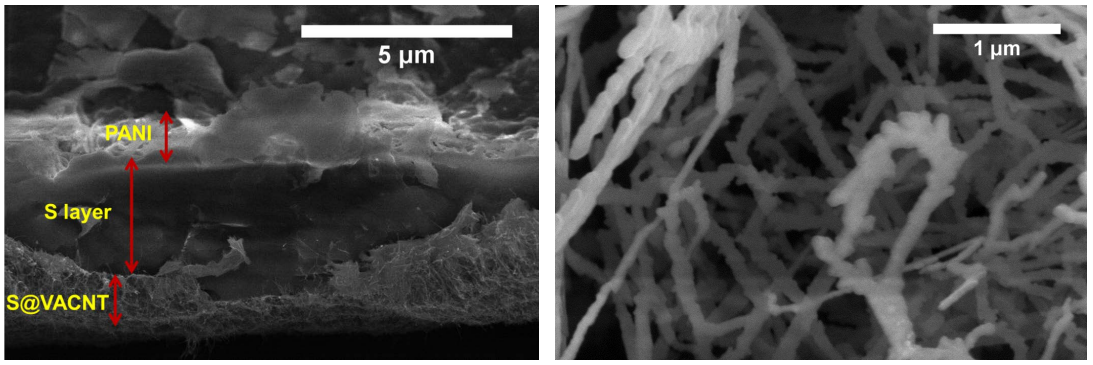

FIGURE 3.17: **Sectional view SEM image of PANI@S@VACNT.**

sulfur loaded on the VACNT carpets. At an angle of incidence 8° (orange line), we observe a large broad peak around 26°, which corresponds to the CNTs. Moreover, we observe the sharp peaks of sulfur and no new peaks are evidenced. This can indicate that no phase transformation of sulfur occurs during the preparation step, as well as no new compound is formed after the evaporation of S on VACNT and the electrodeposition of PANI on S@VACNT. Even after the electrodeposition of PANI, the pattern remains unchanged. This means that PANI does not affect elemental sulfur and we suppose no new phase is formed during the electrodeposition process.

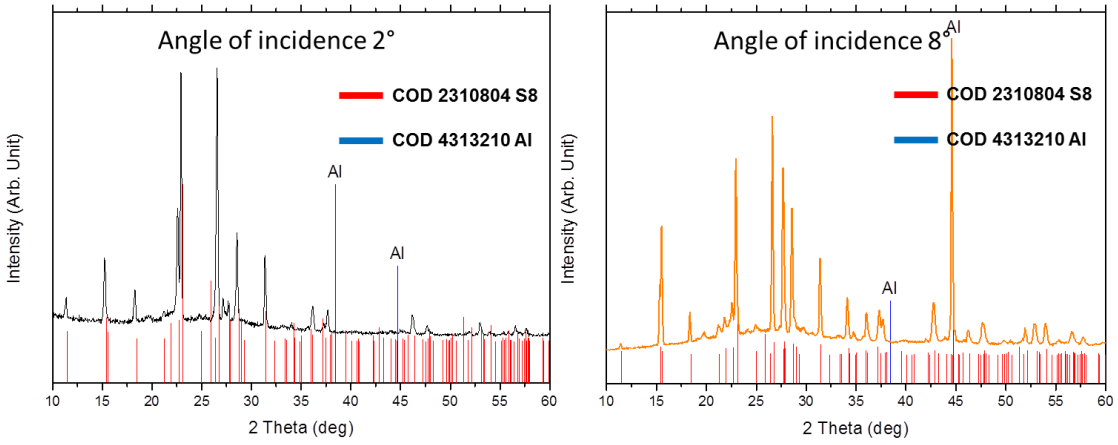

FIGURE 3.18: **GIXRD patterns of PANI@S@VACNT.**

3.2.4.4 Electrochemical testing of PANI@S@VACNT nanostructured electrode

Coin half-cells were used to evaluate the lithiation/ delithiation performance of the PANI@S@VACNT nanostructured electrode within 1.6-2.5 V potential range and a C/20 rate. The loading mass of sulfur was about 1.20 mg cm^{-2}. Figure 3.19 shows the cycle performance of the PANI@S@VACNT electrode. It can be clearly seen in figure 3.19-a that an impressive first lithiation capacity of 1650 mAh g^{-1} is obtained, which is 98% of the theoretical capacity of sulfur. The conductive VACNT carpets acting as a nanostructured current collector, reduce the effective resistance from the highly insulating sulfur cathodes. Therefore, the huge enhancement in the active sulfur mass utilization can be attributed to the electrode surface at nanoscale contact with the conductive network of the CNT carpets, which allows electrons to flow freely through the cathode and accelerates the kinetics of the electrochemical reactions. In addition, the use of conductive polymers to the cathode materials enhance the electrical conductivity, as well as the mechanical properties of the electrode, which undergoes significant volume changes upon electrochemical cycling. However, the lithiation capacity drop to 895 mAh g^{-1} in the 2nd cycle and gradually fades in the later cycles. After 40 cycles, the lithiation capacity drops to 113 mAh g^{-1}. Although the capacity of such electrodes is lower after several cycles, as compared to the first lithiation capacity, it is still higher than the corresponding value obtained in case of electrodes consisting only of elemental sulfur with CNTs. This improvement trend is due to the combination of VACNTs and PANI which appear beneficial for preventing polysulfides from dissolution and increasing the electronic conductivity.

During the first cathodic reduction process of PANI@S@VACNT, one peak at around 2.4 V and a noisy broad peak around 2.0 V vs Li/Li^+ are observed. The peak at 2.4 V corresponds to the reduction of sulfur to high-order polysulfides (Li_2S_x, $4<x<8$), while the broad one at around 2.0 V can be assigned to the reduction of higher-order polysulfides to lower-order polysulfides (Li_2S_2 and/ or Li_2S). In the following anodic oxidation process, two peaks at approximately 2.25 and 2.45 V are observed and can be attributed to the conversion of lithium sulfides to polysulfides and sulfur as shown in figure 3.19-b.

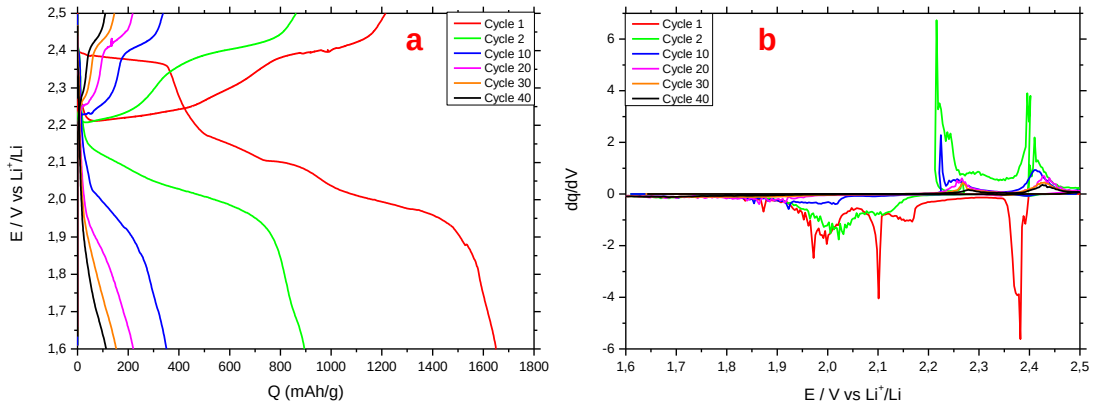

FIGURE 3.19: **a) Lithiation/ delithiation profiles and b) the differential capacity plot of the PANI@S@VACNT electrode obtained after one, two, ten, twenty, thirty, and forty cycles between 1.6-2.5 V vs Li/ Li^+ at a C/20 rate.**

3.2.5 Comparison of the performance of the PANI@S@VACNTs and the Al_2O_3@S@VACNTs nanostructured electrodes

The cyclabilities of the PANI@S@VACNTs and the Al_2O_3@S@VACNTs nanostructured cathodes are compared in figure 3.20. In the first cycle, the PANI@S@VACNT (triangle) electrode shows a higher lithiation capacity of 1650 mAh g^{-1} compared to 1559 mAh g^{-1} for the S@VACNT@Al_2O_3 (square) electrode, maybe due to the conductive nature of the polymer compared to the insulating nature of the alumina. The lithiation capacities of the the PANI@S@VACNT and the Al_2O_3@S@VACNT electrodes are 113 and 164 mAh g^{-1} after the 40th cycle, respectively. However, after the tenth cycle, the Al_2O_3@S@VACNTs (square) electrode remains more stable during cycling and presents a better lithiation capacity as compared to the PANI@S@VACNT electrode. This may be explained either by the inhomogeneous electrodeposition of PANI layer or the 1μm thickness of PANI which may not be enough to absorb the dissolved sulfur. It should be noted that the Coulombic efficiency of the Al_2O_3@S@VACNT (empty squares) electrode was mostly above 96% after the first five cycles. By contrast, the Coulombic efficiency of the PANI@S@VACNT electrode (filled squares) fluctuated during the cycling and only reached 95% after 37 cycles. From this electrochemical evaluation of both type of cathode electrodes, it can be concluded that Al_2O_3@S@VACNT electrode exhibits a better electrochemical performance with capacity retention and cycle life in comparison to PANI@S@VACNT electrode. After 40 testing cycles, lithiation capacities of 113 and 164 mAh g^{-1} are obtained for PANI@S@VACNTs and the Al_2O_3@S@VACNTs, respectively and the Coulombic efficiency remained above 94%. The values of lithiation

capacities are acceptable compared to that of commercial cathodes such as, $LiCoO_2$, $LiNi_{0.33}Mn_{0.33}Co_{0.33}O_2$ and $LiNi_{0.8}Co_{0.15}Al_{0.05}O_2$ which have a typical specific capacity in commercial cells of 145, 170 and 200 mAh g^{-1}, respectively.[25] Tentatively, we can attribute the decrease in the specific capacity for both types of the electrodes to the dissolution of the thick sulfur layer formed on VACNT carpets in the electrolyte. The remaining sulfur nanoparticles on the VACNTs are supposed responsible for the obtained capacities of the half coin cell. Therefore, in order to obtain stable and higher capacities during cyling, a better control of the evaporated sulfur i.e., formation of S NPs only, is required. This study suggests that with a better control of the thickness of the evaporated alumina or the electrodeposited PANI, we can make a promising progress to develop high performance Li/S batteries. Certainly, VACNTs nanostructured current collector, thanks to their high specific surface area, light weight, flexibility, and robustness, seemed to be particularly adapted to accommodate large amounts of sulfur in the electrode, without hindering the cyclability which requires to be further improved by appropriate development of better protective coatings.

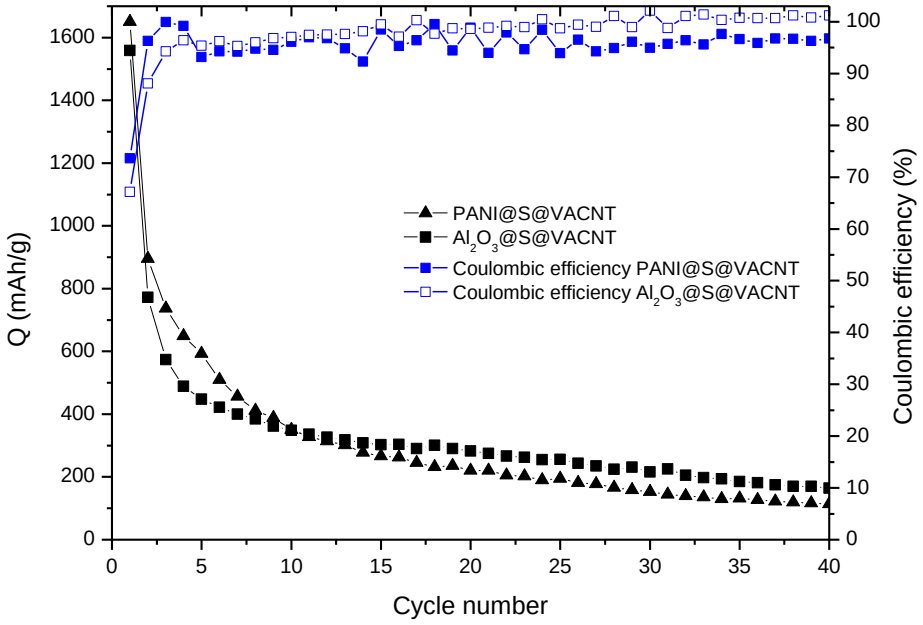

FIGURE 3.20: **Comparison of the cycling performance of PANI@S@VACNT and Al_2O_3@S@VACNT nanostructured electrodes at a C/20 rate.**

3.3 Nickel nanoparticles: an alternative material for the nanostructured cathode

As previously mentioned in Chapter 1, $LiNiO_2$ is a very promising cathode material since it has a high theoretical capacity and is relatively excellent in terms of economics and environmental fingerprint, but its preparation is more difficult compared with other cathode materials. The next section gives a detailed description of the main steps that were followed for obtaining the nickel based nanostructured cathode electrode.

3.3.1 Experimental set-up

Nickel nanoparticles were deposited on the VACNTs using a pulsed electrodeposition process in a Watts bath which is a mixture of nickel(II) sulfate hexahydrate (330 g L^{-1} $NiSO_4.6H_2O$), nickel(II) chloride hexahydrate (45 g L^{-1} $NiCl_2.H_2O$), and boric acid (45 g L^{-1} H_3BO_3). Nickel sulfate is the major source of the nickel ions in this solution, while nickel chloride improves the anode corrosion and increases the conductivity and the uniformity of nickel thickness distribution. Boric acid is added in the nickel containing solution for buffering purposes. Two parameters mostly impact the quantity of deposited nickel: the number of sweeps and the deposition voltage. Various deposition voltages were investigated systematically for covering the sidewalls of the VACNTs.
The nanoparticles were deposited by the electrodeposition process in the Watts bath solution and different electrodeposition voltages were tested, -4.5 V, -3.5 V, -2.5V and -1.5V during 5 ms, and the rest time in the open circuit voltage was 90 ms. The total number of pulses was set at 500. The WE was VACNT on Al, the CE was graphite and the RE was Ag/AgCl.

3.3.2 Morphological and structural characterization of the Ni@VACNTs assembly

The obtained Ni@VACNTs nanostructured electrode are illustrated in figure 3.21. As observed from the SEM images for all considered pulses, we have a rather homogenous deposition with Ni nanoparticles covering all the surface and the side-walls of the VACNT carpets. As shown in figure 3.21, the number of Ni NPs deposited on the VACNTs decreases with the decrease in the pulse voltage. These findings were confirmed by different TEM analyses, shown in figure 3.22, performed on areas belonging to each type of sample. The detailed analyses of the TEM images allowed us to estimate the size of the deposited Ni NPs that we found it varies between 30 and 60 nm.

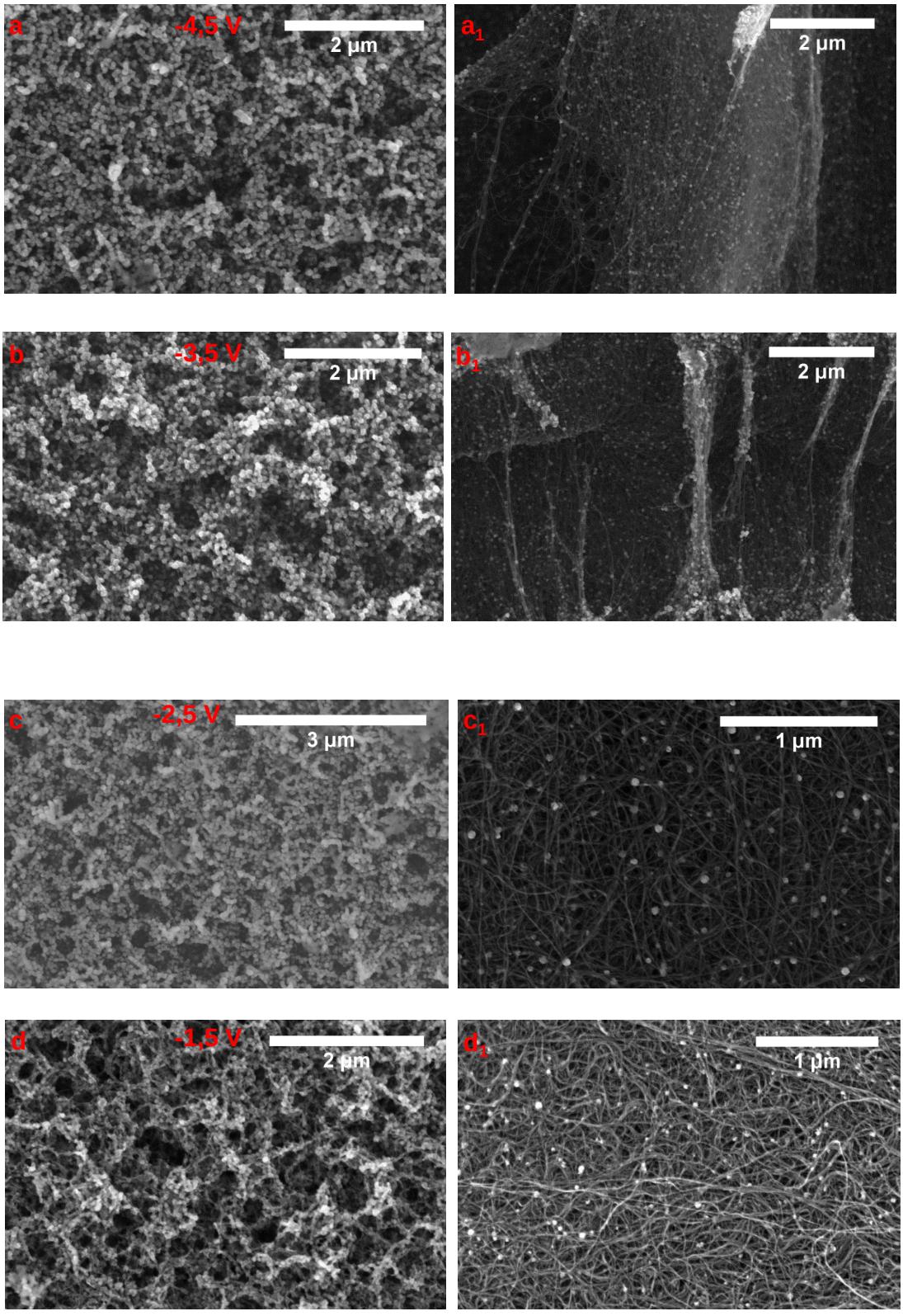

FIGURE 3.21: **SEM images of the Ni@VACNTs where Ni NPs were deposited by PED. a), b), c) and d) top view of the SEM images obtained at -4.5, -3.5, -2.5 and -1.5 electrodeposition voltage, respectively and a_1, b_1, c_1 and d_1 a closer view on a specific area of a), b), c) and d).**

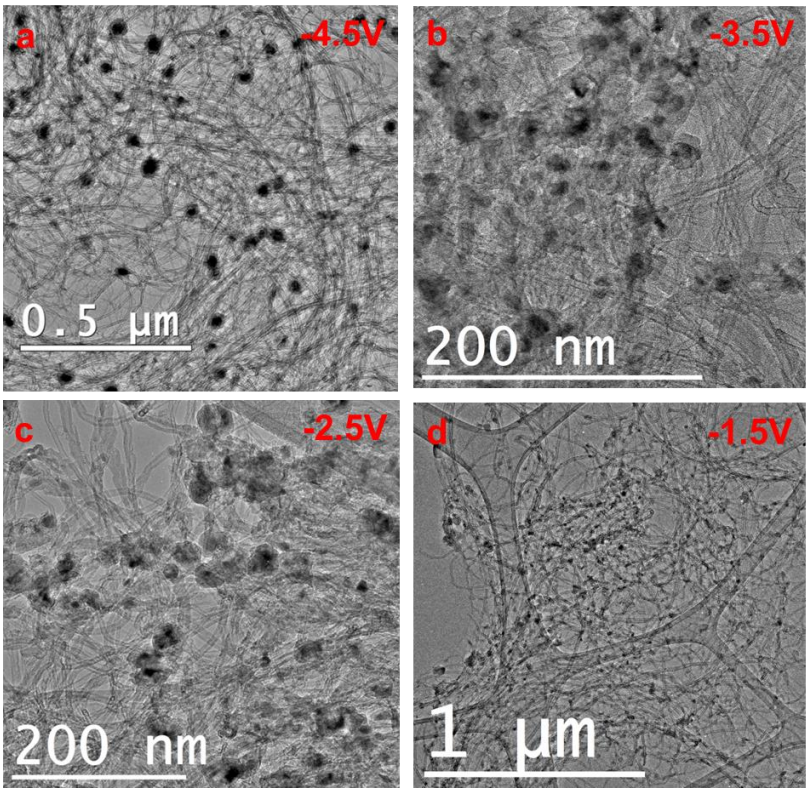

FIGURE 3.22: **TEM analyses of the Ni@VACNTs where Ni NPs were deposited by PED. a), b), c) and d) TEM images obtained at -4.5, -3.5, -2.5 and -1.5 electrodeposition voltage, respectively.**

Additionally, taking into account that the length of the VACNT carpets is quite important, i.e 7-10μm, the question that can arise at this point is: how deep within the CNTs side-walls the deposition is conformal. In order to find about, TEM analyses have been performed on a cross-section FIB lamella prepared on a sample for which a deposition pulse of -4.5V was used (see figure 3.23). The SEM image in figure 3.23-a shows that the deposition of Ni NPs on the side-walls of VACNT carpet is homogeneous up to a certain in-depth, about 5μm, with the Ni NPs having a bigger diameter due to the FIB preparation method that might favour the coalescence of the Ni NPs.

In order to study the structure and chemical character of the Ni NPs, detailed HRTEM analysis together with a chemical analysis using both the EDX (energy dispersive X-Rays) and EELS (electron energy loss spectroscopy) [253–256] techniques where performed (refer to Appendix A-2) . By using both, the STEM-HAADF and energy filtered imaging mode of the electron microscope, we evidenced a polycrystalline structure with small grains presenting different orientations, which correspond to a metallic Ni structure with a thin oxide layer at the surface with a NiO structure. This structure is the most stable within the NiO bulk structures as reported in the literature.[257] Figure 3.24 illustrates the chemical map of Ni NPs represented in a), with the elemental maps of O and C

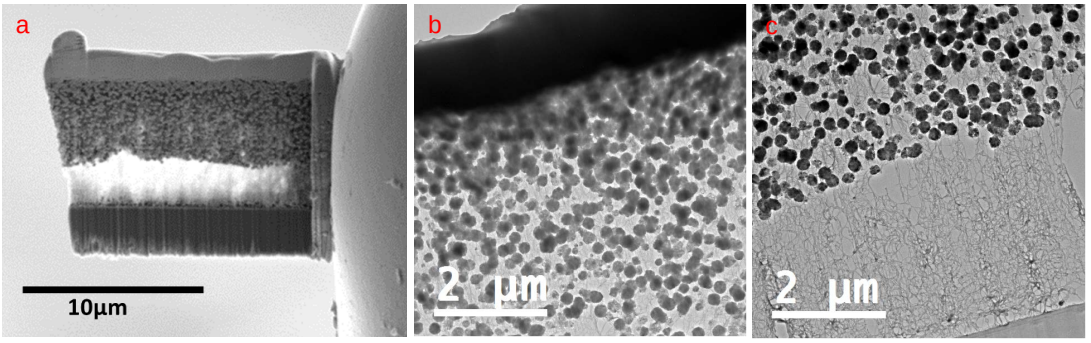

FIGURE 3.23: **a) SEM and b) and c) TEM images on a FIB cross-section lamella prepared on a Ni@VACNTs assembly obtained using an electrodeposition pulse of -4.5V illustrating the inhomogeneous deposition of the Ni NPs up to a certain in-depth.**

in b) and c), respectively on the K ionization edge using the three window method for the extraction of the signal. The relative map illustrated in figure 3.24-d evidences the metallic character of the Ni NPs with a thin O layer on their surface. This can be due to the exposure of the samples to air during the different experimental manipulations. The Ni decorated VACNT carpets need to be subsequently treated in order to form NiO_2 nanoparticles.

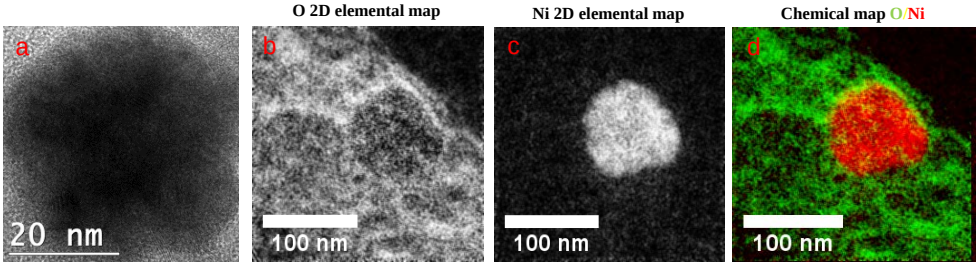

FIGURE 3.24: **HR-TEM and elemental maps recorded using the EFTEM imaging mode of the electron microscope evidencing the NiO structure for all the Ni NPs deposited using the PED process.**

It is worth mentioning that, for the NiO@VACNT assembly to be compatible for its use as nanostructured electrode in Li-ion batteries, the active material, i.e. NiO, has to present an advanced oxidation degree equivalent to NiO_2 which is not the case for our NPs. Thus, in order to make them compatible for our purposes, we tried to modify the oxidation degree of all NiO NPs deposited by PED by annealing all the NiO@VACNT assembly at 500°C for 10 hours under water vapor atmosphere. The results after this annealing process are summarized in figure 3.25. A closer investigation on the different

NPs obtained after the annealing step shows that the Ni NPs present a core-shell structure with different outershell sizes ranging from 5-20 nm (see figure 3.25-b-c) specific to two types of NiO populations. The EDX STEM-HAADF chemical analyses reveal that for both types of Ni NPs, the oxidized shells are presenting the same oxidation degree as before the annealing step. These findings were confirmed by the XRD measurements (see figure 3.26-b) which show that the heating step was unfortunately not enough to obtain NiO_2 NPs.

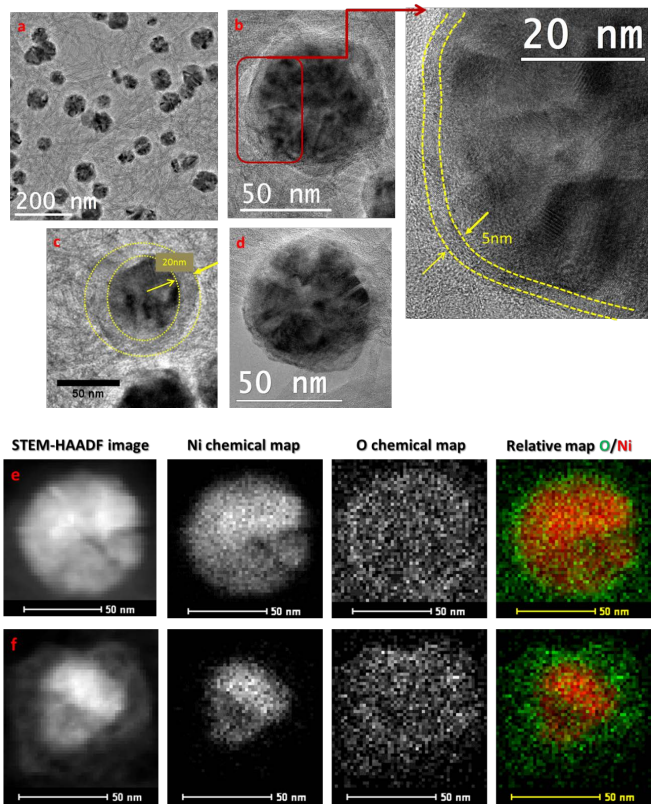

FIGURE 3.25: **HR-TEM and STEM-HAADF analyses of the different NiO NPs after annealing at 500°C for 10h under water vapor atmosphere. The TEM images in a) b) c) and d) reveal morphological and structural information of the Ni NPs evidencing the presence of a small and thick shell for the identified NPs. The STEM-HAADF chemical analyses is given in e) and f).**

To confirm the TEM analyses, figure 3.26 shows the X-ray diffraction spectra of NiO sample before and after annealing in order to obtain NiO_2. The XRD patterns shows a significant amount of line broadening which is a characteristic of material in form of nanoparticles. The dominant peaks of Ni (PDF 04-0850) are at 44.50°, 51.86° and 76.39° while NiO (PDF 44-1159) exhibits prominent peaks at 37.26°, 43.29°, and 62.88°.[258] The XRD was performed after the electrodeposition process as shown in 3.26-a. From figure 3.26-a, the peaks of NiO and metallic nickel are clearly seen. After annealing, in

figure 3.26-b, the peaks corresponding to metallic nickel disappear and that of NiO is still evident but with a higher intensity.

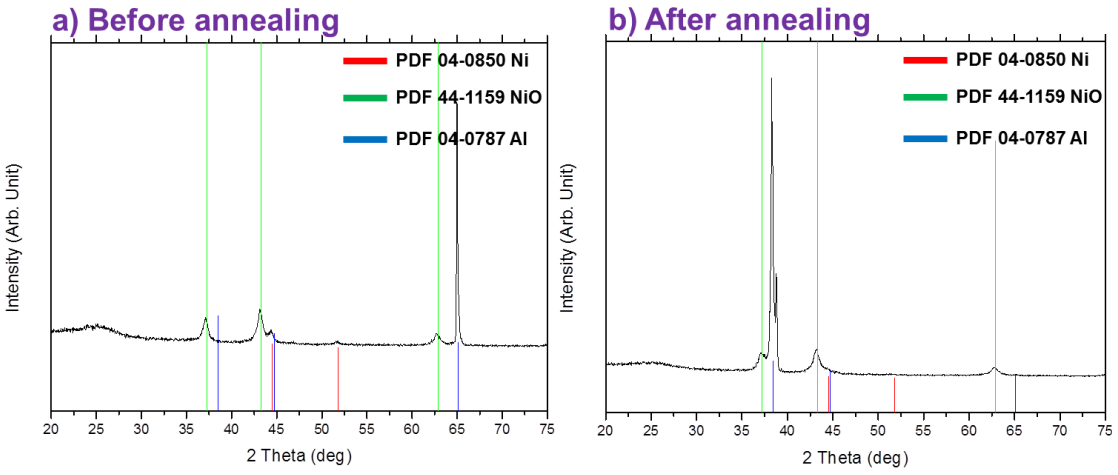

FIGURE 3.26: **XRD patterns of Ni@VACNT: a) after the electrodeposition process and b) after annealing under water vapor atmosphere at 500°C for 10 hours.**

3.3.3 Electrochemical testing of NiO@VACNTs nanostructured electrode

Even if we did not obtain the desired product (NiO_2), we tested the electrochemical performance of NiO in a half coin-cell. The loading mass of the NiO was 0.5 mg cm^{-2}. Figure 3.27 shows the galvanostatic lithiation/ delithiation curves of the NiO@VACNT nanostructured electrode. These electrochemical testing was carried out at the voltage range of 2.5 to 3.4 V at a C/20 rate. In the first cycle, the lithiation capacity reached $\sim$ 200 mAh g^{-1}. For the delithiation process, the first cycle did not reach 4.2 V which corresponds to the voltage range of NiO_2, confirming our characterizations of the formation of NiO instead of NiO_2. Therefore, we performed a cut-off at 3.4 V. Within this voltage range, we succeeded in performing electrochemical testing for NiO@VACNT nanostructured electrode, i.e. we showed that they are accessible electrochemically, and thus we were able to validate the "nanostructuration approach" principle. Our as-fabricated material (NiO) is more appropriate for an anode electrode use, because NiO has a high theoretical capacity of 718 mAh g^{-1}, is nontoxic and low cost material.

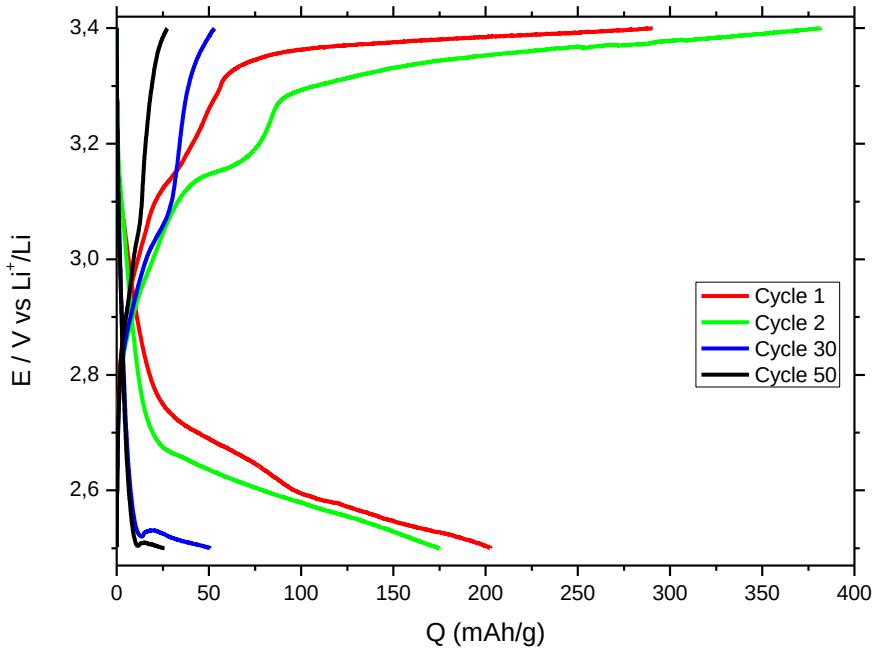

FIGURE 3.27: **Electrochemical performance of the NiO@VACNT nanostructured electrode obtained after fifty cycles between 2.5-3.4V vs Li/ Li^+ at a C/20 rate.**

3.4 Conclusion

The set of results presented in this Chapter, dedicated to the implementation of the experimental set-up for the fabrication of novel nanostructured cathodes for Li-ion batteries, highlight the unique potential of the nanostructuration approach. The first part of the Chapter presented the elaboration of the nanostructured cathode based on an original approach which combines the use of sulfur nanoparticles as active material together with a coating layer of sulfur with an metal oxide and/ or polymer deposited on the vertically-aligned cabon nanotubes that act as a nanostructured current collector for rechargeable Li/S batteries. The electrode was free from any binder or conductive additives which lowers the cost and toxicity associated with electrode manufacturing. The S@VACNTs coating with PANI and/ or Al_2O_3 helped retaining the integrity of the electrode structure during cycling and the current collector nanostructuration provided numerous electrical and ionic pathways for the electrochemical reaction, facilitating the mechanisms of lithiation and delithiation. Moreover, the external coating appear as a potential solution for confining the soluble polysulfide intermediates formed within the electrode structure during cycling because of the good electrolyte-absorption ability of the PANI@S@VACNT or the Al_2O_3@S@VACNT electrodes. Further work is required to achieve better confinement and to avoid the irreversible loss of the active materials.

These promising characteristics of the as-fabricated nanostructured cathodes exhibited nonetheless a high specific capacity in the first cycle, very close to the theoretical capacity of sulfur. The nanostructured electrode approach is a promising strategy for making the rechargeable Li/S batteries a commercial reality in the future.
The second part of the Chapter was dedicated to the fabrication of the NiO@VACNT nanostructured cathodes. The detailed analyses based on electron microscopy advanced techniques on the obtained NiO@VACNT nanostructured electrode validated the PED electrodeposition process. The combination of the STEM-HAADF EDX and XRD analyses, however pointed out a low oxidation degree for the Ni NPs. Unfortunatelly, the different approaches used to obtain the targeted metallic dioxide (MO_2) were not succesful during the time of this thesis.

Chapter 4

Anode nano-fabrication

Following the Chapter 3 which was dedicated to the experiments performed for the nano-fabrication of the positive electrode of the Li-ion battery, the present Chapter is dedicated to the nano-fabrication of the negative electrode of the Li-ion battery. The Chapter begins with a brief overview of the silicon material as potential candidate to be used as an anode material in LIBs. Thereafter, the details regarding the nanofabrication techniques developed for synthetizing Si@VACNT nanostructured electrodes, which to a good extent enabled us to have control over the silicon loading (mass) and the total surface area, will be discussed. The last part of the Chapter will be dedicated to the results obtained during the electrochemical testing performed under different conditions to evaluate the suitability of Si@VACNT electrodes for use as Li-ion anodes. In particular, the ability of Si@VACNT nanostructured electrode to accommodate silicon volume changes upon cycling is examined.

The nano-fabrication of materials has been identified as a viable solution to implement high capacity storage materials that are mechanically stable for long term cycling.[259–261] Nanomaterials also exhibit other properties that may be beneficial for use in electrochemical storage. The nanostructured active materials enable electrode reactions to occur, which cannot take place for micron-sized materials, decrease the diffusion length of Li^+ ions during cycling which remarkably improves the rate capability of the electrode material. In addition, the nanostructured Li-alloy materials render the phase transitions that accompany alloy formation more facile, accommodate the volume expansion during lithiation and reduce fracturing of the electrodes. Furthermore, many nanomaterials can offer enhanced mechanical support and electrical percolation within a network.

In brief, the approach chosen for the nano-fabrication of Si@VACNT electrodes comprise the growth of vertically aligned carbon nanotube carpets followed by their decoration with silicon nanoparticles. The schematic illustration of the preparation process is shown in figure 4.1. VACNTs are first grown on a Cu substrate using a CVD technique, where

Fe is used as a catalyst and methane serves as the carbon source for the growth of CNTs. The deposition of the silicon is performed by a CVD technique using a SiH_4/H_2 mixture of gases.

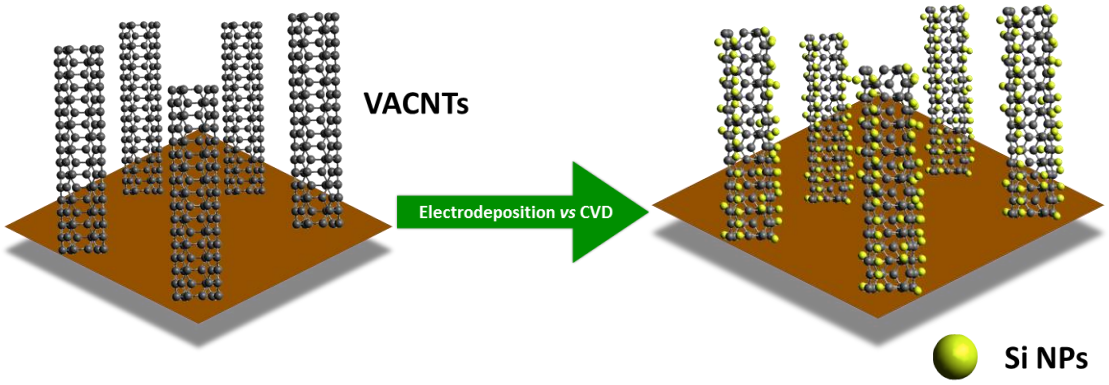

FIGURE 4.1: **Schematic illustration showing the nano-fabrication of the hybrid nanostructured anode.**

4.1 Advantages and disadvantages of silicon as active material

Silicon is the second most abundant element (27.7%) in the earth crust after oxygen.[262] Si is well known for its semiconductor properties and its use in solar cells, computer chips, etc. Si has drawn attention as a promising candidate for use as a anode material in LIBs. It has the highest theoretical capacity of 4200 mAh g^{-1} for lithium insertion at fully lithiated phase ($Li_{22}Si_5$, that is significantly higher than that of commercialized graphite (372 mAh g^{-1}). However, the fully lithiated phase of Si at room temperature, $Li_{15}Si_4$, leads to a maximum capacity of 3579 mAh g^{-1}.[263, 264] The delithiation potential of the Si is around 0.4V vs Li/Li^+, slightly above that of graphite. The potential difference with the cathode will therefore be lower than for a cell using a graphite electrode, which is detrimental to the energy density. This loss is largely compensated by the huge excess of capacity obtained by using this material as compared to graphite. The fact that the working potential of a Si based anode is somewhat higher than the lithium reduction potential can also be seen as an advantage because it reduces the risk of lithium deposition on the surface of the electrode during fast charging, and thus contributes to improving the safety of the battery. However, the main drawback for the use of Si as a

Li-ion battery electrode resides in the considerable volume variation which is associated with the formation of Li_xSi alloys as illustrated in the graph of figure 4.2.[265] A volume increase of the order of 300% is observed for the alloys rich in lithium with respect to the initial volume of Si (before alloying).

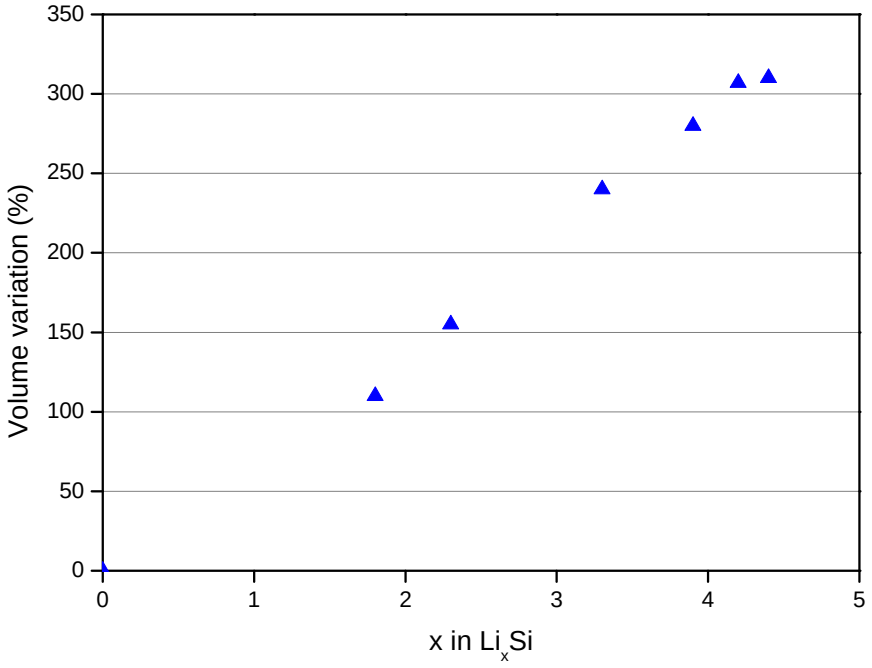

FIGURE 4.2: **Volume variations of different compositions of Li_xSi alloy with respect to silicon.[265]**

Such structural variations in the Si anodes have several serious consequences as explained below and schematically illustrated in figure 4.3 [18]:

- Anode material pulverization: the large volume expansion/ contraction during lithium insertion/ extraction induces large amounts of stress. This cause cracking and pulverization of the Si material, which leads to a loss of electrical contact between the resulting Si particles. This mechanism could explain most of the capacity fading for usual Si anodes (figure 4.3-a).

- Morphology and volume change of the whole Si electrode: the volume changes and contact loss between the Si particles affect the morphology of the entire electrode and ultimately causes the active material to peel-off from the current collector. These particles can no longer participate in cyling, resulting in failure of the cell. This problem adds another challenge for the full-cell design.

- Instability and irregularity of the SEI: in order to achieve a LIB with good cyclability, a stable and continuous SEI layer is considered critical. In the case of

graphite electrodes, the SEI is formed in the first cycle and then acts as a surface passivation to avoid the subsequent degradation of the electrolyte and the irreversible consumption of ions. The SEI layer needs to be dense and stable, and it should be ionically conducting and electronically insulating in order to prevent further side chemical reactions from occurring. In the case of Si electrodes, the formation of this passivating SEI film on the Si surface has been confirmed by Fourier transform infrared Spectroscopy (FTIR) [266] and by X-ray photoelectron spectroscopy (XPS).[59] This SEI layer was not found to be sufficiently stable and does not act as a perfect surface passivation. The SEI stability at the interface between Si and the liquid electrolyte is a critical factor to obtain longer cycle life. The huge volume change of Si makes it very challenging to form a stable SEI. As shown in figure 4.3-b, Si particles expand out towards the electrolyte upon lithiation and contract during delithiation. The SEI formed in the lithiated (expanded) state can be cracked as the particles shrink during delithiation. This re-exposes the fresh Si surface to the electrolyte and the SEI forms again, resulting in thicker and thicker SEI upon charge/ discharge cycling.

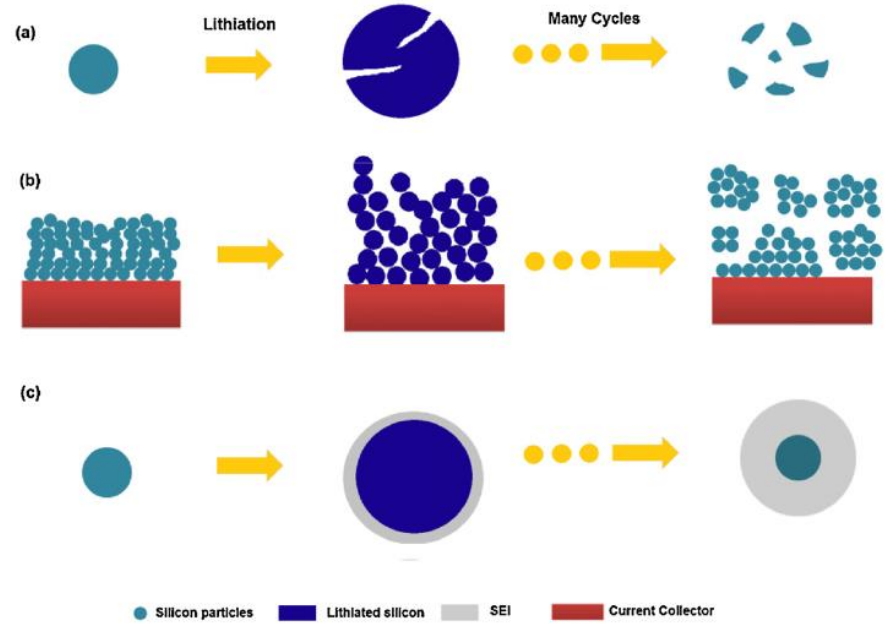

FIGURE 4.3: **Si electrode failure mechanisms: (a) Anode material pulverization. (b) Morphology and volume changes of the whole Si electrode. (c) Continuous SEI growth.**[18]

4.2 Mechanisms of lithiation and delithiation of silicon

The electrochemical reactions of lithium with different anode materials are not similar. In graphite carbon anode, the electrochemical reaction takes place as Li^+ ions are intercalated and extracted between the graphite layers, inducing minimal structural changes. In silicon anode, the electrochemical reaction takes place as Li^+ ions alloy and dealloy with the electrode material, severely changing the crystal structure of silicon. It is found that the reactions follow the equilibrium Li-Si phase diagram at high temperature, forming different intermetallic compounds and showing multiple voltage plateaus in the galvanostatic voltage curve (black line in figure 4.4). However, at ambient temperature, there is only a two-phase region at about 0.1V during the first lithiation and a plateau at 0.45V during the first delithiation (green and red lines in figure 4.4).[18] The electro-

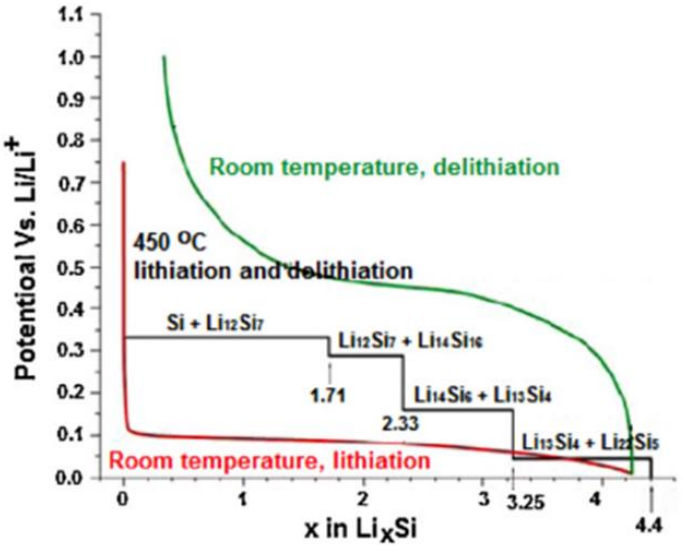

FIGURE 4.4: **Si electrochemical lithiation and delithiation curve at ambient temperature and high temperature. Black line: theoretical voltage curve at 450°C. Red and green lines: lithiation and delithiation of crystalline Si at ambient temperature, respectively.**[18]

chemical reaction of Li with Si at room temperature has been studied extensively during the past decade, due to the potential use of silicon as an anode material in high energy density LIBs. Recent studies of crystalline Si (c-Si) [264, 267, 268], sputtered amorphous Si [269], and active/ inactive Si alloy anodes [268] have explained many of the features in the voltage curve of crystalline silicon. The current knowledge of the electrochemistry of bulk crystalline Si is summarized in the voltage curve shown in figure 4.5. The initial lithiation of crystalline Si results in a low voltage plateau (I in figure 4.5) corresponding

to a two-phase region in which lithiated amorphous Si is formed (a-Li_xSi).[264, 267, 268] A detailed in situ XRD study by Li and Dahn [264] has recently shown that the capacity of this plateau is about 3250 mAh g^{-1}. At this capacity all the crystalline Si has reacted completely to form a-Li_xSi. At higher capacities, Li and Dahn observed the formation of the $Li_{15}Si_4$ phase (II in figure 4.5). $Li_{15}Si_4$ is the highest lithiated phase achievable for the ambient-temperature lithiation of bulk Si and corresponds to a capacity of 3579 mAh g^{-1}.[264, 268] From X-ray data, the calculated density of this phase was 1.179 g cm^{-3}.[268] This means that when Si is fully lithiated to $Li_{15}Si_4$ it undergoes a volume expansion of 280% and has a maximum theoretical volumetric capacity of 2190 mAh cm^{-3}. The delithiation of $Li_{15}Si_4$ results in a plateau corresponding to a two-phase region in which delithiated amorphous Si is formed (III in figure 4.5).[264, 268] If this phase is then lithiated, the voltage curve follows two sloping plateaus, indicative of single-phase regions (IV in figure 4.5). The reasons why the lithiation of amorphous Si results in two plateaus are so far not fully understood. If the lithiation of the amorphous Si is limited to above 50mV, the Si remains amorphous and two sloping plateaus are also present during delithiation (V in figure 4.5). Allowing the voltage to drop below 50mV (VI in figure 4.5) results in the crystallization of the $Li_{15}Si_4$ phase, indicated by a small peak in the differential capacity (VI in figure 4.5) and its characteristic plateau during the subsequent delithiation (VII in figure 4.5).[268]

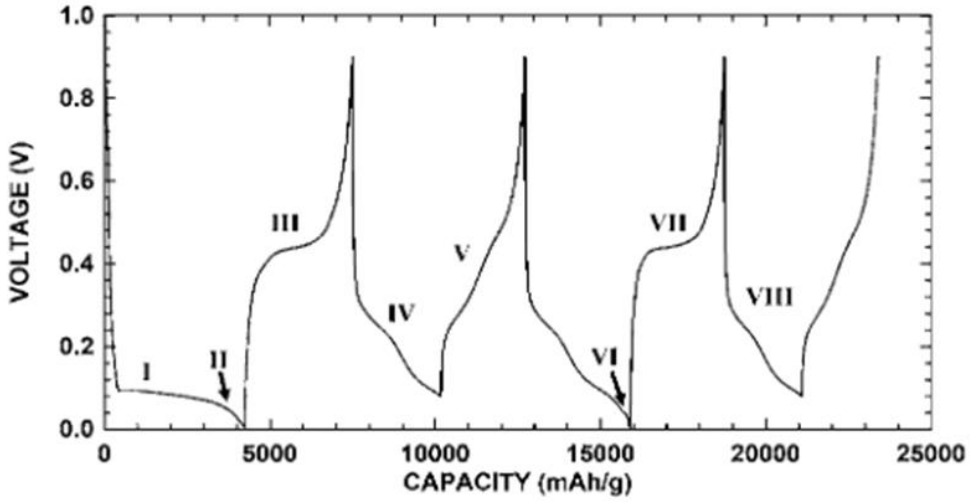

FIGURE 4.5: **Voltage curve of a crystalline Si electrode cycled in a way to illustrate the electrochemical conversion of crystalline Si to amorphous Si, amorphous Si to crystalline $Li_{15}Si_4$, and $Li_{15}Si_4$ back to amorphous Si.[268]**

Amorphous-Si (a-Si) is commonly employed directly as the starting material in many negative electrodes for LIBs. The reaction of a-Si with Li is different from crystalline Si. Based on electrochemical measurements, researchers have generally assumed that a-Si is lithiated via a single-phase reaction.[270] Galvanostatic lithiation of a-Si reveals a sloping potential profile, as opposed to the flatter potential profile during lithiation of c-Si. As an example, figure 4.6 shows galvanostatic potential profiles for half cells with three different active materials in the working electrode: single-crystalline Si nanowires (NWs), amorphous Si NWs, and polycrystalline Si NWs.[271] Both single- and polycrystalline Si feature a relatively flat lithiation potential beginning at about 160mV vs. Li/ Li^+, which is the mark of a two-phase reaction since it signifies a constant activity of Li in the lithiated phase. Besides, lithiation of a-Si begins at about 300mV, and the trace slopes downward to eventually meet the crystalline curves. This sloping profile traditionally suggests a single-phase reaction, since the Li activity is not constant in the lithiated phase. However, recent in-situ TEM experiments [272] have revealed more complex two-phase lithiation behavior. Although there is not yet a commonly accepted mechanism, Wang et al [272] reported that the lithiation occurs by the movement of a sharp phase boundary between the a-Si and an amorphous Li_xSi (a-Li_xSi, x $\sim$ 2.5) according to their in-situ experiment. Such amorphous-amorphous interface exists until the remaining a-Si is consumed. Then a second step of lithiation starts without a visible interface which results in the final product of a-Li_xSi (x $\sim$ 3.75). The distinction between the single-phase and two-phase lithiation behavior is important since the two different reaction mechanisms theoretically cause different stress evolution and fracture mechanisms.

4.3 Nanostructured silicon anode

Tremendous efforts have been devoted for developing Si anodes for LIBs in various forms in order to overcome the aforementioned issues and thus obtain better capacity retention and cycle life. Among all the approaches, nanostructuring is the most promising method, although it is still far from practical application. During the last decades, an explosion of research activity has been focused on designing nanostructured Si anodes for LIBs with the purpose of preventing fracture and mechanical degradation with cycling. Researchers have found that Si nanomaterials exhibit a better cycle life than micron-scale particles. This is most likely due to better accommodation of lithiation-induced strain, without fracture. In addition, shorter diffusion lengths in nanostructured materials lead to facile kinetics. Silicon nanostructures (without binders, conductive material, or other additives), such as nanowires [48, 84, 273, 274], nanotubes [275–278], nanoparticles [279, 280], thin films [281, 282] hybrid structures [70–73, 283, 284], etc have been designed and tested as negative electrodes and have brought major breakthrough in

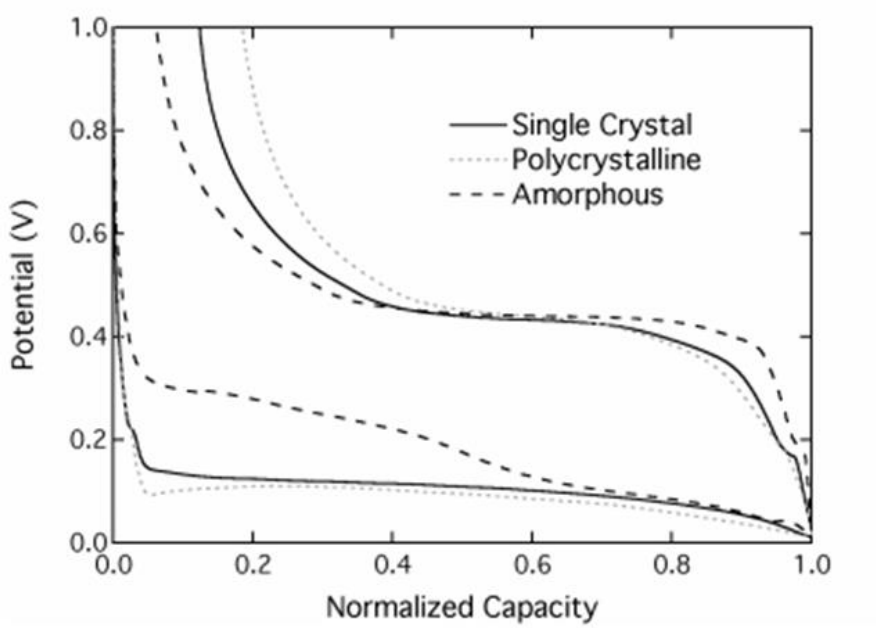

FIGURE 4.6: **First cycle galvanostatic curves for single-crystalline Si NWs, amorphous Si NWs, and polycrystalline Si NWs.**[271]

the field, allowing the achievement of high capacity and good cyclability of the battery. However, improvements in cycle life and electrode material design are still necessary to meet the goals for renewable energies. A brief description of different nanostructured Si materials used as anodes is given below:

- Silicon nanowires: Silicon nanowires (SiNWs) have attracted a great deal of attention for aplications in LIBs anodes due to several advantages. Their structure allows for the accommodation of the important volume changes during repeated lithiation/ delithiation without cracking, offers direct 1-D electronic pathway for rapid charge transport and affords effective lithium insertion and extraction due to the contact of Li^+ ions over large specific surface area. Additionally, direct synthesis of the SiNWs on the current collector improves the electrical conduction of the electrode. For example, SiNW anodes synthesized via VLS process have been found to accommodate the volume changes caused by lithium insertion and extraction.[84] As shown in figure 4.7, the VLS-grown NWs undergo reversible lithium insertion and extraction without significant pulverization or detachment from the current collector. The VLS-grown SiNW anodes maintained reversible capacity of 2000 mAh g^{-1} after 80 cycles as reported in later studies.[84] Peng et al [273] have prepared self-aligned SiNWs fabricated by facile metal assisted etching of Si as anode for LIBs. This method has several advantages over the VLS process:

low cost, large surface area, and facile procedure. The SiNWs anodes showed a discharge capacity of about 0.5 mAh.cm^{-2} in the third cycle and cycling stability for 9 consecutive cycles. However, due to difficulties in estimating the weight of the SiNWs on the substrate, the reported capacity could not be compared with that obtained for SiNWs synthesized by VLS technique. In addition, because the nanowires were attached to the Si substrate, a lower electrical conductivity between the anode and the current collector was expected and the substrate might have pulverized and cracked after repeated cycling. These disadvantages limit the practical applications of the metal assisted method for the preparation of LIB anodes.

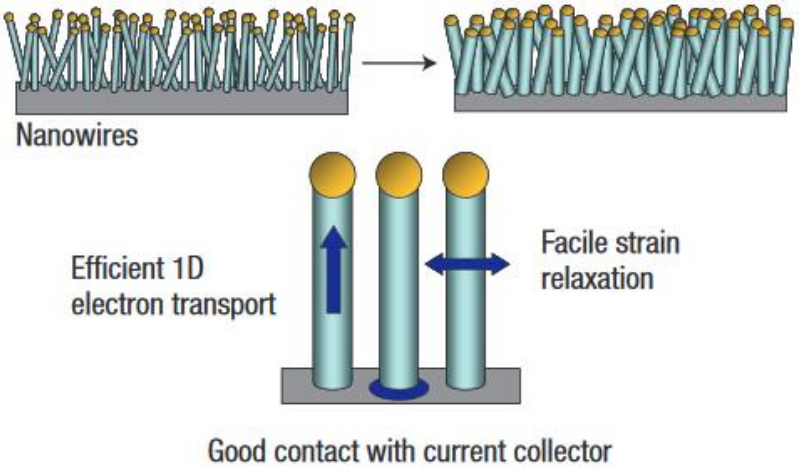

FIGURE 4.7: **Schematic of SiNWs electrode assembled on the current collector.**[84]

- Si nanotubes: Silicon nanotubes (SiNTs) are attractive nanostructures for Li-ion battery applications due to the hollowness that offers additional space for the expansion during the lithiation/ delithiation processes, preventing the mechanical pulverization of Si. Park et al [275] prepared SiNTs by reductive decomposition of a Si precursor in an alumina template and etching, which increased the surface area accessible to the electrolyte and allowed the Li^+ ions to intercalate inside and outside the tube. The fabricated SiNTs showed reversible discharge and charge capacities of 3648 and 3247 mAh g^{-1}, respectively, with a Coulombic efficiency of 89% at the first cycle. Wu et al [276] created double walled SiNTs with a hollow tube of Si coated in a mechanically confining silicon oxide outer layer. During lithiation, the inner silicon layer expanded inward, filling the empty core of the

tube. The researchers reported a capacity of 940 mAh g^{-1} at the high rate of 12 C, and an 88% capacity retention after 6000 cycles at 10C. The loading reported for these electrodes, however, was 0.02-0.1 mg cm^{-2}, which is far from the necessary loading for commercial batteries. In addition, their synthesis method generally involves complicated and costly synthesis routes in order to create the necessary void space, rendering them impractical for commercial use.

- Si thin film: Methods such as CVD [285], magnetron sputtering [286], pulsed laser deposition [287], and vacuum evaporation [288] have been employed to fabricate Si thin film anodes for LIBs. The assembly of ultrafine Si materials into a continuous film constitutes an effective approach to overcome the volume change issue, enhance the contact area, and suppress the movement of free Si particles. Studies have been conducted on Si thin film anodes in order to evaluate the lithium insertion mechanism [289], the stress evolution within the anode upon cycling [286, 290] and surface film formation.[291] Even though the reversibility and capacity retention of the Si thin film anodes have been enhanced, cracking and pulverization were still observed on thin film Si anodes after prolonged repeated lithiation/ delithiation.

- Hybrid structures: Among all these different approaches, the concept of combining silicon particles and carbon nanotubes has been scarcely explored. Kumta and co-workers have exploited the combined merits of two materials: silicon and CNTs by synthesizing arrays of vertically aligned silicon/carbon nanotubes.[70] The performance of this hybrid structure, that was scrapped off from a quartz substrate and included additives, exhibited a capacity of about 1000 mAh g^{-1} at C/10 rate at the end of the 100 th cycle. In another study, Kumta et al [71] found the capacity of Si/CNTs directly synthesized at the surface of the current collector to be 800 mAh g^{-1} at a current density of 400 mA g^{-1}. More recently, Kumtas team fabricated a novel electrode based on Si-coated- MWCNTs collected on a copper foil. At the end of the 50th cycle, the capacity reached 2000 mAh g^{-1} at current density of 300 mA g^{-1}.[73] Du et al [283] synthesized MWCNT@Si nanocomposites by magnesiothermic reduction of pre-synthesized MWCNT@SiO_2 nanocables. After 70 cycles at current density of 400 mA g^{-1}, the anode, i.e. the active material, acetylene black and the binder, exhibited a capacity of 520 mAh g^{-1}. Mangoloni et al [284] combined functionalized silicon quantum dots with carbon nanotubes and a polymer to form a liquid dispersion that was coated onto copper foil, followed by annealing. This electrode structure delivered a capacity around 1000 mAh g^{-1} for 200 cycles. In 2012, Gohier et al [72] at the laboratory of physics of interfaces and thin films (LPICM) reported a hierarchical hybrid nanostructure based on vertically aligned carbon nanotubes directly grown onto

stainless steel foil on which silicon nanoparticles were deposited via CVD process. This kind of electrode exhibited an optimum rate capability compared to those found in literature so far. An impressive electrochemical performance was reached at a high C rate, up to 15 C. The capacity of VACNTs/Si was 760 mAh g^{-1} at 15 C, although the electrode loading mass was far from the expectancy for use in commercial LIBs. This electrochemical performance highlights the potential of such a hierarchical nano-architectured anode. Owing to the impressive results obtained by Gohier et al, we decided to perform additional research studies in order to gain a deeper insight on this hybrid structure.

4.4 Electrodeposition of Silicon

Since the silicon deposition potential is outside the permissible range when using an aqueous solvent, the electrodeposition has not been a preferred route in the search for new silicon production processes until now. Silicon is deposited only at a very high negative potential (-2.6V relative to a ferrocene/ ferrocinium (Fc/Fc^+) reference electrode) which is much lower than the limit of reduction of an aqueous solvent due to the hydrogen reduction. However, with the emergence of new ionic liquid solvents (green solvents) [292, 293] belonging to the category of molten salts, this process of elaboration is no longer impossible to implement. These solvents possess a large electrochemical window which makes it possible to produce silicon by electrodeposition on a large scale and with good quality control of the deposited material.
The ionic solvent used here for the deposition of silicon is 1-Butyl-1-methylpyrrolidinium bis(trifluoromethylsulfonyl) imide ([BMP]Tf_2N) or ($P_{1,4}$) (Solvionic S.A.). It is stable in the presence of water and air, but must be handled in a glove box in order to not reduce its electrochemical window of 5.5 V [-3.5; +2 V].[294, 295] The ionic liquid $P_{1,4}$ is composed of a bis (trifluoromethylsulfonyl) imide ($C_2F_6NO_4S_2$) anion and a 1-butyl-1-methylpyrrolidinium ($C_9H_{20}N$) cation. These two ions define the physical properties of the solvent (conductivity, viscosity, melting temperature, etc). The main morphological difference between an ionic liquid and an aqueous solvent lies in the size of the ions composing this solvent. The cations and anions of our ionic solvent are of a size much greater than the ions usually encountered in the aqueous solvent, are not planar and occupy a large volume compared to other types of ions. This can be problematic in electrochemical deposition if one of the ions easily adsorbs onto the substrate [296] and blocks the Si deposition sites. For ionic liquids and in order to produce pure Si, we must pay particular attention to the purity of the solvent, which must not contain any water molecules. We have already mentioned in the introduction that the electrochemical window of the solvent could be reduced if it contained molecules of water. If this window is

decreased, it may no longer contain within the Si reduction potential and thus prevent the deposition. Moreover, a peak of water reduction, between -0.6 and -1.4V vs. Pt, may occur when the solvent is not pure.[297] This reduction dominates over that of Si due to the lower potential at which it occurs, thus influencing the morphology of the electrodeposited Si NPs.[297]

For the deposition of nanostructured Si by electrodeposition, silicon tetrachloride ($SiCl_4$), 99.998% pure (Sigma-Aldrich) is used as Si precursor. This type of precursor containing chloride ions must be used under controlled atmosphere. Indeed, silicon tetrachloride reacts strongly with water according to the following reaction:

$SiCl_4 + 2H_2O \rightarrow SiO_2 + 4HCl$

This reaction is thermodynamically favored and instantaneous resulting in a release of heat as well as acid vapors, it is therefore very dangerous for the human. For safety, the precursor was handled under controlled atmosphere in an argon glove box containing less than 1 ppm of water and oxygen. The $SiCl_4$ vapor pressure is 560 hPa (37.7 °C) [298], so this precursor is highly volatile and we preferentially achieve the mixture by adding $SiCl_4$ to the ionic liquid so that it is diluted in the solution preventing it from evaporation.

Silicon NPs were deposited on the VACNTs as the active material for the negative electrode at room temperature. The working-solution for the electrodeposition consisted of 1 mol.L^{-1} of $SiCl_4$ in 1-Butyl-1-methylpyrrolidinium bis(trifluoromethylsulfonyl) imide. The following reduction reaction occurs in the cell:

$Si^{4+} + 4\ e^- \rightarrow Si^0$

In the present work, we used a three-electrodes configuration represented in figure 4.8 in which the electrodes are set as follows: VACNTs grown directly on a Cu substrate was used as the WE, platinum wires were used as the CE and a pseudo-reference electrode. The pseudo-reference electrode, which can be a silver (Ag) or platinum (Pt) wire, is chemically inert and its potential is adjusted to the potential prevailing in the solution provided that at least one couple is present. The pseudo-reference potential is determined by comparison with another reference electrode. Here we can determine the reference potential of platinum wire in our environment by comparing them to the experiments conducted by Endres et al [299] under the same conditions. The platinum wire in this medium therefore has a reference potential equivalent to that of the ferrocene / ferrocinium pair because the silicon deposition potential is equivalent in both cases for the same solvent and the same concentration of Si (IV) (-2.6 to -2.8V vs. Fc/Fc^+ or Pt).

Two electrodeposition methods were used to deposit the Si NPs, cycling voltammetry (CV) and PED, using the same solution and concentration of silicon.

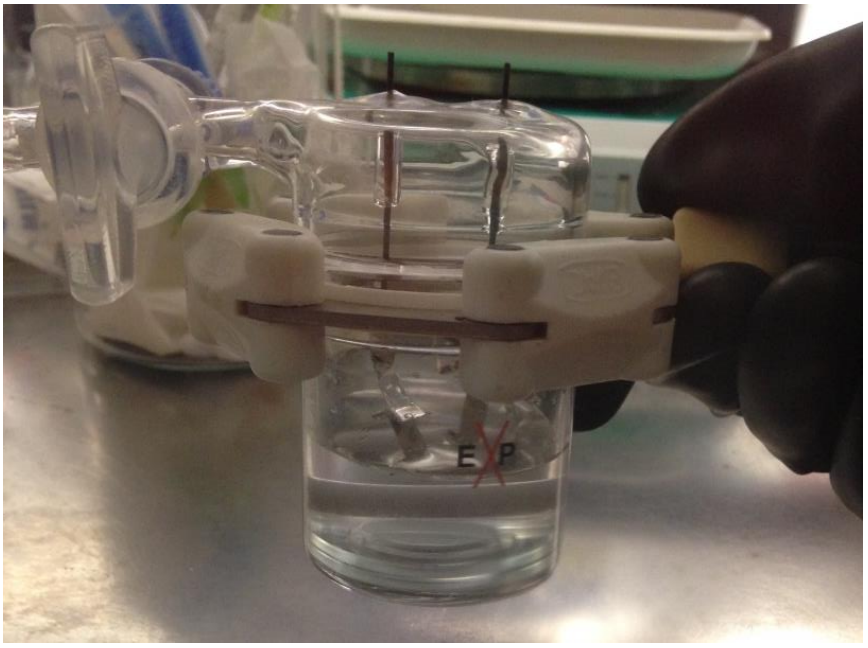

FIGURE 4.8: **The set-up of the fabricated cell used for the electrodeposition of silicon.**

4.4.1 Cycling voltammetry technique

Cycling voltammetry (CV) is an electro-analytical measurement technique that is often used to investigate mass transport and rate-limiting step associated with diffusion-controlled processes (refer to Appendix C-1).[300] Typically, during the electrodeposition using this method, current versus potential responses are acquired, that have the shape characteristic of a diffusion-controlled reaction of the species dissolved in solution and contain several discernible features that relate to the anodic and cathodic reactions occurring at the working electrode.

In our experiments, silicon NPs were deposited in a concentrated solution of 1 mol. L^{-1} on VACNT carpets at room temperature while continuously stirring the solution to obtain a homogeneous deposition. The cyclic voltammograms were recorded at a scan rate of 10 mV s^{-1} during 6 cycles. Figure 4.9 shows a cyclic voltammogram curve acquired using a solution composed of 1-Butyl-1-methylpyrrolidinium bis(trifluoromethylsulfonyl) imide on VACNT carpets that contains $SiCl_4$. As observed in the CV curve obtained at a scan rate of 10 mV s^{-1} using platinum as pseudo-reference electrode, two peaks can be identified. The first peak, around -2.8 V, corresponds to the reduction of Si^{4+} ions and the deposition of Si NPs. The second peak at around -1.8 V vs. Pt corresponds to the presence of water in the solvent. The substrate was washed with acetonitrile in order to remove all residues from the ionic liquid. A gray-white deposit is observed on

the working electrode. As it will be shown in the next section, the physico-chemical characterizations carried out on such a deposit will confirm the presence of Si NPs, thus validating the success of the electrodeposition method.

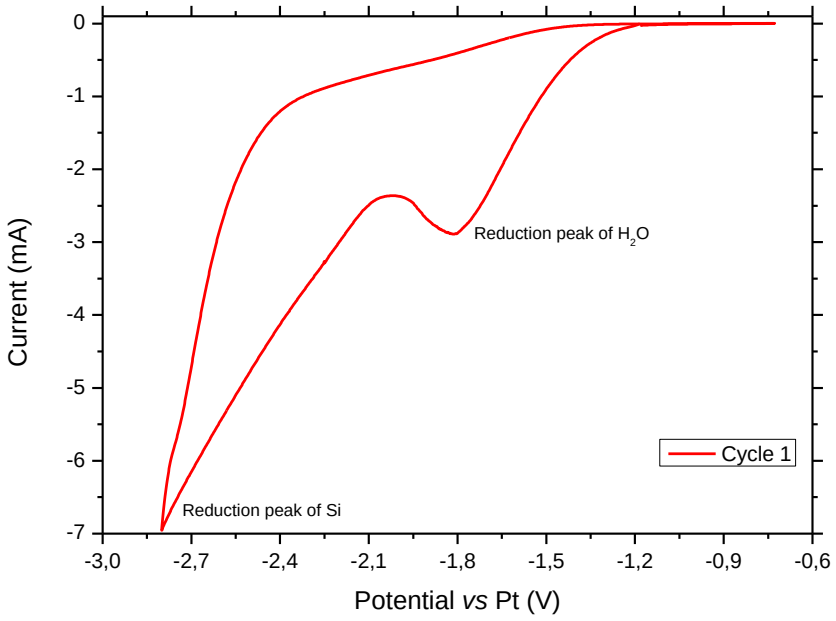

FIGURE 4.9: **Cyclic voltammogram carried out on a VACNTs carpet at room temperature and Si (IV) concentration of 1 M (The CV scan was acquired at a scan rate of 10 mV s^{-1} using platinum as pseudo-reference electrode).**

4.4.1.1 SEM and TEM characterizations of Si NPs obtained by CV

SEM and TEM analyses were performed to check the homogeneity of the deposition process and to access the morphological and structural information of the electrodeposited Si NPs. Representative top and cross-sectional SEM images of the Si@VACNTs are shown in figure 4.10 where we can clearly see the success of the deposition method for the decoration of VACNTs despite the implementation of an ionic liquid solution. However, the deposition is rather inhomogeneous with a thick Si layer covering the tubes which is composed of agglomerated Si aggregates with sizes between 50 and 200 nm as shown in figure 4.10-a. The SEM investigations on the cross-sectional orientation of the samples, see figure 4.10-b, shows the presence of Si NPs covering the sidewalls of the VACNTs. TEM investigations revealed that the Si NPs have a small size and are firmly attached to the VACNT walls, thus providing a good electrical contact for the device. In addition, the Si@VACNTs electrode has good chemical and mechanical stability.

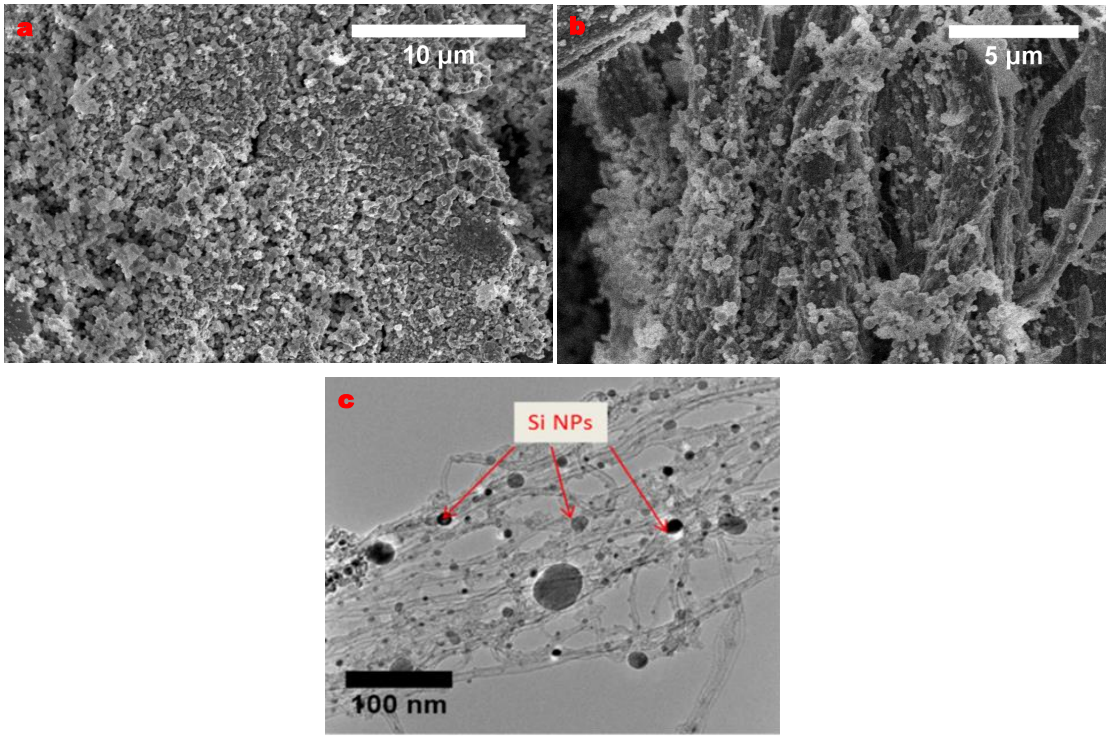

FIGURE 4.10: **SEM and TEM images of the Si@VACNTs deposited by CV. a) Top-view and b) Cross-sectional view and c) TEM image illustrating the presence of small Si NPs on the tube sidewalls.**

4.4.1.2 Electrochemical performance

The electrochemical performance of the nanostructured Si@VACNTs electrode was performed in a half-cell with the Si@VACNTs assembly used as the positive electrode vs Li/ Li^+. Similar to the cathode in Chapter 3, the terms of lithiation and delithiation will be used throughout this Chapter. Electrochemical tests were carried out using a coin cell configuration, CR2032, and have been assembled in an argon-filled glove box in which oxygen and H_2O concentrations were kept below 1 ppm. Lithium metal foil was used as CE and was separated from the WE with two separators. The electrolyte was homemade and composed of 1 M lithium hexafluorophosphate ($LiPF_6$) salt in ethylene carbonate (EC) and dimethyl carbonate (DMC), with a 1:1 volumetric ratio and for certain experiments with the addition of an additif FEC (5wt%). The mass of Si NPs deposited by the CV technique was measured by taking the difference of the mass of the CNT before and after electrodeposition and was found to be 0.43 mg cm^{-2}. We firstly used an electrolyte without an FEC additif. In figure 4.11-a, the galvanostatic lithium-insertion/ extraction curves of Si@VACNTs electrodes are plotted between 0.02 and 1.5 V at a rate of C/3. The first lithiation cycle achieves a capacity of 6793.36 mAh g^{-1}, which quickly decays to 1638.81 mAh g^{-1} after 20 cycles. The first delithiation

cycle attains a value of 1511.73 mAh g^{-1} and remains stable after 20 cycles. The curve splits into two parts: half the capacity recovered between 1.5V and 0.2V vs Li/Li^+ corresponding to the SEI formation which is also indicated in the broad peak of figure 4.11-b at around 0.6V and the other half of the capacity is attributed to the lithium alloying process. It is known that a broad irreversible peak between 0.6 and 1 V corresponding to the SEI layer formation appears in the first cycle as shown in the red curve of figure 4.11-b. However, this broad peak remains visible until the 20th cycle and it is not yet well understood. In addition, the peaks corresponding to the lithiation and delithiation of amorphous silicon are not clearly visible in figure 4.11-b. Despite that the Si peaks are not visible, the obtained specific capacities in figure 4.11-a can only be attributed to the alloying and dealloying process of Si and not to the intercaltion of Li into CNTs. It can be explained by the absence of a peak at 0.10 V corresponding to intercalation of Li into CNTs, suggesting an ignorable effect on the intercalation reaction kinetics of Li^+ ions into CNTs [301], and to the relatively lower mass of the CNTs (0.11 mg cm^{-2}) compared to the deposited Si NPs.

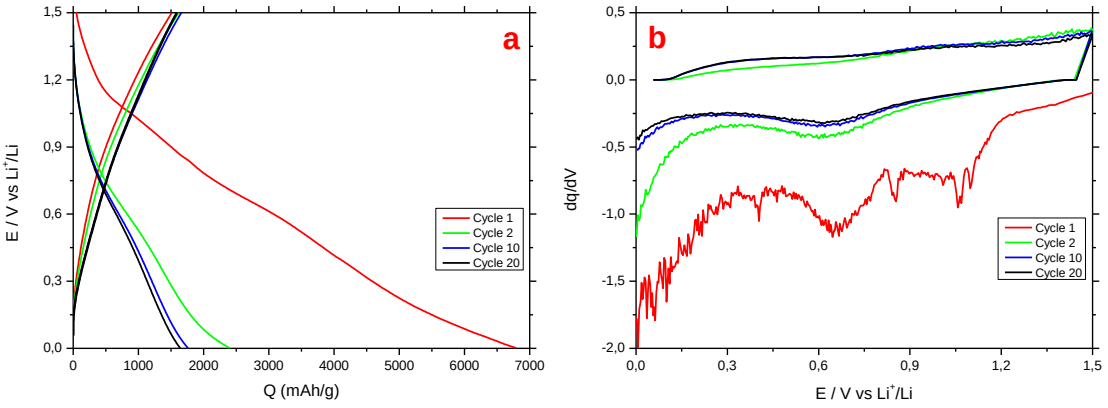

FIGURE 4.11: **Galvanostatic lithium-insertion/ extraction curves of Si@VACNTs electrodes between 0.02 and 1.5 V at a rate of C/3. a) Voltage vs. capacity plot and b) the differential capacity with the cell potential plot.**

4.4.2 Pulse electrodeposition technique

Pulse electrodeposition (PED) technique is a second approach used for the decoration of VACNTs with Si nanoparticles. Contrary to the previously described technique, the CV method, short pulses will be applied during the electrodeposition. Similar to the CV method, the solution used in the present study was 1-Butyl-1-methylpyrrolidinium

bis(trifluoromethylsulfonyl) imide with $SiCl_4$. Here again, the WE consisted of VACNT carpets grow on a Cu substrate, the CE was a platinum wire and the pseudo-RE was a platinum wire. A short pulse of -3 V was applied between the WE and the pseudo-RE during 5 ms, followed by a longer rest time of 90 ms in the open circuit potential (OCP). The PED was performed at various sweeps (2000, 3000, 6000, 8000) in order to obtain a high mass of Si and to adjust the size of the deposited NPs. The same pulse shape as in figure 3.4 was used here. The reduction and deposition of Si^{4+} ions occur during the pulse on time. During the rest time (off time), there is no current passing through the cell and hence, there is no reduction/ oxidation taking place at the electrodes.

4.4.2.1 SEM characterization of Si NPs obtained by PED

The influence of the number of pulses on the morphology of silicon electrodeposits is illustrated in figure 4.12. In this case, all the experimental conditions were kept the same while only changing the number of pulses. Figure 4.12-a,b, and c show the morphology of the Si@VACNTs after pulse electrodeposition at different number of pulses; 2000, 3000, and 6000, respectively. It can be seen that the distribution of the Si NPs is not homogeneous on the surface of the VACNT carpets and that the Si NPs form a colony on certain areas on the surface. Moreover, it can be noticed that the number of Si electrodeposits increases with increasing the number of pulses and the average particle size of the Si NPs increases from 50 to 180 nm with increasing the number of pulses. From figure 4.12-d and d_1, it is evident that the Si NPs are dispersed all over the surface of the CNT carpets.The bright areas in figure 4.12-d indicate a higher density of Si NPs.

4.4.2.2 Electrochemical performance

As for the nanostructured anode fabricated using the CV technique, the electrochemical caracterization of the anode fabricated using the PED method was achieved in a half cell using an electrolyte without any additif. The mass of Si NPs deposited by the PED technique with 8000 pulses was found to be 0.08 mg cm^{-2}. Figure 4.13-a illustrates the voltage-capacity plots of Si@VACNTs nanostructured electrodes obtained by PED. The first specific lithiation and delithiation capacities are 1131.6 and 265 mAh g^{-1}, respectively, and the initial Coulombic efficiency is 23%. The first cycle irreversible capacity loss mainly originated from the reduction of the electrolyte, resulting in the formation of the SEI film on the surface of the Si@VACNTs, or from irreversible Li^+ insertion into the active material. After 20 cycles of galvanostatic lithiation and delithiation, the anode which was produced using 8000 pulses, exhibited 204.5 and 194.2 mAh g^{-1} of lithiation and delithiation capacities, respectively and 95% Coulombic efficiency. One can notice a

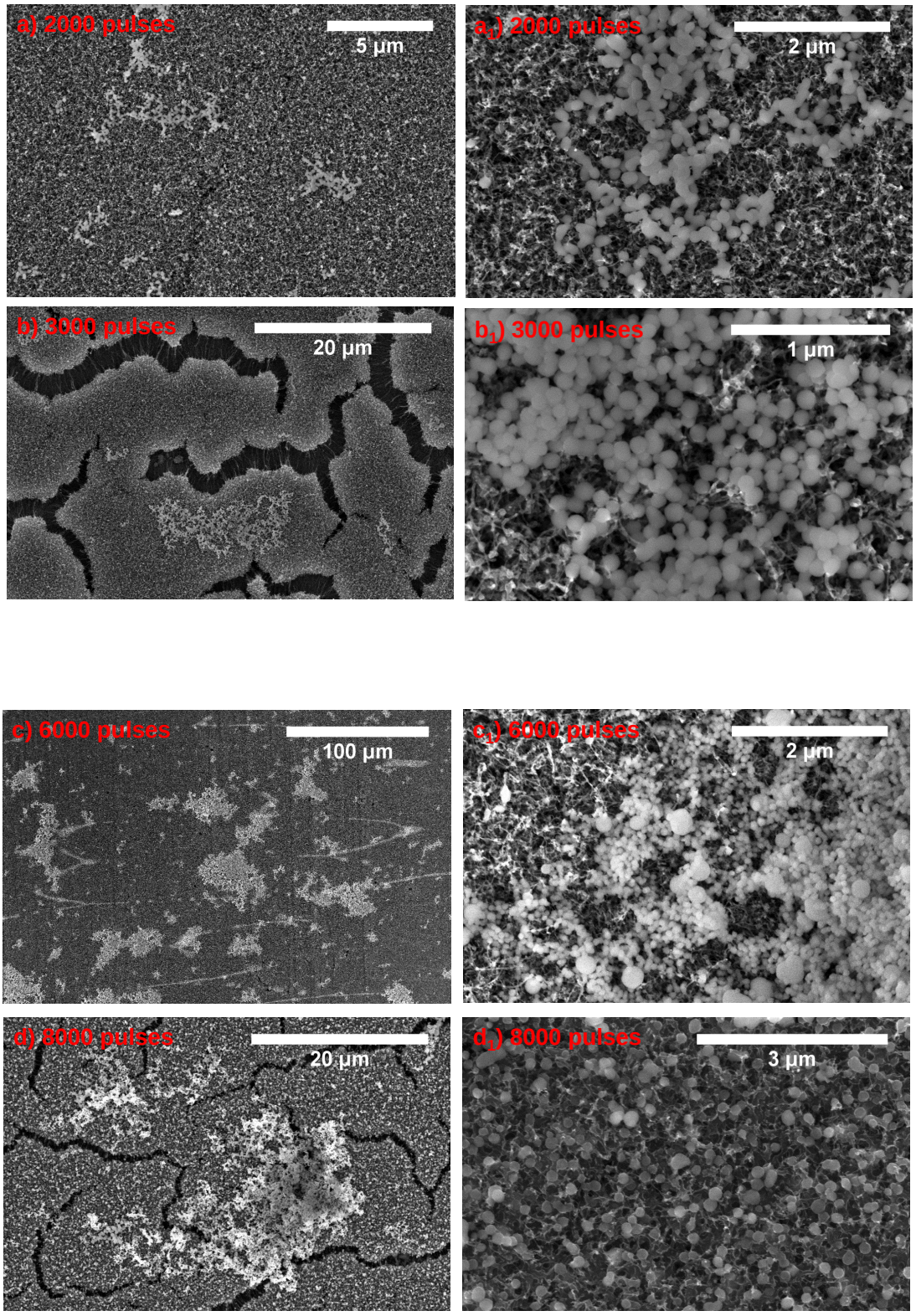

FIGURE 4.12: **SEM images of the Si@VACNTs where Si NPs were deposited by PED. a), b), c) and d) top view of the SEM images obtained after 2000, 3000, 6000 and 8000 pulses, respectively and a_1, b_1, c_1 and d_1 a closer view on a specific area of a), b), c) and d).**

huge capacity loss directly after the first cycle which can be attributed to the small mass of the silicon active material deposited by PED. The plot of the differential capacity vs the potential of the cell is presented in figure 4.13-b. The peak at 0.6 V corresponds to the formation of the SEI layer. Unfortunately, the silicon peaks do not appear in the plot confirming the low capacities obtained during the cycling.

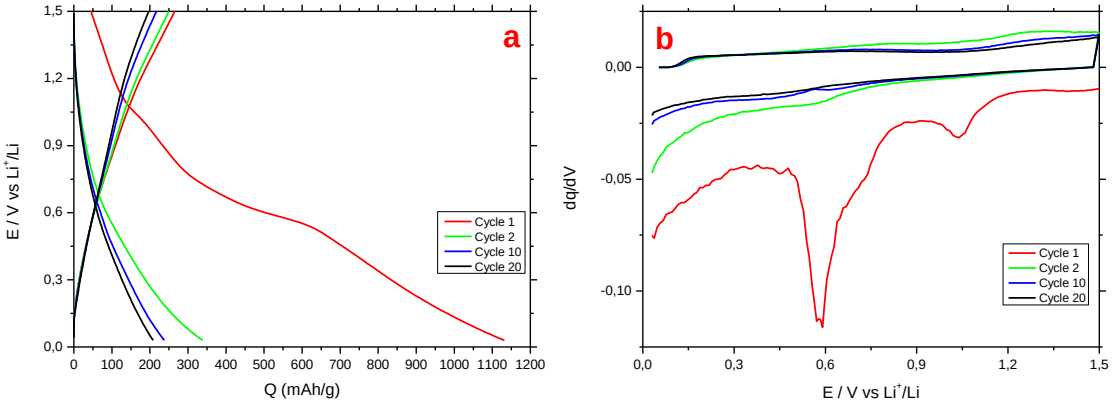

FIGURE 4.13: **Galvanostatic lithium-insertion/ extraction curves of Si@VACNTs electrodes between 0.02 and 1.5 V at a rate of C/20. a) Voltage vs. capacity plot and b) the differential capacity with the cell potential plot.**

4.4.3 Comparison of the performance of the CV and PED techniques

Figure 4.14 shows the cycle performance of the Si@VACNTs electrodes obtained by the CV (square) and by the PED (triangle) techniques at a C/20 rate between 0.02 and 1.5 V. The lithiation specific capacity of the as-fabricated Si@VACNTs nanostructured electrode obtained by the CV method delivers a higher capacity (2000 mAh g^{-1}) during the 20 cycles compared to that obtained by the PED method (200 mAh g^{-1}). The Coulombic efficiency is shown in blue filled squares (CV) and empty squares (PED) in figure 4.14. While being low during the first three cycles, the Coulombic efficiency reaches a stable value of around 97% starting from the 16th cycle for the two methods. During the first three cycles, the Coulombic efficiency of the CV method is slightly lower than that of the PED. Starting from the 6th cycle, the CV efficiency becomes higher than the PED efficiency. This can be explained by the higher mass of Si NPs in the CV method and a higher adhesion of the Si NPs on the sidewalls of the CNTs (see figure

4.10) in comparison to the PED method where the Si NPs were deposited mainly on the surface of VACNT carpets (see figure 4.12).

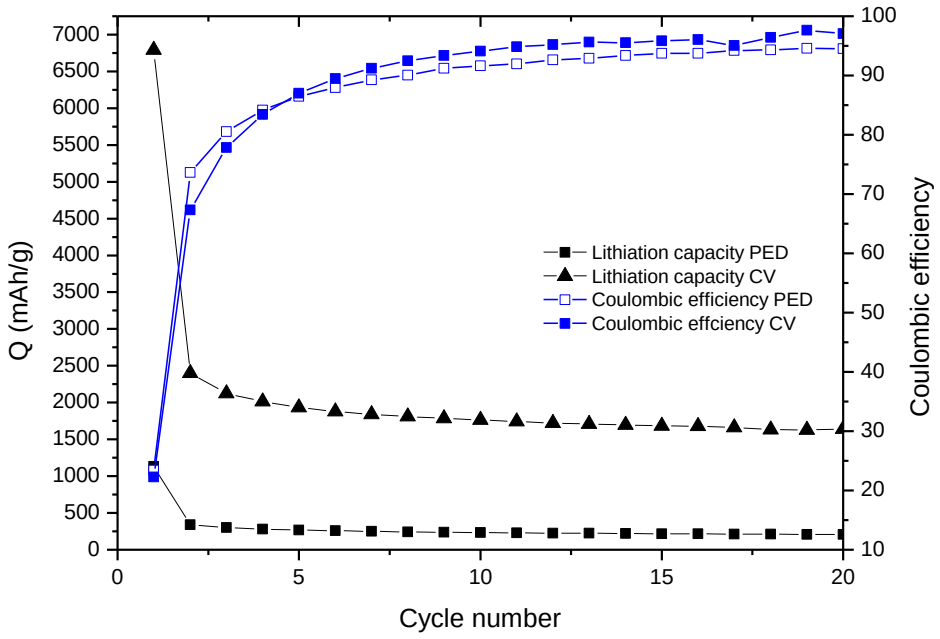

FIGURE 4.14: **Comparison of the cycling performance of Si@VACNTs electrodes obtained by CV and PED techniques between 0.02 and 1.5 V at a rate of C/20.**

4.5 Chemical Vapor Deposition technique

Chemical vapor deposition is another established strategy especially suitable for preparing Si NPs on various substrates. Gaseous silicon reactants, such as silane (SiH_4), silicon tetrachloride ($SiCl_4$), etc. are generally used in the CVD growth. This gas is then transported to the substrate which is positioned in a furnace in which the temperature and pressure can be controlled. Under certain conditions, the gas can then be dissociated at the surface of the sample and thus cause the formation of a deposit of Si. The dissociation of the gas may occur under the effect of temperature ranging from $\sim$ 300 up to well above 1000°C depending on the gas precursor employed.[302]

4.5.1 First approach

The deposition of Si NPs was carried out using chemical vapor deposition with SiH_4 gas at 500°C and 7 mbar in order to produce amorphous silicon on for 4-6μm VACNT

carpets. An advantage of amorphous silicon over crystalline silicon is that the latter tends to experience solid-state amorphization during the first Si lithiation cycle, which can lead to fracture and promote capacity fade.[303] Silane decomposes according to the following reaction:

$SiH_4 \rightarrow Si + 2H_2$

At this low temperature, the kinetic energy for each silicon atom is too low to form crystalline structure. As a result, amorphous silicon preferably forms at temperature below 650°C.[304]

The sample was loaded into the reactor preheated at 500°C and the furnace was purged with H_2 gas. After 5 minutes of heating the sample, the SiH_4 gas was introduced into the reactor and a tungsten filament placed at the H_2 gas inlet was heated at 72W (approx. 1000°C) in order to etch the excess silicon on the surface of the CNTs. This can help the Si NPs to embed easily the CNTs. The gas flow rates were 30 sccm and 10 sccm for H_2 and SiH_4, respectively. The pressure was maintained at 7 mbar and the synthesis duration were chosen to be 15 minutes, 25 minutes and 35 minutes. The loading mass of the Si active material was accurately determined by weighing the change of the mass, using a quartz crystal microbalance, before and after Si deposition.

4.5.1.1 SEM and TEM characterizations of Si NPs obtained by CVD

Figures 4.15-a, b and c show the cross-sectional SEM images of the Si@VACNTs nanostructured electrode obtained at three different deposition durations: 15 minutes, 25 minutes and 35 minutes, respectively. A closer view on each sample (figure 4.15-a_1, b_1 and c_1) clearly show that increasing the deposition time, the size of the Si NPs increases until a thin film is formed and covers the CNT sidewalls at 35 minutes of deposition.

TEM observations of the three synthesized nanostructured electrodes, presented in figure 4.16-a, b and c, reveal a homogenous deposition of the Si NPs mainly on the CNT sidewalls and a changing morphology with deposition time. We observe that after 15 minutes of deposition, Si NPs form on the nanotube sidewalls with an ellipsoidal morphology and a homogenous size between 10-20 nm. Regarding their preferential localization on the sidewalls of the tubes, we believe that this is related to the presence of defects within the external tube graphitical structure. These defects can be considered as anchorage points for the silicon precursor that nucleates as Si seads and starts growing during the SiH_4 gas decomposition. If the growth process lasts 25 minutes, we observe that the size of the Si NPs increases up to 40 nm (see figure 4.16-b_1) and the nanoparticles are more dense all around the carbon nanotube presenting a rather spherical morphology. When the deposition time is increased up to 35 minutes, we have a formation of a Si shell all

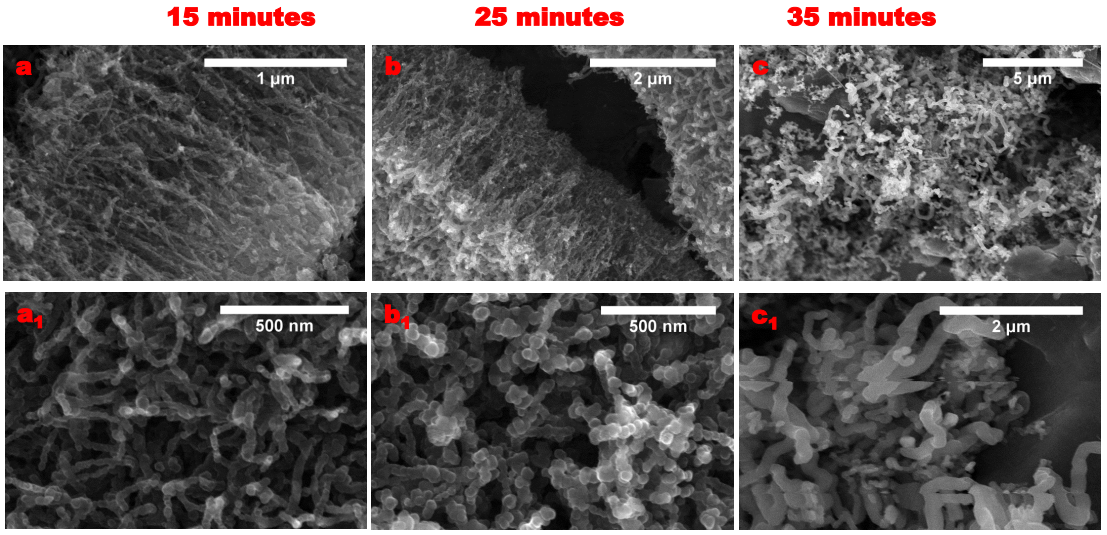

FIGURE 4.15: **SEM images of Si@VACNTs hybrid structure obtained by CVD with a deposition time of a) 15 min, b) 25 min and c) 35 min. a_1), b_1) and c_1) are higher magnification images of a), b) and c), respectively.**

around the carbon nanotube (see figure 4.16-c_1). The electrochemical performance of each nanostructured electrode is presented in the following section.

4.5.1.2 Electrochemical performance

The Si@VACNT nanostructured electrodes fabricated by the CVD technique described above were cycled against metallic lithium using a coin cell configuration and this time an electrolyte with FEC additif was used. The mass of deposited Si was determined by weighing measurements before and after Si deposit on a VACNT carpets. The mass of Si for the lighter and higher loaded electrodes corresponding to 15 minutes and 25 minutes deposition were found to be 0.20 mg cm^{-2} and 1.2 mg cm^{-2}, respectively. Figures 4.17-a and 4.18-a show the lithiation/ delithiation voltage vs. capacity profiles for the 15 minutes and 25 minutes of Si deposition on VACNT anodes after the 1st, 2nd, 10th, 100th and 400th cycles at a rate of C/10, respectively. It can be clearly seen that lithiation during the first cycle resulted in a very high capacity of 3499.8 mAh g^{-1} for the anodes prepared at 15 minutes and 3858.2 mAh g^{-1} for the 25 minutes deposition time which are close to the expected theoretical capacity 3580 mAh g^{-1} determined from the silicon content. During the subsequent delithiation, a capacity of 3442.6 mAh g^{-1} for the 15 minutes and 3571.8 mAh g^{-1} for the 25 minutes deposition anodes were obtained, resulting in a first cycle irreversible loss of only 2% and 8% for the 15 and 25 minutes, respectively. Such irreversible loss values are better than the commercially available

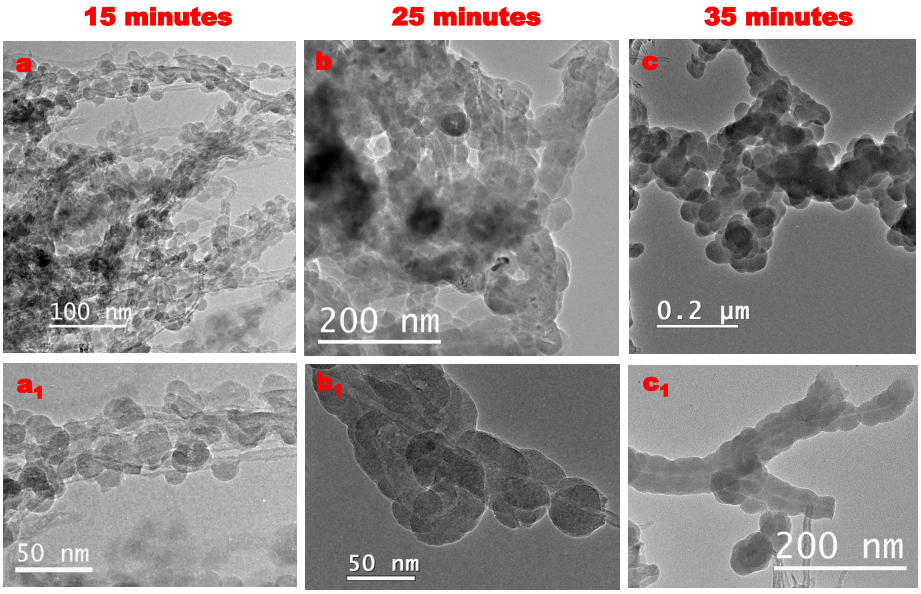

FIGURE 4.16: **TEM analysis of the Si@VACNTs hybrid structure obtained by CVD with a deposition time of a) 15 min, b) 25 min and c) 35 min. a_1), b_1) and c_1 are higher magnification TEM images of the samples obtained for the three different deposition durations illustrating the morphology and the localization of the deposited Si NPs.**

graphite based anodes.[305] In addition, the remarkably low first cycle irreversible loss, it is much better compared to other silicon anode reports [70, 72, 73, 84, 306, 307] and is a signature of the unique hierarchical electrode design comprising of nanoscale Si deposits and coverage of the VACNTs prompting favorable lithium ions and electrons transport resulting in a low irreversible loss between lithiation and delithiation processes. The low first cycle irreversible loss is of great importance regarding the efforts to commercialize silicon anodes in a full Li-ion cell, by helping to efficiently balance the weights of anode and cathode. The two large capacities obtained presume that all of the Si deposited on the aligned CNT is electrochemically active and, thus, suggest the efficacy of the current approach employed in this work. The very high first lithiation capacities, for the 15 and 25 minutes anodes, also suggest that the Si@VACNT electrode is mainly composed of silicon, owing to the low density of the CNTs. The VACNT carpet can be considered to not contribute to any significant capacity. Hence accordingly, in the current work, the CNTs were not accounted for calculating the theoretical capacity of the electrode. The plots of the differential capacity with the cell potential for the corresponding cycles for the hybrid nanostructures obtained after 15 and 25 minutes of Si deposition are shown in figure 4.17-b and figure 4.18-b, respectively. During the 1st lithiation cycle, a peak at 0.227 V and a peak at 0.205 V are observed in figure 4.17-b and figure 4.18-b followed by

a sharp peak at 0.023 V and 0.055 V for the 15 minutes and 25 minutes of Si deposition, respectively. The peaks at 0.227 V and at 0.205 V correspond to the long flat plateau in the first lithiation voltage profile in figures 4.17-a and 4.18-a, which are widely considered by several researchers as the lithiation of amorphous silicon and the presence of a two phase region. These phases correspond to the unlithiated amorphous silicon and partially lithiated silicon phases (Li_xSi) that co-exist until the voltage reaches 0.1 V, wherein complete lithiation of the parent amorphous silicon phase occurs, and become amorphous Li_xSi phase.[71, 274, 307, 308] Below 0.1 V, further lithiation of Li_xSi phase continues to occur and is represented by the peak at 0.023 V. The formation of crystalline intermetallic phases is not expected due to the sluggish kinetics.[84, 263, 264, 269, 309] When cycled at an extremely slow rate of C/100, Li and Dahn [264] reported the formation of $Li_{15}Si_4$ phase at ∼60 mV during first lithiation. However, similar to Moni and Kumtas recent report [309], this phase formation is not observed in this work, possibly due to the fact that the electrode was cycled at a moderate current rate (C/10), which may likely bypass the formation of $Li_{15}Si_4$ phase.

During the delithiation step, two major peaks are observed: one at 0.304 V and another at 0.459 V in figure 4.17-b and one at 0.288 V and another at 0.449 V in figure 4.18-b, which correspond to the phase transition between amorphous Li_xSi alloys and the formation of amorphous silicon, respectively.[274, 308] However, in the 2nd and the subsequent cycles, the lithiation of amorphous silicon to form the Li_xSi alloys is slightly shifted to higher potential values and is consistent with other reports in the literature.[307, 308] The differential capacity curves for the lithiation and the delithiation reactions superimpose very well till the 400th cycle indicating that there are no additional reactions occurring while cycling the hybrid nanostructures.

As the cycle proceeded in both figures 4.17-b and 4.18-b, the peaks diminished gradually. The same trend was observed in both voltage vs. capacity plots where the capacity decayed with increasing cycle numbers (see figures 4.17-a and 4.18-a). Moreover, the capacity of the heavily loaded (25 min) electrode decayed faster than that of the lighter loaded (15 min) one, although the heavily-loaded one had relatively higher initial capacity. This suggests that the electrode having more active material, i.e. Si, possessed higher initial capacity but experienced faster capacity decay. The capacity fading might be due to two main possible reasons, such as thicker SEI layer residing in the Si@VACNT electrodes, leading to inhibition of Li transport and to increase of the internal impedance [310] and loss of active material due to Si@VACNT structural deformation.

Unfortunately, the electrode obtained after 35 minutes of Si deposition (with 4.5 mg cm^{-2} of silicon) could not be cycled due to the thick layer of Si on top of the CNTs which resulted in severe cracking of the electrode during coin-cell mounting.

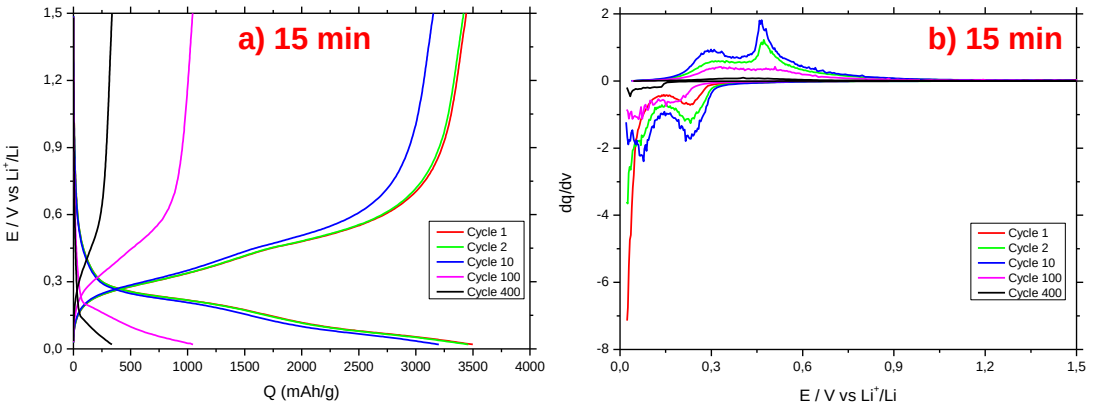

FIGURE 4.17: **Voltage vs. capacity plot and the differential capacity with the cell potential plot of lighter loaded Si@VACNTs nanostructured electrode. a) Voltage vs. capacity plot and b) the differential capacity with the cell potential plot cycled in the potential window of 0.02-1.5 V vs Li/ Li^+ at a rate of C/10.**

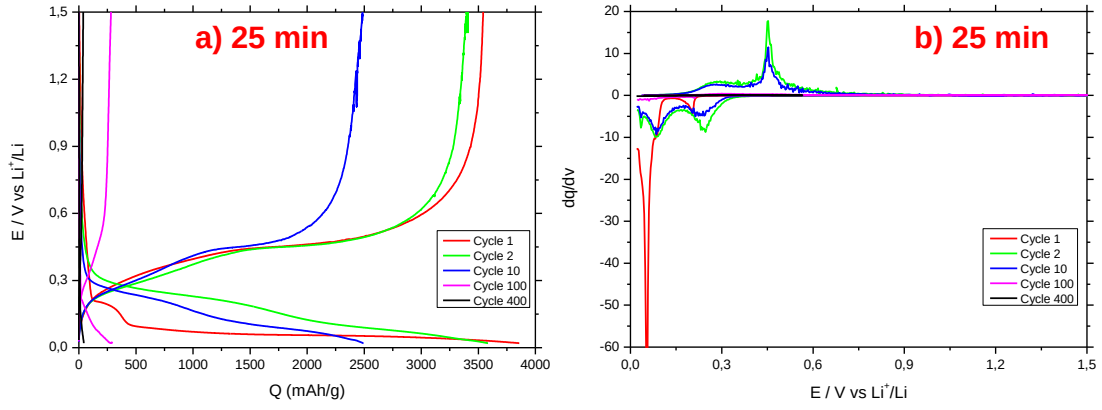

FIGURE 4.18: **Voltage vs. capacity plot and the differential capacity with the cell potential plot of heavily loaded Si@VACNTs nanostructured electrode. a) Voltage vs. capacity plot and b) the differential capacity with the cell potential plot cycled in the potential window of 0.02-1.5 V vs Li/ Li^+ at a rate of C/10.**

The lithiation/ delithiation capacities plot for 400 cycles of the lighter and higher loaded Si@VACNT nanostructured anode are shown in figure 4.19 (left panel). The first lithiation and delithiation capacities are 3499.8 and 3442.6 mA g^{-1} , respectively, with an initial Coulombic efficiency of 98%, corresponding to an irreversible capacity loss of 2% for the lighter loaded electrode (15 minutes of Si deposition). In the subsequent cycles, the Coulombic efficiency, however reaches 99.95% and remains relatively stable. The specific capacity of the Si@VACNT anode decreases between 1 and 200 cycles, exhibiting an average fade rate of $\sim$ 0.41% per cycle. When the capacity drops to around 650 mAh g^{-1}, furthermore it gradually stabilzes to about 450 mAh g^{-1}, where it remains stable until 400 cycles. At C/10 rate, retention of $\sim$450 mAh g^{-1} specific capacity indicates the promising nature of this Si@VACNT nanostructured anode which show a higher capacity compared to the theoretical capacity of graphite even after 400 cycles. The cycling stability plot for 400 cycles for the higher loaded Si@VACNT nanostructred anode is shown in figure 4.19 (right panel). The first lithiation and delithiation capacities are 3858.2 and 3571.7 mA g^{-1} , respectively, with an initial Coulombic efficiency of 92%, corresponding to an irreversible capacity loss of 8% for the higher loaded electrode (25 minutes of Si deposition). The electrode exhibits an average fade rate of $\sim$ 1.8% between the second and 100th cycle. At the end of 100 cycles, a capacity close to 300 mAh g^{-1} is obtained when cycled at the C/10 rate. This capacity continues to decrease until it reaches a value of 56 mAh g^{-1} at 400 cycles. This severe capacity fading can be explained by the excessive amount of silicon present on the VACNTs which might have caused cracking and pulverization of the electrode.

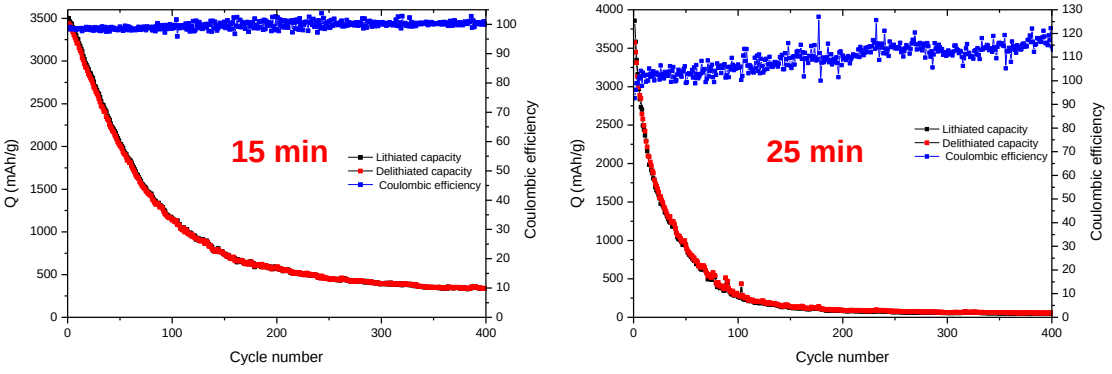

FIGURE 4.19: **Lithiation/ delithiation capacities and Coulombic efficiency of Si@VACNT electrode during 400 cycles.** Left: lighter loaded electrode and Right: higher loaded electrode.

4.5.1.3 Rate capability

It should be noted that the recovered capacity depends on the current applied. Indeed, a high current makes it possible to lithiation or delithiation of the electrode faster. However, the transport of Li^+ ions within the electrode and the transport of electrons to the current collector can become limited when the current density becomes too high, which translates into a recovered capacity less than the theoretical capacity of the material. A rate capability consists in recording the capacity of the electrode at different current regimes. The current is expressed as C/n, where n is the number of hours required for full lithiation or delithiation of the battery. Thus, the 1C regime is the current which must be applied to insert or extract 3.75 Li for a Si in one hour, which corresponds to 3.58 A g^{-1}. The rate capability is achieved by applying a low current and gradually increasing it. Several cycles are usually performed at each regime.

In order to investigate the performance or the amount of charge stored in Si@VACNT electrodes, galvanostatic measurements were performed at various rates from C/20 to 8C and the loading mass of Si NPs on the VACNT carpets was 0.30 mg cm^{-2}. Figure 4.20-a displays the specific capacities of the electrode obtained as a function of the lithiation/ delithiation rate, and demonstrates a very good cyclability. Specific delithiation capacities of 2800, 2650, 2497, 1945, 894, 2305 mAh g^{-1} were obtained at C/20, C/10, C/2, 2C, 8C and C/20 rates, respectively. The specific delithiation capacity decreased gradually with increasing the C rate. However, the Si@VACNT capacities are found to be 2 up to 7-fold higher (depending on the C rate) than the practical capacity achieved with graphite electrodes. Furthermore, it is possible to recover the initial capacity value after lithiation/ delithiation measurements at high C rates, indicating a very good reversibility and no degradation of the Si@VACNT nanostructured anodes when cyled at high rates. These outstanding performances validate our nano-fabricated hybrid electrode approach and demonstrate the high rate capability of the hierarchical hybrid nanostructured anodes. Comparing with the literature [70, 71, 73, 283] for an analog hybrid structure (CNTs and Si), we obtain great initial lithiation/ delithiation capacities when cycling at a moderate rate (2800 mAh g^{-1}). Also at higher rates we measure higher capacities when comparing to the analog hybrid structures and even to the commercial anode (graphite) in LIBs. An impressive Coulombic efficiency was obtained in the first cycles, around 95%, corresponding to an irreversible capacity loss of only 5%, due to our VACNT carpets which ensure an excellent electron transport to and from silicon nanoparticles, thus validating the potential of our fabrication of the nanotructured current collectors. At the end of the cycling, the Coulombic efficiency increases to 98%. Figures 4.20-b,c and d show the differential capacity versus potential for the C/20 at the beginning of the cycling, at 8C rate and at the end of the cycling,

returning to C/20 rate. We clearly observe the peaks of lithiation and delithiation corresponding to the amorphous silicon at a C/20 rate. However, at higher rate, we observe one peak for the lithiation and another for the delithiation. The absence of one peak for each of the lithiation and the delithiation processes can be explained as follows: due to the very high rate of cycling, the Si NPs do not have enough time to go through a phase transition, which leads to the disappearence of one of the peaks.

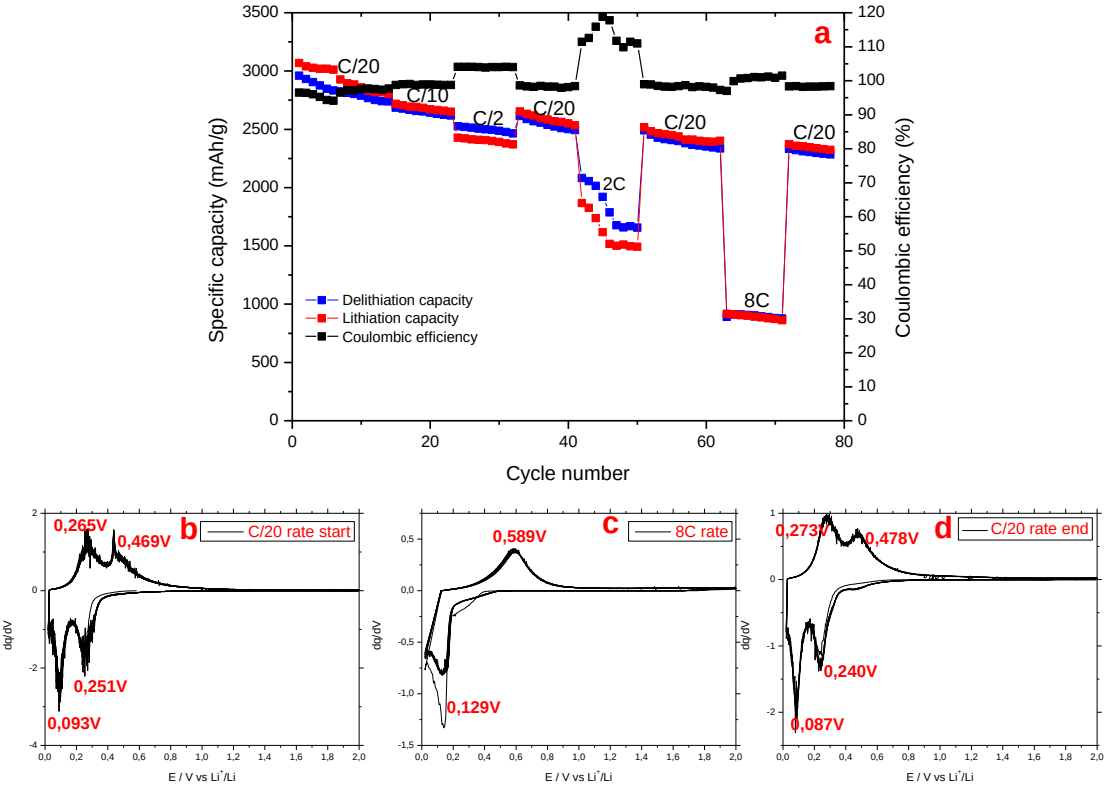

FIGURE 4.20: **a) Rate capability plot of the Si@VACNT nanostructured anode obtained at different C rates between 0.02-2 V vs Li/ Li^+. b) and c) Plots of differential capacity versus cell potential of the hybrid Si@VACNT nanostructure anode.**

4.5.2 Second approach

As seen from the above presented approach, in order to increase the mass of silicon deposited on the electrode, an increase in the deposition time of silicon on 4-6μm height VACNTs was performed. This approach revealed that with the increase in the deposition time, the Si@VACNT structure only accommodates the low silicon loading, however it struggles with the high silicon loading which could not be electrochemically tested. Since silicon is known for the highest specific capacity and greatest volume change during cycling, the amount of Si loading not only affects the cycling performance (e.g., specific capacity of our electrode, Coulombic efficiency), but also the electrode integrity. As an

attempt to improve this, a different approach was studied. It consists of the growth of longer CNTs in order to increase the number of Si NPs deposited all over the side-walls while keeping a low areal (in respect of nanotube's area) density. In this case, we can obtain a higher mass of silicon and deposition of true Si NPs, instead of a thick silicon layer that encompass the tubes, thus avoiding the cracking of the electrode. Different samples of VACNT carpets were prepared under the same growth conditions, as described in Chapter 2, except for the CNTs growth duration. The first sample was prepared with a growth time of 10 minutes, the second with 20 minutes and the third with 30 minutes. The VACNT carpets obtained have a tube length of 7, 13 and 25 μm for the 10, 20 and 30 minutes, respectively. Silicon deposition was performed by CVD process where the grown VACNTs were loaded at the same time into the reactor. The deposition was carried out at 550°C with a mixed flow rate of 10 sccm SiH_4 and 30 sccm H_2, and a tungsten filament power of 72W. The pressure was set at 7 mbar and the synthesis duration was 15 minutes. The mass of silicon was determined by measuring the mass of the substrate each time before and after the silicon deposition using a quartz crystal microbalance.

4.5.2.1 SEM and electrochemical characterizations of Si NPs obtained by CVD

Figure 4.21 presents the SEM images of the hybrid Si@VACNT nanostructures, which distinctly show the Si NPs attached to the CNTs (see figure 4.21-a_1-b_1-c_1). The overall configuration of the CNT carpets remains intact after silicon deposition, as shown in figure 4.21-a-b-c. It is clear that the CNT surface provide the desired sites for Si NPs to nucleate and grow during the subsequent SiH_4 decomposition step. We observe that the silicon particles covered the CNTs homogeneously, despite the length of the tubes. With an increase in the length of the carpet, the mass of silicon increases: 1.50, 2.56 and 4.11 mg cm^{-2} for 7, 13 and 25 μm of CNTs, respectively.

The electrochemical characteristics of the three samples with different loading mass were cycled against metallic lithium using a coin cell configuration at C/20 rate and were compared in figure 4.22-a. An areal capacity of around 1.6 mAh cm^{-2} is obtained for sample 1 with a silicon mass of 1.50 mg cm^{-2} that is stable during the subsequent cycles. This capacity can be compared to or even better than the surface capacity obtained for silicon nanowires ($\sim$ 0.9 mAh cm^{-2}).[311] Sample 2 corresponds to a deposited mass of 2.56 mg cm^{-2}, and shows a surface capacity of 5.5 mAh cm^{-2}. We observe an increase in the lithiation capacity starting from the second cycle which can be attributed to the activation of more silicon atoms reacting with lithium.[70] This capacity is 1.4 times higher than that of commercial graphite based electrode. Sample 3 with a deposited mass

of 4.11 mg cm^{-2} gives a surface capacity of 12.6 mAh cm^{-2}. Unfortunately, because they were assembled in coin cells recently, at the time when this manuscript was written, the Si@VACNT are still in their first cycles, which prevents as from showing any results on further cycles. The presented cycles show no obvious capacity decay.

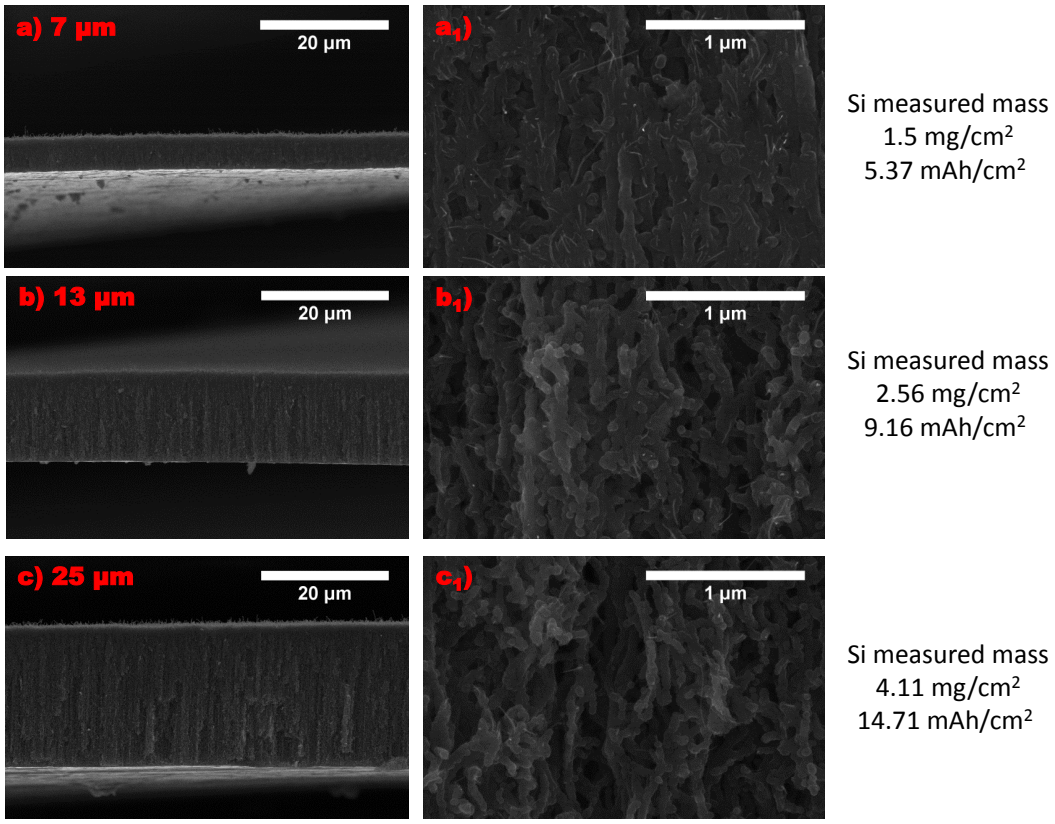

FIGURE 4.21: **SEM images of Si@VACNT anode with different lengths of VACNT. a) 7μm, b) 13μm and c) 25μm. a_1), b_1) and c_1 are higher magnification images of a), b) and c), respectively.**

To highlight the excellent cycling performances of our electrodes and to provide a comparison, our hybrid nanostructures were compared to a forest of silicon nanotrees [311], a commercial graphite electrode whose maximum surface capacity at low speed is slightly greater than 4 mAh cm^{-2} and silicon composite electrodes derived from the recent literature [312] and deposited on a current collector which is a copper foam, which makes it possible to achieve these high loading masses while retaining interesting electrochemical performances.

In order to compare to a commercial graphite electrode, we use the tests performed by the author in ref [311]. The graphite electrode was taken from a commercial battery of type NCR18650PF of the brand Panasonic, displaying an energy of 2900 mAh. It corresponds to the state of the art electrode in terms of energy density. A small sample of the negative electrode was then cut and reassembled in a coin cell, against a metal lithium counter electrode. The electrolyte used was a commercial one, very similar to

that used for cycling nanotrees of silicon electrodes, but with an EC/ DEC/DMC ternary electrolyte (2/1/2) instead of the EC/DMC binary. The electrochemical windows used for the cycling of this electrode were 0 V for lithiation and 1 V for the delithiation. A capacity of about 4 mAh cm^{-2} was obtained at very low C rate, as expected. The electrode was capable of maintaining this capacity without significant loss up to C/10 rate, but for a C/2 rate the capacity decreased up to 1.3 mAh cm^{-2}.

The comparison was also carried out with high loading masses silicon-based electrodes. These are results published recently by Mazouzi et al [312] and correspond to the best silicon based electrodes fabricated so far. Two examples from this work are presented in 4.22-b. Mazouzi et al. carried out these tests by limiting the maximum capacity to 1200 mAh g^{-1}. Despite this limitation, the surface capacity remains lower than that of our most loading mass electrode.

Comparing to the literature [311–313] dealing with nanowires, hybrid structure (Si and CNT) and silicon composites based electrodes, our silicon nanostructure based electrodes show, to the best of our knowledge, the best surface capacity of 12.6 mAh cm^{-2}.

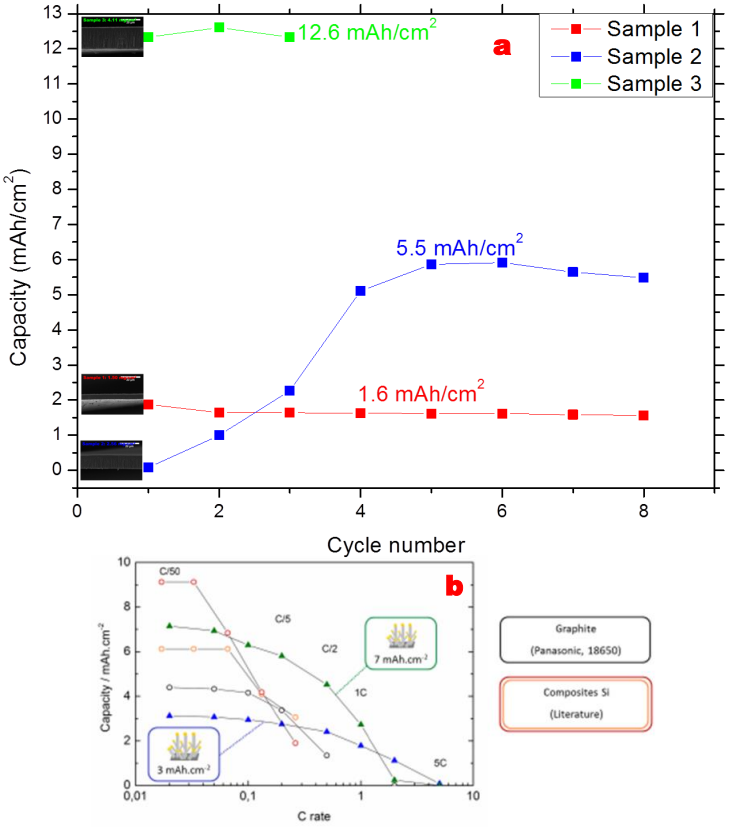

FIGURE 4.22: **a) Comparison of the lithiation areal capacity of our electrodes in function of the deposited silicon mass. b) Comparison of the lithiation areal capacity of the silicon nanotrees, the silicon composite based electrodes and the commercial graphite.[311, 312]**

4.6 Conclusion

It has been proven in literature that nanoparticles with smaller diameters show a higher specific capacity and better capacity retention because of the reduced tendency for particle cracking. However, the particle-based anode material is also hindered by electrochemical aggregation and electrode destruction after repeated expansion/ contraction. To address these issues, nanoparticles were dispersed into matrices so that stress generated from volume expansion during lithiation could be quickly released. The matrix did not experience huge volumetric change which might buffer the huge expansion of silicon, maintaining the structural integrity of the electrode and enhancing the electric conductivity and cycling stability. In our approach a hierarchical nanostructure Si@VACNT was directly synthesized onto the copper current collector through a simple two-step CVD process, removing the use of polymer binder or carbon additives. The direct synthesis of the VACNT on the current collector ensured that every tube is electrically end-connected onto the current collector, thus provided an overall nanostructured current collector and maximized the electron and the Li^+ transport.
The Si@VACNT with loading up to 4.11 mg cm^{-2} of silicon could be fabricated and showed an excellent surface capacity of 12.6 mAh cm^{-2}, the highest value for nanostructured silicon anodes obtained so far.

Chapter 5

Towards a full battery based on nanostructured electrodes

5.1 Motivation

Half cells use pure lithium foil as the counter electrode, because it provides an essential source of unlimited amount of Li^+ ions to the system. However, this overabundance of Li^+ ions can cause plating at the anode, short circuiting, and might lead to overheating, fire, or even explosion. Due to these safety concerns, metallic lithium foil is not appropriate for commercial LIBs. In order to avoid the use of elemental lithium and to make a safer Li-ion battery, a high capacity anode material, such as silicon, i.e. different than metallic lithium, can be used where the source of lithium will be provided in the cathode, i.e. sulfur when its lithiated (Li_2S).

In the previous Chapters, we have evaluated the properties and the electrochemical performances of sulfur cathode and silicon anode for LIBs application. Separate half-cell tests have showed superior high capacity and good cyclability when they are coupled with lithium metal foil. Now, it is the appropriate time to integrate sulfur and silicon into a full battery by combining Si@VACNT anode with S@VACNT cathode.

5.2 Half-cell test of Si@VACNT anode

The challenge faced by Si-S battery is the choice of electrolyte. Currently, the optimized electrolyte for Si is $LiPF_6$ dissolved in EC-DMC-FEC mixed solvent, and for Li-S battery is LITFSI dissolved in (DME-DOL) system. The question that arise is which type of electrolyte is better to use, or whether it is required to develop new electrolyte system

which will need comprehensive dedicated research".

To this end, we tested the Si@VACNT in the same electrolyte used for S in order to find out whether it is compatible. In our experiments, Si@VACNT electrodes were tested in a half-cell configuration with lithium foil counter electrode and the same electrolyte employed in the S@VACNT/ Li half-cells. Si@VACNT was cycled between 0.02 and 2 V at a rate of C/20 against a metallic lithium foil, and the electrolyte was 1 M LiTFSI in DOL/DME (1:1) + 0.25 M $LiNO_3$. The areal weight of the Si anode electrode was 0.62 mg cm^{-2}. Assuming a specific capacity of 3580 mAh g^{-1} for Si, we expect a theoretical capacity of the electrode to be 2.21 mAh cm^{-2}. Figure 5.1 shows the initial five lithiation/ delithiation cycles of the Si anode in a Si/Li half-cell at a rate of C/20. It can be observed that the first lithiation capacity reaches the calculated theoretical capacity (2.91 mAh cm^{-2}), following a potential profile which is a characteristic of amorphous silicon. After the first lithiation and delithiation cycle, the specific lithiation and delithiation capacity decreases to a constant value of 1.32 mAh cm^{-2}, corresponding to 45% of the theoretical areal capacity of the anode. The higher capacity observed in the first lithiation is attributed to SEI formation on the Si surface. The voltage profile is similar to that in a $LiPF_6$/ EC/ DEC electrolyte suggesting similar chemistry, except for the plateau at 1.4 V which can be attributed to the SEI formation. Silicon anodes have been proven to work in this type of electrolyte.[224]

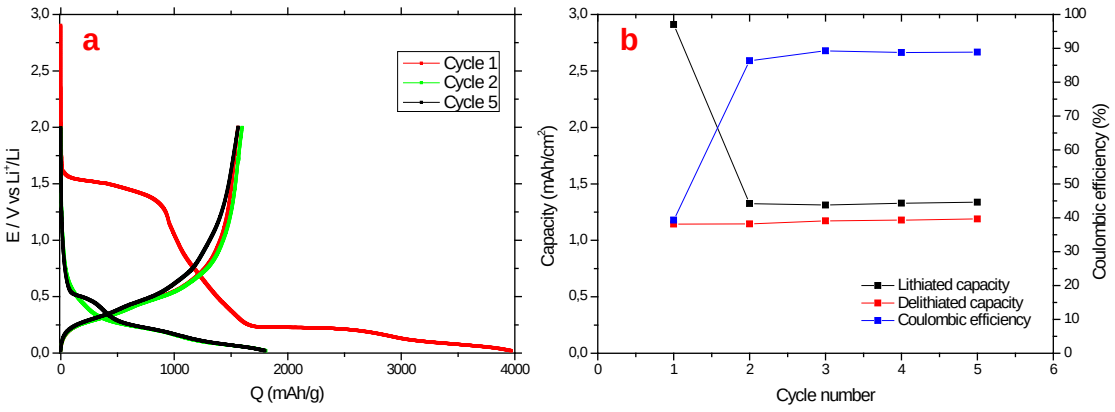

FIGURE 5.1: **a) Lithiation/ delithiation capacities and Coulombic efficiency of Si@VACNT electrode in the same electrolyte employed for sulfur electrodes. b) Areal capacities of Si@VACNT electrode.**

5.3 Lithiation of Al_2O_3@S@VACNT

Sulfur as a cathode material has many benefits, such as abundance, low cost, high energy, and environmental benignity. Because of the lack of lithium in the sulfur cathode before cycling, lithium metal is usually used as the anode which has safety issues, impeding the commercialization of Li/S batteries. In this regard, lithium sulfide (Li_2S), the fully lithiated state of sulfur with a theoretical capacity of 1166 mAh g^{-1}, is a more desirable cathode material compared to sulfur as it could allow lithium-free anodes to be used, such as graphite, Si, Sn, and metal oxides.[224, 314–317]

In order to convert S into Li_2S, three different approaches can be used:

- Organic lithium salts (e.g. n-butyl-lithium): These metal organic salts are usually air-sensitive and toxic, and can only be used in a well-protected environment for safety concern.
- Commercially available Li_2S: commercially available lithium sulfide consists of 30 to 100 μm sized particles and has no electrochemical activity due to the large particle size, and is not suitable for battery application due their prices which are 400 times higher than for elemental sulfur. In addition, Li_2S is usually delivered with other lithium salt impurities.[318]
- Lithiation of the S electrode: It is an easy and a cheap approach to obtain lithium sulfide. It consists of assembling the as-fabricated electrode Al_2O_3@S@VACNT in battery (for example a coin cell) against metallic lithium foil.

5.4 Towards the full-cell

The Al_2O_3@S@VACNT was lithiated for one cycle at a rate of C/20 with a cut-off at 1.7 V in a coin-type half cell and was then disassembled in a glove box for further use. It should be noted that the lithium present in the electrode contributes non-negligible to its mass. Therefore, it is the total mass of the electrode material and not just the mass of sulfur which must be taken into account in determining the specific capacity of the electrodes. The mass loading of sulfur in the electrode was 0.75 mg cm^{-2}. After lithiation, we measured a mass of 1 mg cm^{-2} corresponding to Li_2S.

The prelithiation is meant to intercalate Li into the electrode active material by putting extra Li in the electrodes prior to electrochemical testing. It has the advantage of compensating the Li loss due to SEI formation in the first cycles and reduction of the initial irreversible capacity loss to some extent. The prelithiation of Si@VACNT

electrodes was carried out in a glove box before the assembly of the full-cell. The Si@VACNT electrode was pressed against a metallic lithium foil after having carefully deposited a drop of electrolyte ($LiPF_6$ EC:DMC + FEC 5wt%) on its surface to allow the conduction of the lithium ions.[319]

In the full-cell, the silicon mass in the anode was balanced with the mass of Li_2S in the cathode. The cycling of Li_2S/Si full-cell was investigated using Al_2O_3@Li_2S@VACNT cathode and Si@VACNT anode of theoretical capacities of 1.15 and 1.60 mAh cm^{-2}, respectively between 1.3-2.6V at a C/20 rate.
Figure 5.2 shows the voltage profile of the first charge and discharge cycles for a Li_2S/Si battery at a rate of C/20, which corresponds to 58 mA g^{-1} with respect to Li_2S. The average discharge voltage of the Li_2S/Si full-cell is ∼1.7 V, since the silicon anode has an average discharge potential of ∼0.4 V versus Li/Li^+. The first charge and discharge capacities reach 365 and 486 mAh g^{-1}, respectively. However, from the second cycle the capacities drop to reach 3 mAh g^{-1}. Although no additives were used, an initial specific energy of 353 Wh kg^{-1} for the full cell was obtained. This value is similar to that of commercial Li-ion batteries (364 Wh kg^{-1}). To calculate this practical value for the $LiCoO_2$/graphite system, equation 5.1 was used with the following values: cathode capacity: 140 mAh g^{-1}, anode capacity: 330 mAh g^{-1}, operating voltage: 3.7 V.

$$E = \frac{C_c * C_a}{C_c + C_a}(V_c - V_a) \tag{5.1}$$

Despite its non optimized configuration, the sulfur-silicon lithium-ion battery developed here offers a good performance in the first cycle. Compared with the specific capacities of the half cell for sulfur and silicon, the specific capacity of the Li_2S/Si full cell decays faster. This could be caused by the following factors: 1) in full cells, there is a limited supply of Li^+ ions, which can be irreversibly lost in side reactions. However, Li^+ ions that would be lost in a full cell configuration can be restored by the Li metal counter electrode in half cells, which is a virtually unlimited source of Li^+ ions. 2) unsatisfactory mass balance of the two electrodes, and 3) deposition of polysulfide on Si consumes both the cathode and anode, leading to a fast capacity decay.

The full cell test has shown preliminary results of the Li_2S@VACNT/ Si@VACNT full battery with promising performances. However, there are still many unsolved issues, such as the stability in the capacities during cycling. Great efforts in optimizing both electrode materials as well as suitable electrolyte system are essential.

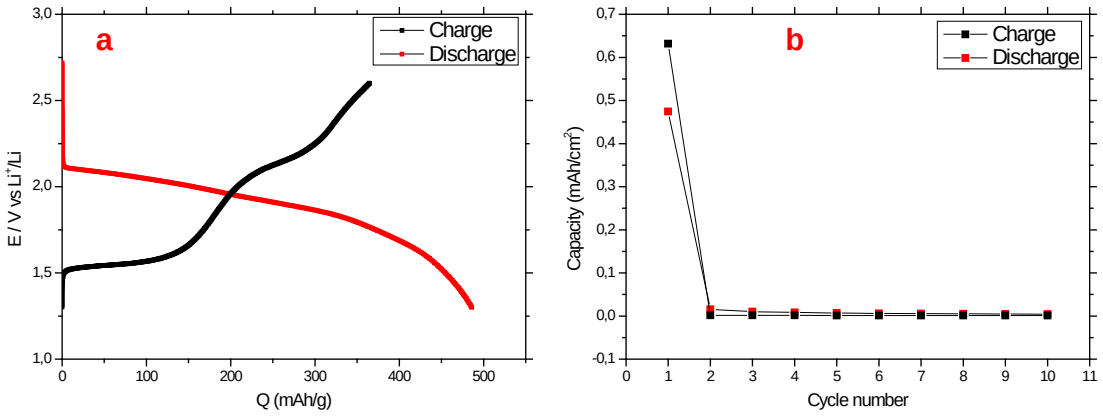

FIGURE 5.2: **a) Charge/ Discharge capacities of the full cell during the first cycle. b) Areal capacities of the full cell.**

General Conclusion and Perspectives

The energy storage market was increasing steadily over the last decades. The global increase of energy consumption, environmental pollution associated with the emission of CO_2 and depletion of fossil fuels have driven the development of alternative energy technologies based on renewable sources. Rechargeable lithium-ion batteries (LIBs) are considered as one of the most promising candidates for their high energy density and high operating voltage. Despite their widespread use, rechargeable LIBs face various materials and interfaces challenges that for the moment, exclude them from high power and high performance applications.

The work presented in this manuscript explored a very promising and original approach for the implementation and development of a new fabrication technique for the LIB electrodes based on the bottom-up nanostructuration principle. Applied to different active materials, in particular, sulfur and silicon nanoparticles, the emphasis was to fabricate and cycle each electrode separately (sulfur nanoparticles-decorated-carbon-nanotubes for the cathode and silicon nanoparticles-decorated-carbon-nanotubes for the anode) and evaluate its performance in front of metallic lithium. One of the challenges was to assemble the complete nanostructured battery based on the fabricated nanostructured electrodes and test its performance.

Due to their large surface area, high electrochemical accessibility, good electrical conductivity, and well-aligned directional structures, vertically aligned carbon nanotube (VACNT) carpets were the basic materials used for the fabrication of the electrodes. VACNTs help to improve the charge or ion storage and delivery in energy devices. The first part of the work was to achieve and control the synthesis of VACNTs on two different substrates, aluminum (Al) and copper (Cu). The VACNTs have been synthesized by hot filament-assisted chemical vapor deposition, directly on the current collector Al and/ or Cu. Dense and vertically aligned carbon nanotubes with different lengths were successfully prepared at low temperature (600°C). The VACNTs length was controlled

by modifying the growth time at fixed experimental conditions. The height of the nanotubes is an important parameter to be taken into account since to the specific surface area of the VACNT structure is proportional to it. By adjusting properly the growth parameters, mainly the growth time, we were able to synthesize VACNTs with varied lengths between 7 to 47 μm and diameters ranging from 2 to 5 nm. This synthesis technique has the advantage of providing direct contact of each nanotube with the Al and/or Cu macroscopic current collector, allowing for the design of the nanostructured current collector. The transport of electrons and ions was ensured throughout the electrode without the need of binders or conductive additive.

The second and most important part of the work concerns the cathode and anode nanofabrication. As a first step, the design and fabrication of the nanostructured cathode, based on sulfur as active material, was achieved. Sulfur has a theoretical specific capacity of 1675 mAh g^{-1}, that is five times higher than those of traditional transition metal oxides or phosphate. In addition, sulfur has other advantages, such as low cost and environmental safeness. However, sulfur has its own drawbacks such as low electrical conductivity, dissolution of polysulfides in the electrolyte and volume expansion of sulfur during cycling. These problems lead to poor electrochemical performances and low cycle life. To overcome these problems associated with sulfur, the use of nanomaterials and a good conductive material into the electrode are crucial. A series of experimental designs were carried out in this study to fabricate various nanomaterials, to construct and to improve the performances of sulfur cathodes for Li/S batteries. Sulfur nanoparticles (S NPs) were deposited on the VACNT carpets using two different methods: electrodeposition and physical vapor deposition (PVD). These two methods are considered to be a simple way to fabricate the sulfur electrode with the use of low cost and commercial products. The electrodeposition process was carried out by using a three electrode configuration in a working-solution composed of sodium sulfide and sulfuric acid aqueous solution. Since the electrodeposition of the S NPs was not homogeneous on all the VACNT carpet length, a second method based on a home-made ampoule system was used to improve the deposition of the S NPs. We observed that, after the sulfur evaporation, $\sim$1.0 mg cm^{-1} of sulfur loading mass was deposited on the VACNTs. A thin sulfur film on the surface of the VACNT was formed as well as evaporated S NPs encompass the whole nanotubes. The electrochemical performances of the obtained S@VACNT electrode were tested in a half coin cell. An impressive capacity of lithiation was obtained in the first cycle, very close to the theoretical capacity of sulfur. However, this capacity dropped during cycling due to the dissolution of soluble lithium polysulfides. Therefore, optimization of the electrode fabrication was indispensable. To achieve successful Li/S batteries, it is essential to trap the intermediate polysulfides effectively to improve the cycle life of the sulfur electrode. Coating is an attractive approach for sulfur cathodes

to prevent side-reaction shuttle effect. Metal oxide and conducting polymer have been employed in this work to adsorb lithium polysulfides in order to improve the elctrochemical performance of the Li/S batteries. Thin alumina (Al_2O_3) coating material for sulfur electrodes was successfully evaporated by a home-made evaporator and the polyaniline (PANI) polymer was deposited by an electrodeposition process. This approach, with Al_2O_3 and PANI coating, demonstrated a significant improved cycle stability of sulfur cathodes. The study clearly claimed thickness effect of the coating layers on the electrochemical performance of sulfur cathodes. The two electrodes Al_2O_3@S@VACNT and PANI@S@VACNT have shown high initial lithiation/ delithiation capacities and at the end of cycling they still presented a good specific capacity compared to commercial cathodes.
Besides the S@VACNT electrode, nickel-based-nanostructured cathode was fabricated in the attempt to obtain $LiNiO_2$ material. Nickel nanoparticles (Ni NPs) were deposited by a pulse electrodeposition process (PED) in a Watts bath. A homogeneous deposition was obtained on the surface and to a certain in-depth of the side-walls of the VACNTs. The XRD and TEM analyses revealed the formation of NiO_x particles. The Ni NPs were first heated under water vapor atmosphere in order to transform them to NiO_2 particles. Those particles should then be lithiated to be compatible for their use as a cathode in LIBs. However, after we characterized the post-heated sample, we found that the particles remained NiO_x and fully oxidized to NiO_2. This prevented us from performing further investigations on this Ni-based material.

As a second step in this work, the nanofabrication of the anode was achieved. Silicon has the highest theoretical specific capacity for lithium storage (3580 mAh g^{-1}, over 10 $\times$ higher than conventional graphite at 372 mAh g^{-1}), and is considered as a promising anode material to achieve high energy density required by rechargeable battery systems in the near future. There are two main challenges that impede applications of silicon as anode for LIBs: large volumetric change for silicon lithiation and delithiation (over 300 % volume change) and the solid electrolyte interphase (SEI) on silicon anodes. Silicon nanostructures have shown great potential to maintain a high capacity while accommodating repetitive volumetric change for alloying and dealloying reactions. In this work, silicon nanoparticles (Si NPs) were deposited on VACNT carpets by two different approaches: electrodeposition and CVD with the aim of creating high capacity, long life anodes for LIBs. The electrodeposition processes were established using two different methods, cycling voltammetry (CV) and PED. By applying both CV and PED techniques, the deposition of Si NPs on VACNT carpets was inhomogeneous. The electrochemical performances of the Si@VACNT obtained by CV were higher than the PED technique due to higher mass and better adhesion of the Si NPs.

In the second approach, the CVD method was used for the decoration of the VACNTs. Si NPs were deposited at different deposition duration, temperatures, and on VACNTs with different lengths. The first study was done on 4-6 μm VACNTs and at 500°C by varying the deposition time. After 15 minutes of deposition, Si NPs were formed on the side-walls of the tubes with an ellipsoidal morphology and a homogenous size between 10 to 20 nm. Increasing the deposition time to 25 minutes, the size of the particles increased up to 40 nm, and to 35 minutes, the formation of a silicon shell around the CNTs was seen. The loading mass of Si were 0.20, 1.2 and 4.5 mg cm^{-1} corresponding to 15, 25 and 35 minutes deposition duration, respectively. For the electrochemical performances, the electrodes synthesized at 15 and 25 minutes were cycled in a half coin cell up to 400 cycles. The lighter loaded electrode (15 minutes) exhibited a better cycle life compared to the higher loaded electrode (25 minutes). This implies that the Si@VACNT structure only accommodates low silicon loading, but still struggles with high silicon loading. However, the lighter loaded Si@VACNT electrode exhibited an impressive rate capability of 894 mAh g^{-1}, achieved at 8C rate, indicating that the as-fabricated electrode sustain very high C rates without structural damaging.

In order to obtain higher mass of silicon, different lengths of CNTs have been decorated with Si NPs using the same deposition time (15 minutes) and temperature (550°C). From the SEM analyses, we observed that the Si NPs covered the overall VACNTs in a homogeneous manner. We could establish that with the increase in the carpet length, the mass of silicon increased as follows: 1.50, 2.56 and 4.11 mg cm^{-2} for 7, 13 and 25 μm of CNTs, respectively. These loading masses correspond to an areal capacity of 1.6, 5.5 and 12.6 mAh cm^{-2} obtained from experiments. The 12.6 mAh cm^{-2} obtained value is three times higher than the areal capacity of commercial graphite and that of nanostructured silicon-based anodes found in literature.
A hierarchical-hybrid electrode nanostructure aims to improve the cycling performance of Si-based electrodes by accommodating silicon volume variations using the merits of VACNT carpets. These findings will hopefully contribute to bringing electrodes with higher Si content to the market, enabling batteries with improved energy density, cost and safety, all of which are essential for a society based on renewable energy sources.

The third part demonstrates a new type of rechargeable LIB containing Li_2S and Si as the active materials in the cathode and anode, respectively. The theoretical specific energy of this new battery is four times that of state-of-the art battery technology. Additionally, this new battery system will avoid the intrinsic safety issues associated with the use of metallic lithium in Li/S batteries.

Perspectives:

Several perspectives are interesting to be explored in order to extend this work.
Regarding the cathode materials, there is still plenty of room for the improvement of the electrochemical performances of the as-fabricated electrodes. The development of Li/S batteries is an important direction for the elaboration of secondary high energy batteries. Some suggestions concerning the Li/S battery are presented below:

- Improvement and control of the sulfur evaporation (in our case using the ampoule technique) in order to better control the formation of the sulfur layer.
- S@VACNTs coating (with alumina in our case) is a promising route in our opinion. The use of a cold source for the alumina coating will avoid the evaporation of S NPs encountered with the high temperature used in the previous evaporation method.
- Finally, increasing the S NPs loading mass remains one of the most important perspective. Therefore, the deposition of S on longer VACNTs can provide a higher loading mass.
- Perform in-depth studies on the chemical or physical methods that will allow us to obtain NiO_2 NPs for the possible incorporation of nickel based cathode in LIBs. For instance, perform the annealing step of the Ni NPs under oxygen atmosphere that might help in the formation of NiO_2 particles.

Concerning the anode, silicon is a promising anode material to increase the capacity of LIBs. Owing to its theoretical capacity of 3580 mAh g^{-1}, it is essential to improve the cycling performance and the cycle life of Si@VACNT nanostructured electrode in order to be able to commercialize it.
Future works can be envisioned:

- Investigate the cycle life of the Si@VACNT electrode with higher-loaded mass under which the capacity remains stable.
- Perform the rate capability for the higher loaded Si@VACNT electrode.
- Design and explore a new approach based on the deposition of Si nanowires on the sidewalls of the CNTs instead of Si NPs.

Since this work presented the first trial of using a full cell based on Li_2S@VACNT as cathode and Si@VACNT as anode, we believe that extensive work has still to be done in order to optimize the full cell performances (energy and power densities) at low and elevated temperatures. Furthermore, the thermal stability of the system needs to be characterized, as it is crucial for safety.

Finally, for all the systems, it is essential to establish a correlation between the structure of nano-composites (NPs dispersal and location) and the performances of the device (their properties and their stability during cycling). One solution for doing that relies on the implementation and the development of new *in-situ* and *in-operando* TEM observations and analyses that will give a "direct vision" on the electrochemical processes that occur during the nanostructured electrode synthesis.

Appendix A

Appendix

A.1 Scanning electron Microscopy

Scanning Electron Microscopy (SEM) is an important tool used to for observing and analyzing the topography of the surface of a material. The principle of SEM is to use a focused beam of high energy electrons, the beam hits the specimen surface, generating different types of signals including secondary electrons, back-scattered electrons, transmitted electrons, and characteristic X-rays (fluorescence). The signals that derive from electron-sample interactions can be used to reveal information about the sample's morphology. The secondary electrons are used for the observation of the samples. By scanning the sample and collecting the secondary electrons that are emitted, an image displaying the topography of the surface is created.

A.2 Transmission electron Microscopy

Transmission Electron Microscopy (TEM) has become a powerful characterization and observation technique, allowing for the exploration of matter at very high spatial resolution, down to atomic level, due to the use of fast electrons with wavelengths in the order of some hundredth of Angstrom. The characterization include: morphology, size distribution, crystalline structure, strain, defects and chemical information. The principle of TEM is based on the interaction between a strongly accelerated electron beam and the materials-samples; an interaction which is rather strong and generates a multitude of signals: passed or transmitted electrons if the sample is thin enough, electrons scattered elastically, inelastically or backscattered, photons X. By analyzing these signals, we can obtain a multitude of information on samples, concerning their shape, surface topography and possible porosity or crystallographic structure. TEM samples must be very

thin (typically, sample thickness is less than 200 nm, depending on their composition and the expected information from TEM characterization).

Figure A.1-a illustrates a simplistic representation of a transmission electron microscope with in figure A.1-b the various signals produced by the possible interactions between electrons and the material.[320] An electron beam is first generated in the part called electron gun or accelerator. The most common types of TEM have thermionic guns capable of accelerating the electrons through a selected potential difference in the range of 60-200 kV. The appropriate electron energy depends upon the nature of the specimen and the information required. For instance, if the specimen is relatively thick a very high resolution is required, it is an advantage to use much higher electron energies. Below the electron gun are two or more condenser lenses. They demagnify the beam emitted by the gun and control its diameter as it illuminates the specimen. This enables the operator to control the area of the specimen which is illuminated by the beam and thus the intensity of illumination. Below the condenser lies the specimen chamber. A very small specimen must be held in precisely the correct position inside the objective lens, but should also be capable of being moved several micrometers and tilted by large angles. The role of the objective lens is to form the first intermediate image and diffraction pattern, one or other of which is enlarged by the subsequent projector lenses and displayed on the viewing screen. The first image produced by the objective lens usually has a magnification of 50-100 times. This is further magnified by a series of intermediate and projector lenses and is finally projected onto the fluorescent screen. Some specialized microscopes have an energy filter below the specimen, which can be tuned to allow the passage of only elastically scattered electrons or electrons which have suffer a particular energy loss. This has advantage in, for example, high resolution electron microscope, since inelastic scattering degrades image quality.[321]
Nowadays the last generation electron microscopes have two different illumination modes: the Bright Field mode (BF) which corresponds to the conventional microscopy and the Scanning Transmission Electron Microscopy mode (STEM). Contrary to the TEM mode which uses a parallel beam for the image formation, in the STEM mode the electrons are focused in a small probe which rasters the sample and in each point different signals are collected by two types of detectors, i.e. the transmitted electrons using an in-axis detector and the electrons scattered under various angles using an off axis detector. In STEM mode the images resolution strongly depends on the probe size and on the shape of the studied object. The size of the probe is strongly related to the alignements of the microscope which must supply a concentrated enough and intense beam to have a good signal to noise ratio in the reordered images.

Some imaging modes used in this work are listed below:

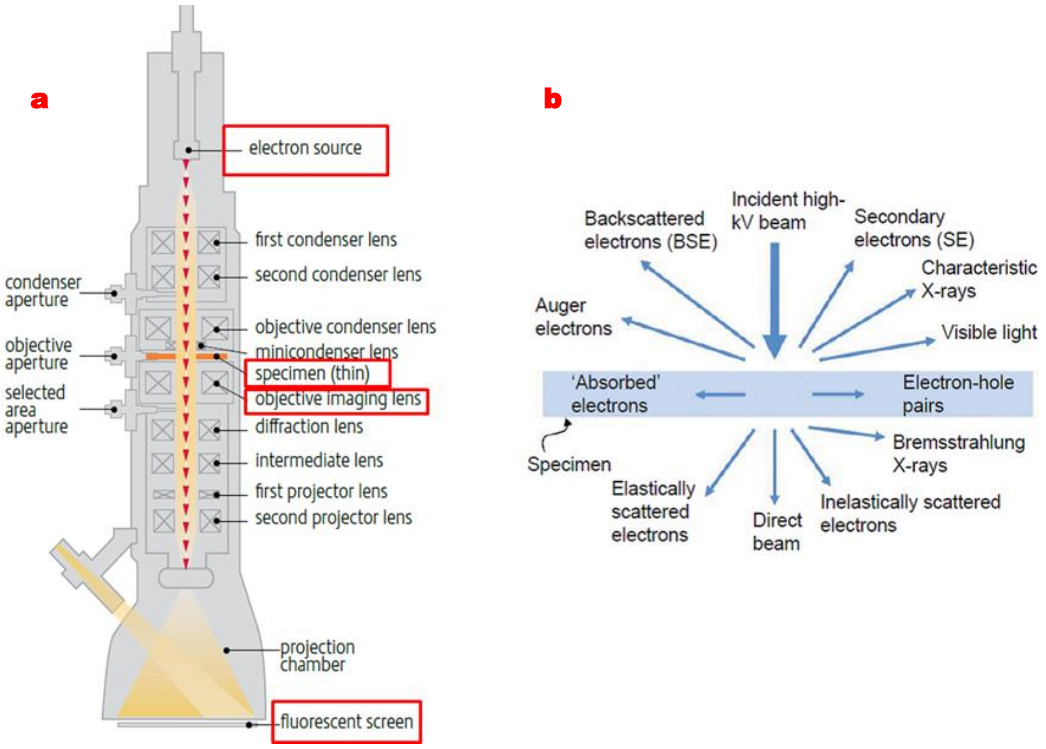

FIGURE A.1: **a) A simplistic representation of a transmission electron microscope with in (b) the various signals produced by the possible interactions between electrons and the material.**
[320]

- **High-resolution TEM (HR-TEM)**: The imaging mechanism of HR-TEM is phase contrast, which uses the interference of the transmitted beam and diffracted beams to form images at atomic level. HR-TEM is useful for the imaging of atom arrangements in projection.

- **High angle annually dark field (HAADF)-STEM imaging**: HAADF-STEM imaging collects incoherently scattered electrons at high angles to form images, which gives contrast dependent on atomic number and specimen thickness. It is also called Z contrast.

  When we use accessories to study the chemical composition of an object, we speak about analytical electronic microscopy. If we consider the plan illustrated in figure A.1-b the analytical electron microscopy uses X-rays and electrons scattered inelastically.

- **Energy-dispersive X-ray spectroscopy (EDX or EDS)**: is a powerful-yet easy to use-technique that is ideal for revealing what elements, and by inference chemical compounds, are present in a particular specimen. Basically, EDS consists of detecting the characteristic X-rays produced by each element after bombarding a sample with high energy electrons in an electron microscope.[322]

- **Electron energy loss spectroscopy (EELS)**: Only electrons with particular energy losses ("energy windows") are chosen by energy slit to form images. Since the energy losses are characteristic of the elements in the sample, EFTEM can be used for elemental/ chemical mapping. It can also be used to improve the contrast in images and diffraction patterns by removing inelastically scattered electrons.[253–256]

Appendix B

Appendix

B.1 X-ray diffraction

The X-ray diffraction (XRD) is a non-destructive and most commonly used technique which can reveal information on the crystallographic structure and the chemical composition, and the physical properties (thickness, roughness and density) of a sample. X-rays are generated from an X-ray tube when the anode material (here copper as usually used) is irradiated with a beam of high-energy electrons. The high-energy electrons are accelerated by a high voltage electric field. X-ray radiation is a type of electromagnetic wave with wavelengths of the order of 10-10 m.[323] Therefore, the X-rays can be scattered by each set of lattice planes at a characteristic angle, and the scattering patterns are related to the crystal structure of the given material. This is because each material has a set of unique d-spacing, which correspond to the XRD pattern. The Braggs law presents the diffraction condition from planes with a given d-spacing:

$$n\lambda = 2dsin\theta \tag{B.1}$$

Where n is an integer, λ is the wavelength of the incident X-ray beam, d is the distance between atomic planes in a crystal, and θ is the angle of the incidence. In simple structures, the peaks in an X-ray diffraction pattern are directly related to the atomic distances through equation B.1. Figure B.1 shows an incident X-ray beam interacting with the atoms arranged in a periodic manner. The atoms, represented as spheres in the diagram below, can be viewed as forming different sets of planes in the crystal. Here, the Braggs law illustrates that a set of parallel planes with index (hkl) and the interplanar spacing d_{hkl} produces a diffracted beam when X-rays of wavelength λ impinge upon the planes at an angle θ and are reflected at the same angle. XRD patterns are unique for compounds in terms of crystal structures and components. With the help of a

comprehensive database, the phase component along with the crystal structures of a sample can be identified.

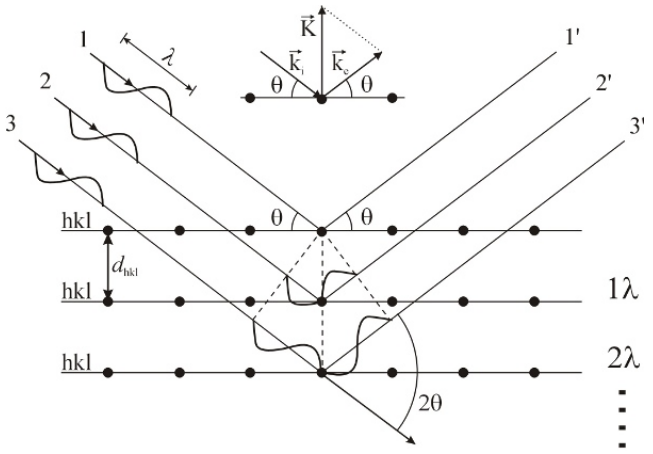

FIGURE B.1: **Schematic illustration of the Braggs law.**[323]

The Bragg-Brentano geometry (symmetric θ-θ) is classically used for XRD analysis of powder or bulk sample. In this reflection geometry, the divergent and diffracted beams are focused at a fixed radius from the sample position. In the case of thin layers, the penetration depth of X-rays mostly exceeds the thickness of the layer. This causes a large fraction of the intensity to reflect from the substrate rather than the film itself when θ-θ configuration is utilized. This technique is known as the grazing incidence X-ray diffraction (GIXRD), and it makes it possible to obtain depth-resolved structural information by probing the sample under different angles of incidence. The incident angle, denoted by ω, is fixed at a small angle (exceeding the critical angle of total reflection, typically between 0.3° and 3°). During the measurement, ω is kept constant while the detector is moved along the 2θ circle so that the angle between the sample surface and the outgoing beam is 2θ-ω. The incident beam travels on the film surface of interest, reinforcing its diffraction pattern, while the signal from the substrate is reduced or avoided due to the small angle of incidence ω (see figure B.2). This distinguishes GIXRD from the symmetric θ-θ configuration but both are coplanar configurations.[324]

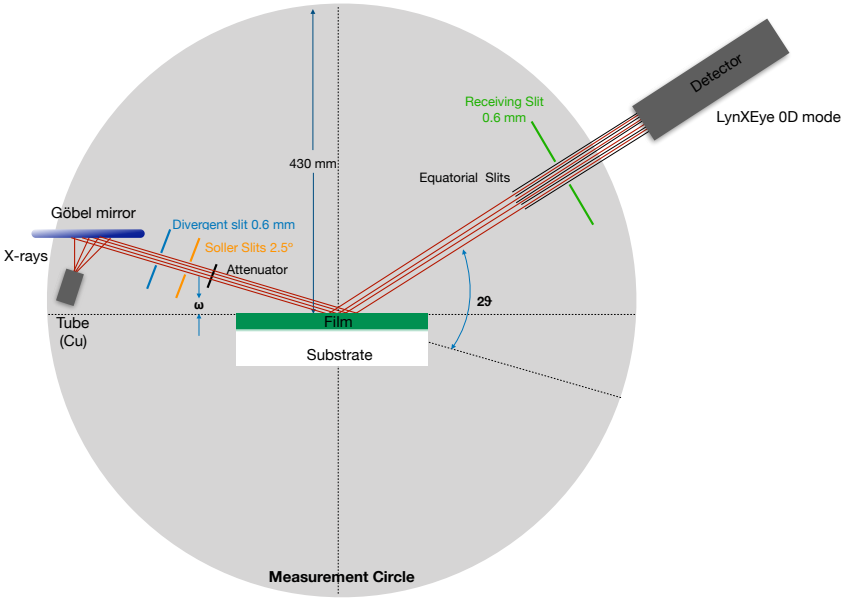

FIGURE B.2: **Schematic of GIXRD geometry.**

Appendix C

Appendix

C.1 Cyclic Voltammetry

Cyclic voltammetry (CV) is an essential technique to study the electrochemical reactions (oxidation and reduction) of the batteries. It is an electrochemical technique in which the potential of the working electrode is scanned between two potential limits at a certain scan rate. The current is recorded and the voltammogram is the representation of the current vs. the applied potential. The potential is applied with respect to a reference electrode and the current is measured between the working electrode and the counter electrode. CV scan starts with a current at zero flow. During the sweep scan, the analytes that can reduce (oxidize, depending on sweep direction) will produce a current over a range of potential. This technique is very useful for studying electrochemical processes (i.e. reduction and oxidation reactions) which occur in a battery and it provides information about the potentials at which the reactions take place within a given electrochemical window.[300]

C.2 Galvanostatic cycling

For Li-ion batteries, Galvanostatic Cycling with Potential Limitation (GCPL) is a commonly used technique to determine the specific capacity, cycling performance and Coulombic efficiency of electrode materials. The capacity is generally derived from the current (A or mA) and the time (h), and the unit of capacity is Ah or mAh. GCPL measurements are normally conducted by applying a constant current density defined as C-rate. The lithiation/ delithiation capacity can be calculated by the equation given below:

$$Q = I \times t \tag{C.1}$$

where I is the current density and t is the time of completion of one cycle.[300]

Résumé de la thèse

Grâce à leurs hautes densités d'énergie et de puissance, les batteries Lithium-Ion (LIBs) sont l'un des meilleurs candidats pour le stockage d'énergie à grande échelle dans les systèmes d'énergie renouvelable et les véhicules électriques. Cependant, l'état actuel de la technologie lithium-ion ne répond pas aux exigences de puissance et de sécurité d'usage requises pour ces applications. Il est bien connu que la performance d'une LIB dépend fortement du choix des matériaux d'électrode. Afin de développer des batteries à fortes densités d'énergie et de puissance, des matériaux d'électrode innovants doivent être développés pour répondre aux critères suivants: forte abondance naturelle, faible coût, respect de l'environnement, grande capacité de stockage et une bonne cyclabilité. Le soufre (S) et le silicium (Si) sont tous les deux les matériaux théoriquement les plus prometteurs respectivement pour la cathode et l'anode car ayant les capacités théoriques les plus élevées (1675 mAh g^{-1} et respectivement 3580 mAh g^{-1}). Néanmoins, leur utilisation pratique dans les LIBs est limitée à ce jour. En effet, le Souffre présente un caractère isolant et est sujet à la dissolution des polysulfures dans l'électrolyte généré pendant le cyclage. Le Silicium quant à lui subit d'importantes variations de volume lors du cyclage qui impactent la durée de vie de ces électrodes. L'un des moyens de surmonter ces défis est d'utiliser des matériaux nanostructurés.

Cette thèse est consacrée à la fabrication ascendante (bottom-up) de matériaux nanostructurés hybrides hiérarchisés à base de nanotubes de carbone alignés verticalement (VACNTs) décorés par des nanoparticules (NPs). En fonction de leur utilisation comme cathode ou anode, des nanoparticules de S ou Si ont été déposées. En raison de leur structure unique et de leurs propriétés électroniques, les VACNTs agissent comme une matrice de support et un excellent collecteur de courant, améliorant ainsi les voies de transport électroniques et ioniques. La nanostructuration et le contact du soufre avec un matériau hôte conducteur améliore sa conductivité, tandis que la nanostructuration du silicium permet d'accommoder plus facilement les variations de volume pendant les réactions électrochimiques. Dans la première partie de la thèse, nous avons synthétisé des VACNTs par une méthode de dépôt chimique en phase vapeur (HF-CVD) directement sur des fines feuilles commerciales d'aluminium et de cuivre sans aucun prétraitement

des substrats. Dans la deuxième partie, nous avons décoré les parois latérales des VACNTs avec différents matériaux d'électrode, dont des nanoparticules de S et de Si. Nous avons également déposé et caractérisé des nanoparticules de nickel (Ni) sur les VACNTs en tant que matériaux alternatifs pour l'électrode positive. Aucun additif conducteur ou aucun liant polymère n'a été ajouté à la composition d'électrode. La décoration des nanotubes de carbone a été effectuée par deux méthodes différentes: méthode humide par électrodéposition et méthode sèche (par dépôt physique en phase vapeur (PVD) ou par CVD). Les structures hybrides obtenues ont été testées électrochimiquement séparément dans une pile bouton contre une contre-électrode de lithium. A notre connaissance, il s'agit de la première étude de l'évaporation du soufre sur les VACNTs et de la structure résultante (appelée ici S@VACNTs). Des essais préliminaires sur les cathodes nanostructurées obtenues (S@VACNTs revêtus d'alumine ou de polyaniline) ont montré qu'il est possible d'atteindre une capacité spécifique proche de la capacité théorique du soufre. La capacité surfacique de S@VACNTs, avec une masse de S de 0.76 mg cm^{-2}, à un régime C/20 atteint une capacité de 1.15 mAh cm^{-2} au premier cycle. Pour les anodes nanostructurées au silicium (Si@VACNTs), avec une masse de Si de 4.11 mg cm^{-2}, on montre une excellente capacité surfacique de 12.6 mAh cm^{-2}, valeur la plus élevée pour les anodes à base de silicium nanostructurées obtenues jusqu'à présent. Dans la dernière partie de la thèse, les électrodes nanostructurées fabriquées ont été assemblées afin de réaliser la batterie complète (Li_2S/Si) et sa performance électrochimique a été testée. Les capacités surfaciques obtenues pour les électrodes nanostructurées de S et de Si ouvrent la voie à la réalisation d'une LIB à haute densité d'énergie, entièrement nanostructurée, et démontrent le grand potentiel du concept proposé à base d'électrodes nanostructurées hybrides hiérarchisées.

Bibliography

[1] N. S. Lewis and G. Crabtree. Basic research needs for solar energy utilization. Technical report, Department of energy, Washington, DC, 2005.

[2] International Energy Outlook 2016 U.S. Energy Information Administration. EIA projects 48% increase in world energy consumption by 2040., 2016.

[3] D. B. Botkin and D. Perez. *Powering the future: a scientist's guide to energy independence.* 2010.

[4] UNEP. Towards a green economy: pathways to sustainable development and poverty eradication. Technical report, Nairobi, Kenya, 2011.

[5] K. Tomabechi. Energy resources in the future. *Energies*, 3:686–695, 2010.

[6] H. Ibrahim, A. Ilinca, and J. Perron. Energy storage systems- Characteristics and comparisons. *Renew. Sust. Energy Rev*, 12:1221–1250, 2008.

[7] X. Luo, J. Wang, M. Dooner, and J. Clarke. Overview of current development in electrical energy storage technologies and the application potential in power system operation. *Appl. Energy*, 137:511–536, 2015.

[8] C. Liu, F. Li, LP. MA, and HM. Cheng. Advanced materials for energy storage. *Adv. Mater.*, 22:E28–E62, 2010.

[9] M. J. Pitkethly. Nanomaterials the driving force. *Nano Today*, 7:20–29, 2004.

[10] K. Candace, M. T. McDowell, and Y. Cui. Silicon nanowire electrodes for lithium-ion battery negative electrodes. In R. Yazami, editor, *Nanomaterials for Lithium-Ion Batteries: Fundamentals and Applications*, pages 2–62. USA, 2014.

[11] G. Pancaldi. On hybrid objects and their trajectories: Beddoes, Davy and the Battery. *Notes Rec. R. Soc.*, 63:247–262, 2009.

[12] A. Leblanc-Soreau, M. Dannot, L. Trichet, and J. Rouxel. Les intercalaires A_xTiS_2 et A_xZrS_2. Structure et liaisons. (A = Li, Na, K, Rb, Cs). *Mat. Res. Bull*, 9:191–198, 1974.

[13] M. S. Whittingham. Electrical energy storage and intercalation chemistry. *Science*, 192:1126–1127, 1976.

[14] M. S. Whittingham and F. R. Gamble. The lithium intercalates of the transition metal dichalcogenides. *Mat. Res. Bull*, 10:363–371, 1975.

[15] M. Armand, L. M. Chabagno, and M. J. Duclot. Second International Meeting on Solid Electrolytes, St Andrews, Scotland. 1978.

[16] M. Armand and D. W. Murphy. Materials for Advanced Bateries, Plenum Press, New York. 1980.

[17] M. Lazzari and B. Scrosati. A cyclable lithium organic electrolyte cell based on two intercalation electrodes. *J. Electrochem. Soc.*, 127:773–774, 1980.

[18] H. Wu and Y. Cui. Designing nanostructured Si anodes for high energy lithium ion batteries. *Nano Today*, 7:414–429, 2012.

[19] D. Linden and T.-B. Reddy. *Handbook of batteries, McGraw-Hill, New York*. 2002.

[20] J.-M Tarascon and M. Armand. Issues and challenges facing rechargeable lithium batteries. *Nature*, 414:359–367, 2001.

[21] B. Diouf and R. Pode. Potential of lithium-ion batteries in renewable energy. *Renew energ*, 76:375–380, 2015.

[22] B. Dunn, H. Kamath, and JM. Tarascon. Electrical energy storage for the grid: a battery of choices. *Science*, 334:928–935, 2011.

[23] B. Xu, D. Qian, Z. Wang, and S.M. Ying. Recent progress in cathode materials research for advanced lithium ion batteries. *Mater. Sci. Eng., R*, 73:51–65, 2012.

[24] K. Mizushima, P.C. Jones, P.J. Wiseman, and J.B. Goodenough. $LixCoO_2$ ($0< x <-1$): A new cathode material for batteries of high energy density. *Mat. Res. Bull*, 15:783–789, 1980.

[25] N. Nitta, F. Wu, J.T. Lee, and G. Yushin. Li-ion battery materials: present and future. *Mater. Today*, 18:252–264, 2015.

[26] T. Ohzuku and A. Ueda. Solidstate Redox reactions of $LiCoO_2$ (R3m) for 4 Volt secondary lithium cells. *J. Electrochem. Soc.*, 141:2972–2977, 1994.

[27] A. K. Padhi, K. S. Nanjundaswamy, and J. B. Goodenough. Phospho-olivines as positive-electrode materials for rechargeable lithium batteries. *J. Electrochem. Soc.*, 144:1188–1194, 1997.

[28] J. Morales, C. Pérez-Vicente, and J.L. Tirado. Cation distribution and chemical deintercalation of $Li_{1-x}Ni_{1+x}O_2$. *Mat. Res. Bull*, 25:623–630, 1990.

[29] M. M. Thackeray, W. I F David, P. G. Bruce, and J. B. Goodenough. Lithium insertion into manganese spinels. *Mat. Res. Bull*, 18:461–472, 1983.

[30] J. Cho and M. M. Thackeray. Structural changes of LiMn2O4 Spinel electrodes during electrochemical cycling. *J. Electrochem. Soc.*, 146:3577–3581, 1999.

[31] Y. Shin and A. Manthiram. Factors influencing the capacity fade of spinel lithium manganese oxides. *J. Electrochem. Soc.*, 151:A204–A208, 2004.

[32] Y.-K. Sun, K.-J. Hong, and J. Prakash. The effect of ZnO coating on electrochemical cycling behavior of spinel $LiMn_2O_4$ cathode materials at elevated temperature. *J. Electrochem. Soc.*, 150:A970–A972, 2003.

[33] H. Huang, S.-C. Yin, and L. F. Nazar. Approaching theoretical capacity of $LiFePO_4$ at room temperature at high rates. *Electrochem. Solid-State Lett.*, 4:A170–A172, 2001.

[34] X. Ji, K. T. Lee, and L. F. Nazar. A highly ordered nanostructured carbonsulphur cathode for lithiumsulphur batteries. *Nat. Mater.*, 8:500–506, 2009.

[35] W. Xu, J. Wang, F. Ding, X. Chen, E. Nasybulin, Y. Zhang, and J. G. Zhang. Lithium metal anodes for rechargeable batteries. *Energy Environ. Sci.*, 7:513–537, 2014.

[36] K. Xu. Nonaqueous liquid electrolytes for lithium-based rechargeable batteries. *Chem. Rev.*, 104:4303–4417, 2004.

[37] C. S. Wang, G. T. Wu, and W. Z. Li. Lithium insertion in ball-milled graphite. *J. Power Sources*, 76:1–10, 1998.

[38] D. Guerard and A. Herold. Intercalation of lithium into graphite and other carbons. *Carbon*, 13:337–345, 1975.

[39] Y. Ein-Eli. A new perspective on the formation and structure of the Solid Electrolyte Interface at the graphite anode of Li-ion cells. *Electrochem. Solid-State Lett.*, 2:212–214, 1999.

[40] S. J. An, J. Li, C. Daniel, D. Mohanty, S. Nagpure, and D. L. Wood. The state of understanding of the lithium-ion-battery graphite solid electrolyte interphase (SEI) and its relationship to formation cycling. *Carbon*, 105:52–76, 2016.

[41] T. Ohzuku, A. Ueda, and N. Yamamoto. ZeroStrain Insertion Material of $Li[Li_{1/3}Ti_{5/3}]O_4$ for rechargeable lithium cells. *J. Electrochem. Soc.*, 142:1431–1435, 1995.

[42] K. Ariyoshi, R. Yamato, and T. Ohzuku. Zero-strain insertion mechanism of $Li[Li_{1/3}Ti_{5/3}]O_4$ for advanced lithium-ion (shuttlecock) batteries. *Electrochim. Acta*, 51:1125–1129, 2005.

[43] L. Zhao, Y.-S. Hu, H. Li, Z. Wang, and L. Chen. Porous $Li_4Ti_5O_{12}$ coated with N-doped carbon from ionic liquids for Li-ion batteries. *Adv. Mater.*, 23:1385–1388, 2011.

[44] Y. Ma, B. Ding, G. Ji, and J. Y. Lee. Carbon-encapsulated F-doped $Li_4Ti_5O_{12}$ as a high rate anode material for Li^+ batteries. *ACS NANO*, 7:10870–10878, 2013.

[45] K. Zaghib, M. Dontigny, A. Guerfi, J. Trottier, J. Hamel-Paquet, V. Gariepy, K. Galoutov, P. Hovington, A. Mauger, H. Groult, and C. M. Julien. An improved high-power battery with increased thermal operating range: C-$LiFePO_4$//C-$Li_4Ti_5O_{12}$. *J. Power Sources*, 216:192–200, 2012.

[46] W.-J. Zhang. A review of the electrochemical performance of alloy anodes for lithium-ion batteries. *J. Power Sources*, 196:13–24, 2011.

[47] C.-M. Park, J.-H. Kim, H. Kim, and H.-J Sohn. Li-alloy based anode materials for Li secondary batteries. *Chem. Soc. Rev.*, 39:3115–3141, 2010.

[48] R. Teki, M.-K. Datta, R. Krishnan, T.-C. Parker, T.-M. Lu, P.-N. Kumta, and N. Koratkar. Nanostructured silicon anodes for lithium ion rechargeable batteries. *Small*, 5:2236–2242, 2009.

[49] H. Wu, G. Zheng, N. Liu, T.-J. Carney, Y. Yang, and Y. Cui. Engineering empty space between Si nanoparticles for lithium-ion battery anodes. *Nano Lett.*, 12:904–909, 2012.

[50] P. Poizot, S. Laruelle, S. Grugeon, L. Dupont, and J-M. Tarascon. Nano-sized transition-metal oxides as negative-electrode materials for lithium-ion batteries. *Nature*, 407:496–499, 2000.

[51] J. Cabana, L. Monconduit, D. Larcher, and M.-R. Palacin. Beyond intercalation-based Li-ion batteries: the state of the art and challenges of electrode materials reacting through conversion reactions. *Adv. Mater.*, 22:E170–E192, 2010.

[52] L. Xu and B. Lu. 3D-Frame structure NiO@CNTs for ultrafast charge slow discharge lithium ion batteries. *Electrochim. Acta*, 210:456–461, 2016.

[53] J.-B. Goodenough and Y. Kim. Challenges for rechargeable Li batteries. *Chem. Mater*, 22:587–603, 2010.

[54] V. Etacheri, R. Marom, R. Elazari, G. Salitra, and D. Aurbach. Challenges in the development of advanced Li-ion batteries: a review. *Energy Environ. Sci.*, 4:3243–3262, 2011.

[55] Q. Li, J. Chen, L. Fan, X. Kong, and Y. Lu. Progress in electrolytes for rechargeable Li-based batteries and beyond. *Green Energy & Environment*, 1:18–42, 2016.

[56] D. Aurbach, K. Gamolsky, B. Markovsky, Y. Gofer, M. Schmidt, and U. Heider. On the use of vinylene carbonate (VC) as an additive to electrolyte solutions for Li-ion batteries. *Electrochim. Acta*, 47:1423–1439, 2002.

[57] L. Chen, K. Wang, X. Xie, and J. Xie. Effect of vinylene carbonate (VC) as electrolyte additive on electrochemical performance of Si film anode for lithium ion batteries. *J. Power Sources*, 174:538–543, 2007.

[58] T. Jaumann, J. Balach, U. Langklotz, V. Sauchuk, M. Fritsch, A. Michaelis, V. Teltevskij, D. Mikhailova, S. Oswald, M. Klose, G. Stephani, R. Hauser, J. Eckert, and L. Giebeler. Lifetime vs. rate capability: Understanding the role of FEC and VC in high energy Li-ion batteries with nano-silicon anodes. *Energy Storage Materials*, 6:26–35, 2017.

[59] N.-S. Choi, K.-H. Yew, K.-Y. Lee, M. Sung, H. Kim, and S.-S. Kim. Effect of fluoroethylene carbonate additive on interfacial properties of silicon thin-film electrode. *J. Power Sources*, 161:1254–1259, 2006.

[60] Y.-M. Lin, K.-C. Klavetter, P.-R. Abel, N.-C. Davy, J.-L. Snider, A. Heller, and C.-B. Mullins. High performance silicon nanoparticle anode in fluoroethylene carbonate-based electrolyte for Li-ion batteries. *Chem. Commun.*, 48:7268–7270, 2012.

[61] N. Angulakshmi and A. M. Stephan. Efficient electrolytes for lithium-sulfur batteries. *Front. Energy Res.*, 3:17, 2015.

[62] D. Aurbach. Review of selected electrode-solution interactions which determine the performance of Li and Li ion batteries. *J. Power Sources*, 89:206–218, 2000.

[63] E. Peled. The electrochemical behavior of alkali and alkaline earth metals in nonaqueous battery systemsthe Solid Electrolyte Interphase model. *J. Electrochem. Soc.*, 126:2047–2051, 1979.

[64] M. Gauthier, T.-J. Carney, A. Grimaud, L. Giordano, N. Pour, H.-H. Chang, D.-P. Fenning, S.-F. Lux, O. Paschos, C. Bauer, F. Maglia, S. Lupart, P. Lamp, and Y. Shao-Horn. ElectrodeElectrolyte Interface in Li-ion batteries: current understanding and new insights. *J. Phys. Chem. Lett.*, 6:4653–4672, 2015.

[65] Cornelia Breitkopf and Karen Swider-Lyons. *Springer handbook of electrochemical energy.* 2017.

[66] A. H. Whitehead and M. Schreiber. Current collectors for positive electrodes of lithium-based batteries. *J. Electrochem. Soc.*, 152:A2105–A2113, 2005.

[67] S-T. Myung, Y. Hitoshi, and Y-K. Sun. Electrochemical behavior and passivation of current collectors in lithium-ion batteries. *J. Mater. Chem.*, 21:9891–9911, 2011.

[68] A. N. Dey. Electrochemical alloying of lithium in organic electrolytes. *J. Electrochem. Soc.*, 118:1547–1549, 1971.

[69] S. W. Kim and K. Y. Cho. Current collectors for flexible lithium ion batteries: A review of materials. *J. Electrochem. Sci. Technol.*, 6:10–15, 2015.

[70] W. Wang and P.-N. Kumta. Nanostructured hybrid silicon/carbon nanotube heterostructures: reversible high-capacity lithium-ion anodes. *ACS NANO*, 4:2233–2241, 2010.

[71] W. Wang, R. Epur, and P.-N. Kumta. Vertically aligned silicon/carbon nanotube (VASCNT) arrays: Hierarchical anodes for lithium-ion battery. *Electrochem. Commun.*, 13:429–432, 2011.

[72] A. Gohier, B. Laik, K-H Kim, J-L Maurice, J-P. Pereira-Ramos, C. S. Cojocaru, and P. Tran Van. High-rate capability silicon decorated vertically aligned carbon nanotubes for li-ion batteries. *Adv. Mater.*, 24:2592–2597, 2012.

[73] R. Epur, M. Ramanathan, M. K. Datta, D. H. Hong, P. H. Jampani, B. Gattu, and P.-N. Kumta. Scribable multi-walled carbon nanotube-silicon nanocomposite: A viable lithium-ion battery system. *Nanoscale*, 7:3504–3510, 2015.

[74] I. Lahiri and W. Choi. Carbon nanostructures in Lithium ion batteries: past, present, and future. *Crit. Rev. Solid State Mater. Sci.*, 38:128–166, 2013.

[75] A.-S. Arico, P. Bruce, B. Scrosati, J.-M. Tarascon, and W. van Schalkwijk. Nanostructured materials for advanced energy conversion and storage devices. *Nat. Mater.*, 4:366–377, 2005.

[76] Y.-G. Guo, J.-S. Hu, and L.-J. Wan. Nanostructured materials for electrochemical energy conversion and storage devices. *Adv. Mater.*, 20:2878–2887, 2008.

[77] Y. Wang, H. Li, P. He, E. Hosono, and H. Zhou. Nano active materials for lithium-ion batteries. *Nanoscale*, 2:1294–1305, 2010.

[78] P. Roy and S. K. Srivastava. Nanostructured anode materials for lithium ion batteries. *J. Mater. Chem. A,*, 3:2454–2484, 2015.

[79] N. Meethong, H.-Y.S. Huang, S. A. Speakman, W. C. Carter, and Y.-M. Chiang. Strain accommodation during phase transformations in olivine-based cathodes as a materials selection criterion for high-power rechargeable batteries. *Adv. Funct. Mater*, 17:1115–1123, 2007.

[80] K.-T. Lee and J. Cho. Roles of nanosize in lithium reactive nanomaterials for lithium ion batteries. *Nano Today*, 6:28–41, 2011.

[81] P. Balaya, A. J. Bhattacharyya, J. Jamnik, Yu. F. Zhukovskii, E. A. Kotomin, and J. Maier. Nano-ionics in the context of lithium batteries. *J. Power Sources*, 159:171–178, 2006.

[82] P.-G. Bruce, B. Scrosati, and J.-M. Tarascon. Nanomaterials for rechargeable lithium batteries. *Angew. Chem. Int. Ed*, 47:2930–2946, 2008.

[83] J. Yang, M. Winter, and J. O. Besenhard. Small particle size multiphase Li-alloy anodes for lithium-ion batteries. *Solid State Ion.*, 90:281–287, 1996.

[84] C.-K. Chan, H. Peng, G. Liu, K. McIlwrath, X.-F. Zhang, R.-A. Huggins, and Y. Cui. High-performance lithium battery anodes using silicon nanowires. *Nat. Nanotech.*, 3:31–35, 2008.

[85] A. Aqel, K. M. M. Abou El-Nour, R. A. A. Ammar, and A. Al-Warthan. Carbon nanotubes, science and technology part (I) structure, synthesis and characterisation. *Arabian J. Chem.*, 5:1–23, 2012.

[86] Y. Guo and W. A. Goddard. Is carbon nitride harder than diamond? No, but its girth increases when stretched (negative Poisson ratio). *Chem. Phys. Lett.*, 237:72–76, 1995.

[87] Hugh O Pierson. *Handbook of carbon, graphite, diamond and fullerenes properties, processing and applications.* 1993.

[88] H. W. Kroto, J. R Heath, S. C. O'brien, R. F. Curl, and R. E. Smalley. C_{60}: Buckminsterfullerene. *Nature*, 318:162–163, 1985.

[89] M. Monthioux and V. L. Kuznetsov. Who should be given the credit for the discovery of carbon nanotubes? *Carbon*, 44:1621–1623, 2006.

[90] S. Iijima. Helical microtubules of graphitic carbon. *Nature*, 354:56–58, 1991.

[91] S. Iijima and T. Ichihashi. Single-shell carbon nanotubes of 1-nm diameter. *Nature*, 363:603–605, 1993.

[92] D. S. Bethune, C. H. Kiang, M. S. De Vries, G. Gorman, R. Savoy, J. Vazquez, and R. Beyers. Cobalt-catalysed growth of carbon nanotubes with single-atomic-layer walls. *Nature*, 363:605–607, 1993.

[93] A. Eatemadi, H. Daraee, H. Karimkhanloo, M. Kouhi, N. Zarghami, A. Akbarzadeh, M. Abasi, Y. Hanifehpour, and S. W. Joo. Carbon nanotubes: properties, synthesis, purification, and medical applications. *Nanoscale Res. Lett.*, 9, 2014.

[94] M.S. Dresselhaus, G. Dresselhaus, and R. Saito. Physics of carbon nanotubes. *Carbon*, 33:883–891, 1995.

[95] S. Frank, P. Poncharal, Z. L. Wang, and W. A. de Heer. Carbon nanotube quantum resistors. *Science*, 280:1744–1746, 1998.

[96] H.-Y. Chiu, V. V. Deshpande, H. W. Ch. Postma, C. N. Lau, C. Mikó, L. Forró, and M. Bockrath. Ballistic phonon thermal transport in multiwalled carbon nanotubes. *Phys. Rev. Lett.*, 95:226101, 2005.

[97] Z. Yao, C. L. Kane, and C. Dekker. High-field electrical transport in single-wall carbon nanotubes. *Phys. Rev. Lett.*, 84:2941–2944, 2000.

[98] P. R. Bandaru. Electrical properties and applications of carbon nanotube structures. *J. Nanosci. Nanotechnol*, 7:1239–1267, 2007.

[99] Ch. Laurent, E. Flahaut, and A. Peigney. The weight and density of carbon nanotubes versus the number of walls and diameter. *Carbon*, 48:2994–2996, 2010.

[100] E. W. Wong, P. E. Sheehan, and C. M. Lieber. Nanobeam mechanics: elasticity, strength, and toughness of nanorods and nanotubes. *Science*, 277:1971–1975, 1997.

[101] F. Li, H. M. Cheng, S. Bai, and G. Su. Tensile strength of single-walled carbon nanotubes directly measuredfrom their macroscopic ropes. *Appl. Phys. Lett.*, 77:3161–3163, 2000.

[102] S. Iijima, C. Brabec, A. Maiti, and J. Bernholc. Structural flexibility of carbon nanotubes. *J. Chem. Phys.*, 104:2089–2092, 1996.

[103] S. Berber, Y-K. Kwon, and D. Tomanek. Unusually high thermal conductivity of carbon nanotubes. *Phys. Rev. Lett.*, 84:4613–4616.

[104] E. T. Thostenson, C. Li, and T-W. Chou. Nanocomposites in context. *Compos. Sci. Technol.*, 65:491–516, 2005.

[105] B. J. Landi, M. J. Ganter, C. D. Cress, R. A. DiLeo, and R. P. Raffaelle. Carbon nanotubes for lithium ion batteries. *Energy Environ. Sci.*, 2:638–654, 2009.

[106] J. Zhang, C. Yang, Y. Wang, T. Feng, W. Yu, J. Jiang, X. Wang, and X. Liu. Improvement of the field emission of carbon nanotubes by hafnium coating and annealing. *Nanotechnology*, 17:257–260, 2006.

[107] E. Bekyarova, M. Davis, T. Burch, M. E. Itkis, B. Zhao, S. Sunshine, and R. C. HAddon. Chemically functionalized single-walled carbon nanotubes as ammonia sensors. *J. Phys. Chem. B*, 108:19717–19720, 2004.

[108] F. Valentini, S. Orlanducci, E. Tamburri, M. L. Terranova, A. Curulli, and G. Palleschi. Single-walled carbon nanotubes on tungsten wires: a new class of microelectrochemical sensors. *Electroanalysis*, 17:28–37, 2005.

[109] M. Yang, Y. Yang, Y. Liu, G. Shen, and R. Yu. Platinum nanoparticles-doped sol-gel/carbon nanotubes composite electrochemical sensors and biosensors. *Biosens. Bioelectron.*, 21:1125–1131, 2006.

[110] C. Qiu, Z. Zhang, M. Xiao, Y. Yang, D. Zhong, and L-M. Peng. Scaling carbon nanotube complementary transistors to 5-Nm gate lengths. *Science*, 355:271–276.

[111] E. Frackowiak, S. Gautier, H. Gaucher, S. Bonnamy, and F. Beguin. Electrochemical storage of lithium in multiwalled carbon nanotubes. *Carbon*, 37:61–69, 1999.

[112] Z. Xiong, Y.S. Yun, and H-J. Jin. Applications of carbon nanotubes for lithium ion battery anodes. *materials*, 6:1138–1158, 2013.

[113] E. Frackowiak, K. Metenier, V. Bertagna, and F. Beguin. Supercapacitor electrodes from multiwalled carbon nanotubes. *Appl. Phys. Lett.*, 77:2421–2423, 2000.

[114] N. Rajalakshmi, K.S. Dhathathreyan, A. Govindaraj, and B. C. Satishkumar. lectrochemical investigation of single-walled carbon nanotubes for hydrogen storage. *Electrochim. Acta*, 45:4511–4515, 2000.

[115] M. B. Jakubinek, B. Ashrafi, Y. Zhang, Y. Martinez-Rubi, C. T. Kingston, A. Johnston, and B. Simard. Single-walled carbon nanotubeepoxy composites for structural and conductive aerospace adhesives. *Composites Part B*, 69:87–93, 2015.

[116] C. Kingston, R. Zepp, A. Andrady, D. Boverhof, R. Fehir, D. HAwkins, J. Roberts, P. Sayre, B. Shelton, Y. Sultan, V. Vejins, and W. Wohlleben. Release characteristics of selected carbon nanotube polymer composites. *Carbon*, 68:33–57, 2014.

[117] B. Jin, H-B. Gu, W. Zhang, K-H PArk, and G. Sun. Effect of different carbon conductive additives on electrochemical properties of $LiFePO_4$-C/Li batteries. *J Solid State Electrochem*, 12:1549–1554, 2008.

[118] H. Zhang, G. Cao, Z. Wang, Y. Yang, Z. Shi, and Z. Gu. Carbon nanotube array anodes for high-rate Li-ion batteries. *Electrochim. Acta*, 55:2873–2877, 2010.

[119] J. Lee, J. Bae, J. Heo, I. T. Han, S. N. Cha, D. K. Kim, M. Yang, H. S. Han, W. S. Jeon, and J. Chung. Effect of randomly networked carbon nanotubes in silicon-based anodes for lithium-ion batteries. *J. Electrochem. Soc.*, 156:A905–A910, 2009.

[120] W. Guoping, Z. Qingtang, Y. Zuolong, and Q. MeiZheng. The effect of different kinds of nano-carbon conductive additives in lithium ion batteries on the resistance and electrochemical behavior of the $LiCoO_2$ composite cathodes. *Solid State Ion.*, 179:263–268, 2008.

[121] X. Li, F. Kang, X. Bai, and W. Shen. A novel network composite cathode of $LiFePO_4$/multiwalled carbon nanotubes with high rate capability for lithium ion batteries. *Electrochem. Commun.*, 9:663–666, 2007.

[122] Y-H Ding, G-L Huang, H-H Li, H-M Xie, H-Z Sun, and J-P Zhang. Double carbon nano coating of $LiFePO_4$ cathode material for high performance of lithium ion batteries. *J Nanosci Nanotechnol*, 15:9630–9635, 2015.

[123] X-M Liu, Z-D Huang, S. Oh, P-C MA, P. C. H. Chan, G. K. Vedam, K. Kang, and J-K Kim. Solgel synthesis of multiwalled carbon nanotube-$LiMn_2O_4$ nanocomposites as cathode materials for Li-ion batteries. *J. Power Sources*, 195:4290–4296, 2010.

[124] B. Gao, A. Kleinhammes, X.P. Tang, C. Bower, L. Fleming, Y. Wu, and O. Zhou. Electrochemical intercalation of single-walled carbon nanotubes with lithium. *Chem. Phys. Lett.*, 307:153–157, 1999.

[125] N. A. Kaskhedikar and J. Maier. Lithium storage in carbon nanostructures. *Adv. Mater.*, 21:2664–2680, 2009.

[126] T. P Kumar, R. Ramesh, Y. Y. Lin, and G. T-K Fey. Tin-filled carbon nanotubes as insertion anode materials for lithium-ion batteries. *Electrochem. Commun.*, 6:520–525, 2004.

[127] C. de las Casas and W. Li. A review of application of carbon nanotubes for lithium ion battery anode material. *J. Power Sources*, 208:74–85, 2012.

[128] S. Yehezkel, M. Auinat, N. Sezin, D. Starosvetsky, and Y. Ein-Eli. Bundled and densified carbon nanotubes (CNT) fabrics as flexible ultra-light weight Li-ion battery anode current collectors. *J. Power Sources*, 312:109–115, 2016.

[129] K. Wang, S. Luo, Y. Wu, X. He, F. Zhao, J. Wang, K. Jiang, and S. Fan. Super-aligned carbon nanotube films as current collectors for lightweight and flexible lithium ion batteries. *Adv. Funct. Mater*, 23:846–853, 2013.

[130] E. T. Thostenson, Z. Ren, and T-W. Chou. Advances in the science and technology of carbon nanotubes and their composites: a review. *Compos. Sci. Technol.*, 61:1899–1912, 2001.

[131] Mukul Kumar. *Carbon nanotube synthesis and growth mechanism*, volume 6. 2010.

[132] C. Journet, W. M. Maser, P. Bernier, A. Loiseau, M. Lamy de la Chapelle, S. Lefrant, P. Deniard, R. Lee, and J. E. Fisher. Large-scale production of single-walled carbon nanotubes by the electric-arc technique. *Nature*, 388:756–758, 1997.

[133] C. Journet and P. Bernier. Production of carbon nanotubes. *Appl. Phys. A*, 67:1–10, 1998.

[134] E. F. Kukovitsky, S. G. L'vov, and N. A. Sainov. VLS-growth of carbon nanotubes from the vapor. *Chem. Phys. Lett.*, 317:65–70, 2000.

[135] K. Jiang, C. Feng, K. Liu, and S. Fan. A vapor-liquid-solid model for chemical vapor deposition growth of carbon nanotubes. *J Nanosci Nanotechnol*, 7:1494–1504, 2007.

[136] D. Takagi, Y. Kobayashi, and Y. Homma. Carbon nanotube growth from diamond. *J. Am. Chem. Soc*, 131:6922–6923, 2009.

[137] S. Shukrullah, N. M. Mohamed, M. S. Shaharun, and M. Y. Naz. Parametric study on vapor-solid-solid growth mechanism of multiwalled carbon nanotubes. *Mater. Chem. Phys.*, 176:32–43, 2016.

[138] M. Kumar and Y. Ando. Chemical vapor deposition of carbon nanotubes: a review on growth mechanism and mass production. *J. Nanosci. Nanotechnol.*, 10:3739–3758, 2010.

[139] A. Castan, S. Forel, L. Catala, I. Florea, F. Fossard, F. Bouanis, A. Andrieux-Ledier, S. Mazerat, T. Mallah, V. Huc, A. Loiseau, and C. S. Cojocaru. New method for the growth of single-walled carbon nanotubes from bimetallic nanoalloy catalysts based on prussian blue analog precursors. *Carbon*, 2017.

[140] J. Prasek, J. Drbohlavova, J. Chamoucka, J. Hubalek, O. Jasek, V. Adam, and R. Kizek. Methods for carbon nanotubes synthesisreview. *J. Mater. Chem.*, 21:15872–15884, 2011.

[141] M.-F. C. Fiawoo, A.-M. Bonnot, H. Amara, C. Bichara, J. Thibault-Penisson, and A. Loiseau. Evidence of correlation between catalyst particles and the single-wall carbon nanotube diameter: a first step towards chirality control. *Phys. Rev. Lett.*, 108:195503, 2012.

[142] S. Sakurai, M. Inaguma, D. N. Futaba, M. Yumura, and K. Hata. Diameter and density control of single-walled carbon nanotube forests by modulating ostwald ripening through decoupling the catalyst formation and growth processes. *Small*, 9:3584–3592, 2013.

[143] A. R. Harutyunyan, B. K. Pradhan, U. J. Kim, G. Chen, and P. C. Eklund. CVD synthesis of single wall carbon nanotubes under Soft conditions. *Nano Lett.*, 2:525–530, 2002.

[144] M. Palizdar, R. Ahgababazadeh, A. Mirhabibi, R. Brydson, and S. Pilehvari. Investigation of Fe/MgO catalyst support precursors for the chemical vapour deposition growth of carbon nanotubes. *J. Nanosci. Nanotechnol.*, 11:5345–5351, 2011.

[145] G. Zhong, S. Hofmann, F. Yan, H. Telg, J. H. Warner, D. Eder, C. Thomsen, W. I. Milne, and J. Robertson. Acetylene: a key growth precursor for single-walled carbon nanotube forests. *J. Phys. Chem. C*, 113:17321–17325, 2009.

[146] U. Narkiewicz, M. Podsiadły, R. Jędrzejewski, and I. Pełech. Catalytic decomposition of hydrocarbons on cobalt, nickel and iron catalysts to obtain carbon nanomaterials. *Appl. Catal., A*, 384:27–35, 2010.

[147] Y. Shirazi, M. A. Tofighy, T. Mohammadi, and A. Pak. Effects of different carbon precursors on synthesis of multiwall carbon nanotubes: purification and functionalization. *Appl. Surf. Sci.*, 257:7359–7367, 2011.

[148] H. Li, D. He, T. Li, M. Genestoux, and J. Bai. Chemical kinetics of catalytic chemical vapor deposition of an acetylene/xylene mixture for improved carbon nanotube production. *Carbon*, 48:4330–4342, 2010.

[149] P. Nikolaev, M. J. Bronikowski, R. Kelley Bradley, F. Rohmund, D. T. Colbert, K.A Smith, and R. E. Smalley. Gas-phase catalytic growth of single-walled carbon nanotubes from carbon monoxide. *Chem. Phys. Lett.*, 313:91–97, 1999.

[150] C. L. Pint, N. Nicholas, S. T. Pheasant, J. G. Duque, A. N. G. Parra-Vasquez, G.Eres, M. Pasquali, and R. H. Hauge. Temperature and gas pressure effects in

vertically aligned carbon nanotube growth from FeMo catalyst. *J. Phys. Chem. C*, 112:14041–14051, 2008.

[151] Yoke Khin Yap. Growth mechanisms of vertically-aligned carbon, boron nitride, and zinc oxide nanotubes. In *AIP Conf. Proc. 1150*, 2009.

[152] J. Zhao, Q.Y. Gao, C. Gu, and Y. Yang. Preparation of multi-walled carbon nanotube array electrodes and its electrochemical intercalation behavior of Li ions. *Chem. Phys. Lett.*, 358:77–82, 2002.

[153] D. T. Welna, L. Qu, B. E. Taylor, L. Dai, and M. F. Durstock. Vertically aligned carbon nanotube electrodes for lithium-ion batteries. *J. Power Sources*, 196:1455–1460, 2011.

[154] H. Zhou, L. Zhang, D. Zhang, S. Chen, P. R. Coxon, X. He, M. Coto, H-K Kim, K. Xi, and S. Ding. A universal synthetic route to carbon nanotube/transition metal oxide nano-composites for lithium ion batteries and electrochemical capacitors. *Sci. Rep.*, 6:37752, 2016.

[155] K-H. Kim, A. Gohier, J. E. Bourée, M. Chatelet, and C-Sorin Cojocaru. The role of catalytic nanoparticle pretreatment on the growth of vertically aligned carbon nanotubes by hot-filament chemical vapor deposition. *Thin Solid Films*, 575:84–91, 2015.

[156] T. de los Arcos, M. G. Garnier, J. W. Seo, P. Oelhafen, V. Thommen, and D. Mathys. The influence of catalyst chemical state and morphology on carbon nanotube growth. *J. Phys. Chem. B*, 108:7728–7734, 2004.

[157] Q. Li, X. Zhang, R. F. DePaula, L. Zheng, Y. Zhao, L. Stan, T. G. Holesinger, P. N. Arendt, D. E. Peterson, and Y. T. Zhu. Sustained growth of ultralong carbon nanotube arrays for fiber spinning. *Adv. Mater.*, 18:3160–3163, 2006.

[158] M.S. Dresselhaus, G. Dresselhaus, and P. Avouris. *Carbon Nanotubes Synthesis, Structure, Properties, and Applications.* Berlin, springer edition, 2001.

[159] A. Bogner, P.-H. Jouneau, G. Thollet, D. Basset, and C. Gauthier. A history of scanning electron microscopy developments: Towards wet-STEM" imaging. *Micron*, 38:390–401, 2007.

[160] D. Su. Advanced electron microscopy characterization of nanomaterials for catalysis. *Green Energy & Environment*, 2:70–83, 2017.

[161] B. Padya, K. V. P. Prabhakar, and P. K. Jain. Synthesis of vertically aligned carbon nanotube arrays by injection method in CVD. *J Nanosci Nanotechnol*, 10:4960–4966, 2010.

[162] T. Yamada, T. Namai, K. Hata, D. N. Futaba, K. Mizuno, J. Fan, M. Yudasaka, M. Yumura, and S. Iijima. Size-selective growth of double-walled carbon nanotube forests from engineered iron catalysts. *Nat. Nanotech.*, 1:131–136, 2006.

[163] Y. Yun, V. Shanov, Y. Tu, S. Subramaniam, and M. J. Schulz. Growth mechanism of long aligned multiwall carbon nanotube arrays by water-assisted chemical vapor deposition. *J. Phys. Chem. B*, 110:23920–23925, 2006.

[164] D. Herbert and J. Ulam. Electric dry cells and storage batteries., 1962.

[165] M. Barghamadi, A. Kapoor, and C. Wen. A review on Li-S batteries as a high efficiency rechargeable lithium battery. *J. Electrochem. Soc.*, 160:A1256–A1263, 2013.

[166] S. S. Zhang. Liquid electrolyte lithium/sulfur battery: Fundamental chemistry, problems, and solutions. *J. Power Sources*, 231:153–162, 2013.

[167] Y-J. Choi, Y-D. Chung, C-Y. Baek, K-W. Kim, H-J. Ahn, and J-H. Ahn. Effects of carbon coating on the electrochemical properties of sulfur cathode for lithium/-sulfur cell. *J. Power Sources*, 184:548–552, 2008.

[168] R. D. Rauh, F. S. Shuker, J. M. Marston, and S. B. Brummer. Formation of lithium polysulfides in aprotic media. *J. Inorg. Nucl. Chem.*, 39:1761–1766, 1977.

[169] R. D. Rauh, K. M. Abraham, G. F. Pearson, J. K. Surprenant, and S. B. Brummer. A lithium/dissolved sulfur battery with an organic electrolyte. *J. Electrochem. Soc.*, 126:523–527, 1979.

[170] Y. V. Mikhaylik and J. R. Akridge. Polysulfide shuttle study in the Li/S battery system. *J. Electrochem. Soc.*, 151:A1969–A1976, 2004.

[171] V. S. Kolosnitsyn and E. V. Karaseva. Lithium-sulfur batteries: Problems and solutions. *Russ. J. Electrochem.*, 44:506–509, 2008.

[172] Z. W. Seh, W. Li, J. J. Cha, G. Zheng, Y. Y, M. T. McDowell, P-C. Hsu, and Y. Cui. Sulphur-TiO_2 yolk-shell nanoarchitecture with internal void space for long-cycle lithium-sulphur batteries. *Nat. Commun.*, 4(1331), 2013.

[173] S-E. Cheon, S-S. Choi, J-S. Han, Y-S. Choi, B-H. Jung, and H. S. Lim. Capacity fading mechanisms on cycling a high-capacity secondary sulfur cathode. *J. Electrochem. Soc.*, 151:A2067–A2073, 2004.

[174] Y-X. Yin, S. Xin, Y-G. Guo, and L-J. Wan. Lithium-sulfur batteries: Electrochemistry, materials, and prospects. *Angew. Chem. Int. Ed*, 52:13186–13200, 2013.

[175] B. Zhang, C. Lai, Z. Zhou, and X. P. Gao. Preparation and electrochemical properties of sulfur-acetylene black composites as cathode materials. *Electrochim. Acta*, 54:3708–3713, 2009.

[176] J-J. Chen, X. Jia, Q-J. She, C. Wang, Q. Zhang, M-S. Zheng, and Q-F. Dong. The preparation of nano-sulfur/MWCNTs and its electrochemical performance. *Electrochim. Acta*, 55:8062–8066, 2010.

[177] C. Wang, J-J. Chen, Y-N. Shi, M-S. Zheng, and Q-F. Dong. Preparation and performance of a core-shell carbon/sulfur material for lithium/sulfur battery. *Electrochim. Acta*, 55:7010–7015, 2010.

[178] Y-S. Su and A. Manthiram. A facile in situ sulfur deposition route to obtain carbon-wrapped sulfur composite cathodes for lithium-sulfur batteries. *Electrochim. Acta*, 77:272–278, 2012.

[179] B. Zhang, X. Qin, G. R. Li, and X. P. Gao. Enhancement of long stability of sulfur cathode by encapsulating sulfur into micropores of carbon spheres. *Energy Environ. Sci.*, 3:1531–1537, 2010.

[180] S. Xin, L. Gu, N-H. Zhao, Y-X. Yin, L-J. Zhou, Y-G. Guo, and L-J. Wan. Smaller sulfur molecules promise better lithium-sulfur batteries. *J. Am. Chem. Soc.*, 134:18510–18513, 2012.

[181] X. Li, Y. Cao, W. Qi, L. V. Saraf, J. Xiao, Z. Nie, J. Mietek, J-G. Zhang, B. Schwenzer, and J. Liu. Optimization of mesoporous carbon structures for lithium-sulfur battery applications. *J. Mater. Chem.*, 21:16603–16610, 2011.

[182] X. Tao, X. Chen, Y. Xia, H. Huang, Y. Gan, R. Wu, F. Chen, and W. Zhang. Highly mesoporous carbon foams synthesized by a facile, cost-effective and template-free Pechini method for advanced lithium-sulfur batteries. *J. Mater. Chem. A,*, 1:3295–3301, 2013.

[183] J. Schuster, G. He, B. Mandlmeier, T. Yim, K-T. Lee, T. Bein, and L. F. Nazar. Spherical ordered mesoporous carbon nanoparticles with high porosity for lithium-sulfur batteries. *Angew. Chem. Int. Ed.*, 124:3651 –3655, 2012.

[184] S-C. Han, M-S. Song, H. Lee, H-S. Kim, H-J. Ahn, and J-Y. Lee. Effect of multi-walled carbon nanotubes on electrochemical properties of lithium/sulfur rechargeable batteries. *J. Electrochem. Soc.*, 150:A889–A893, 2003.

[185] L. Yuan, H. Yuan, X. Qiu, L. Chen, and W. Zhu. Improvement of cycle property of sulfur-coated multi-walled carbon nanotubes composite cathode for lithium/sulfur batteries. *J. Power Sources*, 189:1141–1146, 2009.

[186] W. Wei, J. Wang, L. Zhou, J. Yang, B. Schumann, and Y. Nuli. CNT enhanced sulfur composite cathode material for high rate lithium battery. *Electrochem. Commun.*, 13:399–402, 2011.

[187] J. Guo, Y. Xu, and C. Wang. Sulfur-impregnated disordered carbon nanotubes cathode for lithium-sulfur batteries. *Nano Lett.*, 11:4288–4294, 2011.

[188] Y-J. Choi, K-W. Kim, H-J. Ahn, and J-H. Ahn. Improvement of cycle property of sulfur electrode for lithium/sulfur battery. *J. Alloys Compd.*, 449:313–316, 2008.

[189] G. Zheng, Y. Y, J. J. Cha, S. S. Hong, and Y. Cui. Hollow carbon nanofiber-encapsulated sulfur cathodes for high specific capacity rechargeable lithium batteries. *Nano Lett.*, 11:4462–4467, 2011.

[190] M. Rao, X. Song, and E. J. Cairns. Nano-carbon/sulfur composite cathode materials with carbon nanofiber as electrical conductor for advanced secondary lithium/sulfur cells. *J. Power Sources*, 205:474–478, 2012.

[191] L. Ji, M. Rao, H. Zheng, L. Zhang, Y. Li, W. Duan, J. Guo, E. J. Cairns, and Y. Zhang. Graphene oxide as a sulfur immobilizer in high performance lithium/-sulfur cells. *J. Am. Chem. Soc.*, 133:18522–18525, 2011.

[192] S. Evers and L. F. Nazar. Graphene-enveloped sulfur in a one pot reaction: a cathode with good coulombic efficiency and high practical sulfur content. *Chem. Commun.*, 48:1233–1235, 2012.

[193] J-Q. Huang, X-F. Liu, Q. Zhang, C-M. Chen, M-Q Zhao, S-M. Zhang, W. Zhu, W-Z. Qian, and F. Wei. Entrapment of sulfur in hierarchical porous graphene for lithium-sulfur batteries with high rate performance from -40 to 60°C. *Nano Energy*, 2:314–321, 2013.

[194] B. H. Jeon, J. H. Yeon, K. M. Kim, and I. J. Chung. Preparation and electrochemical properties of lithium-sulfur polymer batteries. *J. Power Sources*, 109:89–97, 2002.

[195] N. Jayaprakash, J. Shen, S. S. Moganty, A. Corona, and L. A. Archer. Porous hollow carbon@sulfur composites for high-power lithium-sulfur batteries. *Angew. Chem. Int. Ed.*, 50:5904–5908, 2011.

[196] Y. Fu, Y-S. Su, and A. Manthiram. Highly reversible lithium/dissolved polysulfide batteries with carbon nanotube electrodes. *Angew. Chem.*, 125:7068–7073, 2013.

[197] Y-S. Su and A. Manthiram. A new approach to improve cycle performance of rechargeable lithium-sulfur batteries by inserting a free-standing MWCNT interlayer. *Chem. Commun.*, 48:8817–8819, 2012.

[198] S. S. Zhang and D. T. Tran. A proof-of-concept lithium/sulfur liquid battery with exceptionally high capacity density. *J. Power Sources*, 211:169–172, 2012.

[199] J-Z. Wang, L. Lu, M. Choucair, J. A. Stride, X. Xu, and H-K. Liu. Sulfur-graphene composite for rechargeable lithium batteries. *J. Power Sources*, 196:7030–7034, 2011.

[200] F-F. Zhang, X-B. Zhang, Y-H. Dong, and L-M. Wang. Facile and effective synthesis of reduced graphene oxide encapsulated sulfur via oil/water system for high performance lithium sulfur cells. *J. Mater. Chem.*, 22:11452–11454, 2012.

[201] Y. Cao, X. Li, I. A. Aksay, J. Lemmon, Z. Nie, Z. Yang, and J. Liu. Sandwich-type functionalized graphene sheet-sulfur nanocomposite for rechargeable lithium batteries. *Phys. Chem. Chem. Phys.*, 13:7660–7665, 2011.

[202] B. Wang, K. Li, D. Su, H. Ahn, and G. Wang. Superior electrochemical performance of sulfur/graphene nanocomposite material for high-capacity lithium-sulfur batteries. *Chem. Asian J.*, 7:1637–1643, 2012.

[203] H. Sun, G-L. Xu, Y-F. Xu, S-G. Sun, X. Zhang, Y. Qiu, and S. Yang. A composite material of uniformly dispersed sulfur on reduced graphene oxide: Aqueous one-pot synthesis, characterization and excellent performance as the cathode in rechargeable lithium-sulfur batteries. *Nano Res.*, 5:726–738, 2012.

[204] W. Ahn, K-B. Kim, K-N. Jung, K-H. Shin, and C-S. Jin. Synthesis and electrochemical properties of a sulfur-multi walled carbon nanotubes composite as a cathode material for lithium sulfur batteries. *J. Power Sources*, 202:394–399, 2012.

[205] L. Zhu, W. Zhu, X-B. Cheng, J-Q. Huang, H-J. Peng, S-H. Yang, and Q. Zhang. Cathode materials based on carbon nanotubes for high-energy-density lithium-sulfur batteries. *Carbon*, 75:161–168, 2014.

[206] S. Dorfler, M. Hagen, H. Althues, J. Tubke, S. Kaskel, and M. J. Hoffmann. High capacity vertical aligned carbon nanotube/sulfur composite cathodes for lithium-sulfur batteries. *Chem. Commun.*, 48:4097–4099, 2012.

[207] J. Wang, J. Chen, K. Konstantinov, L. Zhao, S. H. Ng, G. X. Wang, Z. P. Guo, and H. K. Liu. Sulphur-polypyrrole composite positive electrode materials for rechargeable lithium batteries. *Electrochim. Acta*, 51:4634–4638, 2006.

[208] Y. Fu and A. Manthiram. Orthorhombic bipyramidal sulfur coated with polypyrrole nanolayers as a cathode material for lithium-sulfur batteries. *J. Phys. Chem. C*, 116:8910–8915, 2012.

[209] Y. Fu and A. Manthiram. Enhanced cyclability of lithium-sulfur batteries by a polymer acid-doped polypyrrole mixed Ionic-electronic conductor. *Chem. Mater.*, 24:3081–3087, 2012.

[210] F. Wu, J. Chen, L. Li, T. Zhao, and R. Chen. Improvement of rate and cycle performence by rapid polyaniline coating of a MWCNT/sulfur cathode. *J. Phys. Chem. C*, 115:24411–24417, 2011.

[211] L. Xiao, Y. Cao, J. Xiao, B. Schwenzer, M. H. Engelhard, L. V. Saraf, Z. Nie, G. J. Exarhos, and J. Liu. A soft approach to encapsulate sulfur: polyaniline nanotubes for lithium-sulfur batteries with long cycle life. *Adv. Mater.*, 24:1176–1181, 2012.

[212] F. Wu, S. Wu, R. Chen, J. Chen, and S. Chen. Sulfur-polythiophene composite cathode materials for rechargeable lithium batteries. *Electrochem. Solid-State Lett.*, 13:A29–A31, 2010.

[213] F. Wu, J. Chen, R. Chen, S. Wu, L. Li, S. Chen, and T. Zhao. Sulfur/polythiophene with a core/shell structure: synthesis and electrochemical properties of the cathode for rechargeable lithium batteries. *J. Phys. Chem. C*, 115:6057–6063, 2011.

[214] W. Li, G. Zheng, Y. Yang, Z. W. Seh, N. Liu, and Y. Cui. High-performance hollow sulfur nanostructured battery cathode through a scalable, room temperature, one-step, bottom-up approach. *Proc. Natl. Acad. Sci. USA*, 110:7148–7153, 2013.

[215] J. Wang, J. Wang, C. Wan, K. Du, J. Xie, and N. Xu. Sulfur composite cathode materials for rechargeable lithium batteries. *Adv. Funct. Mater*, 13:487–492, 2003.

[216] L. Yin, J. Wang, J. Yang, and Y. Nuli. A novel pyrolyzed polyacrylonitrile-sulfur@MWCNT composite cathode material for high-rate rechargeable lithium/-sulfur batteries. *J. Mater. Chem.*, 21:6807–6810, 2011.

[217] S.H. Chung and A. Manthiram. A polyethylene glycol-supported microporous carbon coating as a polysulfide trap for utilizing pure sulfur cathodes in lithium-sulfur batteries. *Adv. Mater.*, 26:7352–7357, 2014.

[218] Y. Fu, Y-S. Su, and A. Manthiram. Sulfur-carbon nanocomposite cathodes improved by an amphiphilic block copolymer for high-rate lithium-sulfur batteries. *ACS Appl. Mater. Interfaces*, 4:6046–6052, 2012.

[219] M-S. Song, S-C. Han, H-S. Kim, J-H. Kim, K-T. Kim, Y-M. Kang, H-J. Ahn, S. X. Dou, and J-Y. Lee. Effects of nanosized adsorbing material on electrochemical properties of sulfur cathodes for Li/S secondary batteries. *J. Electrochem. Soc.*, 151:A791–A795, 2004.

[220] Y. Zhang, Y. Zhao, A. Yermukhambetova, Z. Bakenov, and P. Chen. Ternary sulfur/polyacrylonitrile/$Mg_{0.6}Ni_{0.4}O$ composite cathodes for high performance lithium/sulfur batteries. *J. Mater. Chem. A,*, 1:295–301, 2013.

[221] Y. J. Choi, B. S. Jung, D. J. Lee, J. H. Jeong, K. W. Kim, H. J. Ahn, K. K. Cho, and H. B. Gu. Electrochemical properties of sulfur electrode containing nano Al_2O_3 for lithium/sulfur cell. *Phys. Scr.*, T129:62–65, 2007.

[222] X. Ji, S. Evers, R. Black, and L. F. Nazar. Stabilizing lithium-sulphur cathodes using polysulphide reservoirs. *Nat. Commun.*, 2:325, 2011.

[223] S. Evers, T. Yim, and L. F. Nazar. Understanding the nature of absorption/adsorption in nanoporous polysulfide sorbents for the Li-S battery. *J. Phys. Chem. C*, 116:19653–19658, 2012.

[224] Y. Yang, M. T. McDowell, A. Jackson, J. J. Cha, S. S. Hong, and Y. Cui. New nanostructured Li_2S/silicon rechargeable battery with high specific energy. *Nano Lett.*, 10:1486–1491, 2010.

[225] J. Hassoun, J. Kim, D-J. Lee, H-G. Jung, S-M. Lee, Y-K. Sun, and B. Scrosati. A contribution to the progress of high energy batteries: A metal-free, lithium-ion, silicon-sulfur battery. *J. Power Sources*, 202:308–313, 2012.

[226] J. Hassoun and B. Scrosati. A high-performance polymer tin sulfur lithium ion battery. *Angew. Chem. Int. Ed*, 49:2371–2374, 2010.

[227] X. Fang, X. Guo, Y. MAo, C. Hua, L. Shen, Y. Hu, Z. Wang, F. Wu, and L. Chen. Mechanism of lithium storage in MoS_2 and the feasibility of using Li_2S/Mo nanocomposites as cathode materials for lithium-sulfur batteries. *Asian J. Chem.*, 7:1013–1017, 2012.

[228] Y. Yang, G. Zheng, S. Misra, J. Nelson, M. F. Toney, and Y. Cui. High-capacity micrometer-sized Li_2S particles as cathode materials for advanced rechargeable lithium-ion batteries. *J. Am. Chem. Soc*, 134:15387–15394, 2012.

[229] W. Ruythooren, K. Attenborough, S. Beerten, P. Merken, J. Fransaer, E. Beyne, C. Van Hoof, J. De Boeck, and J. P. Celis. Electrodeposition for the synthesis of microsystems. *J. Micromech. Microeng*, 10:101–107, 2000.

[230] A. A. Pasa and M. L. Munford. Electrodeposition, 2006.

[231] H. H. Lou and Y. Huang. Electroplating, 2006.

[232] F. Nasirpouri. *Electrodeposition of Nanostructured Materials*. Springer International Publishing, 2017.

[233] D. M. Mattox. *Handbook of pysical vapor deposition (PVD) processing.* Noyes Publications, Westwood, KJ, 1998.

[234] Q. Jia, S. Shan, L. Jiang, and Y. Wang. One-step synthesis of polyaniline nanofibers decorated with silver. *J. Appl. Polym. Sci.*, 115:26–31, 2010.

[235] X. Zhao, H-J. Ahn, K-W. Kim, K-K. Cho, and J-H. Ahn. Polyaniline-coated mesoporous carbon/sulfur composites for advanced lithium sulfur batteries. *J. Phys. Chem. C*, 119:7996–8003, 2015.

[236] S. S. Zhang. Effect of discharge cutoff voltage on reversibility of lithium/sulfur batteries with $LiNO_3$-contained electrolyte. *J. Electrochem. Soc.*, 159:A920–A923, 2012.

[237] S. S. Zhang. Role of $LiNO_3$ in rechargeable lithium/sulfur battery. *Electrochim. Acta*, 70:344–348, 2012.

[238] Z. Li and L. Yin. Nitrogen-doped MOF-derived micropores carbon as immobilizer for small sulfur molecules as a cathode for lithium sulfur batteries with excellent electrochemical performance. *ACS Appl. Mater. Interfaces*, 7:4029–4038, 2015.

[239] S. Zheng, F. Yi, Z. Li, Y. Zhu, Y. Xu, C. Luo, J. Yang, and C. Wang. Copper-stabilized sulfur-microporous carbon cathodes for LiS batteries. *Adv. Funct. Mater*, 24:4156–4163, 2014.

[240] X. Li, M. Rao, D. Chen, H. Lin, Y. Liu, Y. Liao, L. Xing, and W. Li. Sulfur supported by carbon nanotubes and coated with polyaniline: Preparation and performance as cathode of lithium-sulfur cell. *Electrochim. Acta*, 166:93–99, 2015.

[241] J. Wang, J. Yang, J. Xie, and N. Xu. A novel conductive polymer-sulfur composite cathode material for rechargeable lithium batteries. *Adv. Mater.*, 14:963–965, 2002.

[242] Y. Yang, G. Yu, J. J. Cha, H. Wu, M. Vosgueritchian, Y. Yao, Z. BAo, and Y. Cui. Improving the performance of lithium-sulfur batteries by conductive polymer coating. *ACS NANO*, 5:9187–9193, 2011.

[243] H. Wang, Y. Yang, Y. Liang, J. T. Robinson, Y. Li, A. Jackson, Y. Cui, and H. Dai. Graphene-wrapped sulfur particles as a rechargeable lithium-sulfur battery cathode material with high capacity and cycling stability. *Nano Lett.*, 11:2644–2647, 2011.

[244] K. T. Lee, R. Black, T. Yim, X. Ji, and L. F. Nazar. Surface-initiated growth of thin oxide coatings for Li-sulfur battery cathodes. *Adv. Energy Mater.*, 2:1490–1496, 2012.

[245] H. Kim, J. T. Lee, D-C. Lee, A. Magasinski, W-il. Cho, and G. Yushin. Plasma-enhanced atomic layer deposition of ultrathin oxide coatings for stabilized lithium-sulfur batteries. *Adv. Energy Mater.*, 3:1308–1315, 2013.

[246] J. Xu, B. Jin, H. Li, and Q. Jiang. Sulfur/alumina/polypyrrole ternary hybrid material as cathode for lithium-sulfur batteries. *Int. J. Hydrog. Energy*, 42:20749–20758, 2017.

[247] Las Positas College. Vaccum Technology. In *Las Positas College Vacuum Technology 60A and 60 B*, chapter 14, page 171. 2002.

[248] A. Yermukhambetova, Z. Bakenov, Y. Zhang, J. A. Darr, D. J. L. Brett, and P. R. Shearing. Examining the effect of nanosized $Mg_{0.6}Ni_{0.40}$ and Al_2O_3 additives on S/polyaniline cathodes for lithium-sulphur batteries. *J. Electroanal. Chem*, 780:407–415, 2016.

[249] S. Zheng, P. Han, Z. Han, H. Zhang, Z. Tang, and J. Yang. High performance C/S composite cathodes with conventional carbonate-based electrolytes in Li-S battery. *Sci. Rep.*, 4:4842, 2014.

[250] L. Qiu, S. Zhang, L. Zhang, M. Sun, and W. Wang. Preparation and enhanced electrochemical properties of nano-sulfur/poly(pyrrole-co-aniline) cathode material for lithium/sulfur batteries. *Electrochim. Acta*, 55:4632–4636, 2010.

[251] X. Yu, J. Xie, Y. Li, H. Huang, C. Lai, and K. Wang. Stable-cycle and high-capacity conductive sulfur-containing cathode materials for rechargeable lithium batteries. *J. Power Sources*, 146:335–339, 2005.

[252] K. Zhang, J. Li, Q. Li, J. Fang, Z. Zhang, Y. Lai, and Y. Tian. Improvement on electrochemical performance by electrodeposition of polyaniline nanowires at the top end of sulfur electrode. *Appl. Surf. Sci.*, 285:900–906, 2013.

[253] C. Colliex, T. Manoubi, and O. L. Krivanek. EELS in the electron microscope: A review of present trends. *J . Electron Microsc.*, 35:307–313, 1986.

[254] P. Bayle-Guillemaud, G. Radtke, and M. Sennour. Electron spectroscopy imaging to study ELNES at a nanoscale. *J. Microsc.*, 210:66–73, 2003.

[255] L. Roiban, L. Sorbier, C. Pichon, P. Bayle-Guillemaud, J. Werckmann, M. Drillon, and O. Ersen. Three-dimensional chemistry of multiphase nanomaterials by energy-filtered transmission electron microscopy tomography. *Microsc. Microanal.*, 18:1118–1128, 2012.

[256] O. Ersen, I. Florea, C. Hirlimann, and C. Pham-Huu. Exploring nanomaterials with 3D electron microscopy. *Mater. Today*, 18:395–408, 2015.

[257] L. Wang, T. Maxisch, and G. Ceder. A first-principles approach to studying the thermal stability of oxide cathode materials. *Chem. Mater*, 19:543–552, 2007.

[258] J. T. Richardson, R. Scates, and M. V. Twigg. X-ray diffraction study of nickel oxide reduction by hydrogen. *Appl. Catal., A*, 246:137–150, 2003.

[259] S. L. Candelaria, Y. Shao, W. Zhou, X. Li, J. Xiao, J-G. Zhang, Y. Wang, J. Liu, J. Li, and G. Cao. Nanostructured carbon for energy storage and conversion. *Nano Energy*, 1:195–220, 2012.

[260] G. Jeong, Y-U. Kim, H. Kim, Y-J. Kim, and H-J. Sohn. Prospective materials and applications for Li secondary batteries. *Energy Environ. Sci.*, 4:1986–2002, 2011.

[261] L. Ji, Z. Lin, M. Alcoutlabi, and X. Zhang. Recent developments in nanostructured anode materials for rechargeable lithium-ion batteries. *Energy Environ. Sci.*, 4:2682–2699, 2011.

[262] The Editors of Encyclopædia Britannica. Silicon (Si) chemical element.

[263] M. N. Obrovac and L. Christensen. Structural changes in silicon anodes during lithium insertion/extraction. *Electrochem. Solid-State Lett.*, 7:A93–A96, 2004.

[264] J. Li and J. R. Dahn. An in Situ X-ray diffraction study of the reaction of Li with crystalline Si. *J. Electrochem. Soc.*, 154:A156–A161, 2007.

[265] X. Xianxia, H. Liu, and J. Zhang. *Lithium-ion batteries: advanced materials and technologies.* Crc press edition, 2011.

[266] I. A. Profatilova, N-S. Choi, K. H. Yew, and W-U. Choi. The effect of ethylene carbonate on the cycling performance of a Si electrode. *Solid State Ion.*, (179):2399–2405, 2008.

[267] P. Limthongkul, Y-ll Jang, N. J. Dudney, and Y-M. Chiang. Electrochemically-driven solid-state amorphization in lithium-silicon alloys and implications for lithium storage. *Acta Mater.*, 51:1103–1113, 2003.

[268] M. N. Obrovac and L. J. Krause. Reversible cycling of crystalline silicon powder. *J. Electrochem. Soc.*, 154:A103–A108, 2007.

[269] T. D. Hatchard and J. R. Dahn. In situ XRD and electrochemical study of the reaction of lithium with amorphous silicon. *J. Electrochem. Soc.*, 151:A838–A842, 2004.

[270] B. Key, M. Morcrette, J-M. Tarascon, and C. P. Grey. Pair distribution function analysis and solid state NMR studies of silicon electrodes for lithium ion batteries: understanding the (de)lithiation mechanisms. *J. Am. Chem. Soc.*, 133:503–512, 2011.

[271] M. T. McDowell, S. W. Lee, C. Wang, and Y. Cui. The effect of metallic coatings and crystallinity on the volume expansion of silicon during electrochemical lithiation/delithiation. *Nano Energy*, 1:401–410, 2012.

[272] J. W. Wang, Y. He, F. Fan, X. H. Liu, S. Xia, Y. Liu, C. T. Harris, H. Li, J. Y. Huang, S. X. MAo, and T. Zhu. Two-phase electrochemical lithiation in amorphous silicon. *Nano Lett.*, 13:709–715, 2013.

[273] K. Peng, J. Jie, W. Zhang, and S-T. Lee. Silicon nanowires for rechargeable lithium-ion batteries anodes.. *Appl. Phys. Lett.*, 93:033105, 2008.

[274] L-F. Cui, R. Ruffo, C.-K. Chan, H. Peng, and Y. Cui. Crystalline-amorphous core-shell silicon nanowires for high capacity and high current battery electrodes. *Nano Lett.*, 9:491–495, 2009.

[275] M. H. Park, M. G. Kim, J. Joo, K. Kim, J. Kim, S. Ahn, Y. Cui, and J. Cho. Silicon nanotube battery anodes. *Nano Lett.*, 9:3844–3847, 2009.

[276] H. Wu, G. Chan, J. W. Choi, I. Ryu, Y. Yao, M. T. McDowell, S. W. Lee, A. Jackson, Y. Yang, L. Hu, and Y. Cui. Stable cycling of double-walled silicon nanotube battery anodes through solid-electrolyte interphase control. *Nat. Nanotech.*, 7:310–315, 2012.

[277] Z. Wen, G. Lu, S. Mao, H. Kim, S. Cui, K. Yu, X. Huang, P. T. Hurley, O. Mao, and J. Chen. Silicon nanotube anode for lithium-ion batteries. *Electrochem. Commun.*, 29:67–70, 2013.

[278] M. L. Carreon, A. K. Thapa, J. B. Jasinski, and M. K. Sunkara. The capacity and durability of amorphous silicon nanotube thin film anode for lithium ion battery applications. *ECS Electrochem. Lett.*, 4:A124–A128, 2015.

[279] B. Zhu, Y. Jin, Y. Tan, L. Zong, Y. Hu, L. Chen, Y. Chen, Q. Zhang, and J. Zhu. Scalable production of Si nanoparticles directly from low grade sources for lithium-ion battery anode. *Nano Lett.*, 15:5750–5754, 2015.

[280] H. S. Choi, S. J. Kim, H. W. Choi, C-E. Park, Y. J. Gao, Y. Hang, S-Y. Jeong, J-P. Kim, J-S. Bae, and C-R. Cho. Enhanced cycle stability of silicon nanoparticles coated with nitrogen-doped carbon layer for lithium-ion battery anode. *Curr. Appl. Phys.*, 17:1087–1093, 2017.

[281] T. Takamura, S. Ohara, M. Uehara, J. Suzuki, and K. Sekine. A vacuum deposited Si film having a Li extraction capacity over 2000 mAh/g with a long cycle life. *J. Power Sources*, 129:96–100, 2004.

[282] M. Ulldemolins, F. LeCras, B. Pecquenard, V. P. Phan, L. Martin, and H. Martinez. Investigation on the part played by the solid electrolyte interphase on the electrochemical performances of the silicon electrode for lithium-ion batteries. *J. Power Sources*, 206:245–252, 2012.

[283] Y. Chen, N. Du, H. Zhang, and D. Yang. Facile synthesis of uniform MWCNT@Si nanocomposites as high-performance anode materials for lithium-ion batteries. *J. Alloys Compd.*, 622:966–972, 2015.

[284] L. Zhong, J. Guo, and L. Mangolini. A stable silicon anode based on the uniform dispersion of quantum dots in a polymer matrix. *J. Power Sources*, 273:638–644, 2015.

[285] H. Jung, M. Park, S. H. Han, H. Lim, and S-K. Joo. Amorphous silicon thin-film negative electrode prepared by low pressure chemical vapor deposition for lithium-ion batteries. *Solid State Commun.*, 125:387–390, 2003.

[286] V. A. Sethuraman, M. J. Chon, M. Shimshak, V. Srinivasan, and P. R. Guduru. In situ measurements of stress evolution in silicon thin films during electrochemical lithiation and delithiation. *J. Power Sources*, 195:5062–5066, 2010.

[287] E. Biserni, N. Garino, A. LiBAssi, P. Bruno, and C. Gerbaldi. Mesoporous silicon nanostructures by pulsed laser deposition as Li-ion battery anodes . *ECS Trans*, 62:107–115, 2014.

[288] S. Ohara, J. Suzuki, K. Sekine, and T. Takamura. A thin film silicon anode for Li-ion batteries having a very large specific capacity and long cycle life. *J. Power Sources*, 136:303–306, 2004.

[289] B. Peng, F. Cheng, Z. Tao, and J. Chen. Lithium transport at silicon thin film: Barrier for high-rate capability anode. *J. Chem. Phys.*, 133:034701, 2010.

[290] V. A. Sethuraman, V. Srinivasan, A. F. Bower, and P. R. Guduru. In situ measurements of stress-potential coupling in lithiated silicon. *J. Electrochem. Soc.*, 157:A1253–A1261, 2010.

[291] J. Christensen. Modeling diffusion-induced stress in Li-ion cells with porous electrodes. *J. Electrochem. Soc.*, 157:A366–A380, 2010.

[292] H. Tokuda, K. Hayamizu, K. Ishii, M. A. B. H. Susan, and M. Watanabe. Physicochemical properties and structures of room temperature ionic liquids. 2. Variation of alkyl chain length in imidazolium cation. *J. Phys. Chem. B*, 109:6103–6110, 2005.

[293] F. Endres, A. P. Abott, and D. MacFarlane. *Electrodeposition in ionic liquids.* Wiley VCH, 2008.

[294] D. R. MacFarlane, P. Meakin, J. Sun, N. Amini, and M. Forsyth. Pyrrolidinium imides: A new family of molten salts and conductive plastic crystal phases. *J. Phys. Chem. B*, 103:4164–4170, 1999.

[295] Solvionic. 1-Butyl-1-Methylpyrrolidinium Bis(trifluoromethylsulfonyl)imide.

[296] F. Endres, O. Höfft, N. Borisenko, L. H. Gasparotto, A. Prowald, R. Al-Salman, T. Carstens, R. Atkin, A. Bund, and S. Zein El Abedin. Do solvation layers of ionic liquids influence electrochemical reactions? *Phys. Chem. Chem. Phys.*, 12:1724–1732, 2010.

[297] F. Martineau. *Elaboration de nanofils et de nanotubes de silicium par électrodéposition en liquide ionique et propriétés d'émission associées.* PhD thesis, Reims Champagne-Ardenne, 2011.

[298] SigmaAldrich. Silicon tetrachloride.

[299] S. Zein El Abedin, N. Borissenko, and F. Endres. Electrodeposition of nanoscale silicon in a room temperature ionic liquid. *Electrochem. Commun.*, 6:510–514, 2004.

[300] A. J. Bard and L. R. Faulkner. *Electrochemical Methods Fundamental and Applications.* JOHN WILEY and SONS, INC., New York, 2nd edition, 2001.

[301] Q. Xiao, Y. Fan, X. Wang, R. A. Susantyoko, and Q. Zhang. A multilayer Si/CNT coaxial nanofiber LIB anode with a high areal capacity. *Energy Environ. Sci.*, 7:655–661, 2014.

[302] M. R. Zamfir, H. T. Nguyen, E. Moyen, Y. H. Lee, and D. Pribat. Silicon nanowires for Li-based battery anodes: a review. *J. Mater. Chem. A*,, 1:9566–9586, 2013.

[303] X. H. Liu, J. W. Wang, S. Huang, F. Fan, X. Huang, Y. Liu, S. Krylyuk, J. Yoo, S. A. Dayeh, A. V. Davydov, S. X. Mao, S. T. Picraux, S. Zhang, J. Li, T. Zhu, and J. Y. Huang. In situ atomic-scale imaging of electrochemical lithiation in silicon. *Nat. Nanotech.*, 7:749–756, 2012.

[304] W. O. Filtvedt, A. Holt, P. A. Ramachandran, and M. C. Melaaen. Chemical vapor deposition of silicon from silane: Review of growth mechanisms and modeling/scaleup of fluidized bed reactors. *Sol. Energ. Mat. Sol. Cells*, 107:188–200, 2012.

[305] C. Yuqin, L. Hong, W. Lie, and L. Tianhong. Irreversible capacity loss of graphite electrode in lithium-ion batteries. *J. Power Sources*, 68:187–190, 1997.

[306] A. Magasinski, P. Dixon, B. Hertzberg, A. Kvit, J. Ayala, and G. Yushin. High-performance lithium-ion anodes using a hierarchical bottom-up approach. *Nat. Mater.*, 9:353–358, 2010.

[307] R. Epur, M. K. Datta, and P.-N. Kumta. Nanoscale engineered electrochemically active silicon-CNT heterostructures-novel anodes for Li-ion application. *Electrochim. Acta*, 85:680–684, 2012.

[308] J. P. Maranchi, A. F. Hepp, and P.-N. Kumta. High capacity, reversible silicon thin-film anodes for lithium-ion batteries. *Electrochem. Solid-State Lett.*, 6:A198–A201, 2003.

[309] M. K. Datta and P.-N. Kumta. In situ electrochemical synthesis of lithiated silicon-carbon based composites anode materials for lithium ion batteries. *J. Power Sources*, 194:1043–1052, 2009.

[310] Y. Oumellal, N. Delpuech, D. Mazouzi, N. Dupre, J. GAubicher, P. Moreau, P. Soudan, B. Lestriez, and D. Guyomard. The failure mechanism of nano-sized Si-based negative electrodes for lithium ion batteries. *J. Mater. Chem.*, 21:6201–6208, 2011.

[311] L. Leveau. *Etude de nanofils de silicium comme matériau d'électrode négative de batterie lithium-ion.* PhD thesis, Ecole Polytechnique, 2015.

[312] D. Mazouzi, D. Reyter, M. Gauthier, P. Moreau, D. Guyomard, L. Roue, and B. Lestriez. Very high surface capacity observed using Si negative electrodes embedded in copper foam as 3D current collectors. *Adv. Energy Mater.*, 4:1301718, 2014.

[313] J. K. Lee, C. Oh, N. Kim, J-Y. Hwang, and Y-K. Sun. Rational design of silicon-based composites for high-energy storage devices. *J. Mater. Chem. A,*, 4:5366–5384, 2016.

[314] J. Hassoun, Y-K. Sun, and B. Scrosati. Rechargeable lithium sulfide electrode for a polymer tin/sulfur lithium-ion battery. *J. Power Sources*, 196:343–348, 2011.

[315] Y. Fu, C. Zu, and A. Manthiram. In Situ-formed Li_2S in lithiated graphite electrodes for lithium-sulfur batteries. *J. Am. Chem. Soc.*, 135:18044–18047, 2013.

[316] L. Wang, Y. Wang, and Y. Xia. A high performance lithium-ion sulfur battery based on a Li_2S cathode using a dual-phase electrolyte. *Energy Environ. Sci.*, 8:1551–1558, 2015.

[317] H. Jha, I. Buchberger, X. Cui, S. Meini, and H. A. Gasteiger. Li-S batteries with Li_2S cathodes and Si/C anodes. *J. Electrochem. Soc.*, 162:A1829–A1835, 2015.

[318] M. Kohl, J. Bruckner, I. Bauer, H. Althues, and S. Kaskel. Synthesis of highly electrochemically active Li_2S nanoparticles for lithium-sulfur-batteries. *J. Mater. Chem. A,*, 3:16307–16312, 2015.

[319] N. Liu, L. Hu, M. T. McDowell, A. Jackson, and Y. Cui. Prelithiated silicon nanowires as an anode for lithium-ion batteries. *ACS NANO*, 5:6487–6493, 2011.

[320] D. B. Williams and C. B. Carter. Transmission Electron Microscopy. In *Transmission Electron Microscopy A Textbook for Materials Science*, pages 22–32. Plenum press New York and London, 1996.

[321] P. J. Goodhew, J. Humphreys, and R. Beanland. *Electron Microscopy and Analysis*. Third edit edition, 2000.

[322] R. F. Egerton. *Electron Energy-Loss Spectroscopy in the Electron Microscope*. 2011.

[323] H. Stanjek and W. Hausler. Basics of X-ray diffraction. *Hyperfine Interact.*, 154:107–119, 2004.

[324] P. Dutta. Grazing incidence X-ray diffraction. *Curr. Sci.*, 78:1478–1483, 2000.

université PARIS-SACLAY
ÉCOLE DOCTORALE
INTERFACES
Approches Interdisciplinaires : Fondements, Applications et Innovation

Titre : Fabrication d'électrodes nanostructurées hybrides hiérarchisées à base de nanotubes de carbone décorés par des nanoparticules pour les batteries Li-Ion

Mots clefs : stockage d'énergie, batterie lithium-ion, nanomatériaux, nanostructures, cathode, anode
Résumé : Cette thèse est consacrée à la fabrication ascendante (bottom-up) de matériaux nanostructurés hybrides hiérarchisés à base de nanotubes de carbone alignés verticalement (VACNTs) décorés par des nanoparticules (NPs). En fonction de leur utilisation comme cathode ou anode, des nanoparticules de soufre (S) ou silicium (Si) ont été déposées. En raison de leur structure unique et de leurs propriétés électroniques, les VACNTs agissent comme une matrice de support et un excellent collecteur de courant, améliorant ainsi les voies de transport électroniques et ioniques. La nanostructuration et le contact du S avec un matériau hôte conducteur améliore sa conductivité, tandis que la nanostructuration du Si permet d'accommoder plus facilement les variations de volume pendant les réactions électrochimiques. Dans la première partie de la thèse, nous avons synthétisé des VACNTs par une méthode de dépôt chimique en phase vapeur (HF-CVD) directement sur des fines feuilles commerciales d'aluminium et de cuivre sans aucun prétraitement des substrats. Dans la deuxième partie, nous avons décoré les parois latérales des VACNTs avec différents matériaux d'électrode, dont des nanoparticules de S et de Si. Nous avons également déposé et caractérisé des nanoparticules de nickel (Ni) sur les VACNTs en tant que matériaux alternatifs pour l'électrode positive. Aucun additif conducteur ou aucun liant polymère n'a été ajouté à la composition d'électrode. La décoration des nanotubes de carbone a été effectuée par deux méthodes différentes: méthode humide par électrodéposition et méthode sèche (par dépôt physique en phase vapeur (PVD) ou par CVD). Les structures hybrides obtenues ont été testées électrochimiquement séparément dans une pile bouton contre une contre-électrode de lithium. A notre connaissance, il s'agit de la première étude de l'évaporation du soufre sur les VACNTs et de la structure résultante (appelée ici S@VACNTs). Des essais préliminaires sur les cathodes nanostructurées obtenues (S@VACNTs revêtus d'alumine ou de polyaniline) ont montré qu'il est possible d'atteindre une capacité spécifique proche de la capacité théorique du soufre. La capacité surfacique de S@VACNTs, avec une masse de S de 0.76 mg cm^{-2}, à un régime C/20 atteint une capacité de 1.15 mAh cm^{-2} au premier cycle. Pour les anodes nanostructurées au silicium (Si@VACNTs), avec une masse de Si de 4.11 mg cm^{-2}, on montre une excellente capacité surfacique de 12.6 mAh cm^{-2}, valeur la plus élevée pour les anodes à base de silicium nanostructurées obtenues jusqu'à présent. Dans la dernière partie de la thèse, les électrodes nanostructurées fabriquées ont été assemblées afin de réaliser la batterie complète (Li_2S/Si) et sa performance électrochimique a été testée. Les capacités surfaciques obtenues pour les électrodes nanostructurées de S et de Si ouvrent la voie à la réalisation d'une LIB à haute densité d'énergie, entièrement nanostructurée, et démontrent le grand potentiel du concept proposé à base d'électrodes nanostructurées hybrides hiérarchisées.

Title : Fabrication of hierarchical hybrid nanostructured electrodes based on nanoparticles decorated carbon nanotubes for Li-Ion batteries

Keywords : Energy storage, lithium-ion battery, nanomaterial, nanostructure, cathode, anode
Abstract : This thesis is devoted to the bottom-up fabrication of hierarchical hybrid nanostructured materials based on active vertically aligned carbon nanotubes (VACNTs) decorated with nanoparticles (NPs). Owing to their unique structure and electronic properties, VACNTs act as a support matrix and an excellent current collector, and thus enhance the electronic and ionic transport pathways. The nanostructuration and the confinement of sulfur (S) in a conductive host material improve its conductivity, while the nanostructuration of silicon (Si) accommodates better the volume change during the electrochemical reactions. In the first part of the thesis, we have synthesized VACNTs by a hot filament chemical vapor deposition (HF-CVD) method directly over aluminum and copper commercial foils without any pretreatment of the substrates. In the second part, we have decorated the sidewalls and the surface of the VACNT carpets with various LIB's active electrode materials, including S and Si NPs. We have also deposited and characterized nickel (Ni) NPs on CNTs as alternative materials for the cathode electrode. No conductive additives or any polymer binder have been added to the electrode composition. The CNTs decoration has been done systematically through two different methods: wet method by electrodeposition and dry method by physical vapor deposition (PVD). The obtained hybrid structures have been electrochemically tested separately in a coin cell against a lithium counter-electrode. Regarding the S evaporation on VACNTs, and the S@VACNTs structure, these topics are investigated for the first time to the best of our knowledge. Preliminary tests on the obtained nanostructured cathodes (S@VACNTs coated with alumina or polyaniline) have shown that it is possible to attain a specific capacity close to S theoretical storage capacity. The surface capacity of S@VACNTs, with 0.76 mg cm^{-2} of S, at C/20 rate reaches 1.15 mAh cm^{-2} at the first cycle. For the nanostructured anodes Si@VACNTs, with 4.11 mg cm^{-2} of Si showed an excellent surface capacity of 12.6 mAh cm^{-2}, the highest value for nanostructured silicon anodes obtained so far. In the last part of the thesis, the fabricated nanostructured electrodes have been assembled in a full battery (Li_2S/Si) and its electrochemical performances experimentally tested. The high and well-balanced surface capacities obtained for S and Si nanostructured electrodes pave the way for realization of high energy density, all-nanostructured LIBs and demonstrate the large potentialities of the proposed hierarchical hybrid nanostructures' concept.

Université Paris-Saclay
Espace Technologique / Immeuble Discovery
Route de l'Orme aux Merisiers RD 128 / 91190 Saint-Aubin, France